Universidade do Minho
Escola de Engenharia

António Ventura Gouveia

Constitutive models for the material nonlinear analysis of concrete structures including time-dependent effects

Novembro de 2011

Universidade do Minho
Escola de Engenharia

António Ventura Gouveia

Constitutive models for the material nonlinear analysis of concrete structures including time-dependent effects

Modelos constitutivos para a análise não linear material de estruturas de betão incluindo efeitos diferidos

Tese de Doutoramento
Estruturas /Engenharia Civil

Trabalho efectuado sob a orientação de
Professor Doutor Joaquim António Oliveira de Barros

e co-orientação de
Professor Doutor Álvaro Ferreira Marques Azevedo

Novembro de 2011

To my lovely wife Cris
and my wonderful daughters Raquel, Gabriela and Matilde

Acknowledgments

This research was carried out at the Department of Civil Engineering of the University of Minho, Portugal, under the supervision of Prof. Joaquim Barros and co-supervision of Prof. Álvaro Azevedo.

I express my gratitude to Prof. Joaquim Barros for his support, encouragement, advice, several interesting discussions and friendship. I also thank all the teachings handed down over the years, since I started as his undergraduate student.

I would also like to express my gratitude to Prof. Álvaro Azevedo for his support, encouragement, recommendations, fruitful discussions and friendship.

The financial support provided by the Fundação para a Ciência e Tecnologia (Portuguese Foundation for the Science and Technology) and the European Social Fund, Grant number SFRH/BD/23326/2005, is gratefully acknowledged.

I am grateful to the friends from the Civil Engineering Department of the University of Minho, especially to Prof. Sena Cruz, for his support, fruitful discussions about some topics related to this work and for his friendship and in a later phase to Prof. Miguel Azenha for the productive discussions and friendship. The validation of some developed numerical tools by the researchers Inês Costa, Bernardo Neto, Hadi Baghi and Matteo Breveglieri is appreciated.

The support and friendship of the colleagues from the Civil Engineering Department of the School of Technology & Management of the Polytechnic Institute of Viseu are gratefully valued.

To all my friends that always supported and encouraged me during the development of the present work I would like to express my gratitude.

Finally, my gratitude to all my family, Manel, Lena, Rafa, Pipa, Xinha, Ana, Fernando, Bruno, Paulo and in particular to my wife, Cris, my daughters, Raquel, Gabriela and Matilde, my father, António and my mother-in-law, Mariazinha. This work was only possible because of their unconditional support, love and friendship. Thanks for your patience.

I would also like to perpetuate the memory of my mother, Laurentina, and my father-in-law, Aguiar. God's presence during this work was also fundamental. Thanks for the gift of life.

This research was funded by the National Strategic Reference Framework 2007-2013, Operational Program Human Potential (QREN/POPH) - Tipology 4.1 - Advanced Training [subsidized by the European Social Fund (FSE) and by National funds from the Ministry of Science, Technology and Higher Education (MCTES-FCT)].

Abstract

In recent years concrete technology has been improved significantly due, mainly, to the development of self-compacting concrete, ultra-fluid cement based materials, high performance fiber reinforced concrete and engineered cement composites. These developments have their main applicability in the pre-casting industry, where the earliest demoulding of the pre-cast elements is an important aim for economic reasons. Due to the relatively high cost of these advanced cement based materials, optimization of the behavior of structural elements made with these materials is a fundamental issue for their competitiveness. As a consequence, these materials are, in general, applied to relatively thin elements that require special attention in terms of shear and punching resistance. With the aim of studying these types of structures, a multi-directional fixed smeared crack model for plane shells has been developed. This model implements an innovative approach for capturing the behavior of laminar structures failing in punching, which is based on the adoption of a softening diagram to simulate the behavior of the out-of-plane shear stress components.

Since most advanced cement based materials have relatively high binder content, the risk of cracking at an early age should be evaluated using models that can estimate the heat generated by the hydration of pozolanic components and the induced stress fields. For this purpose, a FEM-based heat transfer model has been developed and integrated into a mechanical model that can simulate the crack initiation and propagation in structures discretized with solid finite elements. The mechanical model is a 3D multi-directional smeared crack model with the capability of simulating the behavior of structures failing in punching and shear. Shrinkage and creep are also a concern mainly for service limit states due to crack opening limits.

In the last two decades fiber reinforced polymer composite materials have also been used for the structural rehabilitation of concrete structures, mainly for the flexural and shear strengthening of reinforced concrete beams. The prediction of the behavior of the shear

strengthened beams requires the use of crack constitutive models to simulate the decrease of the shear stress degradation with the crack opening evolution, in agreement. Two numerical approaches are proposed to simulate this phenomenon. One is based on the use of a softening crack shear stress versus crack shear strain diagram to model the fracture mode II, while in the other the total crack shear stress is obtained from the total crack shear strain adopting a crack shear modulus that decreases with the crack normal strain.

Fiber reinforcement mechanisms are more effectively mobilized when support redundancy of a structure is high, since the stress redistribution capacity provides to this type of structure an ultimate load that is much higher than the load at crack initiation. However, the supporting conditions of a structure can change during the loading process, and even a loss of contact can occur. To simulate accurately these situations, linear, nonlinear and unilateral support conditions are numerically implemented.

To increase the robustness of the developed numerical models, innovative numerical strategies are implemented in the stress update phase of the nonlinear finite element analysis process. Furthermore, to improve the convergence performance of the finite element nonlinear analyses an arc-length algorithm is implemented.

All the numerical models are implemented in the FEMIX 4.0 FEM package, using the ANSI-C computer language.

Resumo

Nos últimos anos tem havido um crescente melhoramento a nível dos processos tecnológicos do betão, principalmente devido ao desenvolvimento de betão auto-compactável, de materiais de matriz cimentícia ultra-fluídos e de betões de elevado desempenho reforçados com fibras. Estes desenvolvimentos têm particular aplicação na indústria de pré-fabricação, onde a rápida desmoldagem dos elementos pré-fabricados é um objectivo importante por razões económicas. Devido aos custos relativamente elevados destes materiais avançados de matriz cimentícia, a optimização do comportamento de elementos estruturais constituídos por esses materiais é fundamental para assegurar a sua competitividade. Em consequência, estes materiais são, em geral, aplicados a elementos relativamente delgados que podem exigir uma atenção especial em termos de resistência ao corte e ao punçoamento. Neste contexto, no presente trabalho é desenvolvido um modelo de fendilhação para cascas planas com a possibilidade da ocorrência de múltiplas fendas fixas distribuídas, integrando uma abordagem inovadora para simular o fenómeno de punçoamento. Esta abordagem é baseada na adopção de um diagrama com amolecimento que simula o comportamento das componentes de corte transversal.

Estes materiais avançados de matriz cimentícia têm uma quantidade de ligante relativamente elevado, pelo que a possibilidade de ocorrência de fendilhação nas primeiras idades deve ser avaliada usando modelos que permitam estimar o calor gerado pela hidratação do ligante durante o seu processo de cura, bem como a determinação das correspondentes tensões. Para o efeito, no presente trabalho é desenvolvido um modelo de transferência de calor baseado no método dos elementos finitos, o qual é integrado num modelo mecânico que permite simular o início de fendilhação e a sua propagação em estruturas discretizadas por elementos finitos de volume. Este modelo de fendilhação 3D tem a possibilidade de simular a ocorrência de múltiplas fendas fixas distribuídas, bem como o comportamento de estruturas cujo modo de ruptura é condicionado pelas componentes de corte. A retracção e a fluência também são fenómenos de relevância em estruturas constituídas por estes tipos de materiais, principalmente em estados limites de

serviço por abertura de fenda, pelo que a sua modelação foi também integrada no modelo termo-mecânico.

Nas últimas duas décadas, materiais de matriz polimérica reforçados com fibras contínuas têm sido utilizados na reabilitação estrutural de estruturas de betão, principalmente para o reforço à flexão e ao corte de vigas de betão armado. A previsão do comportamento das vigas reforçadas ao corte requer o uso de modelos constitutivos capazes de simular a diminuição da capacidade de transferência de tensão de corte com a evolução da abertura de fenda. Duas abordagens numéricas são propostas para este fim. Uma delas baseia-se na utilização de um diagrama de amolecimento para a modelação do modo II de fractura. A outra suporta-se numa formulação total para a relação entre a tensão e a extensão de corte na fenda, adoptando um módulo de rigidez correspondente ao modo II de fractura que diminui com a extensão normal à fenda.

De forma a aumentar a robustez dos modelos numéricos desenvolvidos, foram implementadas algumas estratégias de actualização do estado de tensão no material durante o processo de análise não linear. Com o objectivo de melhorar as características de convergência dos métodos numéricos utilizados foram introduzidos algoritmos baseados na técnica *arc-length*. Condições de apoio com comportamento linear, não linear e unilateral também foram numericamente implementadas.

Todos os modelos numéricos foram implementados no software de elementos finitos FEMIX usando a linguagem de programação ANSI-C.

Contents

Chapter 4 – Modeling of the crack shear component

Chapter 5 – Multi-fixed smeared 3D crack model to simulate the behavior of concrete structures

Chapter 6 – Thermo-mechanical model

Chapter 7 - Conclusions

List of symbols and abbreviations

Abbreviations

CFRP – Carbon fibre reinforced polymer

CM – Coarse mesh

CMOD – Crack mouth opening displacement

CMSD – Crack mouth sliding displacement

CrCS – Crack coordinate system

EBR – Externally bonded reinforcement

ETS – Embedded through-section

FEM – Finite element method

FRC – Fiber reinforced concrete

GCS – Global coordinate system

IP – Integration point

NSM – Near surface mounted

RC – Reinforced concrete

RM – Refined mesh

SCC – Self-compacting concrete

SFRC – Steel fiber reinforced concrete

SFRSCC – Steel fiber reinforced self-compacting concrete

List of symbols

Roman letters

$A_{F-\delta}^{\exp}$ – areas beneath the experimental load-deflection curves

$A_{F-\delta}^{num}$ – areas beneath the numerical load-deflection curves

A_T – rate constant

$\underline{a}$ – displacement vector

$\underline{a}_n$ – vector of the nodal displacements

b – scale factor that converts the magnitude of load to the magnitude of the displacement

$C(t,t_0)$ – specific creep

c – specific heat of the material

$\underline{D}^{cr}$ – crack constitutive matrix

$\underline{D}$ – tangent constitutive matrix

D_{ni}^{cr} – opening fracture mode stiffness modulus for the i^{th} trilinear stress-strain softening branch

D_I^{cr} – crack constitutive matrix component relative to the crack normal opening mode (mode I)

D_{II}^{cr} – crack constitutive matrix component relative to the crack in-plane sliding mode (mode II)

$D_{III,\sec}^{ij}$ – secant constitutive matrix *ij* component relative to the crack out-of-plane sliding mode (mode III)

$D_{III,\sec}$ – secant stiffness relative to the crack out-of-plane sliding mode (mode III)

$\underline{D}_{mf,e}^{co}$ – constitutive matrix of in-plane membrane and bending components for concrete in elastic regime

$\underline{D}_{mf}^{crco}$ – constitutive matrix of in-plane membrane and bending components for cracked concrete

$\underline{D}_{s}^{crco}$ – constitutive matrix of out-of-plane shear components for cracked concrete

$\underline{D}^{co}$ – constitutive matrix

$\underline{D}^{crco}$ – constitutive matrix of the cracked concrete

$D_{t_i}^{cr}$ – sliding stiffness modulus in the $\hat{t}_i$ direction

D_n^{cr} – fracture mode I stiffness modulus

d_f – steel fiber diameter

E_a – apparent activation energy

$\dot{E}_{out}$ – rate of energy conducted out the infinitesimal control volume

$\dot{E}_{in}$ – rate of energy conducted in the infinitesimal control volume

$\dot{E}_g$ – rate of thermal energy generation

$\dot{E}_{st}$ – rate of the energy stored within the infinitesimal control volume

E_c, E – concrete elasticity modulus

$\underline{F}$ – vector of the forces that are equivalent to the external applied loads

$\underline{F}_n$ – load in the current combination n

$\underline{F}_{n-1}$ – vector of the load in the previous combination $n-1$

$\underline{F'}\left(\underline{a}_n\right)$ – vector of the internal equivalent nodal forces

$\underline{F}_{\dot{Q}}^e$ – vector corresponding to the element internal heat generation

$\underline{F}_{\bar{q}}^e$ – vector corresponding to the boundary where the heat flux is imposed

$\underline{F}_{q_T}^e$ – vector corresponding to the heat flux where the temperature is prescribed

$\underline{F}_c^e$ – vector containing the values corresponding to the convection boundary

$f\left(\alpha_T\right)$ – normalized heat generation rate

f_c – compressive strength

f_{ct} – tensile strength

f – generic function

G_c – concrete elastic shear modulus

G_f^I – mode I (in-plane) fracture energy

G_f^{III} – mode III (out-of-plane) fracture energy

$G_{f,c}^{III}$ – consumed mode III (out-of-plane) fracture energy

h_c – convection heat transfer coefficient

h_r – radiation heat transfer coefficient

$J\left(t,t_0\right)$ – compliance function or creep function

$\underline{K}$ – stiffness matrix

$\left(\underline{K}_T\right)_n^{q-1}$ – tangential stiffness matrix in the $q-1$ iteration of the current combination n

$\underline{K}_c^e$ – element conduction matrix

$\underline{K}_{conv}^e$ – element convection matrix

$\underline{K}_t^e$ – element transient matrix

k – material thermal conductivity

l_b – crack bandwidth

l_f – steel fiber length

n – generic combination

n,t – crack local coordinate system

OP – out-of-plane

p_1 – shear degradation factor

p_2 – parameter defining the mode I fracture energy available to the new crack

$\dot{Q}$ – internal heat generation rate per unit volume

Q_{total} – accumulated heat of the cement (or binder) hydration

$Q(t)$ – accumulated heat generated until a certain instant t

q – generic iteration

q_x'' – heat flux in x direction

q_c'' – convective heat flux

q_e'' – emitted heat flux

R – universal gas constant

s – sliding displacement

T – temperature at the body surface

T_∞ – fluid temperature

dT/dx – temperature gradient

$\underline{T}^{cr}$ – transformation matrix from the coordinate system of the finite element to the local crack coordinate system

w – opening displacement

x_i – element local coordinate system

Greek letters

α_i – fracture parameters used to define the trilinear stress-strain softening diagram

α_{th} – threshold angle

α – coefficient of thermal

β – shear retention factor

$\Delta a_{n,i}^{q}$ – i^{th} component of the vector $\Delta \underline{a}_n^q$

Δa_{j-i} – predefined incremental displacement between these two components

Δa_i – predefined incremental magnitude

$\Delta \underline{\varepsilon}_{mf}$ – vector containing the in-plane membrane and bending strain incremental components

$\Delta \underline{\varepsilon}_{\ell}^{cr}$ – vector of the crack strain in the local crack coordinate system

$\Delta \underline{\varepsilon}^{cr}$ – incremental crack strain vector

$\Delta \underline{\varepsilon}^{co}$ – vector of the uncracked concrete between the cracks

$\Delta \underline{\varepsilon}$ – strain increment

$\Delta \underline{\varepsilon}^{m}\left(t_n\right)$ – incremental mechanical strain vector

$\Delta \gamma_t^{cr}$ – the incremental crack shear strain

$\Delta \underline{\sigma}_{mf}$ – vector containing the in-plane membrane and bending stress incremental components

$\Delta \underline{\sigma}_{\ell}^{cr}$ – incremental local crack stress vector

$\Delta \underline{\sigma}$ – stress increment

$\Delta \tau_t^{cr}$ – increment of the crack shear stress

$\Delta \underline{F}_n$ – incremental load vector in the load combination n

ΔF_n – incremental load in combination n

ΔT – temperature variation

Δt – incremental time step

$\delta \underline{a}_n^q$ – iterative displacement vector of in the q iteration of the combination n

$\varepsilon^{in}(t_0)$ – initial strain at loading

$\varepsilon^{c}(t)$ – creep strain at time $t > t_0$,

$\varepsilon^{s}(t)$ – shrinkage strain

$\varepsilon^{T}(t)$ – thermal strain

$\varepsilon^{m}(t)$ – mechanical strain

ε – emissivity

ε^{crco} – elasto-cracked strain

ε^{cr} – crack strain

ε^{co} – elastic concrete strain

ε_n^{cr} – crack normal strain

$\varepsilon_{n,i}^{cr}$ – crack normal strain used to define point *i* in the trilinear stress-strain softening diagram

$\varepsilon_{n,u}^{cr}$ – ultimate crack normal strain

$\underline{\varepsilon}_s$ – vector containing the out-of-plane shear strain components

$\underline{\varepsilon}^{cr}$ – crack strain vector

$\underline{\varepsilon}_{prev}^{cr}$ – crack strain vector in a previous state

γ_{ij} – out-of-plane shear strain *ij* component

γ_p^{OP} – out-of-plane peak shear strain

γ^{OP} – out-of-plane shear strain

$\gamma_{ij,p}^{OP}$ – out-of-plane peak shear strain for the *ij* component

γ_u^{OP} – out-of-plane ultimate shear strain

$\gamma_{ij,u}^{OP}$ – out-of-plane ultimate shear strain for the *ij* component

$\gamma_{\max}^{OP}$ – out-of-plane maximum shear strain in the softening branch

$\gamma_{ij,\max}^{OP}$ – out-of-plane maximum shear strain *ij* component in the softening branch

γ_t^{cr} – total shear crack strain

λ – factor

ν – Poisson's ratio

θ – angle between the element local coordinate system and the crack local coordinate system

ξ_i – fracture parameters used to define the trilinear stress-strain softening diagram

ρ – mass per unit volume

ρc – volumetric heat capacity

σ – Stefan-Boltzmann constant

σ_n^{cr} – crack normal stress

$\underline{\sigma}_{prev}$ – stress vector in a previous state

$\underline{\sigma}_{\ell,prev}^{\ cr}$ – crack stress vector in a previous state in the local crack coordinate system

$\underline{\sigma}_{\ell,prev}^{\ cr^*}$ – modified crack stress vector (only the shear component) in a previous state in the local crack coordinate system

$\sigma_{n,i}^{cr}$ – crack normal stress used to define point *i* in the trilinear stress-train softening diagram

$\underline{\sigma}_s$ – vector containing the out-of-plane shear stress components

τ_t^{cr} – in-plane crack shear stress

τ_p^{OP} – out-of-plane shear strength

τ^{OP} – out-of-plane shear stress

$\tau_{ij,p}^{OP}$ – out-of-plane shear strength for the *ij* component

τ_{ij} – out-of-plane shear stress for the *ij* component

$\tau_{\max}^{OP}$ – out-of-plane maximum shear stress in the softening branch

$\tau_{ij,\max}^{OP}$ – out-of-plane maximum shear stress *ij* component in the softening branch

$\tau_{t,prev}^{cr}$ – crack shear stress in a previous state

$\varphi\left(t,t_0\right)$ – creep coefficient

$\underline{\Psi}\left(\underline{a}_n\right)$ – vector of the unbalanced forces

List of figures

Chapter 2 –An overview on the modeling of the nonlinear behavior of cement based materials

Chapter 3 – Numerical model for concrete laminar structures

Chapter 4 – Modeling of the crack shear component

Chapter 5 – Multi-fixed smeared 3D crack model to simulate the behavior of concrete structures

Chapter 6 – Thermo-mechanical model

Appendix B

List of tables

Chapter 2 –An overview on the modeling of the nonlinear behavior of cement based materials

Chapter 3 – Numerical model for concrete laminar structures

Chapter 4 – Modeling of the crack shear component

Chapter 5 – Multi-fixed smeared 3D crack model to simulate the behavior of concrete structures

Chapter 6 – Thermo-mechanical model

Chapter 1

Introduction

1.1 INTRODUCTION AND MOTIVATION

Concrete structures are still widely used in civil construction. In the last decades some developments were made on cement based materials to improve their resistance and durability. The introduction of fibers in the concrete mix is presently common in many applications. The benefits of fiber reinforcement in the improvement of the concrete post-cracking resistance are well recognized. Fibers also reduce the maximum crack width, decrease the crack spacing and increase the energy absorption capacity of cement based materials.

Recent experimental studies with fiber reinforced cement composites, in terms of optimizing the toughness of these materials, have conducted to the development of high performance fiber reinforced cement composites of high tensile strength, and also engineered cementitious composites presenting tensile strain stiffening behavior with high tensile strain at peak tensile stress (Li and Fischer 2002, Naaman 2007). The development of self-compacting concrete (SCC) (Okamura 1997, Okamura and Ouchi 2003) has increased the potentialities of cement based materials. Combining the SCC capacity to flow and fill the interior of the formwork passing through the obstacles, with the benefits of steel fiber reinforcement, a new high performance material has resulted, being designated steel fiber reinforced self-compacting concrete (SFRSCC).

The durability of concrete structures can be largely affected by early age concrete damage, such as the occurrence of micro-cracks at an early stage of the development of the material mechanical properties. Several causes are behind the early age concrete damage, such as the tensile stresses due to restrained shrinkage, or the thermal stresses as a result of the heat generated during the hydration process.

Concrete is a composite material with high nonlinear behavior, due to its heterogeneous composition based on constituents of distinct stiffness and strength, and on an interface that is the weakest link of the concrete micro-structure. Concrete has a tensile strength that is about 10 percent of its compressive strength, exhibiting an almost linear elastic behavior up to peak stress. After cracking, the concrete behavior is largely dependent on its energy absorption capacity, which is significantly improved when fibers are used.

To accurately simulate the behavior of concrete structures for serviceability and ultimate limit states, sophisticated models must be used in order to capture the essential features of this material. In the present work, constitutive models for the material nonlinear analysis of concrete structures are presented. These models have been implemented in version 4.0 of the FEMIX computer code (Azevedo et al. 2003, Sena-Cruz et al. 2007). The predictive performance of these models is assessed using results available in the literature, and also several sets of results obtained from experimental programs carried out with SFRSCC (Barros et al. 2005a), and with reinforced concrete beams shear and flexurally strengthened with Carbon Fibre Reinforced Polymer (CFRP) laminates (Barros et al. 2011).

1.2 OBJECTIVES

The recent improvements made in concrete technology and the study of its rheological and mechanical properties must be accompanied by the development of numerical models capable of simulating its behavior. Thus, the main objectives of the present work are the development of numerical tools for the simulation of concrete structures considering the concrete nonlinear behavior and its time-dependent effects. With this purpose, the main achievements of the present work are:

- development of a constitutive model for the simulation of laminar structures, with special attention on the prediction of the shear failure mode that can occur in this type of structures when subjected to high concentrated loads;
- development of a multi-fixed smeared 3D crack model capable of predicting the behavior of structures discretized with solid finite elements – the three fracture modes can be simulated with stress-strain diagrams capable of reproducing a softening or a stiffening behavior;
- development of a thermal model with general purposes, including the heat development due to the hydration process during the concrete hardening phase to analyze structures since early ages;
- addition of new functionalities to the multi-fixed smeared 3D crack to perform transient linear and nonlinear analyses taking into account the time-dependent effects, such as shrinkage, creep and temperature;
- implementation of new strategies to avoid the numerical instabilities observed in some simulations of concrete structures under plane stress state using the multi-fixed smeared 2D crack constitutive model available in the FEMIX computer code;
- implementation of additional numerical solution procedures into FEMIX to enable the nonlinear finite element analysis of structures with complex behavior.

1.3 OUTLINE OF THE THESIS

Chapter 2 consists on an overview of recent developments about cement based materials. Models to simulate crack initiation and propagation in these materials are presented, and their main characteristics are discussed. Time-dependent phenomena, like shrinkage, creep and temperature variation are also presented, and the importance of their numerical simulation to predict the cracking risk at early age is analyzed. Numerical techniques used in nonlinear finite element analysis that have been implemented in the FEMIX computer code are briefly discussed and their benefits in terms of numerical robustness are presented.

In chapter 3 the developed numerical model for the simulation of concrete laminar structures is presented. The multi-fixed smeared crack model is implemented under the

framework of the Reissner-Mindlin theory adapted to the case of layered shells, in order to simulate the damage due to crack initiation and propagation. Special attention is dedicated to the simulation of the out-of-plane shear components by proposing softening stress-strain diagrams to improve the predictive performance of laminar structures where the out-of-plane shear is the governing failure mode. A strategy to simulate supports with linear and nonlinear behavior is presented, and special considerations are made on unilateral support conditions. Improvements in the internal algorithms associated with the stress update and the crack status change are described and their advantages are discussed. The performance and the accuracy of the developed numerical tools are assessed using the results from a punching experimental test of a panel fabricated with steel fiber reinforced self-compacting concrete (SFRSCC) (Barros et al. 2005a).

In chapter 4 two strategies to improve the degradation of the shear stress transfer with the crack opening evolution are described. One is based on the simulation of the crack shear stress-shear strain relationship with a total approach instead of an incremental approach. The other is based on the use of a softening diagram for the simulation of the relationship between the crack shear stress and the crack shear strain components. All the relevant aspects related with their implementation in the finite element computer code are described in detail. These strategies are validated by performing numerical simulations using results available in the literature and results available from an experimental program with reinforced concrete beams shear and flexurally strengthened with composite materials (Barros et al. 2011).

In chapter 5 a multi-fixed smeared 3D crack model developed for the simulation of the nonlinear behavior of concrete structures discretized with solid finite elements is described. The principal aspects of its implementation in the finite element computer code are also detailed. Special attention is dedicated to the modeling of the shear fracture modes, being the utilization of the simulation strategies described in chapter 4 discussed. The numerical model is appraised using the results available from a punching experimental test with a module of a panel fabricated with SFRSCC. This module is a structurally representative of this panel for this type of loading configuration.

In chapter 6 a thermal model with general purposes is presented. The inclusion of heat development due to the hydration process during the concrete hardening phase to analyze structures since its early ages is described. The time-dependent effects are coupled with the multi-fixed smeared 3D crack model described in chapter 5. All the relevant aspects related to the transient linear and nonlinear analysis and its implementation in the finite element computer code are discussed. The performance and the accuracy of the developed numerical models are assessed using results available in the literature.

Finally, the major conclusions are presented in chapter 7 and some suggestions for future research are also given.

Chapter 2

An overview on the modeling of the nonlinear behavior of cement based materials

2.1 CEMENT BASED MATERIALS

Concrete is the most common material used in the construction industry. In terms of its internal structure, concrete can be defined as a mixture of cement, sand (fine aggregate), gravel (coarse aggregate) and water. The chemical reaction, known as hydration, between cement and water leads to a hardening process, and the presence of aggregates (sand and gravel) supplies the necessary strength. In a simple way, the cement paste binds the aggregates together resulting in a rigid structure similar to an artificial rock. Due to its simple fabrication and hardening process (from a liquid to a solid phase), concrete is a material that is adaptable to any structural form, being well accepted in the construction industry.

The mechanical properties of concrete can be obtained by performing several tests. Concrete has a high compressive strength, but low tensile strength. According to the ACI (2005) the tensile strength of concrete in flexure is about 10 to 15 percent of its compressive strength. Since the tensile strength and the post-cracking residual strength of concrete plays an important role in the deflection and crack pattern of a structure under service loads, the addition of other materials to improve its relatively low tensile load

carrying capacity, such is the case of steel bars, is current practice. This type of reinforced concrete is widely used in the construction industry, combining the benefits of the high compressive strength of concrete with those resulting from the high tensile strength of steel. The excellent bond behavior between these two materials is also a positive factor.

Non-continuous (discrete) fibers are an interesting reinforcement solution for cement based materials, since they can increase significantly the post-cracking residual strength of these materials. Fibers also reduce the maximum crack width, which contributes to increase the durability of the concrete and the life cycle of the structure. If randomly distributed in concrete, the fibers can also contribute to prevent early age shrinkage cracking. Various types of fibers are used in concrete mixtures and they can be grouped in steel, glass, synthetic and natural fibers (ACI 1996). To restrain the formation and propagation of cracks due to shrinkage, synthetic fibers are the most used, but steel fibers are also currently adopted. Both types of fibers can also be added to concrete in order to provide reinforcement mechanisms to control the crack propagation for early age and hardened concrete phases. For the case of structural applications steel fibers are still the most widely used due to cost and reinforcement level criteria, being the derived composite designated steel fiber reinforced concrete (SFRC). Depending on the content and geometric characteristics of the steel fibers, diffuse crack patterns can be formed due to the fiber pullout mechanisms provided by fibers bridging the crack lips. When micro-cracks occur due to shrinkage, the fibers can assure a relatively high residual tensile strength of the SFRC, limiting the crack width to a small value, and permitting an eventual healing or sealing of the cracks (ACI 1996). Furthermore, the addition of steel fibers to a concrete mix improves the impact resistance, the energy dissipation capacity, the shear and flexural strength of concrete, and the resistance to concrete spalling (ACI 1993).

In the past two decades, with the development of self-compacting concrete (SCC), also designated self-consolidating concrete (Okamura 1997, Okamura and Ouchi 2003), new advantages have emerged for the concrete technology. SCC can be defined as a concrete mix that has the ability to flow and fill the interior of the formwork, passing through any obstacles or reinforcing bars, and consolidating under its own weight, without vibration.

According to the Precast/Prestressed Concrete Institute (2003), a SCC must satisfy the following rheological requirements:

- filling ability – the ability of SCC to flow under its own weight, without vibration, and fill completely all formwork spaces;
- passing ability – the ability of SCC to flow through complex spaces, e.g., between steel reinforcing bars;
- stability – the ability of SCC to remain homogeneous during its transport, placement, and after placement, i.e., resisting to segregation.

With the addition of steel fibers to the SCC, a high performance material is obtained, since the benefits of the SCC can be combined with those derived from the reinforcement mechanisms provided by the steel fibers. Research on the optimization of the mix design of steel fiber reinforced self-compacting concrete (SFRSCC) and on the characterization of its properties were made by several authors (Barros et al. 2005a, Pereira 2006, Dhonde et al. 2007).

Engineered cementitious composites (ECC) are the most recent advance in the concrete technology. This material exhibits a tensile strain-hardening behavior after crack initiation, and the post-cracking behavior is characterized by the formation of diffuse crack patterns (Li and Fischer 2002). Therefore, the ECC can be classified as a high performance fiber reinforced cement composite (HPFRCC) (Naaman and Reinhardt 2003, Naaman 2007).

To retrieve the benefits of the improvements introduced in the concrete technology along the years, computer programs should be able to simulate with high accuracy the behavior of structures built with these new types of concrete. For this purpose, these programs should incorporate constitutive models capable of reproducing the behavior of these materials. In the present work constitutive models for the analysis of concrete structures are described. In the next sections a brief overview about crack constitutive models, time-dependent effects and numerical strategies for the material nonlinear analysis of cement based materials are presented.

2.2 CRACK CONSTITUTIVE MODELS FOR CEMENT BASED MATERIALS

Presently, several finite element approaches are available to analyze the nonlinear behavior of complex structures subject to arbitrary loads. The most recent ones are capable of modeling the behavior of concrete structures presenting brittle failure modes, and accurately predict crack formation and propagation.

Discrete cohesive fracture models (discrete) with fragmentation algorithms, strong discontinuity approaches (continuum) with the embedded discontinuities method, and the extended finite element method are examples of advanced methodologies that, together with powerful mesh refinement algorithms, reveal great efficiency in modeling the concrete fracture initiation and propagation (Yu et al. 2007). Alternative methods are based on damage models (de Borst and Gutiérrez 1999), smeared crack models (Bazant and Oh 1983)] and microplane models (Bazant 1984). These methods are less precise in the prediction of the local phenomena related to crack propagation, but, in terms of computational effectiveness and assessment of the global behavior of a concrete structure, are more appropriate to analyze complex structures with a large number of degrees of freedom.

As shown by de Borst (2002), "fixed and rotating smeared crack models, but also microplane models, can be conceived as a special case of (anisotropic) damage models". These three FEM-based solutions are closely related and produce similar results. Taking into account the main characteristics of all these approaches, the multi-directional fixed smeared crack model (de Borst 1987, Rots 1988, Dahlblom and Ottosen 1990), already implemented in the FEMIX 4.0 computer program (Azevedo et al. 2003, Sena-Cruz 2007) for plane stress problems, has been improved and extended to plane shells and structures discretized with solid finite elements. In the implementation process some innovative aspects have been developed. Since the majority of the structures analyzed in this work are made with SFRC, where diffuse crack patterns can be formed, the option for the multi-directional fixed smeared crack model is conceptually justified, as long as an appropriate constitutive law is used to model the post-cracking behavior of these materials.

2.3 TIME-DEPENDENT PHENOMENA

The development of cracks in concrete at early ages, caused by shrinkage and temperature variation, has concerned various researchers over the years. Concrete is a brittle composite that exhibits a low tensile strength in comparison with its compressive strength. If the magnitude of tensile stresses due to shrinkage (for example: plastic, drying or thermal) reaches the tensile strength of concrete, then cracks are formed. Preventing or controlling the magnitude of these cracks, i.e. width and pattern, is important for the durability, performance and aesthetic appearance of the structure.

When shrinkage is actuating, cracking in concrete members only appears if they are not free to shrink (Koenigsfeld and Myers 2003). In fact, tensile stresses do not develop if concrete shrinks freely. In current concrete structures, however, their structural elements are in general partially or totally restrained, and therefore shrinkage cracking has a high probability of occurrence. The degree of shrinkage depends on the water-to-cement (w/c) ratio, relative humidity associated with the temperature of the environment, type of cement and geometric characteristics of the element.

Figure 2.1 illustrates the volume change under unrestrained shrinkage, the stress development, and the cracking phenomenon due to restrained shrinkage (ACI 2001).

To control restrained shrinkage cracking various methods/techniques can be used. All have the same goal: prevent that, at a certain age, the tensile stresses due to shrinkage reach the tensile strength of concrete. To reduce the w/c ratio and to assure proper curing conditions are the most common shrinkage mitigation strategies. Other methods are the use of expansive cements to counteract the shrinkage effect, or the use of Shrinkage Reducing Admixtures (Weiss et al. 1998, D'Ambrosia et al. 2001). Fiber reinforcement has also gained importance due to its cracking control efficiency and facility of distribution in the concrete mixture with minor modifications of the concrete production technology.

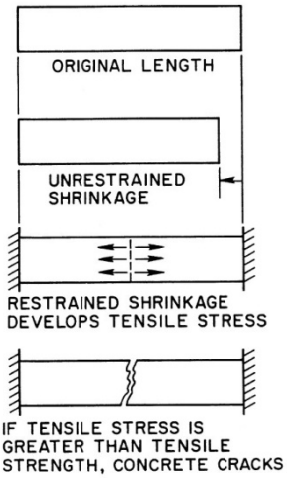

Figure 2.1 – Cracking of concrete due to drying shrinkage and restrain (ACI 2001).

The phenomenon of shrinkage in cement based materials is important because it can be associated with different types of damages that can occur in concrete structures, especially in early ages. Cracks are undesirable because they reduce the load capacity, and expose the reinforcement to eventually aggressive environmental conditions, resulting in a decrease of the service-life of a structure.

The residual stress and concrete strength along the concrete ageing process, represented in Figure 2.2, was presented by Weiss (1999). The concrete cracks when the functions intersect (point A). Weiss also concludes that when the phenomenon of creep is taken into account the stress level decreases due to creep relaxation, delaying the cracking age (point B).

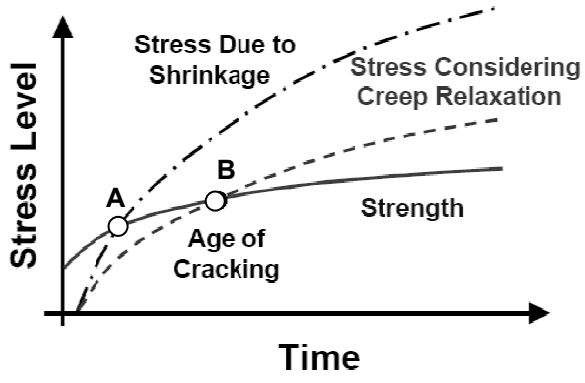

Figure 2.2 – Influence of creep relaxation on the shrinkage cracking of concrete (adapted from Weiss 1999).

In order to predict the stresses related to shrinkage it is necessary to understand the corresponding phenomenon, and, therefore, an overview of the associated terminology and its meaning is presented below.

Bastos and Cincotto (2000) classify the shrinkage according to four criteria: physical state, nature, degree of restriction and permanence, as indicated in Table 2.1. They also discuss the simultaneous occurrence of these types of shrinkage.

Table 2.1– Shrinkage classification (Bastos and Cincotto 2000).

Physical State	Shrinkage at fresh state (Plastic shrinkage) Shrinkage at hardening state
Nature of the phenomenon	Drying shrinkage Hydration shrinkage Autogenous shrinkage Carbonation shrinkage Thermal shrinkage
Degree of restriction	Free shrinkage Restrained shrinkage
Permanence of the phenomenon	Reversible shrinkage Irreversible shrinkage

Weiss (1999) has classified the shrinkage phenomenon in only two main groups: thermal shrinkage and water related shrinkage. Thermal shrinkage is caused by the hydration of the cement or the diurnal or seasonal temperature changes. The water related shrinkage is caused by the loss of water from the concrete. The loss of water due to its movement to the environment causes a volumetric change of the concrete structure, and tensile stresses develop due to partial or total restrain of its movement. Plastic, drying, carbonation and autogenous shrinkage are classified as water related shrinkage. In thin structures water can escape more quickly and, consequently, they are more sensitive to shrinkage than thick structures. Therefore, the development of stresses due to drying shrinkage is more intensive in thin than in thick structures. This type of shrinkage is especially important in

pavements, slabs and bridge decks due to their large area to volume ratio. In contrast, thermal shrinkage is more important in thick structures than in thin structures due to the slower transfer of the cement hydration heat. Shrinkage occurs as a result of the cooling process, being more prominent in this type of structures.

Plastic Shrinkage

Plastic shrinkage is the loss of water (i.e. evaporation) in a fresh concrete surface. Plastic shrinkage occurs at the first hours of concrete curing, and its magnitude depends on the environmental conditions including solar effects, wind speed, temperature and relative humidity. To prevent cracking due to plastic shrinkage, the use of a plastic sheet cover is common to block the early age evaporation of water. Wind breaks and the use of special concrete admixtures are also strategies that reduce plastic shrinkage. Fibers, especially polypropylene fibers, are being considered by designers, suppliers and constructors because they significantly reduce the width of cracks formed due to plastic shrinkage.

Drying Shrinkage

The drying shrinkage occurs in hardened concrete and is caused by the loss of water through the surface. The water movement is affected by the difference between the internal and external relative humidity. Less relative humidity in the atmosphere increases the drying shrinkage and the potential for the occurrence of cracking. The water-to-cement ratio (w/c) also influences this type of shrinkage, since the water content in the pores decreases with the w/c ratio. Therefore, the lower the amount of water available to be expelled through the surface is, the smaller the drying shrinkage effect becomes.

Autogenous Shrinkage

It is the shrinkage that occurs in a concrete volume without interchanges of humidity with the outside environmental conditions. This can occur in the core of a thick concrete structure or in specimens where the loss of water through the surface is not allowed. Due to the hydration reaction of binder materials, there is an internal consumption of water called self-desiccation and, in combination with its volume reduction as a result of the chemical reaction, the autogenous shrinkage occurs.

Carbonation Shrinkage

This type of shrinkage occurs at the surface of the concrete as a result of the reaction between the carbon dioxide (CO2) present in the atmosphere and the hydrated cement. This reaction leads to the shrinkage of the concrete.

Thermal Shrinkage

As a result of hydration of binder materials during the concrete curing phase, an exothermic reaction occurs with the generation of a large quantity of heat. The dissipation of this heat is faster in thin than in thick structures. During the concrete cooling process after the curing phase, and since heating/cooling phases can occur simultaneously in distinct parts of a concrete element, tensile stresses are developed (thermal stresses) in the parts that are shrinking, leading to the formation of cracks. Thermal stresses also occur in hardened concrete due to diurnal and seasonal temperature changes, and the dimensional variation can also cause the development of cracks.

Creep and Shrinkage

According to the ACI (1992) creep can be defined as the time-dependent increase of strain in concrete subjected to sustained stress. Basic creep occurs under conditions of no moisture movement to or from the environment, while drying creep is the additional creep caused by drying.

In Figure 2.2 it can be observed that the creep has an effect of relaxation of the residual stress, resulting an increase in the concrete age when it cracks. The strength increase in this period of time can avoid the formation of cracks, which is a favorable contribution of creep in the context of concrete shrinkage. Shrinkage and creep are time-dependent phenomena that are interrelated and cannot be completely dissociated. In the past years a special attention has been dedicated to the tensile creep of concrete, and its influence on shrinkage induced cracking when the concrete is restrained (Altoubat and Lange 2001, D'Ambrosia et. al. 2001, Bissonnette et al. 2007). When the concrete is restrained it is subjected to tensile stresses and the cracking potential increases. Tensile creep stresses and the corresponding strains counteract the shrinkage strains and have a beneficial effect.

For example, during the first days of a concrete slab on grade, shrinkage is the critical condition. The restrain imposed by the concrete/soil friction introduces tensile stresses in the concrete that, depending on the restrain characteristics, concrete and environmental conditions, cause the formation of cracks. Since the concrete is submitted to tensile stresses during this period, creep strain has a beneficial effect since it decreases the strains due to shrinkage.

The simulation of the time-dependent phenomena, such as shrinkage, creep and temperature variation, is crucial not only to predict the cracking risk, but also to contribute to a more accurate prediction of the global behavior of concrete structures from their early ages to the hardened phase. This approach has been integrated in the FEMIX computer code (Azevedo et al. 2003, Sena-Cruz 2007) and is exposed in chapter 6.

2.4 SOLUTION PROCEDURES FOR NONLINEAR PROBLEMS

2.4.1 **Introduction**

The use of the finite element method (FEM) to obtain the solution of civil engineering problems where no analytical approach is available is very common. According to the FEM, the continuum is divided in several finite elements (Zienkiewicz and Taylor 2000a) and the displacement field is based on shape functions and nodal displacements. When the material exhibits a nonlinear behavior, the resulting equations from the application of the principle of virtual work are also nonlinear, and an incremental/iterative procedure is used to solve the nonlinear system of equations. The Newton-Raphson method is widely used in this framework.

The equilibrium equation of a structure can be written as

$$\underline{K}\,\underline{a} = \underline{F} \tag{2.1}$$

where $\underline{K}$, $\underline{a}$ and $\underline{F}$ are the stiffness matrix, the displacement vector and the vector of the forces that are equivalent to the external applied loads, respectively, corresponding to the

nodal degrees of freedom of the structure. In the context of structural nonlinear analysis, equation (2.1) is not linear, due to the dependence of the stiffness matrix on the nodal displacement vector (Zienkiewicz and Taylor 2000b). To obtain the structural response it is convenient to apply the load incrementally

$$\underline{F}_n = \underline{F}_{n-1} + \Delta\underline{F}_n \tag{2.2}$$

where $\Delta\underline{F}_n$ is the incremental load vector in the load combination n, $\underline{F}_{n-1}$ is the load in the previous combination $n-1$, and $\underline{F}_n$ is the load in the current combination n. In this context, each combination corresponds to an increment of the load. Thus, for the combination n the equation of the unbalanced forces $\underline{\Psi}\left(\underline{a}_n\right)$ can be defined by

$$\underline{\Psi}\left(\underline{a}_n\right) = \underline{F}_n - \underline{F'}\left(\underline{a}_n\right) \tag{2.3}$$

being $\underline{F'}\left(\underline{a}_n\right)$ the vector of the internal equivalent nodal forces, and $\underline{a}_n$ the vector of the nodal displacements. For a current combination n the vector of unbalanced forces must be null, i.e.,

$$\underline{\Psi}\left(\underline{a}_n\right) = \underline{0} \tag{2.4}$$

Equation (2.4) can be solved by the Newton-Raphson method. Considering the first two terms of the Taylor series expansion, equation (2.4) can be approximated as

$$\underline{\Psi}\left(\underline{a}_n^q\right) \approx \underline{\Psi}\left(\underline{a}_n^{q-1}\right) + \left(\frac{\partial\underline{\Psi}}{\partial\underline{a}}\right)_n^{q-1} \delta\underline{a}_n^q = \underline{0} \tag{2.5}$$

where the subscript q is the iteration counter. In equation (2.5)

$$\left(\frac{\partial \underline{\Psi}}{\partial \underline{a}}\right)_n^{q-1} = -\left(\frac{\partial \underline{F}'}{\partial \underline{a}}\right)_n^{q-1} = -\left(\underline{K}_T\right)_n^{q-1} \tag{2.6}$$

is the Jacobian matrix, which, in the context of structural analysis, corresponds to $\left(\underline{K}_T\right)_n^{q-1}$ multiplied by (-1). $\left(\underline{K}_T\right)_n^{q-1}$ is the tangential stiffness matrix in the $q-1$ iteration of the current combination n. Substituting (2.6) in (2.5) yields

$$\left(\underline{K}_T\right)_n^{q-1} \delta \underline{a}_n^q = \underline{\Psi}\left(\underline{a}_n^{q-1}\right) \tag{2.7}$$

An iterative procedure is required to obtain the solution of equation (2.4), and in each iteration the vector of the displacements is updated as follows

$$\underline{a}_n^q = \underline{a}_n^{q-1} + \delta \underline{a}_n^q = \underline{a}_{n-1} + \Delta \underline{a}_n^q \tag{2.8}$$

with

$$\Delta \underline{a}_n^q = \sum_{i=1}^{q} \delta \underline{a}_n^i = \Delta \underline{a}_n^{q-1} + \delta \underline{a}_n^q \tag{2.9}$$

being $\underline{a}_n^0 = \underline{a}_{n-1}$ and $\Delta \underline{a}_n^0 = \underline{0}$ in the beginning of each iteration process.

Figure 2.3 represents a load-displacement relationship of a system with one degree of freedom that presents a post-peak softening. The numerical simulation can be made by applying load increments ΔF, being this technique designated *load control* procedure. It is observed that with the *load control* procedure the numerical solution cannot be obtained for the post-peak phase, i.e., the curve between points A and B. This can be overcome if a *displacement control* procedure is adopted for the numerical simulation, i.e., by applying displacement increments, Δa, instead of load increments. In this case, as shown in Figure 2.4, the post-peak curve can be numerically obtained.

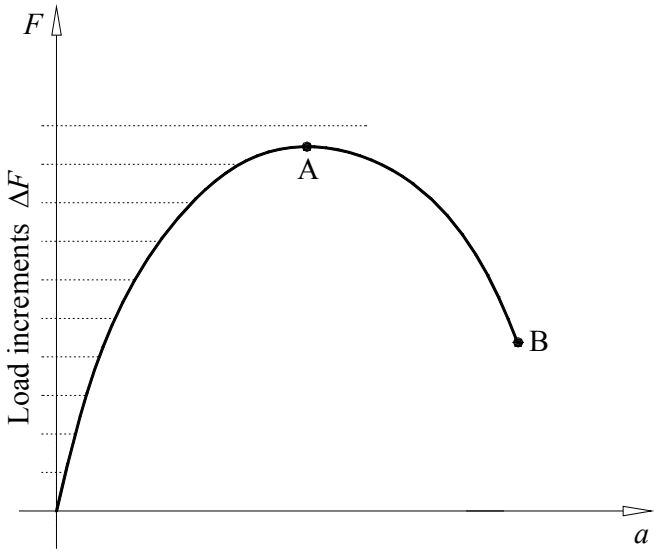

Figure 2.3 – Load control procedure.

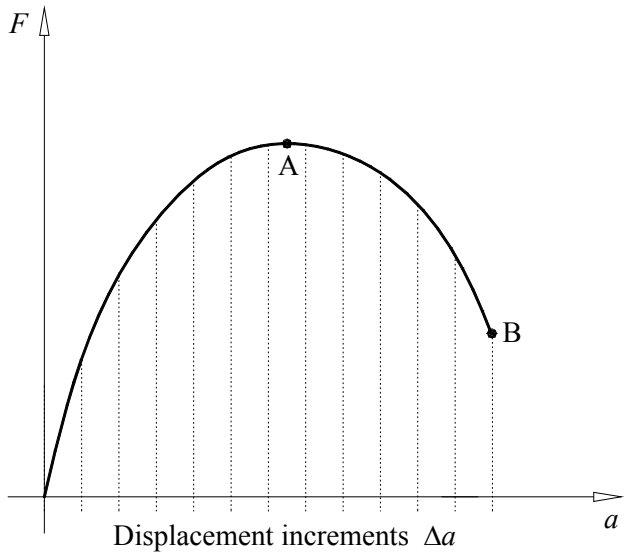

Figure 2.4 – Displacement control procedure.

Figure 2.5 represents a load-displacement response of a structure with a complex behavior. Applying the *load control* procedure, the curve between points A and D is not obtained, i.e., the numerical response includes the points between O and A and the points after D. This is referred to in the literature as a *snap-through* behavior. When a *displacement control* procedure is used, it is verified that the points on the curve between B and C are not obtained, i.e., the numerical response only includes the points between O and B and the points after C. This phenomenon is known as *snap-back* behavior. To overcome these

difficulties and obtain the entire numerical response shown in Figure 2.5, several researchers have proposed different numerical strategies, among which stands out the arc-length technique. This technique was originally proposed by Riks (1970) and Wempner (1971), and was subsequently modified by several researchers (Crisfield 1983 and 1986, Bashir Ahmed and Xiao-zu 2004).

To overcome the difficulties associated with solving a system of nonlinear equations, some iterative techniques, such as the arc-length and related methods, introduce a load factor during the iterative process corresponding to the Newton Raphson-method. The load level is now also an unknown and it is necessary to consider an additional equation. This equation constrains the solution to meet a certain criteria.

In the following sections the arc-length technique and related methods are presented. These techniques are implemented in the FEMIX computer code, and the details can be found elsewhere (Ventura-Gouveia et al. 2006).

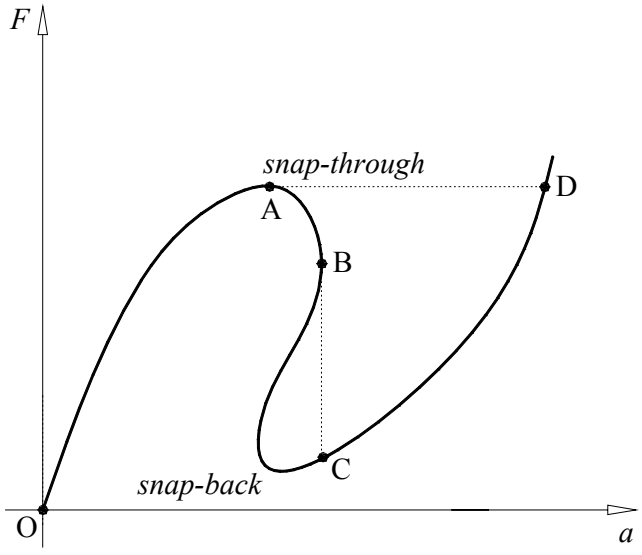

Figure 2.5 – *Snap-through* and *snap-back*.

2.4.2 **Arc-length technique**

Figure 2.6 represents a nonlinear relationship between the load and displacement in a structure with one degree of freedom.

To simulate the nonlinear behavior of this structure an incremental loading procedure is used. Figure 2.6 also represents the load and displacement variation corresponding to the load increment between the combinations $n-1$ and n. The use of an incremental load ΔF_n leads to a solution that moves away from point A, and bypasses the peak corresponding to point C, being the behavior of the structure between points A and D not captured. To reproduce the full path, the load increment is multiplied by a factor λ whose value is set by the following restriction

$$\left(\Delta a_n\right)^2 + \lambda^2 \, b^2 \left(\Delta F_n\right)^2 = \Delta L^2 \tag{2.10}$$

In this equation b is a scale factor that converts the magnitude of load to the magnitude of the displacement.

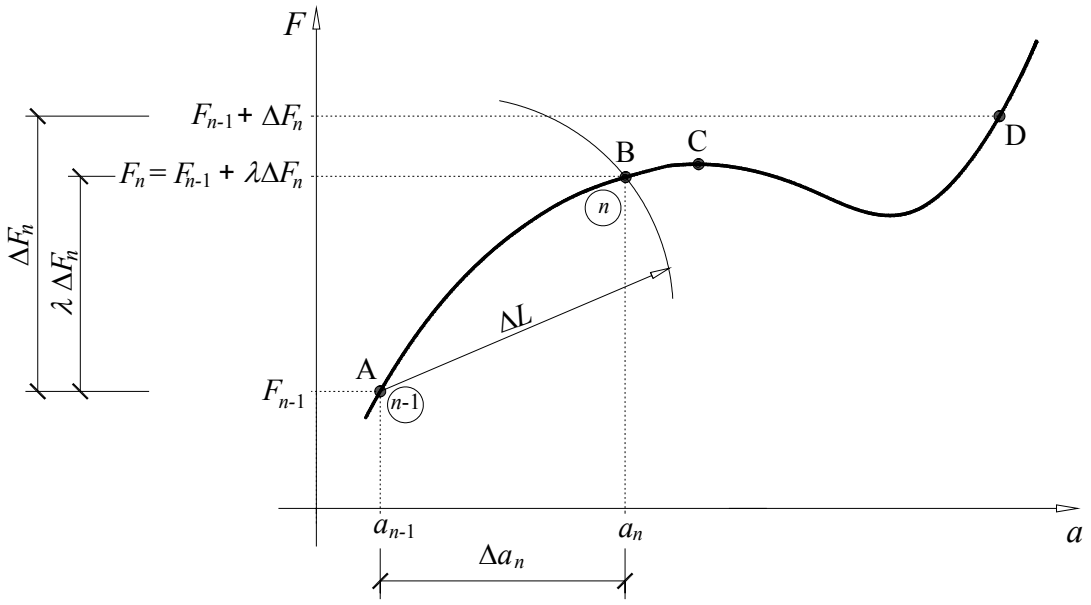

Figure 2.6 – Arc-length technique applied to a system with one degree of freedom ($b = 1.0$).

According to Figure 2.6 the external force is now a function of λ, and using equation (2.3) the unbalanced forces become

$$\Psi_n = \Psi\left(a_n, \lambda\right) = F_n\left(\lambda\right) - F'\left(a_n\right) = F_{n-1} + \lambda \, \Delta F_n - F'\left(a_n\right) = 0 \tag{2.11}$$

In the q iteration, equations (2.10) and (2.11) must be taken into account, resulting, for a system of more than one degree of freedom, in

$$\underline{\Psi}\left(\underline{a}_n^q, \lambda^q\right) = \underline{F}_n^q\left(\lambda^q\right) - \underline{F}'\left(\underline{a}_n^q\right) = \underline{F}_{n-1} + \lambda^q \Delta \underline{F}_n - \underline{F}'\left(\underline{a}_n^q\right) = \underline{0} \tag{2.12a}$$

$$f\left(\Delta \underline{a}_n^q, \lambda^q\right) = \left[\Delta \underline{a}_n^q\right]^T \Delta \underline{a}_n^q + b^2\left(\lambda^q\right)^2 \left[\Delta \underline{F}_n\right]^T \Delta \underline{F}_n - \Delta L^2 = 0 \tag{2.12b}$$

According to Crisfield (1991) the factor b can be considered null for current problems. In the present implementation the factor b is taken into account and can be advantageously used in the solution of nonlinear problems.

In the present work the Newton-Raphson method can be used without the arc-length technique by applying different load increments ΔF_n up to a predefined combination is reached, followed by a set of combinations in which the arc-length technique is used with a constant load increment ΔF_n. In this context the increase of external force is designated by ΔF. Figure 2.7 represents the Newton-Raphson method without and with the arc-length technique.

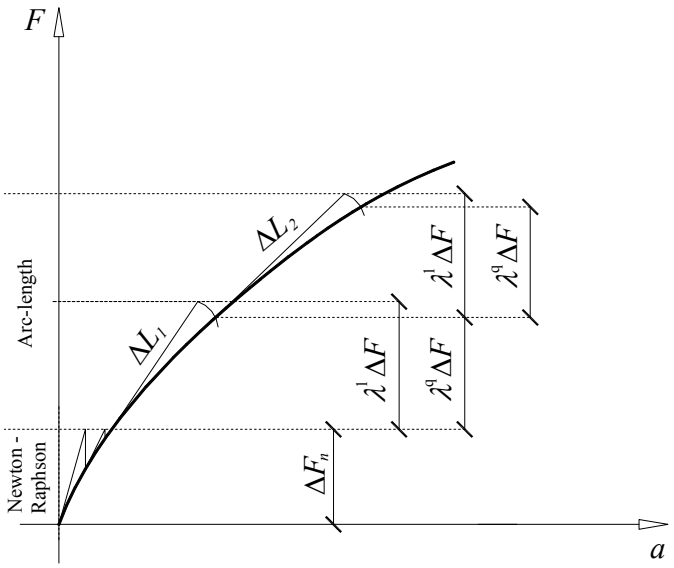

Figure 2.7 – Newton-Raphson method without and with arc-length technique.

The iterative process corresponding to the Newton-Raphson method with the arc-length technique is represented in Figure 2.8.

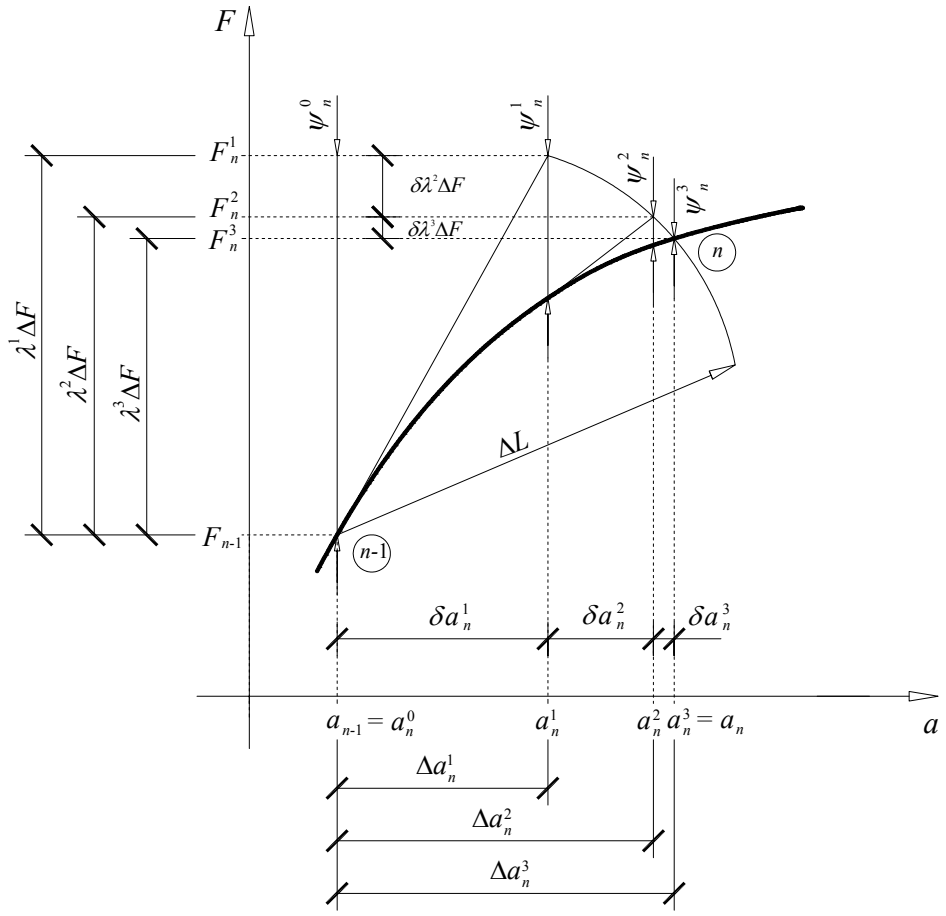

Figure 2.8 – Iterative process associated with the arc-length technique applied to a system with one degree of freedom ($b = 1.0$).

In order to use the Newton-Raphson method to obtain the solution of (2.12), the first two terms of the corresponding Taylor series expansion are considered (Ventura-Gouveia et al. 2006), resulting in

$$\begin{bmatrix} -\left(\underline{K}_T\right)_n^{q-1} & \Delta\underline{F} \\ 2\left[\Delta\underline{a}_n^{q-1}\right]^T & 2b^2\lambda^{q-1}\left[\Delta\underline{F}\right]^T\Delta\underline{F} \end{bmatrix}\begin{bmatrix} \delta\underline{a}_n^q \\ \delta\lambda^q \end{bmatrix} = -\begin{bmatrix} \underline{\Psi}\left(\underline{a}_n^{q-1},\lambda^{q-1}\right) \\ f\left(\Delta\underline{a}_n^{q-1},\lambda^{q-1}\right) \end{bmatrix} \tag{2.13}$$

This system of linear equations has a non-symmetric matrix. To overcome this disadvantage, Crisfield (1991) proposes the replacement of $\Delta \underline{a}_n^q$ in the constraint (2.12b). This development is described in detail in Ventura-Gouveia et al. (2006). In the present exposition only a general approach is made.

Thus, considering (2.12a) and making some developments, yields

$$\left(\underline{K}_T\right)_n^{q-1} \delta \underline{a}_n^q = \underline{\Psi}\left(\underline{a}_n^{q-1}, \lambda^{q-1}\right) + \Delta \underline{F}\, \delta\lambda^q \tag{2.14}$$

Rewritting (2.14) in terms of the iterative displacement, $\delta \underline{a}_n^q$, results in

$$\begin{aligned} \delta \underline{a}_n^q &= \left[\left(\underline{K}_T\right)_n^{q-1}\right]^{-1} \underline{\Psi}\left(\underline{a}_n^{q-1}, \lambda^{q-1}\right) + \left[\left(\underline{K}_T\right)_n^{q-1}\right]^{-1} \Delta \underline{F}\, \delta\lambda^q \\ &= \delta \overline{\underline{a}}_n^{q-1} + \delta\lambda^q \delta \overline{\overline{\underline{a}}}_n^{q-1} \end{aligned} \tag{2.15}$$

being

$$\delta \overline{\underline{a}}_n^{q-1} = \left[\left(\underline{K}_T\right)_n^{q-1}\right]^{-1} \underline{\Psi}\left(\underline{a}_n^{q-1}, \lambda^{q-1}\right) \tag{2.16}$$

and

$$\delta \overline{\overline{\underline{a}}}_n^{q-1} = \left[\left(\underline{K}_T\right)_n^{q-1}\right]^{-1} \Delta \underline{F} \tag{2.17}$$

with

$$\underline{\Psi}\left(\underline{a}_n^{q-1}, \lambda^{q-1}\right) = \underline{F}_{n-1} + \lambda^{q-1} \Delta \underline{F} - \underline{F}'\left(\underline{a}_n^{q-1}\right) \tag{2.18}$$

The successive approximation to the solution is made using equation (2.8), being the load factor λ^q updated with

$$\lambda^q = \lambda^{q-1} + \delta\lambda^q \tag{2.19}$$

Including equations (2.9), (2.15) and (2.19) in equation (2.12b) yields (see Appendix A)

$$a_1 \left(\delta\lambda^q\right)^2 + a_2 \delta\lambda^q + a_3 = 0 \tag{2.20}$$

where $\delta\lambda^q$ is the unknown and

$$\begin{aligned} a_1 &= \left[\delta \underline{\overline{a}}_n^{q-1}\right]^T \delta \underline{\overline{a}}_n^{q-1} + b^2 \left[\Delta \underline{F}\right]^T \Delta \underline{F} \\ a_2 &= 2\left[\delta \underline{\overline{a}}_n^{q-1}\right]^T \left(\Delta \underline{a}_n^{q-1} + \delta \underline{\overline{a}}_n^{q-1}\right) + 2b^2 \lambda^{q-1} \left[\Delta \underline{F}\right]^T \Delta \underline{F} \\ a_3 &= \left[\Delta \underline{a}_n^{q-1} + \delta \underline{\overline{a}}_n^{q-1}\right]^T \left(\Delta \underline{a}_n^{q-1} + \delta \underline{\overline{a}}_n^{q-1}\right) + b^2 \left(\lambda^{q-1}\right)^2 \left[\Delta \underline{F}\right]^T \Delta \underline{F} - \Delta L^2 \end{aligned} \tag{2.21}$$

2.4.3 **Displacement control at a specific variable**

The application of the arc-length technique to the numerical simulation of some structural problems with localized nonlinearities may cause instabilities in the convergence of the incremental/iterative process. This deficiency can be avoided by following a strategy proposed by Batoz and Dhatt (1979) that consists on the restriction of the incremental displacement of a particular variable to a predefined value. This displacement control is made without the addition of any support. This procedure is called displacement control at a specific variable.

The equation (2.12b) is replaced with

$$\Delta a_{n,i}^q = \Delta a_i \tag{2.22}$$

being $\Delta a_{n,i}^q$ the i^{th} component of the vector $\Delta \underline{a}_n^q$ and Δa_i its predefined incremental magnitude.

During the iterative process the incremental value of the i^{th} component of the vector $\Delta \underline{a}_n^q$ remains constant and equal to Δa_i, i.e., the iterative variation of this component, $\delta a_{n,i}^q$, is null. Given this fact, equation (2.9) can be written for the i^{th} component of the vector $\Delta \underline{a}_n^q$ in the following format

$$\Delta a_{n,i}^q = \Delta a_{n,i}^{q-1} + \delta a_{n,i}^q = \Delta a_{n,i}^{q-1} = \Delta a_i \tag{2.23}$$

For a given combination n, the iterative displacements, $\delta \underline{a}_n^q$, are obtained with equation (2.15). Writing this equation for the i^{th} component yields

$$\delta a_{n,i}^q = \delta \overline{a}_{n,i}^{q-1} + \delta \lambda^q \delta \overline{\overline{a}}_{n,i}^{q-1} \tag{2.24}$$

Knowing that the iterative variation $\delta a_{n,i}^q$ is null, and solving equation (2.24) in order to obtain $\delta \lambda^q$ the following expression is obtained

$$\delta \lambda^q = -\frac{\delta \overline{a}_{n,i}^{q-1}}{\delta \overline{\overline{a}}_{n,i}^{q-1}} \tag{2.25}$$

being $\delta \overline{a}_{n,i}^{q-1}$ and $\delta \overline{\overline{a}}_{n,i}^{q-1}$ the i^{th} component of the first member of equations (2.16) and (2.17), respectively.

2.4.4 **Relative displacement control between two specific variables**

As mentioned in the previous section, the numerical simulation of structures where localized nonlinearities occur becomes sometimes impossible due to equation (2.12b). In an attempt to avoid the instability in the convergence of the incremental/iterative process, de Borst (1986) suggests that in equation (2.12b) only some preselected components of vector $\Delta \underline{a}_n^q$ should be considered in the analysis. In certain structures, such is the case of

those governed by the relative movement of the faces of existing critical failure cracks, by selecting two appropriate degrees of freedom (displacement components), one in each face of the crack, and imposing a relative displacement value that represents the movement of the faces of the crack during the loading process of the real structure, these types of instabilities can be avoided. The relative displacement control between these points is accomplished without the addition of any support. In order to implement this technique, equation (2.12b) is replaced with

$$\Delta a_{n,j}^{q} - \Delta a_{n,i}^{q} = \Delta a_{j-i} \tag{2.26}$$

being $\Delta a_{n,i}^{q}$ and $\Delta a_{n,j}^{q}$, respectively, the i and j components of the vector $\Delta \underline{a}_{n}^{q}$, and Δa_{j-i} the predefined incremental displacement between these two components.

During the iterative process the relative incremental value between i and j components of the vector $\Delta \underline{a}_{n}^{q}$ remains constant and equal to Δa_{j-i}, i.e., the relative iterative variation between these components $\left(\delta a_{n,j}^{q} - \delta a_{n,i}^{q}\right)$ is null. Given this fact, equation (2.9) can be written for the i and j components of the vector $\Delta \underline{a}_{n}^{q}$ in the following form

$$\begin{aligned} \Delta a_{n,j}^{q} - \Delta a_{n,i}^{q} &= \left(\Delta a_{n,j}^{q-1} + \delta a_{n,j}^{q}\right) - \left(\Delta a_{n,i}^{q-1} + \delta a_{n,i}^{q}\right) \\ &= \Delta a_{n,j}^{q-1} - \Delta a_{n,i}^{q-1} \\ &= \Delta a_{j-i} \end{aligned} \tag{2.27}$$

For a given combination n, the iterative displacements, $\delta \underline{a}_{n}^{q}$, are obtained with equation (2.15). Writing this equation for the i and j components yields

$$\delta a_{n,i}^{q} = \delta \overline{a}_{n,i}^{q-1} + \delta \lambda^{q} \delta \overline{\overline{a}}_{n,i}^{q-1} \tag{2.28a}$$

$$\delta a_{n,j}^{q} = \delta \overline{a}_{n,j}^{q-1} + \delta \lambda^{q} \delta \overline{\overline{a}}_{n,j}^{q-1} \tag{2.28b}$$

The relative iterative displacement between the i and j components is defined by

$$\delta a_{n,j}^{q} - \delta a_{n,i}^{q} = \left(\delta \overline{a}_{n,j}^{q-1} + \delta\lambda^{q}\delta \overline{\overline{a}}_{n,j}^{q-1}\right) - \left(\delta \overline{a}_{n,i}^{q-1} + \delta\lambda^{q}\delta \overline{\overline{a}}_{n,i}^{q-1}\right) \tag{2.29}$$

Knowing that $\left(\delta a_{n,j}^{q} - \delta a_{n,i}^{q}\right)$ is null, and solving equation (2.29) in order to obtain $\delta\lambda^{q}$, the following expression is obtained

$$\delta\lambda^{q} = -\frac{\delta \overline{a}_{n,j}^{q-1} - \delta \overline{a}_{n,i}^{q-1}}{\delta \overline{\overline{a}}_{n,j}^{q-1} - \delta \overline{\overline{a}}_{n,i}^{q-1}} \tag{2.30}$$

In this equation $\delta \overline{a}_{n,i}^{q-1}$ and $\delta \overline{a}_{n,j}^{q-1}$ are the i and j components of the first member of equation (2.16), and $\delta \overline{\overline{a}}_{n,i}^{q-1}$ and $\delta \overline{\overline{a}}_{n,j}^{q-1}$ are the i and j components of the first member of equation (2.17).

With this procedure, termed relative displacement control between two specific variables, the numerical response of a structure that exhibits a *snap-back* behavior can be obtained (see Figure 2.5). Another possible application of this technique is the simulation of tests in which the opening of the crack is controlled (Crack Mouth Opening Displacement control - CMOD) (Rots 1988).

2.5 SUMMARY AND CONCLUSIONS

In this chapter an overview on the developments of cement based materials in the past years is made. Some models to simulate the crack initiation and propagation of these materials are presented and time-dependent phenomena, like shrinkage, creep and temperature variation are also discussed. Numerical solutions used in nonlinear finite element analysis and implemented in the scope of the present work in the FEMIX computer code are briefly introduced and their benefits in terms of numerical simulation robustness are presented.

Chapter 3

Numerical model for concrete laminar structures

3.1 INTRODUCTION

In this chapter a multi-directional fixed smeared crack constitutive model to simulate the flexural/punching failure modes of concrete laminar structures is presented. The constitutive model is implemented in a computer program based on the finite element method, called FEMIX (Azevedo et al. 2003, Sena-Cruz et al. 2007), being the laminar structures simulated according to the Reissner-Mindlin shell theory (Reissner 1945, Mindlin 1951, Barros and Figueiras 2001). The thickness of the laminar structure is discretized into layers that are assumed to be subjected to a plane stress state. In this approach, the use of constitutive models to simulate the nonlinear behavior, after crack initiation, for the in-plane fracture modes is appropriate in most cases, and the deformational response of a structure subjected to load configurations that induce flexural failure modes can be predicted with sufficient accuracy. However, the simulation of laminar structures failing in punching is a much more complex task, being the treatment of the out-of-plane shear components of paramount importance.

A stress-strain softening diagram is proposed to simulate the mode I fracture propagation, while the in-plane shear crack component depends on a shear retention factor, defined as a constant value or by a crack normal strain dependent law. The in-plane shear crack

component can also be determined by a crack shear stress-strain softening diagram (see Chapter 4).

To capture the punching failure mode, a softening diagram is proposed to model, after crack initiation, the decrease of the out-of-plane shear stress components with the increase of the corresponding shear strain components. With this relatively simple approach, accurate predictions of the behavior of fiber reinforced concrete (FRC) structures failing in bending and in shear can be obtained.

Improvements made in the subalgorithms associated with the stress update and with the critical change of crack status are presented and their advantages are discussed.

The formulation of elastic supports, such as surface, line and point springs, with linear and nonlinear stiffness, is also presented in this chapter, and a special attention is made about unilateral support conditions. With this approach, the loss of contact between a structure and a supporting system, such is the case of a slab supported on ground, can be correctly simulated.

To assess the predictive performance of the model, an experimental punching test of a module of a façade panel fabricated with steel fiber reinforced self-compacting concrete (SFRSCC) is numerically simulated. The influence that some parameters defining the softening diagrams have on the predictive performance of the model for this type of simulations is analyzed.

3.2 GENERAL LAYERED APPROACH TO DISCRETIZE THE THICKNESS OF A LAMINAR STRUCTURE

3.2.1 Introduction

The Reissner-Mindlin theory (Reissner 1945, Mindlin 1951, Barros and Figueiras 2001) is widely used to simulate the behavior of laminar structures. In structural engineering applications, a laminar structure can be defined as a three-dimensional body with two

dimensions that are considerably larger than the other one, which is its thickness. Industrial floors, pavements of buildings or roads, and bridge decks are examples of laminar structures.

Since the last century structures of this type are mainly constructed with cement based materials, such as reinforced concrete (RC) and, more recently, with fiber reinforced concrete (FRC) or steel fiber reinforced self-compacting concrete (SFRSCC). It is known that these materials exhibit a nonlinear behavior, even when subjected to service loads, due to crack formation and propagation. This material nonlinearity may be accentuated when early cracks appear (e.g., due to shrinkage restrain or temperature development), which can compromise the durability of the structure. An accurate prediction of the behavior of such structures is of great importance to improve its service life, and to prevent its excessive deformability and early failure.

3.2.2 **Formulation**

In this section a brief overview of the Reissner-Mindlin formulation applied to a layered plane shell approach is presented. The theory of plates and shells can be found in Timoshenko and Woinkowsky-Krieger (1959), and its implementation using FEM was done by several researchers, such as: Ugural 1981, Huang 1989, Barros 1989, Barros 1995, Oñate 1995.

A plane shell is a flat laminar structure with in-plane and out-of-plane shear deformations. The in-plane deformations can be caused by membrane forces and bending moments. Therefore, a plane shell combines the behavior of a slab (development of bending and out-of-plane shear deformations) with those of a wall (development of membrane deformations).

The basic assumptions of the Reissner-Mindlin theory applied to the case of plane shells are:

- the u_1 and u_2 displacements of the shell middle surface (see Figure 3.1) are not neglected (the presence of membrane deformations is allowed);

- in comparison with the shell thickness, the displacement normal to the shell middle surface, u_3 (see Figure 3.1), is small;
- the stress acting in the direction normal to the shell middle surface, σ_3, is small when compared with the other stress components, being neglected;
- straight fibers normal to the middle surface of the shell are considered to remain straight but not necessarily orthogonal to the middle surface during the deformation process.

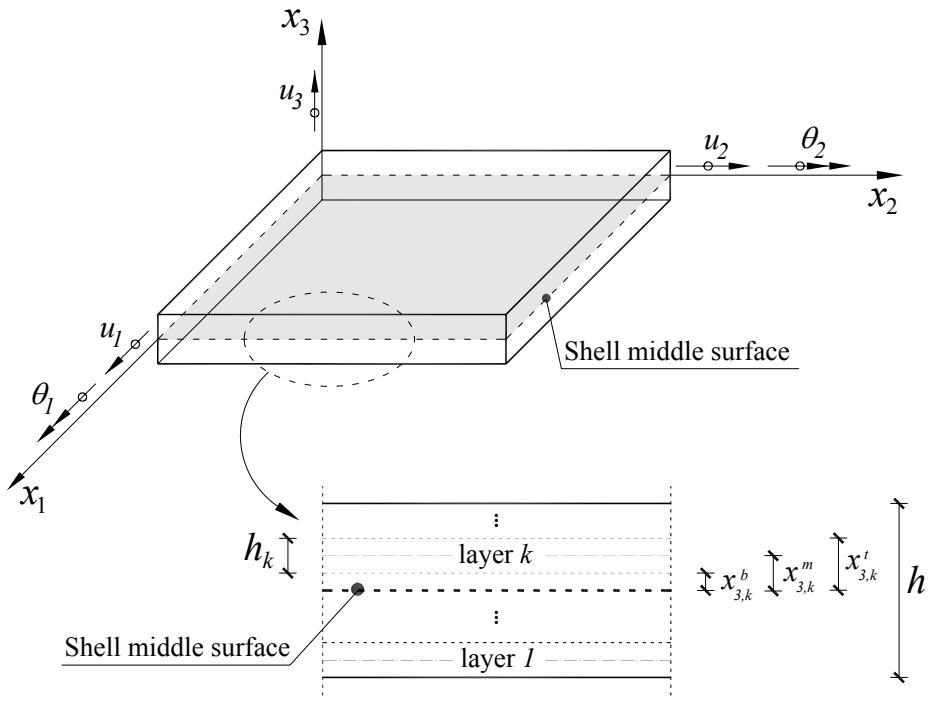

Figure 3.1 – Multi-layer plane shell: displacements, rotations and *k* layer geometry definition.

As mentioned before, the behavior of cement based materials is clearly nonlinear. This nonlinearity results primarily from the fact that this material has a relatively small cracking stress.

A layered shell model to simulate the nonlinear behavior of laminar structures can simulate the damage resulting from crack propagation through the thickness of a shell due to in-plane stresses. In this approach the strains at different levels along the shell thickness (middle surface of each layer) are obtained from the displacements of the finite element

nodes, and the stresses are determined according to the constitutive laws that simulate the behavior of the material of this layer. Thus, for the finite element material nonlinear analysis, a plane shell structure is divided not only in Mindlin shell finite elements, but also in layers through the thickness (see Figure 3.1).

For example, as shown in Figure 3.2, a plane shell element is discretized into an eight-node serendipity 3D Mindlin shell finite element (five degrees of freedom per node). Four or nine node Lagrangian 3D Mindlin shell finite elements are also available in the FEMIX computer code. Each 3D finite element is divided into layers through the thickness. These layers can have thickness and material properties different from each other. The strains and stresses are evaluated at the middle surface of each layer and their relation depends on the constitutive law assigned to the layer. So, the present formulation is implemented with general purposes, and any plane shell structure composed of different materials through the thickness can be numerically simulated.

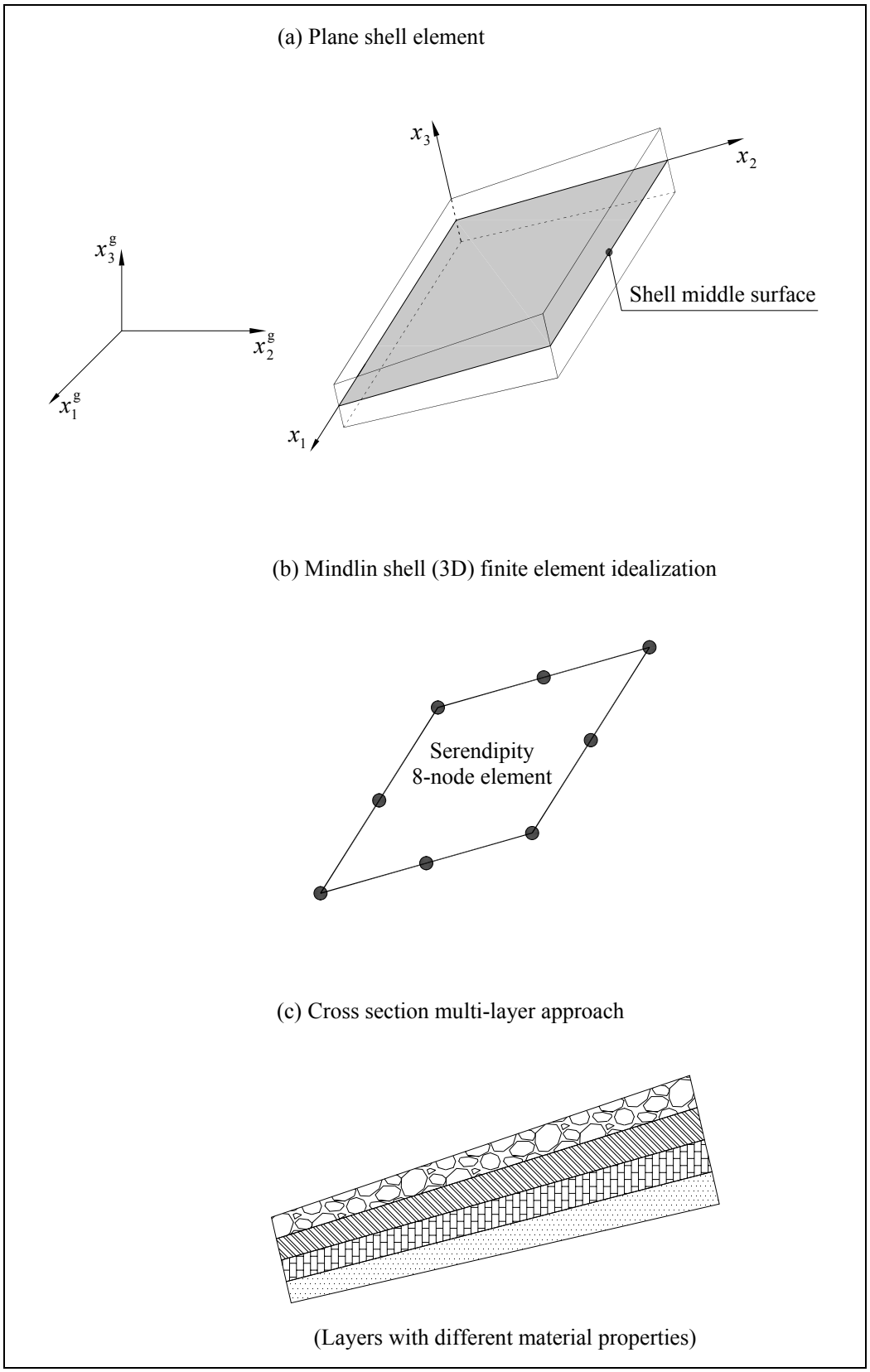

Figure 3.2 – Example of a finite element idealization of a plane shell element according to the multi-layer approach.

When the response of the elements of a structure becomes nonlinear, the stiffness begins to depend on the strain state that these elements are subjected to. In the case of laminar structures, this strain state can vary through the thickness, and in a multi-layer approach, from layer to layer. So, the contribution of each layer to the element stiffness matrix is different, being the stiffness matrix thus obtained called the tangent stiffness matrix.

To account for the material nonlinear behavior, the relationship between the stress and the strain state is established in an incremental way, i.e.

$$\Delta\underline{\sigma} = \underline{D}_T \Delta\underline{\varepsilon} \tag{3.1}$$

where $\underline{D}_T$ is the tangent constitutive matrix, $\Delta\underline{\sigma}$ the incremental stress vector and $\Delta\underline{\varepsilon}$ the incremental strain vector.

In the calculation of the stiffness matrix of each finite element the following procedure is used (see Figure 3.3):

- from the known displacements in the finite element nodes, evaluate the displacements, $\underline{a}$, at the integration points (Gauss Points);
- calculate the strains, $\underline{\varepsilon}$ at the middle surface of each layer;
- calculate the tangent constitutive matrix, $\underline{D}_T$, taking into account the constitutive relation of the material of each layer;
- calculate the element tangent stiffness matrix, $\underline{K}_T^{(e)}$.

3D plane shell element level:	$\underline{a}$		$\underline{K}_T^{(e)}$
	$\Downarrow$		$\Uparrow$
Cross section level (layered approach):	$\underline{\varepsilon}$	$\Rightarrow$	$\underline{D}_T$

Figure 3.3 – Procedure to obtain the tangent stiffness matrix of an element.

Taking into account the through-thickness layer discretization (see Figure 3.1), the element tangent stiffness matrix, $\underline{K}_T^{(e)}$, can be obtained from the submatrices associated with the membrane deformations, $\underline{K}_m^{(e)}$, membrane-bending and bending-membrane deformations, $\underline{K}_{mb}^{(e)}$ and $\underline{K}_{bm}^{(e)}$, bending deformations, $\underline{K}_b^{(e)}$, and out-of-plane shear deformations, $\underline{K}_s^{(e)}$.

The submatrix $\underline{K}_m^{(e)}$ is obtained from

$$\underline{K}_m^{(e)} = \int_{A^{(e)}} \underline{B}_m^T \hat{\underline{D}}_m \underline{B}_m dA \tag{3.2a}$$

where

$$\hat{\underline{D}}_m = \int_{-h/2}^{h/2} \underline{D}_{mb}\ dx_3 = \sum_{k=1}^{N_{layers}} \underline{D}_{mb,k} \left(x_{3,k}^t - x_{3,k}^b \right) \tag{3.2b}$$

In (3.2b) h is the shell thickness, N_{Layers} is the number of layers of the through-thickness discretization, $\underline{D}_{mb,k}$, is the constitutive matrix associated with the membrane-bending deformation of the k layer and $\left(x_{3,k}^t - x_{3,k}^b \right)$ is the k layer thickness h_k.

The submatrices $\underline{K}_{mb}^{(e)}$ and $\underline{K}_{bm}^{(e)}$ are obtained from

$$\underline{K}_{mb}^{(e)} = \int_{A^{(e)}} \underline{B}_m^T \hat{\underline{D}}_{mb} \underline{B}_b dA \tag{3.3a}$$

$$\underline{K}_{bm}^{(e)} = \int_{A^{(e)}} \underline{B}_b^T \hat{\underline{D}}_{bm} \underline{B}_m dA \tag{3.3b}$$

where

$$\underline{\hat{D}}_{mb} = \underline{\hat{D}}_{bm} = \int_{-h/2}^{h/2} \underline{D}_{mb}\ x_3\ dx_3 = \sum_{k=1}^{N_{layers}} \underline{D}_{mb,k}\ x_{3,k}^{m} \left(x_{3,k}^{t} - x_{3,k}^{b} \right) \tag{3.3c}$$

being $x_{3,k}^{m}$ the x_3 coordinate of the middle surface of the k layer.

The submatrix $\underline{K}_b^{(e)}$ is obtained from

$$\underline{K}_b^{(e)} = \int_{A^{(e)}} \underline{B}_b^T \underline{\hat{D}}_b \underline{B}_b dA \tag{3.4a}$$

where

$$\underline{\hat{D}}_b = \int_{-h/2}^{h/2} \underline{D}_{mb}\ x_3{}^2\ dx_3 = \sum_{k=1}^{N_{layers}} \underline{D}_{mb,k} \left(x_{3,k}^{m} \right)^2 \left(x_{3,k}^{t} - x_{3,k}^{b} \right) \tag{3.4b}$$

The submatrix $\underline{K}_s^{(e)}$ is obtained from

$$\underline{K}_s^{(e)} = \int_{A^{(e)}} \underline{B}_s^T \underline{\hat{D}}_s \underline{B}_s dA \tag{3.5a}$$

where

$$\underline{\hat{D}}_s = \int_{-h/2}^{h/2} \underline{D}_s\ dx_3 = \sum_{k=1}^{N_{layers}} \underline{D}_{s,k} \left(x_{3,k}^{t} - x_{3,k}^{b} \right) \tag{3.5b}$$

being $\underline{D}_{s,k}$ the constitutive matrix associated with the out-of-plane-shear deformation of the k layer.

To also take into account the flexural stiffness of each layer, equation (3.3c) is substituted with (Barros 1989)

$$\underline{\hat{D}}_{mb} = \underline{\hat{D}}_{bm} = \int_{-h/2}^{h/2} \underline{D}_{mb}\ x_3\ dx_3 = \sum_{k=1}^{N_{layers}} \underline{D}_{mb,k}\ \frac{\left(x_{3,k}^{t}\right)^2 - \left(x_{3,k}^{b}\right)^2}{2} \tag{3.6}$$

and equation (3.4b) is replaced with

$$\underline{\hat{D}}_{b} = \int_{-h/2}^{h/2} \underline{D}_{mb}\ x_3^{\,2}\ dx_3 = \sum_{k=1}^{N_{layers}} \underline{D}_{mb,k}\ \frac{\left(x_{3,k}^{t}\right)^3 - \left(x_{3,k}^{b}\right)^3}{3} \tag{3.7}$$

Equations (3.6) and (3.7) are used in the current layered model in order to keep it suitable for the analysis of a laminar structure with linear elastic behavior using only one layer.

The $\underline{B}_m$, $\underline{B}_b$ and $\underline{B}_s$ matrices in equations (3.2) to (3.5) are used to obtain the membrane, bending and shear deformations from the corresponding degrees of freedom in the finite element (Barros 1995, Oñate 1995).

The constitutive matrix associated with the membrane-bending deformation of the k layer, $\underline{D}_{mb,k}$, used in equations (3.2) to (3.4) and equations (3.6) and (3.7), depends on the material state or regime assigned to this layer, i.e., linear or materially nonlinear behavior. The definition of these matrices can be found in section 3.3.

The constitutive matrix associated with the shear deformation of the k layer, $\underline{D}_{s,k}$, used in equation (3.5), depends also on the out-of-plane shear material behavior assigned to the layer. The $\underline{D}_{s,k}$ matrix for a linear elastic material is presented in section 3.3, while for a material with nonlinear behavior, $\underline{D}_{s,k}$ is detailed in section 3.4.

As already described in section 2.4, at a given stage of a nonlinear analysis, the nodal forces that are equivalent to the external applied loads must balance the nodal forces that are equivalent to the stress state developed in the structure, named internal equivalent nodal forces, $\underline{f}_{\text{int}}$. These internal equivalent nodal forces are intrinsically dependent on the material behavior, i.e., they depend on the constitutive model assigned to the material.

The calculation of the internal equivalent nodal forces of each finite element is performed according to the following procedure (see Figure 3.4):

- from the known displacements in the finite element nodes, evaluate the displacements, $\underline{a}$, at the integration points (Gauss Points);
- calculate the strains, $\underline{\varepsilon}$ at the middle surface of each layer;
- calculate the stress vector, $\underline{\sigma}$, at the same level of the strain calculation, taking into account the constitutive law of the material where the stress vector is being calculated;
- calculate the generalized forces, $\underline{F}$, by integrating the stresses across the thickness;
- calculate the element internal equivalent nodal forces, $\underline{f}_{\text{int}}^{(e)}$.

3D plane shell element level:	$\underline{a}$		$\underline{f}_{\text{int}}^{(e)}$
	$\Downarrow$		$\Uparrow$
Cross section level (layered approach):	$\underline{\varepsilon}$	$\Rightarrow$	$\underline{\sigma} \Rightarrow \underline{F}$

Figure 3.4 – Scheme to obtain the internal equivalent nodal forces of an element.

In a plane shell decomposed into layers, the element internal equivalent nodal forces can be obtained from the vectors associated with the membrane forces, $\underline{f}_{\text{int},m}^{(e)}$, bending moments, $\underline{f}_{\text{int},b}^{(e)}$, and out-of-plane shear forces, $\underline{f}_{\text{int},s}^{(e)}$.

The vector $\underline{f}_{\text{int},m}^{(e)}$ is obtained from

$$\underline{f}_{\text{int},m}^{(e)} = \int_{A^{(e)}} \underline{B}_m^T \, \underline{\hat{N}} \, dA \tag{3.8a}$$

where

$$\underline{\hat{N}} = \begin{bmatrix} N_1 & N_2 & N_{12} \end{bmatrix}^T = \int_{-h/2}^{h/2} \underline{\sigma}_{mb} \, dx_3 = \sum_{k=1}^{N_{layers}} \sigma_{mb,k} \left(x_{3,k}^t - x_{3,k}^b \right) \tag{3.8b}$$

are the membrane forces.

The vector $\underline{f}_{\text{int},b}^{(e)}$ is obtained from

$$\underline{f}_{\text{int},b}^{(e)} = \int_{A^{(e)}} \underline{B}_b^T \, \underline{\hat{M}} \, dA \tag{3.9a}$$

where

$$\underline{\hat{M}} = \begin{bmatrix} M_1 & M_2 & M_{12} \end{bmatrix}^T = \int_{-h/2}^{h/2} x_3 \, \underline{\sigma}_{mb} \, dx_3 = \sum_{k=1}^{N_{layers}} \sigma_{mb,k} \, x_{3,k}^m \left(x_{3,k}^t - x_{3,k}^b \right) \tag{3.9b}$$

are the bending moments.

The vector $\underline{f}_{\text{int},s}^{(e)}$ is obtained from

$$\underline{f}_{\text{int},s}^{(e)} = \int_{A^{(e)}} \underline{B}_s^T \, \underline{\hat{Q}} \, dA \tag{3.10a}$$

where

$$\underline{\hat{Q}} = \begin{bmatrix} Q_{23} & Q_{31} \end{bmatrix}^T = \int_{-h/2}^{h/2} \underline{\sigma}_s \, dx_3 = \sum_{k=1}^{N_{layers}} \sigma_{s,k} \left(x_{3,k}^t - x_{3,k}^b \right) \tag{3.10b}$$

are the shear forces.

When a particular layer has linear elastic behavior, the equations (3.8b) and (3.9b) are substituted with equations (3.11) and (3.12), respectively (Barros 1989). This is important when the thickness of the plane shell has only one layer (for the case of a linear elastic analysis).

$$\hat{N} = \sum_{k=1}^{N_{layers}} \underline{D}_{mb,k} \, \underline{\overline{\varepsilon}}_m \left(x_{3,k}^t - x_{3,k}^b \right) + \underline{D}_{mb,k} \, \underline{\overline{\varepsilon}}_f \frac{\left(x_{3,k}^t \right)^2 - \left(x_{3,k}^b \right)^2}{2} \tag{3.11}$$

$$\hat{M} = \sum_{k=1}^{N_{layers}} \underline{D}_{mb,k} \, \underline{\overline{\varepsilon}}_m \frac{\left(x_{3,k}^t \right)^2 - \left(x_{3,k}^b \right)^2}{2} + \underline{D}_{mb,k} \, \underline{\overline{\varepsilon}}_f \frac{\left(x_{3,k}^t \right)^3 - \left(x_{3,k}^b \right)^3}{3} \tag{3.12}$$

where $\underline{\overline{\varepsilon}}_m$ and $\underline{\overline{\varepsilon}}_b$ are, respectively, the membrane and bending strains.

In the framework of the finite element method, the stiffness submatrices from equations (3.2) to (3.5) and the vectors from equations (3.8) to (3.10) are calculated applying the Gauss-Legendre integration rule (Cook 1995, Zienkiewicz and Taylor 2000a).

3.3 CRACK CONSTITUTIVE MODEL

3.3.1 **Introduction**

Smeared and discrete crack concepts can be used to model the crack propagation in concrete structures (de Borst et al. 2004). Since fiber reinforcement can assure the formation of diffuse crack patterns, a smeared crack model can be conceptually more

appropriate, and more effective from the computational point-of-view, for the simulation of the behavior of fiber reinforced concrete structures.

3.3.2 **Formulation**

In the context of finite element analysis of materially nonlinear shell structures, the developed constitutive multi-fixed smeared crack model is implemented under the framework of the Reissner-Mindlin theory adapted to the case of layered shells, in order to simulate the progressive damage induced by cracking. So the shell element is discretized into layers, and in each layer a plane stress state is assumed.

In this section the formulation of the multi-fixed smeared crack model, implemented under the framework of the Reissner-Mindlin theory, is presented. Its description refers to a generic (k) concrete layer and to the domain of an integration point (IP) of a finite element. However, to simplify the symbols of the formulation, the subscript k is dropped. The adopted constitutive laws and some model options are also discussed. An incremental approach is used for the in-plane components, while a total approach is adopted for the out-of-plane components.

According to the adopted constitutive law, stresses and strains are related by the following equation

$$\begin{bmatrix} \Delta\underline{\sigma}_{mb} \\ \underline{\sigma}_{s} \end{bmatrix} = \begin{bmatrix} \underline{D}^{co}_{mb} & \underline{0} \\ \underline{0} & \underline{D}^{co}_{s} \end{bmatrix} \begin{bmatrix} \Delta\underline{\varepsilon}_{mb} \\ \underline{\varepsilon}_{s} \end{bmatrix} \tag{3.13}$$

being

$$\Delta\underline{\sigma}_{mb} = \begin{bmatrix} \Delta\sigma_1 & \Delta\sigma_2 & \Delta\tau_{12} \end{bmatrix}^T \tag{3.14}$$

and

$$\Delta\underline{\varepsilon}_{mb} = \left[\Delta\varepsilon_1 \quad \Delta\varepsilon_2 \quad \Delta\gamma_{12}\right]^T \tag{3.15}$$

the vectors of the in-plane incremental stress and incremental strain, while

$$\underline{\sigma}_s = \left[\tau_{23} \quad \tau_{31}\right]^T \tag{3.16}$$

and

$$\underline{\varepsilon}_s = \left[\gamma_{23} \quad \gamma_{31}\right]^T \tag{3.17}$$

are the vectors of the out-of-plane total shear stress and total shear strain.

The vector of the total in-plane stress components, needed for the evaluation of the internal forces in equations (3.8) and (3.9), is obtained by adding to the previous one, $\underline{\sigma}_{mb}^{prev}$, the vector of the in-plane incremental stress components obtained with equation (3.13)

$$\underline{\sigma}_{mb} = \underline{\sigma}_{mb}^{prev} + \Delta\underline{\sigma}_{mb} \tag{3.18}$$

The vector of the in-plane total strain components is also updated with

$$\underline{\varepsilon}_{mb} = \underline{\varepsilon}_{mb}^{prev} + \Delta\underline{\varepsilon}_{mb} \tag{3.19}$$

In equation (3.13), $\underline{D}_{mb}^{co}$ and $\underline{D}_s^{co}$ are, respectively, the in-plane stiffness matrix and the out-of-plane shear stiffness matrix.

3.3.2.1 Linear elastic uncracked concrete

For the case of linear elastic uncracked concrete, $\underline{D}_{mb}^{co}$ of equation (3.13) is the constitutive matrix of concrete with a linear elastic behavior, designated by $\underline{D}_{mb,e}^{co}$, and defined according to the Hooke's law as

$$\underline{D}_{mb,e}^{co} = \frac{E}{1-\nu^2}\begin{bmatrix} 1 & \nu & 0 \\ \nu & 1 & 0 \\ 0 & 0 & (1-\nu)/2 \end{bmatrix} \tag{3.20}$$

while $\underline{D}_{s}^{co}$ in equation (3.1.3) is designated with $\underline{D}_{s,e}^{co}$ and is defined by

$$\underline{D}_{s,e}^{co} = FG_c\begin{bmatrix} 1 & 0 \\ 0 & 1 \end{bmatrix} \tag{3.21}$$

being E the elasticity modulus of concrete, ν the Poisson's ratio, and G_c the shear modulus defined by

$$G_c = \frac{E}{2(1+\nu)} \tag{3.22}$$

The shear correction factor F is introduced in equation (3.21) to take into account the nonuniform out-of-plane shear stress distribution through the thickness of the shell. Its value is considered equal to 5/6 (Barros 1995, Oñate 1995).

3.3.2.2 Linear elastic cracked concrete

In smeared crack models the incremental strain vector $\Delta\varepsilon_{mb}$, derived from the incremental nodal displacements obtained under the framework of a nonlinear FEM analysis, is

decomposed into an incremental crack strain vector, $\Delta\varepsilon_{mb}^{cr}$, and an incremental strain vector of the concrete between cracks, $\Delta\varepsilon_{mb}^{co}$ (Rots 1988, Barros 1995, Sena-Cruz 2004).

$$\Delta\varepsilon_{mb} = \Delta\varepsilon_{mb}^{co} + \Delta\varepsilon_{mb}^{cr} \tag{3.23}$$

In cracked concrete, with the concrete between cracks in linear elastic state, $\underline{D}_{mb}^{co}$ is replaced in equation (3.13) with the in-plane cracked concrete constitutive matrix, $\underline{D}_{mb}^{crco}$, obtained with the following equation (Sena-Cruz 2004)

$$\underline{D}_{mb}^{crco} = \underline{D}_{mb,e}^{co} - \underline{D}_{mb,e}^{co}\left[\underline{T}^{cr}\right]^{T}\left(\underline{D}^{cr} + \underline{T}^{cr}\,\underline{D}_{mb,e}^{co}\left[\underline{T}^{cr}\right]^{T}\right)^{-1}\underline{T}^{cr}\,\underline{D}_{mb,e}^{co} \tag{3.24}$$

where $\underline{D}_{mb,e}^{co}$ is the constitutive matrix defined by equation (3.20) and $\underline{T}^{cr}$ is the matrix that transforms the stress components from the coordinate system of the finite element to the local crack coordinate system

$$\underline{T}^{cr} = \begin{bmatrix} \cos^2\theta & \sin^2\theta & 2\sin\theta\cos\theta \\ -\sin\theta\cos\theta & \sin\theta\cos\theta & \cos^2\theta - \sin^2\theta \end{bmatrix} \tag{3.25}$$

and $\underline{D}^{cr}$ is the crack constitutive matrix

$$\underline{D}^{cr} = \begin{bmatrix} D_I^{cr} & 0 \\ 0 & D_{II}^{cr} \end{bmatrix} \tag{3.26}$$

In equation (3.25), θ is the angle between x_1 and n (see Figure 3.5). In equation (3.26) D_I^{cr} and D_{II}^{cr} represent, respectively, the constitutive components relative to the crack opening mode I (normal) and mode II (in-plane shear).

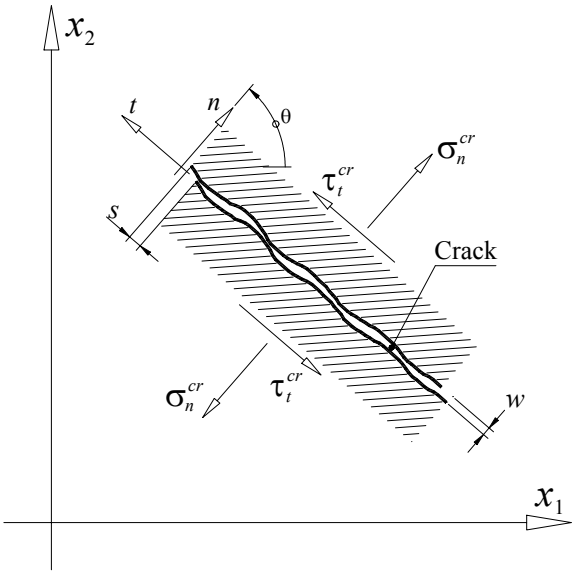

Figure 3.5 – Stress components, relative displacements and local coordinate system of the crack (Sena-Cruz 2004).

To take into account the formation of several cracks at the same IP, the crack constitutive matrix, $\underline{D}^{cr}$, and the transformation matrix, $\underline{T}^{cr}$, of relation (3.24) are substituted with the matrices that include the transformation matrix and the crack constitutive matrix of each crack that can occur at a specific IP (Sena-Cruz 2004).

The crack opening propagation can be simulated with the tensile-softening trilinear diagram represented in Figure 3.6, which is defined by the parameters α_i and ξ_i, relating stress with strain at the transitions between the linear segments that compose this diagram.

The ultimate crack strain, $\varepsilon_{n,u}^{cr}$, is defined as a function of the parameters α_i and ξ_i, the fracture energy, G_f^I, the tensile strength, $\sigma_{n,1}^{cr} = f_{ct}$, and the crack bandwidth, l_b, as follows (Barros 1995, Sena-Cruz 2004)

$$\varepsilon_{n,u}^{cr} = \frac{2}{\xi_1 + \alpha_1\xi_2 - \alpha_2\xi_1 + \alpha_2} \frac{G_f^I}{f_{ct} l_b} \tag{3.27}$$

being

$$\alpha_1 = \sigma_{n,2}^{cr} / \sigma_{n,1}^{cr} \tag{3.28a}$$

$$\alpha_2 = \sigma_{n,3}^{cr} / \sigma_{n,1}^{cr} \tag{3.28b}$$

$$\xi_1 = \varepsilon_{n,2}^{cr} / \varepsilon_{n,u}^{cr} \tag{3.28c}$$

$$\xi_2 = \varepsilon_{n,3}^{cr} / \varepsilon_{n,u}^{cr} \tag{3.28d}$$

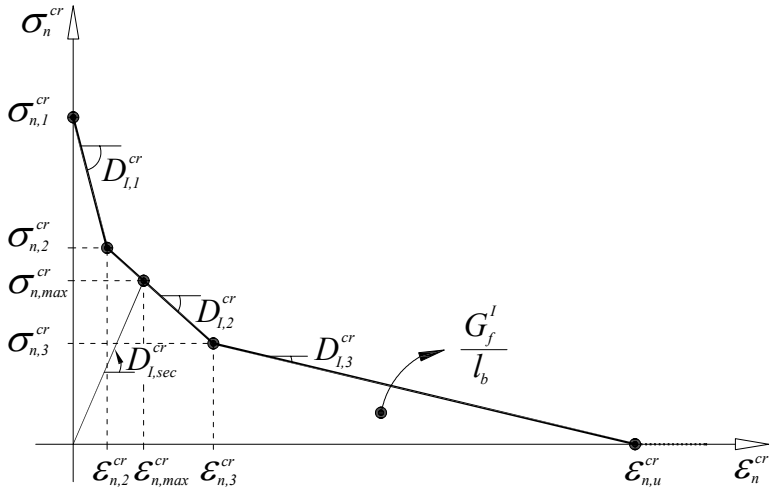

Figure 3.6 – Trilinear stress-strain diagram to simulate the fracture mode I crack propagation ($\sigma_{n,1}^{cr} = f_{ct}$, $\sigma_{n,2}^{cr} = \alpha_1\ \sigma_{n,1}^{cr}$, $\sigma_{n,3}^{cr} = \alpha_2\ \sigma_{n,1}^{cr}$, $\varepsilon_{n,2}^{cr} = \xi_1\ \varepsilon_{n,u}^{cr}$, $\varepsilon_{n,3}^{cr} = \xi_2\ \varepsilon_{n,u}^{cr}$).

An exponential tensile-softening diagram to simulate crack opening propagation is also available. This diagram, proposed by Cornelissen et al. (1986), is represented in Figure 3.7.

The ultimate crack strain, $\varepsilon_{n,u}^{cr}$, is defined as

$$\varepsilon_{n,u}^{cr} = \frac{1}{k} \frac{G_f^I}{f_{ct} l_b} \tag{3.29}$$

where

$$k = \left[\frac{1}{c_2}\left[1+6\left(\frac{c_1}{c_2}\right)^3\right]\right] - \left[\frac{1}{c_2} + c_1^3\left(\frac{1}{c_2}+\frac{3}{c_2^2}+\frac{6}{c_2^3}+\frac{6}{c_2^4}\right)+\frac{1}{2}\left(1+c_1^3\right)\right]\exp\left(-c_2\right) \qquad (3.30)$$

being c_1 = 3.0 and c_2=6.93.

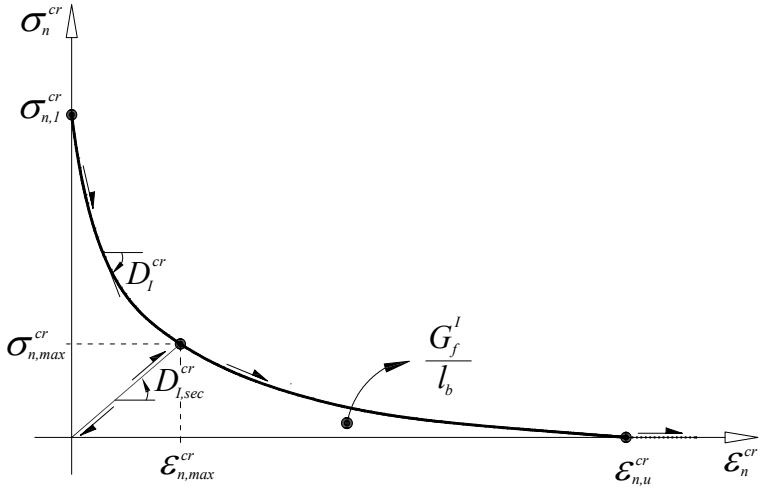

Figure 3.7 – Exponential stress-strain diagram to simulate the fracture mode I crack propagation.

The complete equations that define the trilinear diagram of Figure 3.6 and the exponential diagram of Figure 3.7 are exposed in the Appendix B. A secant approach is used to simulate the unloading and reloading branches in both diagrams.

The value of the fracture energy, G_f^I, can be obtained with the equation proposed in the CEB-FIB (1993) or with experimental tests as described in section 3.7.1.

The parameters α_i and ξ_i that define the shape of the trilinear tensile-softening diagram depend significantly on the composition of the cement based material used, e.g., plain concrete, FRC, SFRSCC. The values of these parameters can be assessed by performing an inverse analysis, as described in section 3.7.1.

The crack bandwidth, l_b, associated with the smeared crack approach, must be mesh dependent to assure mesh objectivity. In the literature, several values or methods for its calculation are presented (Bazant and Oh 1983, Rots 1988, Oliver 1989, Hofstetter and Mang 1995, Lourenço et al. 1997). In the present work, the crack bandwidth can be calculated as the square root of the area associated with the IP of the finite element, as the square root of the area of the finite element, or can adopt a supplied constant value.

The fracture mode II modulus, D_{II}^{cr}, is obtained with

$$D_{II}^{cr} = \frac{\beta}{1-\beta} G_c \tag{3.31}$$

where G_c is the concrete elastic shear modulus (see equation (3.22)) and β is the shear retention factor. The parameter β is defined as a constant value or as a function of the current crack normal strain, ε_n^{cr}, and of the ultimate crack normal strain, $\varepsilon_{n,u}^{cr}$, as follows,

$$\beta = \left(1 - \frac{\varepsilon_n^{cr}}{\varepsilon_{n,u}^{cr}}\right)^{p_1} \tag{3.32}$$

When p_1 is unitary, a linear decrease of β with the increase of ε_n^{cr} is assumed. Larger values of the exponent p_1 correspond to a more pronounced decrease of the parameter β, in order to simulate a higher in-plane shear stress degradation with the increase of the crack opening (Barros et al. 2004).

A softening constitutive law to model the in-plane crack shear stress transfer has also been developed and implemented in the FEMIX computer code. This shear softening law is described in detail in Chapter 4.

The out-of-plane shear stiffness matrix, $\underline{D}_s^{co}$, can be obtained with equation (3.21) if a linear elastic behavior for the transverse shear is assumed, or with an out-of-plane shear softening diagram exposed in detail in section 3.4.

3.4 OUT-OF-PLANE SHEAR SOFTENING DIAGRAM

3.4.1 The punching problem in laminar structures

Punching is a complex phenomenon and one of the most difficult problems to solve in the design of RC laminar structures. Several model approaches have been developed and practically all the design codes for concrete structures have paid specific attention to this type of failure. The Fib technical report nº 12 (Fib 2001) is dedicated to the problem of punching of concrete slabs. An examination of the punching problem is presented, and special attention is dedicated to the numerical simulations of punching using FEM.

Punching is fundamentally a shear failure mode, and in the last decades concerns regarding this phenomenon have increased due to the generalization of the use of thin structures, such as flat plates with small thickness and large dimensions supported by columns (see Figure 3.8). This type of failure can also be a concern in industrial floors subjected to highly concentrated loads.

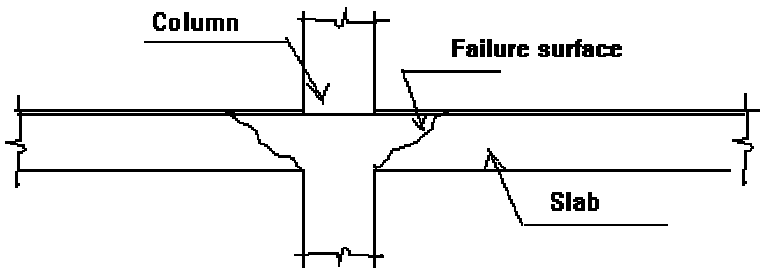

Figure 3.8 – Punching failure surfaces of a flat slab (Ngo 2001).

A concentrated load or reaction acting on a relatively small area of a slab or foundation can cause punching shear failure (EC2 2004). This type of failure may occur along a truncated cone or pyramid around the concentrated load or reaction area (ACI 2005).

The punching shear failure is usually brittle, and in the numerical prediction of the conical failure surface when, for example, a column suddenly perforates the supported slab a tridimensional model is required (Barzegar and Maddipudi 1997a).

A numerical model based on the formulation of the Reissner-Mindlin shell theory applied to the case of a multilayer approach has a lower computational effort in comparison with a full tridimensional model (Polak 2005). To explore the possibility of using the former formulation to predict shear failure modes, a softening diagram is proposed for the out-of-plane shear components of equation (3.13).

3.4.2 **Description of the diagram**

When the tensile strength is reached at an IP of a finite element, the portion of concrete included in its influence area changes from uncracked to cracked state. This local status change affects the global behavior of a structure, and consequently the numerical simulation must be capable of reproducing these phenomena. The use of a multi-fixed smeared crack model to numerically predict the behavior of laminar shell structures failing in bending is, in most cases, acceptable as long as the fracture parameters used in the constitutive crack stress-strain relation are accurately predicted. The prediction of the behavior of a structure that fails in shear or in punching is, however, a much more difficult task, as already mentioned.

The proposed out-of-plane (OP) shear diagram is represented in Figure 3.9. The out-of-plane shear behavior is assumed to be linear elastic for both components until the concrete tensile strength, f_{ct}, is reached. When the portions of concrete associated with the IP change from uncracked to cracked state, the out-of-plane shear stresses ($\tau_{23,p}^{OP}$ and $\tau_{31,p}^{OP}$) are stored for later use, and the relation between each out-of-plane shear stress-strain ($\tau_{23}-\gamma_{23}$ and $\tau_{31}-\gamma_{31}$) follows the softening law depicted in Figure 3.9.

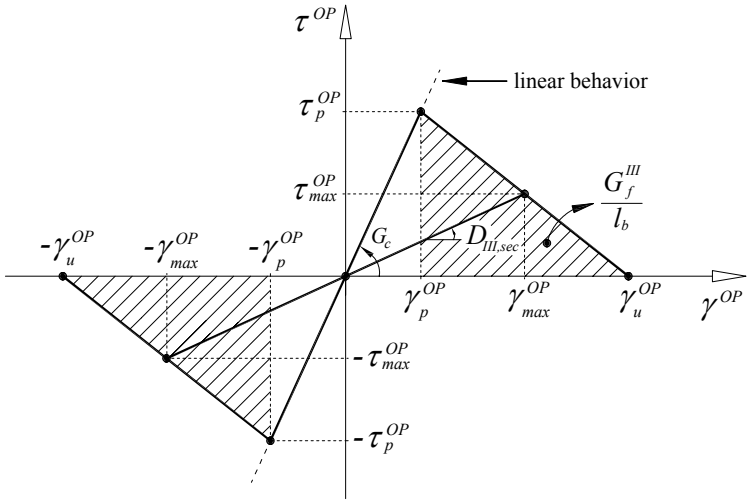

Figure 3.9 – Relationship between out-of-plane (OP) shear stress and shear strain components.

The positive branches of the diagram represented in Figure 3.9 are simulated with the expressions shown in equation (3.33). The negative part can be obtained by analogy.

$$\tau^{OP}\left(\gamma^{OP}\right)=\begin{cases} FG_c\,\gamma^{OP} & 0<\gamma^{OP}\le\gamma_p^{OP} \\ \tau_p^{OP}-\dfrac{\tau_p^{OP}}{\left(\gamma_u^{OP}-\gamma_p^{OP}\right)}\left(\gamma^{OP}-\gamma_p^{OP}\right) & \gamma_p^{OP}<\gamma^{OP}\le\gamma_u^{OP} \\ 0 & \gamma^{OP}>\gamma_u^{OP} \end{cases} \tag{3.33}$$

In the unloading or reloading branch (see section 3.4.3 for the definition of the out-of-plane shear status), the out-of-plane shear stress is calculated with a secant approach, given by

$$\tau^{OP}\left(\gamma^{OP}\right)=\frac{\tau_{max}^{OP}}{\gamma_{max}^{OP}}\gamma^{OP} \tag{3.34}$$

where τ_{max}^{OP} and γ_{max}^{OP} are the maximum out-of-plane shear stress and the maximum out-of-plane shear strain observed in the softening branch before the start of the unloading phase.

The definition of the out-of-plane shear stiffness matrix in equation (3.13), $\underline{D}_s^{co}$, is now based on the diagram represented in Figure 3.9, and named out-of-plane shear cracked concrete constitutive matrix, $\underline{D}_s^{crco}$. Therefore, the $\underline{D}_s^{crco}$ matrix is defined by

$$\underline{D}_s^{crco} = \begin{bmatrix} D_{III,\sec}^{23} & 0 \\ 0 & D_{III,\sec}^{31} \end{bmatrix} \tag{3.35}$$

being

$$D_{III,\sec}^{23} = \frac{\tau_{23,\max}^{OP}}{\gamma_{23,\max}^{OP}}, \quad D_{III,\sec}^{31} = \frac{\tau_{31,\max}^{OP}}{\gamma_{31,\max}^{OP}} \tag{3.36}$$

in accordance with the secant approach shown in Figure 3.9, where $\tau_{ij,max}^{OP}$ and $\gamma_{ij,max}^{OP}$ are the maximum out-of-plane shear stress and shear strain observed in the softening branch of each shear component, respectively.

Each out-of-plane peak shear strain, $\gamma_{23,p}^{OP}$ or $\gamma_{31,p}^{OP}$, is calculated using the stored out-of-plane peak shear stress at crack initiation, $\tau_{23,p}^{OP}$ or $\tau_{31,p}^{OP}$, and the concrete elastic shear modulus, G_c, as follows

$$\gamma_{23,p}^{OP} = \frac{\tau_{23,p}^{OP}}{G_c}, \quad \gamma_{31,p}^{OP} = \frac{\tau_{31,p}^{OP}}{G_c} \tag{3.37}$$

Each out-of-plane ultimate shear strain, $\gamma_{23,u}^{OP}$ or $\gamma_{31,u}^{OP}$, is defined as a function of the corresponding out-of-plane peak shear strain, γ_p^{OP}, the out-of-plane shear strength, τ_p^{OP}, the mode III (out-of-plane) fracture energy, G_f^{III}, and the crack bandwidth, l_b, as follows

$$\gamma_{23,u}^{OP} = \gamma_{23,p}^{OP} + \frac{2G_f^{III}}{\tau_{23,p}^{OP}\, l_b}, \quad \gamma_{31,u}^{OP} = \gamma_{31,p}^{OP} + \frac{2G_f^{III}}{\tau_{31,p}^{OP}\, l_b} \tag{3.38}$$

The present approach assumes that the crack bandwidth used to assure mesh independence when modeling fracture mode I can also be adopted in the out-of-plane fracture process.

To improve a faster loss of out-of-plane shear stress with the increase of out-of-plane shear strain, two alternative diagrams are also implemented in the FEMIX computer code. These diagrams are very similar to the one presented in Figure 3.9. The main difference is located in the softening branch. Instead of a linear softening branch, one of the proposed alternatives is based on the trilinear softening diagram, and the other is based on the exponential Cornelissen diagram used in the definition of crack opening mode I, as described in section 3.3.2.2. These two diagrams are represented in Figure 3.10 and Figure 3.11, respectively. Only the positive branch of the out-of-plane shear stress-strain relationship is represented.

The out-of-plane shear softening trilinear diagram represented in Figure 3.10 is simulated with the expressions shown in equation (3.39). As for the case of equation (3.33), only the positive branch of the diagram is treated. The negative branch can be analogously defined.

$$\tau^{OP}\left(\gamma^{OP}\right) = \begin{cases} FG_c\,\gamma^{OP} & 0 < \gamma^{OP} \le \gamma_p^{OP} \\ \tau_p^{OP} - \dfrac{\tau_p^{OP} - \tau_1^{OP}}{\gamma_1^{OP} - \gamma_p^{OP}}\left(\gamma^{OP} - \gamma_p^{OP}\right) & \gamma_p^{OP} < \gamma^{OP} \le \gamma_1^{OP} \\ \tau_1^{OP} - \dfrac{\tau_1^{OP} - \tau_2^{OP}}{\gamma_2^{OP} - \gamma_1^{OP}}\left(\gamma^{OP} - \gamma_1^{OP}\right) & \gamma_1^{OP} < \gamma^{OP} \le \gamma_2^{OP} \\ \tau_2^{OP} - \dfrac{\tau_2^{OP}}{\gamma_u^{OP} - \gamma_2^{OP}}\left(\gamma^{OP} - \gamma_2^{OP}\right) & \gamma_2^{OP} < \gamma^{OP} \le \gamma_u^{OP} \\ 0 & \gamma^{OP} > \gamma_u^{OP} \end{cases} \tag{3.39}$$

Some constants are defined as follows

$$\tau_1^{OP} = a_1 \, \tau_p^{OP} \tag{3.40a}$$

$$\tau_2^{OP} = a_2 \, \tau_p^{OP} \tag{3.40b}$$

$$\gamma_1^{OP} = b_1 \left(\gamma_u^{OP} - \gamma_p^{OP} \right) \tag{3.40c}$$

$$\gamma_2^{OP} = b_2 \left(\gamma_u^{OP} - \gamma_p^{OP} \right) \tag{3.40d}$$

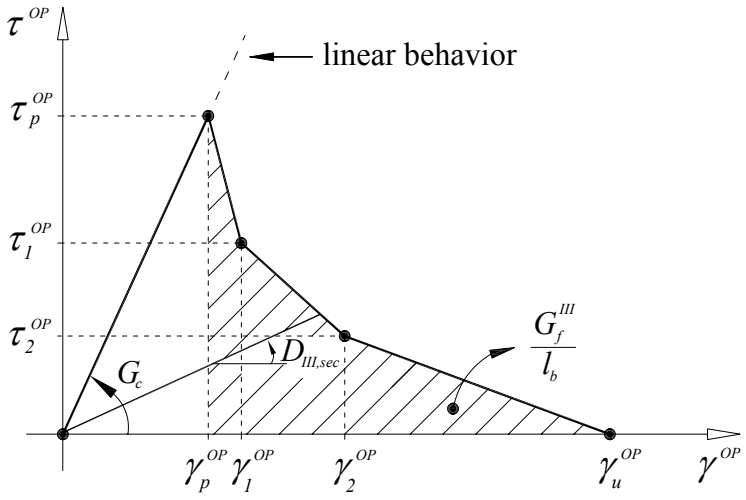

Figure 3.10 – Trilinear softening diagram to simulate the relationship between the out-of-plane shear stress and shear strain components. Only the positive branch is represented.

Each out-of-plane ultimate shear strain, $\gamma_{23,u}^{OP}$ or $\gamma_{31,u}^{OP}$, is defined as a function of the parameters a_i and b_i, the corresponding out-of-plane peak shear strain, γ_p^{OP}, the out-of-plane shear strength, τ_p^{OP}, the mode III (out-of-plane) fracture energy, G_f^{III}, and the crack bandwidth, l_b, as follows

$$\gamma_{23,u}^{OP} = \gamma_{23,p}^{OP} + \frac{2}{b_1 + a_1 b_2 - a_2 b_1 + a_2} \frac{G_f^{III}}{\tau_{23,p}^{OP} \, l_b} \tag{3.41}$$

and

$$\gamma_{31,u}^{OP} = \gamma_{31,p}^{OP} + \frac{2}{b_1 + a_1 b_2 - a_2 b_1 + a_2} \frac{G_f^{III}}{\tau_{31,p}^{OP}\, l_b} \tag{3.42}$$

Some constants are defined as follows

$$a_1 = \tau_1^{OP} \Big/ \tau_p^{OP} \tag{3.43a}$$

$$a_2 = \tau_2^{OP} \Big/ \tau_p^{OP} \tag{3.43b}$$

$$b_1 = \gamma_1^{OP} \Big/ \left(\gamma_u^{OP} - \gamma_p^{OP}\right) \tag{3.43c}$$

$$b_2 = \gamma_2^{OP} \Big/ \left(\gamma_u^{OP} - \gamma_p^{OP}\right) \tag{3.43d}$$

The out-of-plane shear softening exponential diagram is simulated with the expressions shown in equation (3.44). As for the other cases, only the positive branch of the diagram is defined here. The negative branch can be analogously obtained.

$$\tau^{OP}\left(\gamma^{OP}\right) =$$

$$= \begin{cases} FG_c\, \gamma^{OP} & 0 < \gamma^{OP} \le \gamma_p^{OP} \\ \tau_p^{OP}\left[\left(1 + \left(c_1 A\right)^3\right)\exp\left(-c_2 A\right) - A\left(1 + c_1^3\right)\exp\left(-c_2\right)\right] & \gamma_p^{OP} < \gamma^{OP} \le \gamma_u^{OP} \\ 0 & \gamma^{OP} > \gamma_u^{OP} \end{cases} \tag{3.44}$$

In this equation the parameter A is defined by

$$A = \frac{\gamma^{OP} - \gamma_p^{OP}}{\gamma_u^{OP} - \gamma_p^{OP}} \tag{3.45}$$

being c_1 = 3.0 and c_2=6.93.

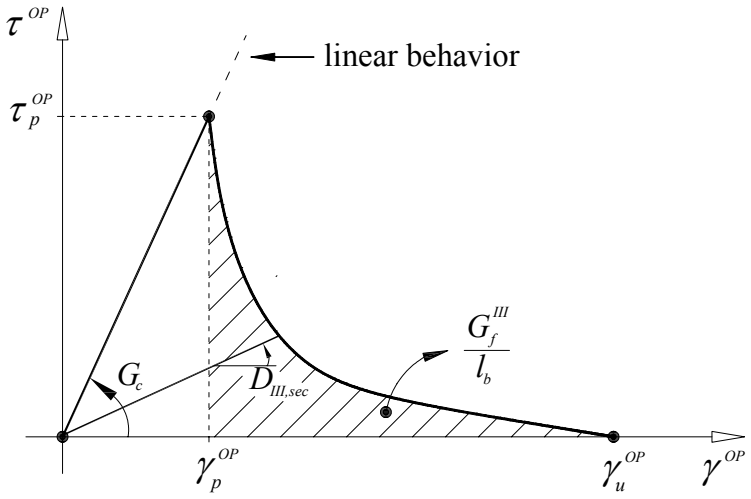

Figure 3.11 – Exponential softening diagram to simulate the relationship between the out-of-plane shear stress and shear strain components. Only the positive branch is represented.

Each out-of-plane ultimate shear strain, $\gamma_{23,u}^{OP}$ or $\gamma_{31,u}^{OP}$, of the exponential softening diagram represented in Figure 3.11 is obtained with the following equation

$$\gamma_{23,u}^{OP} = \gamma_{23,p}^{OP} + \frac{1}{k}\frac{G_f^{III}}{\tau_{23,p}^{OP}\, l_b}, \quad \gamma_{31,u}^{OP} = \gamma_{31,p}^{OP} + \frac{1}{k}\frac{G_f^{III}}{\tau_{31,p}^{OP}\, l_b} \tag{3.46}$$

where the parameter *k* is defined by equation (3.30).

3.4.3 **Out-of-plane shear status**

In section 3.4.2 an out-of-plane shear stress-strain diagram is proposed, and a secant approach for the calculation of the out-of-plane shear cracked concrete constitutive matrix, $\underline{D}_s^{crco}$, is presented.

For the calculation of the internal forces corresponding to the out-of-plane shear components, $\underline{f}_{\text{int},s}^{(e)}$, as described in section 3.2.2, the shear stresses must be calculated. For the case of a nonlinear analysis, the stress history is fundamental in the prediction of the current behavior of the structure. Therefore, to take this into account, the shear strains and stresses are stored and five out-of-plane shear statuses are considered. With this procedure,

the diagram represented in Figure 3.9 is completely defined and, at each loading stage, for a given out-of-plane shear strain the out-of-plane shear stress can be evaluated and, consequently, the corresponding internal forces are obtained.

The five crack statuses are represented in the diagram of Figure 3.12. Two sets of crack statuses are stored, one for each out-of-plane shear component, to account for their independent behavior. The explanation of each status is supplied only for one of these components.

The five out-of-plane shear statuses represented in Figure 3.12 take into account the following assumptions:

- Stiffening status, when the normal stress is smaller than the tensile strength. A linear behavior is assumed for the out-of-plane shear stress-strain relationship;
- Softening status, after the normal stress reaches the concrete tensile strength. A decrease of the out-of-plane shear stress is observed with the increase of the out-of-plane shear strain;
- Unloading status, when a decrease of the out-of-plane shear strain is observed and the previous status is softening. In this case a secant approach is followed;
- Reloading status, when an increase of the out-of-plane shear strain is observed. The branch of the unloading status is followed;
- Free-sliding status, when the out-of-plane shear strain is greater than the out-of-plane ultimate shear strain.

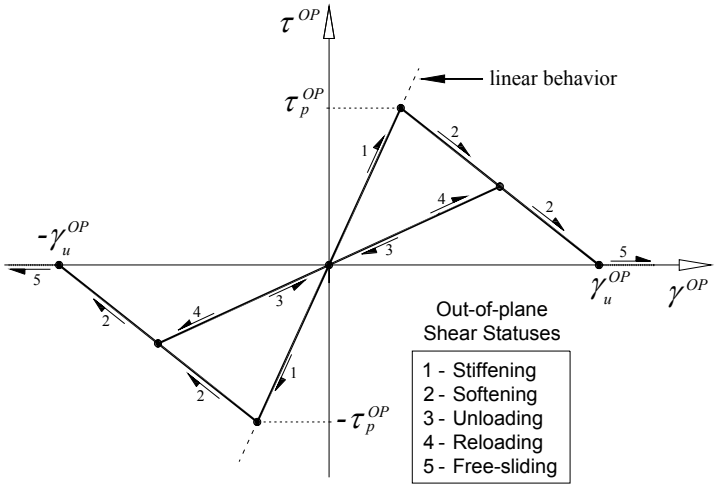

Figure 3.12 – Out-of-plane shear statuses.

When the status is "Free-sliding", the out-of-plane shear modulus $D_{III,\text{sec}}$ is null. When this occurs for both out-of-plane shear components, the matrix $\underline{D}_s^{crco}$ (see equation (3.35)) becomes a null matrix. To avoid numerical instabilities associated with this occurrence, the matrix $\underline{D}_s^{crco}$ is initialized as follows

$$D_{III,\text{sec}}^{23} = 10^{-6} G_c, \quad D_{III,\text{sec}}^{31} = 10^{-6} G_c \tag{3.47}$$

As described in section 3.4.2, a linear behavior for the out-of-plane shear components is considered until the portion of concrete associated with an IP is assigned a cracked status. Afterwards, a softening behavior is followed using one of the diagrams presented in this section.

There is no coupling between the normal (tensile) softening stress-strain diagram (that commands the crack initiation) and the out-of-plane shear softening diagram. Since the out-of-plane shear stress transfer would decrease with the crack opening, a possible strategy to simulate this effect is the activation of a softening diagram for the out-of-plane shear stress components. The softening phase for the out-of-plane shear stress components can be activated when a certain shear stress threshold value is attained. This strategy was implemented in version 4.0 of FEMIX.

3.5 IMPROVEMENTS MADE IN INTERNAL ALGORITHMS

3.5.1 **Stress update**

As mentioned before, the proposed crack constitutive model is implemented in the FEMIX computer code (Azevedo et al. 2003) under a FEM framework, being applied to the Reissner-Mindlin multi-layer shell approach. The computational and algorithmic aspects of this model are similar to the ones implemented by Sena-Cruz (2004) in FEMIX for the case of a multi-fixed smeared crack model used in the context of plane stress analysis.

In this section some problems associated with the internal convergence related to the sub-incrementation of the in-plane incremental strain vector, $\Delta\underline{\varepsilon}_{mb}$, in order to fit the law of the crack mode I are presented. The solution procedure adopted to overcome these problems is also exposed.

Firstly, the assumptions made in the algorithm for the stress update of a generic layer of an IP are presented. In a nonlinear problem the stress update is necessary to obtain the correct evaluation of the internal forces of the element that contains the IP.

All the data related to each layer at the level of an IP, e.g., stress and strain history and information corresponding to the active cracks, is stored for later use. Due to the nonlinear material behavior, an incremental-iterative procedure must be implemented to obtain the solution of the problem, as described in section 2.4 of chapter 2. In a specific iteration of the Newton-Raphson method (with or without the use of the arc-length technique or related methods) the internal forces are calculated and compared with the external forces to verify the equilibrium. This procedure is executed until convergence is achieved.

At the level of an IP the internal forces, $\underline{f}_{\text{int}}$, are obtained with the procedure presented in section 3.2.2. As stated before, the stress vector, $\underline{\sigma}$, calculated at the middle surface of each layer that discretize the thickness of the shell, is obtained from the strain vector $\underline{\varepsilon}$, taking into account the constitutive relation of the material of the corresponding layer. For the in-plane components an incremental approach is used. When the material of a certain layer is in cracked state, and is submitted to an increment $\Delta\underline{\varepsilon}_{mb}$, the corresponding incremental stress vector, $\Delta\underline{\sigma}_{mb}$, must be obtained taking into account the cracked state of the material, and, afterwards, the stress vector $\underline{\sigma}_{mb}$ is updated.

In the stress update procedure of the in-plane components, the following system of nonlinear equations must be solved (Sena-Cruz 2004) (to simplify the notation the subscript *mb* is dropped at this stage)

$$\underline{f}\left(\Delta\underline{\varepsilon}_{\ell}^{cr}\right)=\underline{\sigma}_{\ell,prev}^{cr}+\Delta\underline{\sigma}_{\ell}^{cr}-\underline{T}^{cr}\,\underline{\sigma}_{prev}-\underline{T}^{cr}\,\underline{D}^{co}\Delta\underline{\varepsilon}\;+\underline{T}^{cr}\,\underline{D}^{co}\left[\underline{T}^{cr}\right]^{T}\Delta\underline{\varepsilon}_{\ell}^{cr}=\underline{0} \qquad (3.48)$$

In this equation $\underline{\sigma}_{\ell,prev}^{cr}$ is the crack stress vector of the previous state in the local crack coordinate system ℓ (see Figure 3.5), $\Delta\underline{\sigma}_{\ell}^{cr}$ is the incremental crack stress vector that depends on the current incremental crack strain vector $\Delta\underline{\varepsilon}_{\ell}^{cr}$, $\underline{T}^{cr}$ is the matrix defined by equation (3.25), $\underline{D}^{co}$ is the matrix defined by equation (3.20) and $\underline{\sigma}_{prev}$ is the stress vector of the previous state.

Two algorithms are available to solve equation (3.48), namely the Newton-Raphson method and the fixed-point iteration method. The later is only used when the convergence is not achieved with the former.

It could be verified that in some numerical simulations these internal algorithms did not achieve convergence, causing the interruption of the analysis and forcing the user to perform successive restarts with a smaller load increment. Even with this restart mechanism in some cases the simulation could not proceed.

The problems that justify the non convergence of both iterative methods are the following:

- the sudden change in the stiffness of fracture mode I modulus when the trilinear tensile-softening is used (see Figure 3.6);
- the presence of two cracks in the same IP, with, for example, one of the cracks trying to close and the other trying to become fully open;
- in successive iterations a repeating pattern is observed, i.e., in a specific iteration the crack normal strain evolves from point A to point B (see Figure 3.13) and does not achieve convergence, so in the next iteration it evolves from point A to point C and again fails to achieve convergence. In subsequent iterations this pattern is repeated until the maximum number of iterations is reached and the algorithm stops without convergence;

- with the introduction of a softening constitutive relation for modeling the in-plane crack shear component, as described in chapter 4, these problems are greatly aggravated and also the difficulty in achieving convergence.

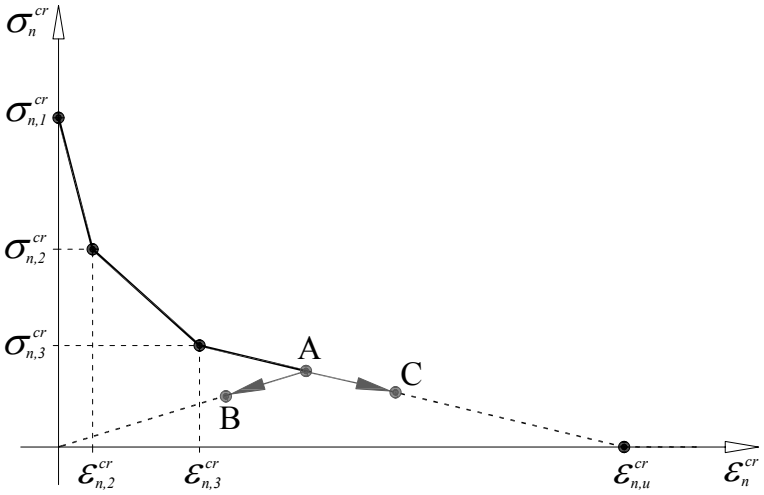

Figure 3.13 – Critical change of the fracture mode I modulus – convergence difficulties.

The convergence of each iterative method is considered to be reached when the infinite norm of the vector $\left\| \underline{f}\left(\Delta \underline{\varepsilon}_{\ell}^{cr}\right) \right\|_{\infty}$ is smaller than a residual value named *Toler*. This parameter is assumed to be equal to $10^{-6} f_c$, being f_c the concrete compressive strength. To overcome the lack of convergence due to the previously enumerated problems, the following procedure is adopted: when the Newton-Raphson method fails to converge, the fixed-point method is activated and in a first phase the situation that leads to the smallest infinite norm of the vector $\underline{f}\left(\Delta \underline{\varepsilon}_{\ell}^{cr}\right)$ is stored; in a second phase the convergence is assumed for this situation, all the vectors are updated and the procedure is continued. Although the enlargement of the *Toler*, a maximum value for it is imposed to prevent an excessive error.

It could also be verified that in some cases the minimum infinite norm of the vector $\underline{f}\left(\Delta \underline{\varepsilon}_{\ell}^{cr}\right)$ was $10^{-5} f_c$ or $10^{-4} f_c$ and the convergence was not achieved due to a very small gap in the internal assumed convergence criterion ($10^{-6} f_c$).

The relation between the global stress vector, $\underline{\sigma}$, and the local crack stress vector, $\underline{\sigma}_{\ell}^{cr}$, is given by

$$\underline{\sigma}_{\ell}^{cr} = \underline{T}^{cr}\,\underline{\sigma} \tag{3.49}$$

When *Toler* is assumed to be greater than $10^{-6} f_c$, the equilibrium imposed by this relation is also affected. However, it must be emphasized that in subsequent iterations these quantities are present in equation (3.48) and consequently the enlargement of *Toler* can be minimized.

In conclusion, with this procedure and in terms of a global analysis, this increase of *Toler* at a specific layer of an IP can be acceptable, being the robustness of the numerical simulation greatly improved.

3.5.2 **Critical crack status change**

In order to fit the tensile-softening diagram associated with the crack mode I, the incremental strain vector, $\Delta\underline{\varepsilon}_{mb}$, must be decomposed when one of the critical status change occurs during the strain increment (Barros 1995, Sena-Cruz 2004). The critical crack statuses are: new crack initiation, closure of an existent crack and reopening of a closed crack.

Therefore, after the calculation of the incremental strain vector, $\Delta\underline{\varepsilon}_{mb}$, a verification of the occurrence of a critical status is made. When one of these occurs, the incremental vector is sub-incremented. For the calculation of the transition point corresponding to a new crack initiation, k_{new}, to a closure of an existent crack, k_{close}, and to the reopening of a closed crack, k_{reopen}, two algorithms are available. One is based on the Newton-Raphson method, and the other is based on the bisection method, being used when the former does not converge (Sena-Cruz 2004).

In some numerical simulations it could be verified that, even with these two algorithms, the value of the transition point could not be obtained, in particular the k_{reopen} and the k_{close} values. In this case the numerical simulation stops and to overcome this problem a restart procedure with a reduced incremental load can be tried, but, in some cases, this restart procedure does not solve the problem.

An exhaustive analysis has been made and it could be verified that additional convergence problems might occur, as described below for a generic *k* layer of a specific IP:

- the transition point for a crack that tries to reopen is obtained, k_{reopen}, and the new stress vector is calculated using the current incremental strain vector $k_{reopen}\Delta\underline{\varepsilon}_{mb}$. With the remaining strain vector, $\left(1-k_{reopen}\right)\Delta\underline{\varepsilon}_{mb}$, a new stress vector is calculated and the verification of the occurrence of a critical status change is performed. At this moment the crack that reopens in the earlier stage is trying to close. This pattern is repeated and the numerical solution cannot be obtained;
- the transition point for a crack that tries to close is obtained, k_{close}, and a new stress vector is calculated using the current incremental strain vector, $k_{close}\Delta\underline{\varepsilon}_{mb}$. With the remaining strain vector, $\left(1-k_{close}\right)\Delta\underline{\varepsilon}_{mb}$, a new stress vector is calculated and the verification of the occurrence of critical status change is made. At this moment the crack that closes in the earlier stage tries to reopen. This pattern is repeated and the numerical solution cannot be obtained;
- when two or more cracks occur, more than one critical crack status change can also occur at the sub-incrementation of the incremental strain vector, $\Delta\underline{\varepsilon}_{mb}$, and the convergence becomes more difficult, even not attained in some cases, e.g., a closed crack tries to reopen and a new crack is initiated.

The solution encountered for these problems is treated separately for the crack reopening and for the crack closing processes. The adopted procedure is similar to the one implemented by (Sena-Cruz 2004) for the case of the initiation of a new crack.

For example, after the calculation of the current $k_{reopen}\Delta\underline{\varepsilon}_{mb}$, the crack is considered a potentially reopened crack. With the remaining strain vector, $\left(1-k_{reopen}\right)\Delta\underline{\varepsilon}_{mb}$, the reopened crack is considered in equation (3.48) and is converted into a definitive reopened crack if the crack at this phase does not close. If the crack closes, the crack that in the first phase has indicated as potentially reopened is not allowed to change its status from closed to reopening, and its historical data is restored.

To permit a future crack reopen, the crack normal stress stored in the historical data to allow a crack reopen is updated with

$$\sigma^{cr}_{n,reopen,new} = \sigma^{cr}_{n} + 10^{-6} f_c \qquad \text{if} \quad \sigma^{cr}_{n} + 10^{-6} f_c > \sigma^{cr}_{n,reopen,prev} \tag{3.50}$$

being $\sigma^{cr}_{n,reopen,prev}$ the crack normal stress stored in the historical data when the crack has closed, $\sigma^{cr}_{n,reopen,new}$ is the new updated crack normal stress for crack reopen, f_c is the compressive strength and σ^{cr}_{n} is the current crack normal stress.

A similar treatment is made for a crack that tries to close. For example, after the calculation of the current $k_{close}\Delta\underline{\varepsilon}_{mb}$, the crack is considered only a potentially closed crack. With the remaining strain vector $\left(1-k_{close}\right)\Delta\underline{\varepsilon}_{mb}$, the closed crack is not considered in the equation (3.48) and is converted into a definitive closed crack, only if at this phase does not try to reopen. If the crack reopens, the crack that in the first phase has indicated as closed is not allowed to change its status, and its historical data is restored.

As describe before, to permit a future crack close, the crack normal strain stored in the historical data to allow a crack closure is updated with

$$\varepsilon^{cr}_{n,close,new} = \varepsilon^{cr}_{n} - 10^{-6} \qquad \text{if} \quad \varepsilon^{cr}_{n} - 10^{-6} < \varepsilon^{cr}_{n,close,prev} \tag{3.51}$$

being $\varepsilon_{n,close,prev}^{cr}$ the crack normal strain stored in the historical data, $\varepsilon_{n,close,new}^{cr}$ the new updated crack normal strain for crack close, and ε_n^{cr} the current crack normal strain.

With the described procedures the starting axes of the crack tensile-softening diagram for the specific crack where such problems occur are marginally moved, as schematically represented in Figure 3.14. It must be stated that the global accuracy is not significantly affected, being the robustness of the numerical simulations significantly improved.

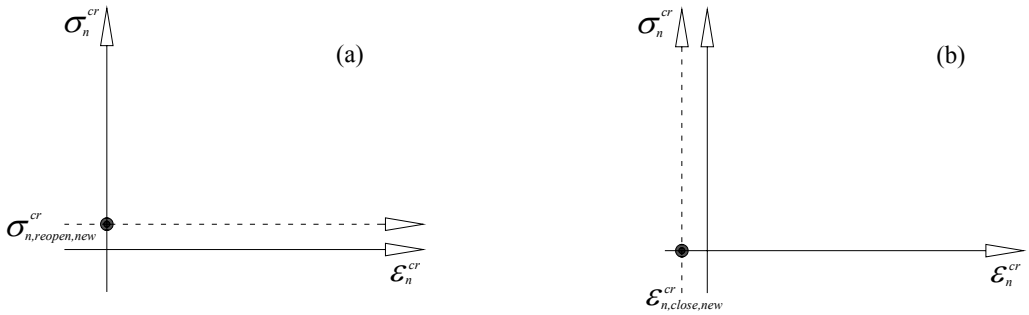

Figure 3.14 – Adopted criteria to: (a) update the crack normal stress for a crack reopen; (b) update the crack normal strain for a crack close.

3.6 SUPPORTS WITH LINEAR AND NONLINEAR BEHAVIOR

3.6.1 **Deformable point, line and surface support system**

A structure can have some of its nodal points connected to elements that can exhibit an elastic or inelastic behavior. These elements can be, for example, the ground supporting system, bars or any other structural element whose deformability is proportional to the load applied to this element, etc. The contribution of these elements to the behavior of a structure is taken into account by adding their stiffness to the stiffness of the structure (Ventura-Gouveia 1996).

In general, they can be considered as point springs, line springs or surface springs, i.e., a point spring when one point of a structure is connected to a deformable element, such as a

plate supported on a column, a line spring when the support conditions of a structure are provided continuously along a line, such as a plate supported on a wall, and a surface spring when the contact between the structure and the supporting system is a surface, such is the case of a slab on grade.

In the framework of the FEM, the contribution of these supporting elements to the stiffness of the global system can be calculated as follows:

Point springs

In this case, the stiffness of the spring is directly added to the diagonal terms of the stiffness matrix of the structure in correspondence with the degrees of freedom of the point that is connected to the spring. This addition process takes into account the coordinate system of the structure and the direction vector of the spring. A generic representation of point springs connected to a structure is represented in Figure 3.15.

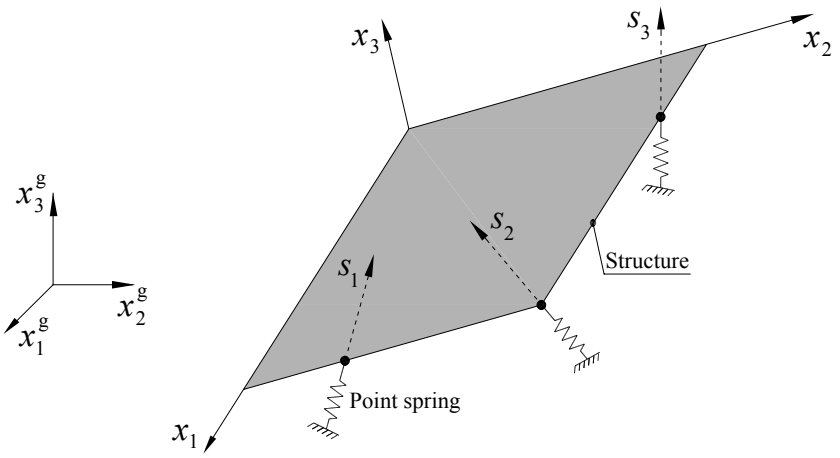

Figure 3.15 – Point springs: global coordinate system, x_i^g, local coordinate system of the structure, x_i, and spring direction vector, s_i.

The point spring stiffness $\underline{K}_s^{point}$ in the global coordinate system is obtained from

$$\underline{K}_s^{point} = \underline{T}^T \, k_s \, \underline{T} \tag{3.52}$$

where $\underline{T}$ is the transformation vector relating the global coordinate system and the spring direction vector (see Figure 3.15) and k_s the spring stiffness.

Line springs

A generic representation of a line spring connected to an edge of a structure is represented in Figure 3.16.

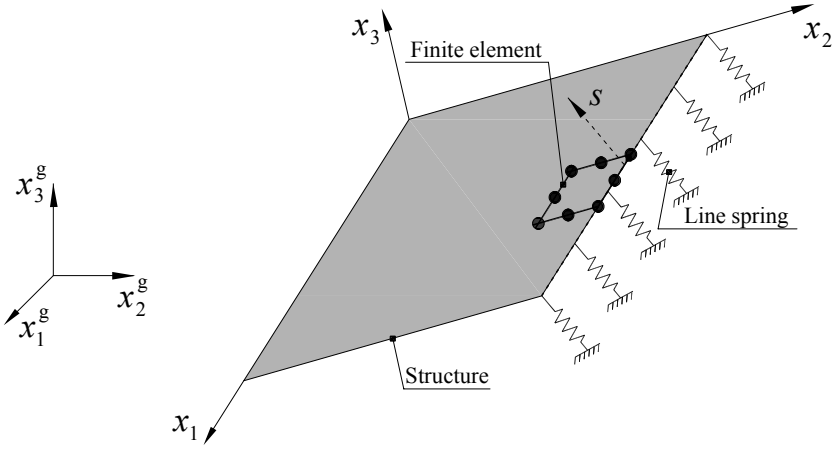

Figure 3.16 – Line spring: global coordinate system, x_i^g, local coordinate system of the structure, x_i, and line spring direction vector, s.

The line spring stiffness $\underline{K}_s^{line}$ contribution to the stiffness of the edge of the finite element where the line spring is connected is obtained with

$$\underline{K}_s^{line} = \int_L \underline{N}^T \, \underline{T}^T k_s \, \underline{T} \, \underline{N} \, dL \tag{3.53}$$

where $\underline{T}$ is the transformation vector relating the global coordinate system and the line spring direction vector (see Figure 3.16), $\underline{N}$ is the matrix of the shape functions of 1D finite elements, and k_s is the spring stiffness.

Surface springs

In Figure 3.17 a surface spring connected to a face of a structure is represented.

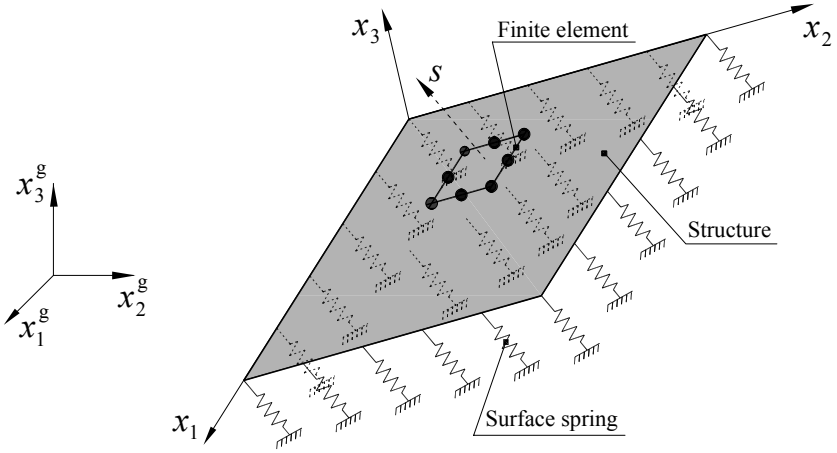

Figure 3.17 – Surface spring: global coordinate system, x_i^g, local coordinate system of the structure, x_i, and surface spring direction vector, s.

The surface spring stiffness $\underline{K}_s^{surf}$ contribution to the stiffness of the finite element where the surface spring is connected is obtained with

$$\underline{K}_s^{surf} = \int_A \underline{N}^T \, \underline{T}^T k_s \, \underline{T} \, \underline{N} \, dA \tag{3.54}$$

where $\underline{T}$ is the transformation vector relating the global coordinate system and the surface spring direction vector (see Figure 3.17), $\underline{N}$ is the matrix of the shape functions of 2D finite elements, and k_s is the spring stiffness.

The spring stiffness, k_s, of equations (3.53) and (3.54) is obtained at each IP using the shape functions of the 1D finite element or the shape functions of the 2D finite element, respectively. With this procedure a line spring with different stiffness values along its length can be numerically simulated, and, in the same way, a surface spring with non

constant stiffness can be treated (for example the simulation of a slab supported on a heterogeneous soil).

The definition of the shape functions used in the above equations can be found elsewhere (Zienkiewicz and Taylor 2000a).

3.6.2 **Unilateral supports**

In the previous section a general approach for the calculation of the contribution of different types of springs for the stiffness matrix of the structure is presented assuming a linear-elastic behavior for the springs. These springs can be connected to the various types of finite elements available in the FEMIX computer code (Azevedo et al. 2003, Sena-Cruz 2004).

Alternatively, there can be situations in which a supporting system can be idealized by a spring system with nonlinear behavior, as for the case of a soil. The evaluation of the tangent soil reaction modulus can be performed with plate-loading tests (Barros and Figueiras 1998), and results of these tests have revealed that the soil pressure-settlement relationship can be simulated with a multilinear or linear-parabolic diagram (Barros and Figueiras 2001).

There are other situations in which the stiffness of the supporting system of a structure depends on the type of load acting on this supporting system, and it can even be neglected for certain type of loading, as for the case of a soil subjected to tensile stresses. These types of supports are named in the present work as unilateral supports. In the next sections details of two diagrams to simulate this type of supports are presented: a linear-parabolic diagram to predict soil nonlinear behavior and its loss of contact with the supported structure; a bilinear-exponential diagram that can be assigned to supports considered to be active only in certain circumstances. A parametric study carried out with a slab on grade is also presented.

3.6.2.1 Linear-parabolic diagram

To provide the developed model with the possibility of numerical simulations of slabs on grade, a linear-parabolic diagram between pressure and settlement has been included in the model (Barros 1995, Barros and Figueiras 2001), being represented in Figure 3.18.

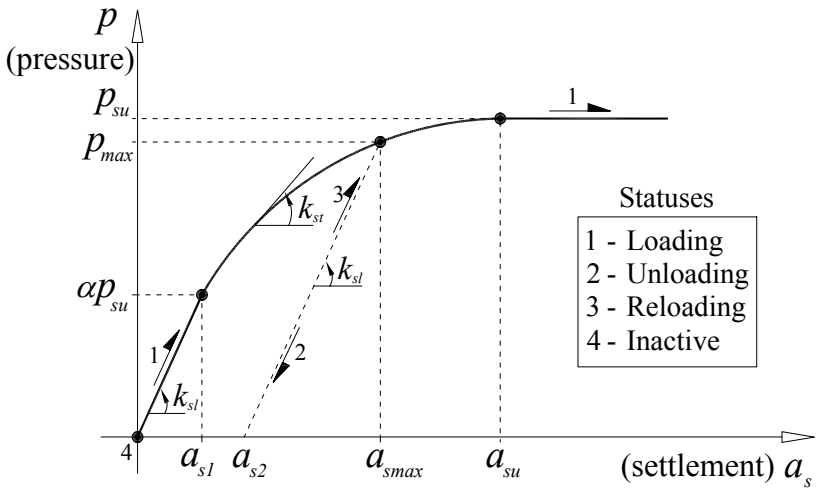

Figure 3.18 – Pressure-settlement linear-parabolic diagram.

The pressure-settlement linear-parabolic diagram is defined by the following expressions

$$p(a_s)=\begin{cases} k_{sl}a_s & 0<a_s\le a_{s1} \\ \dfrac{\gamma k_{sl}}{2a_{su}}a_s^2-\gamma k_{sl}a_s+k_{sl}\dfrac{a_{su}}{2}(\gamma+1) & a_{s1}<a_s\le a_{su} \\ p_{su} & a_s>a_{su} \end{cases} \tag{3.55}$$

where

$$a_{s1}=\alpha\frac{a_{su}}{2} \tag{3.56a}$$

$$\gamma=\frac{\alpha-1}{\dfrac{\alpha^2}{4}-\alpha+1} \tag{3.56b}$$

being α a parameter that defines the transition point from the linear to the parabolic branch (see Figure 3.18). The values of p_{su}, a_{su} and k_{sl} are obtained by curve fitting based on the experimental results of plate-loading tests (Barros and Figueiras 1998).

An elastic branch is assumed for modeling the unloading/reloading phase of the pressure-settlement relation, although the experimental results obtained from plate-loading tests (Barros and Figueiras 1998) reveal that the unloading /reloading cycles can be stiffer than the initial elastic phase.

For the unloading or reloading branch (see Figure 3.18) the pressure is given by the following equation

$$p(a_s) = k_{sl}(a_s - a_{s2}) \qquad a_{s2} < a_s \leq a_{smax} \tag{3.57}$$

being a_{s2} the residual settlement obtained with

$$a_{s2} = a_{smax} - \frac{p_{max}}{k_{sl}} \tag{3.58}$$

where a_{smax} and p_{max} are the maximum applied settlement and the corresponding pressure, pertaining to the pressure-settlement envelope curve, whose values are stored for the evaluation of the unloading-reloading branch.

The soil reaction tangent modulus in the parabolic branch, k_{st}, is obtained with the following equation

$$k_{st}(a_s) = \gamma k_{sl}\left(\frac{a_s}{a_{su}} - 1\right) \tag{3.59}$$

In a nonlinear analysis, as described in section 2.4 of chapter 2, the internal forces must be obtained. With this aim, the element nodal forces that are equivalent to the soil pressure are calculated with

$$\underline{f}^{(e)}_{\text{int},soil} = \int_{A^{(e)}} \underline{N}^T \underline{T}^T p(a_s)\, dA \tag{3.60}$$

where $\underline{T}$ is the transformation vector relating the global coordinate system and the surface spring direction vector, $\underline{N}$ is the matrix of the element surface shape functions where the surface spring is connected, and $p(a_s)$ is defined by the expressions (3.55) or (3.57).

In the framework of the finite element method, the integrals in (3.53), (3.54) and (3.60) are calculated using the Gauss-Legendre quadrature rule (Cook 1995, Zienkiewicz and Taylor 2000a).

The soil contribution to the stiffness of the global structural system is computed with equation (3.54), using the soil reaction tangent modulus, k_{sl} or k_{st}, in the place of k_s, according to the pressure-settlement linear-parabolic diagram represented in Figure 3.18.

This nonlinear behavior, idealized by the linear-parabolic diagram of Figure 3.18, is assigned to the surface springs that are orthogonal to the middle surface of a laminar structure. The friction between the laminar structure and the soil is neglected.

At each stage of a nonlinear analysis the history of some parameters, for example pressure and settlement, must be known. For this reason the FEMIX computer code stores the spring historical data, independent of the historical data related to the elements of the structure. For this purpose the four statuses indicated in Figure 3.18 are considered. With this procedure the diagram is completely defined at each stage of the nonlinear analysis and for the surface spring associated with each IP.

For the case of a slab on grade, when the concrete slab loses contact with the soil at an IP, the portion of soil that corresponds to this IP does not contribute to the stiffness of the slab-soil system and, consequently, the surface spring has an inactive status. When contact is re-established the soil stiffness is taken into account, being its value dependent on the branch of the diagram represented in Figure 3.18 and on the previous status before the spring had became inactive. This information is obtained from the data stored in the spring historical data.

Although the diagram of Figure 3.18 has been idealized for soil-structure simulation, it is also implemented for the simulation of point springs and line springs with nonlinear behavior. The necessary adaptations in the calculation of the stiffness matrix and internal forces are included in the computer code.

3.6.2.2 Bilinear-exponential diagram

The bilinear-exponential diagram described in this section and represented in Figure 3.19 can be assigned to point springs. This diagram is defined by three points, $P_1 = (a_1, F_1)$, $P_2 = (a_2, F_2)$, and $P_3 = (a_3, F_3)$, and by the parameter p used in the definition of the third branch. When a unitary value is attributed to this parameter the third branch is linear.

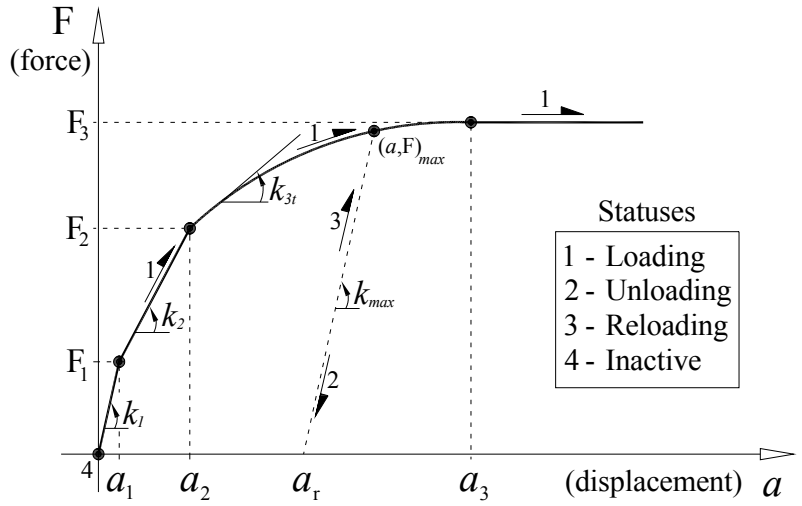

Figure 3.19 – Force-displacement bilinear-exponential diagram.

The equations that define the relation shown in Figure 3.19 are the following

$$F(a)=\begin{cases} k_1 a & 0 < a \le a_1 \\ k_2\left(a-a_2\right)+F_2 & a_1 < a \le a_2 \\ F_3+\left(F_2-F_3\right)\left(\dfrac{a_3-a}{a_3-a_2}\right)^p & a_2 < a \le a_3 \\ F_3 & a > a_3 \end{cases} \tag{3.61}$$

where

$$k_1=\frac{F_1}{a_1} \tag{3.62a}$$

$$k_2=\frac{\left(F_2-F_1\right)}{\left(a_2-a_1\right)} \tag{3.62b}$$

$$k_{3t}=-p\frac{\left(F_2-F_3\right)}{\left(a_3-a_2\right)}\left(\frac{a_3-a}{a_3-a_2}\right)^{p-1} \tag{3.62c}$$

In analogy with the diagram described in section 3.6.2.1, the statuses of this curve are also represented in Figure 3.19. The point internal forces are determined with

$$\underline{f}_{\text{int}}^{point}=\underline{T}^T F \tag{3.63}$$

being $\underline{T}$ the transformation vector relating the global coordinate system and the spring direction vector.

The stiffness matrix is obtained with equation (3.52), considering the substitution of k_s with one of the values defined by expression (3.62).

This diagram can simulate an eventual gap between the structure and a support. This is a very important feature since in some cases a structure becomes in contact with a support only after a certain displacement has occurred. Figure 3.20 represents the simulation of a gap. The value of a_1 is the gap between the structure and the point spring.

A point spring simulated with the nonlinear constitutive relation proposed in this section can be activated to work only in compression or only in tension, e.g., if the support of a structure only works for compression forces, than the loss of contact is activated if a tensile force is applied to the support. This model is available in the FEMIX computer code and can be used to simulate nonlinear unilateral supports.

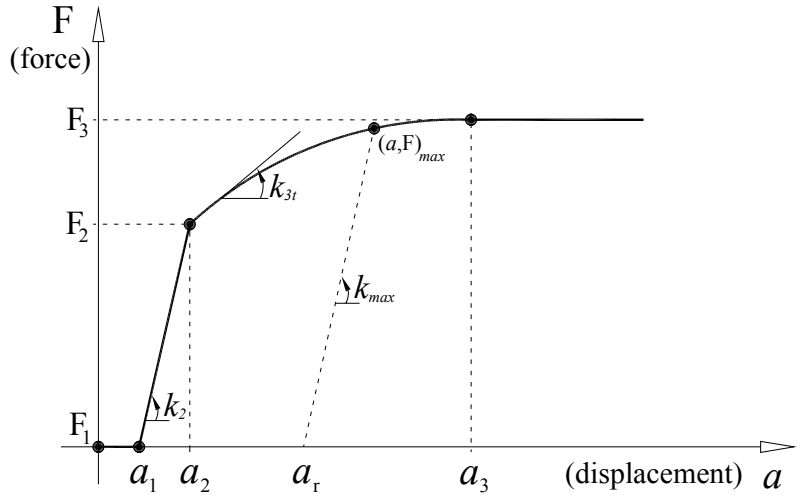

Figure 3.20 – Gap simulation between a support and a structure.

An elastic unloading/reloading is assumed in this diagram (Figure 3.20), being its inclination, k_{max}, assumed as the maximum stiffness provided by equations (3.62). For the case represented in Figure 3.20, k_{max} is equal to k_2. In the unloading/reloading phase the force is obtained with

$$F(a) = k_{max}(a - a_r) \qquad a_r < a \le a_{max} \tag{3.64}$$

being a_r the residual displacement obtained with

$$a_r = a_{max} - \frac{F_{max}}{k_{max}} \tag{3.65}$$

where a_{max} and F_{max} are the maximum applied displacement and the corresponding force pertaining to the force-displacement envelope curve, whose values are stored for the evaluation of the unloading/reloading branch.

3.6.2.3 Parametric study of a slab on grade

Industrial floors are one of the most common applications of steel fiber reinforced concrete (SFRC). Crack control joints are built to concentrate the crack propagation in these weakness-induced surfaces, resulting in a floor divided into panels. The design of a SFRC floor is, in general, restricted to the analysis of a representative panel. For the most common situations a point load in a corner of the panel is the most unfavorable load configuration. The model described in section 3.6.2.1 is used for the soil simulation in a parametric study of a SFRC slab on grade (Barros et al. 2005c). When the concrete slab loses contact with the soil at an IP, the part of the soil that corresponds to this IP does not contribute to the stiffness of the slab soil system. In this study, the influence of the slab thickness (h), the soil reaction modulus (k_s) and the amount of fibers (Q_f) is taken into account, as shown schematically in Figure 3.21.

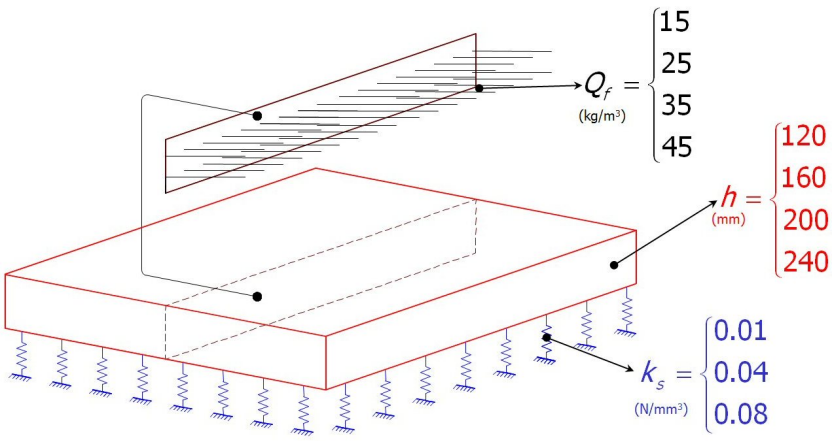

Figure 3.21 – Parametric study of a SFRC slab on grade.

The adopted finite element mesh used to analyze the behavior of the 5×5 m^2 panel is represented in Figure 3.22. Since the elements outside the dashed line square are not affected by any concrete nonlinear phenomenon, they are assumed to behave linearly. The elements located inside this square are assumed to exhibit a nonlinear material behavior. The panel thickness is decomposed in 10 layers of equal thickness. The SFRC fracture parameters used to define the $\sigma_n^{cr} - \varepsilon_n^{cr}$ trilinear diagram adopted to model the fracture mode I are presented in Table 3.1. An average compressive strength of 38 MPa and a Young's Modulus of 32 GPa are considered in the analysis. The soil is simulated with surface springs that are orthogonal to the laminate structure. For example, Figure 3.23 represents the crack pattern for the slab with $h = 160\ mm$, $Q_f = 25 kg/m^3$ and $k_s = 0.01\ N/mm^3$, at a load level corresponding to a maximum crack opening of 0.3 mm. More details about this study can be found elsewhere (Barros et al. 2005c).

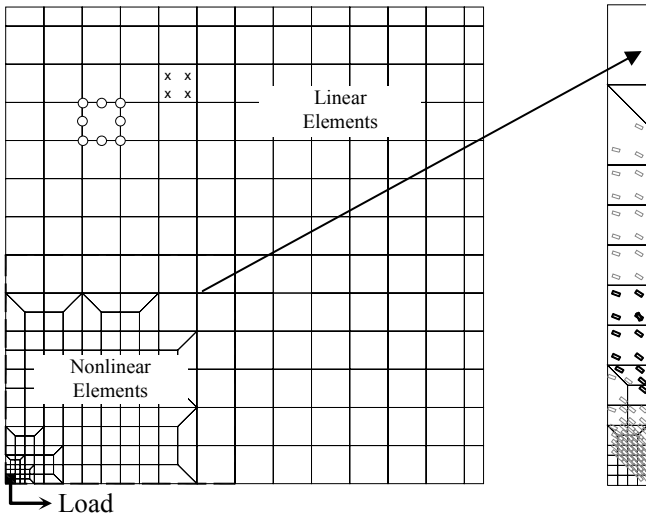

Figure 3.22 – Finite element mesh.

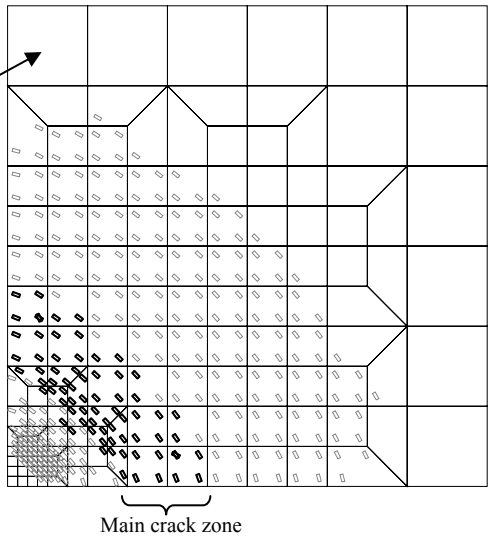

Figure 3.23 – Crack pattern at the slab top surface for a load level corresponding to a maximum crack opening of 0.3 mm.

Table 3.1 - Parameters defining the trilinear diagram of Figure 3.6 for the analyzed SFRC.

Q_f (kg/m^3)	$\sigma_{n,1}^{cr}$ (MPa)	$\frac{\sigma_{n,2}^{cr}}{\sigma_{n,1}^{cr}}$	$\frac{\sigma_{n,3}^{cr}}{\sigma_{n,1}^{cr}}$	$\frac{\varepsilon_{n,2}^{cr}}{\varepsilon_{n,u}^{cr}}$	$\frac{\varepsilon_{n,3}^{cr}}{\varepsilon_{n,u}^{cr}}$	G_f^I (N/mm)
15	2.40	0.35	0.11	2.55	0.10	2.30
25	2.60	0.51	0.31	1.28	0.79	3.90
35	1.95	0.70	0.22	2.97	0.63	3.60
45	3.42	0.60	0.60	0.05	0.14	6.60

3.7 NUMERICAL SIMULATION OF A PUNCHING TEST WITH A MODULE OF SFRSCC PANEL

To access the predictive performance of the developed model, an experimental punching test with a module of a steel fiber reinforced self-compacting concrete (SFRSCC) panel is numerically simulated in this section. The numerical results are compared with the experimental ones, and the influence of some model parameters in the numerical predictions is discussed.

SFRSCC is a relatively recent cement based material that combines the benefits of the self-compacting concrete technology (Okamura 1997) with the advantages of the addition of fibers to a brittle cementitious matrix (Pereira 2006).

To manufacture the lightweight panel system schematically represented in Figure 3.24, which can be applied in building façades, a developed SFRSCC was used and described elsewhere (Barros et al. 2005a). The mix composition of the SFRSCC used to manufacture the panel is presented in Table 3.2. In the composition of the SFRSCC, 30 kg/m^3 of hooked ends steel fibers with a length $\left(l_f\right)$ of 60 mm, a diameter $\left(d_f\right)$ of 0.75 mm, an aspect ratio $\left(l_f/d_f\right)$ of 80 and a yield stress of 1100 MPa were used. At seven days the average value of the compressive strength and modulus of elasticity of this SFRSCC was 52 MPa and 31 GPa, respectively.

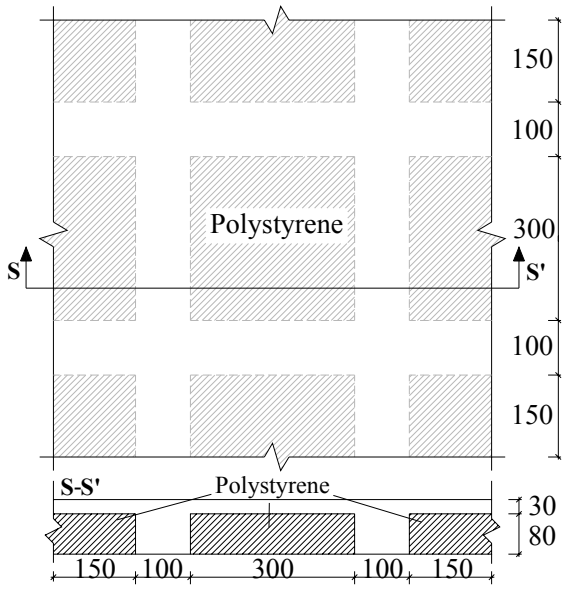

Figure 3.24 – Concept of a lightweight steel fiber reinforced self-compacting concrete panel [all dimensions are in mm] (Barros et al. 2005a).

The flexural strength of this type of structural elements is a key aspect in their design, since, in general, the bending moments of the wind load combination are an important factor in the design process of the panel. To assess the panel flexural behavior, representative modules of the SFRSCC panel system were tested, being the details of the experimental program described elsewhere (Barros et al. 2007a). Numerical simulations of these panels were also made using the developed model and can be found elsewhere (Barros et al. 2007b)

The punching resistance is also a key aspect in the design of this type of panel, since its lightweight zones consist of a thin layer that is only 30 mm thick. To evaluate the punching resistance of these zones, representative modules of the panel system are submitted to a load configuration that implies the occurrence of this type of failure mode (Barros et al. 2005a, Barros et al. 2007a).

In the next sections the results obtained in one of these tests are compared with the numerical simulations in order to assess the predictive performance of the developed model. Several numerical simulations are carried out to assess the influence of some

parameters that define the softening diagrams (Ventura-Gouveia et al. 2011). The objective of these simulations is to understand how each parameter affects the response of a laminar FRC structure failing in punching. The influence of the in-plane mesh and through-thickness refinement of the simulated structure is also analyzed.

The possibility of defining the fracture parameters that characterize the fracture mode I strain-softening diagram by performing an inverse analysis (Barros et al. 2005b) is also discussed. The inverse analysis is based on the results obtained in three point notched beam bending tests carried out according to the RILEM TC 162-TDF recommendations (Vandewalle et al. 2002).

Table 3.2 - Composition for 1 m^3 of SFRSCC including 30 kg/m^3 of fibers

Paste total volume (%)	Cement CEM I 42.5R (kg)	Limestone filler (kg)	Water (dm^3)	Super-plasticizer* (dm^3)	Fine sand (kg)	Coarse sand (kg)	Crushed aggregates (kg)
0.34	364.28	312.24	93.67	6.94	108.59	723.96	669.28

* Third generation based on polycarboxilates (Glenium® 77SCC)

3.7.1 **Evaluation of the mode I fracture properties by inverse analysis**

This section describes the inverse analysis methodology adopted to evaluate the fracture mode I parameters of the SFRSCC used in the panel prototype that was experimentally tested and numerically simulated. Detailed information about this inverse analysis can be found elsewhere (Barros et al. 2005b, Sena-Cruz et al. 2004).

As already mentioned, in the implemented smeared crack constitutive model the post-cracking behavior of SFRSCC under tension can be described by a trilinear stress-strain softening diagram (see Figure 3.6). This function is defined by a set of fracture parameters (α_i, ξ_i, G_f^I, f_{ct} and l_b), being the accuracy of the FEM modeling largely dependent on the values that are assigned to these parameters. In this context, the experimental behavior of an element failed in bending may be predicted by a FEM model,

as long as the correct values of the material fracture parameters are introduced in the constitutive model.

The adopted strategy consists in the evaluation of the ξ_i, α_i and G_f^I parameters that define the shape of the trilinear $\sigma_n^{cr} - \varepsilon_n^{cr}$ constitutive law, based on the minimization of the error parameter

$$err = \left| A_{F-\delta}^{\exp} - A_{F-\delta}^{num} \right| \Big/ A_{F-\delta}^{\exp} \tag{3.66}$$

being $A_{F-\delta}^{\exp}$ and $A_{F-\delta}^{num}$ the areas beneath the experimental and numerical load-deflection curves corresponding to a three point notched beam bending test (Sena-Cruz et al. 2004).

The experimental curve corresponds to the average results observed in prismatic SFRSCC notched specimens, tested according to the RILEM TC 162-TDF recommendations at the age of 7 days (Vandewalle et al. 2002), while the numerical curve consists of the results obtained by FEM analysis, being the specimen, loading and support conditions simulated in agreement with the experimental flexural test setup as represented in Figure 3.25.

In this context, the specimen is modeled with a mesh of 8 node serendipity plane stress finite elements. The Gauss-Legendre integration scheme with 2×2 integration points is used in all elements, with the exception of the elements at the specimen symmetry axis, where 1×2 integration points are used. With this particular integration point layout, the numerical results have a better agreement with the experimental observations, since a vertical crack may develop along the symmetry axis. Linear elastic material behavior is assumed in all the elements, with the exception of those above the notch, along the symmetry axis. In this region an elastic-cracked material model in tension is adopted. The crack bandwidth, l_b, is assumed to be equal to 5 mm, being this value coincident with the width of the notch and of the elements located above it.

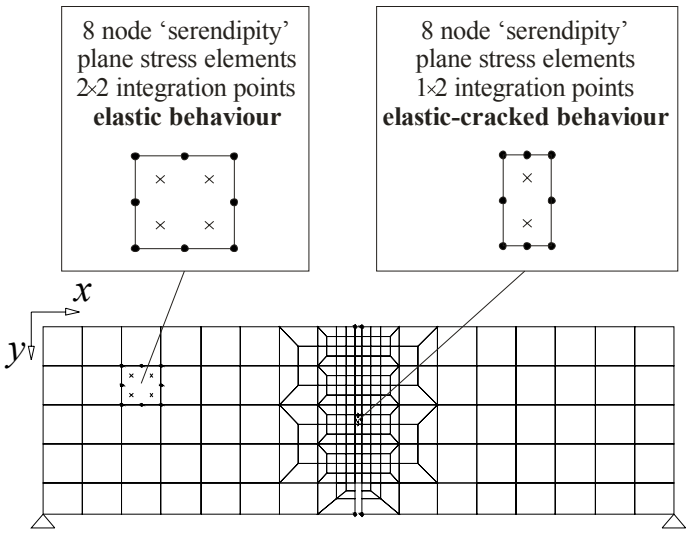

Figure 3.25 – FEM mesh used in the numerical simulation of a three-point notched beam flexural test at 7 days (Pereira et al. 2008).

In Figure 3.26 the results experimentally obtained in the flexural tests are compared with the numerical results. The curve of the numerical simulation, obtained with the optimized fracture parameters, is not perfectly coincident with the experimental curve, suggesting that additional parameters should be considered in order to obtain a better fitting. The values of the fracture parameters ξ_i, α_i and G_f^I that lead to the numerical results represented in Figure 3.26 are listed in Table 3.3.

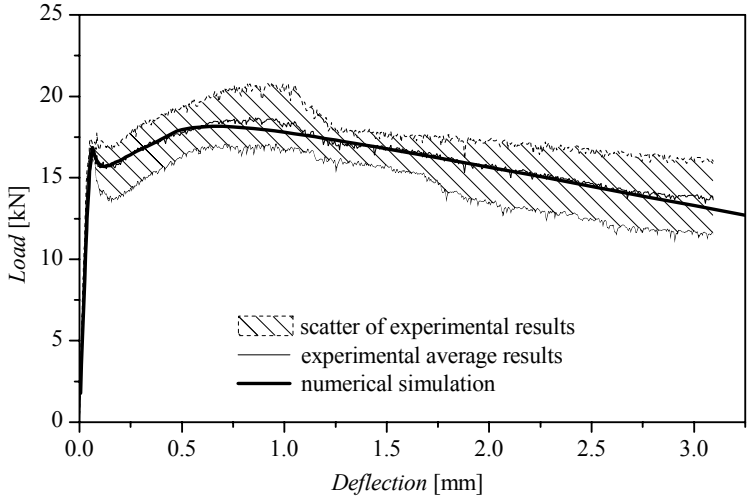

Figure 3.26 – Experimental average results and numerical simulation of the three-point notched beam flexural test at 7 days (Pereira et al. 2008).

3.7.2 **Test setup and values of the parameters used in the numerical simulations**

The punching test of a module of the developed SFRSCC lightweight panel is used to assess the predictive performance of the proposed multi-fixed smeared crack model. The test layout and the test setup are represented in Figure 3.27. More details about the corresponding experimental program can be found elsewhere (Barros et al. 2007a).

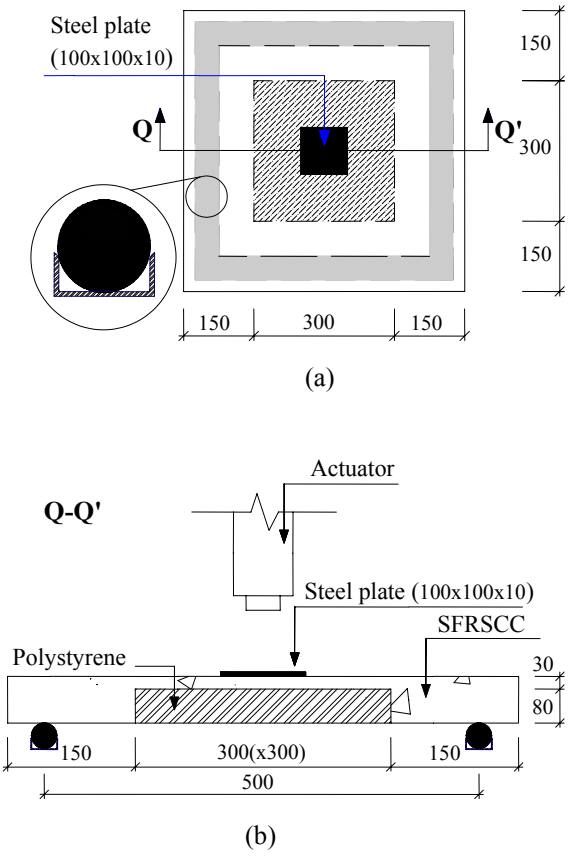

Figure 3.27 – (a) Test panel module, and (b) test setup [all dimensions are in mm] (Barros et al. 2007a).

The influence of mesh refinement and some model parameters in the results of the numerical simulations is assessed and discussed in the next sections, namely: the values adopted for the fracture mode I parameters used to define the trilinear diagram, and the values used to define the out-of-plane shear stress-strain diagram. The numerical simulations are performed using the Newton-Raphson method, with displacement control at a specific variable (see section 2.4.3 of chapter 2).

The values of the parameters of the constitutive model used in the numerical simulations of the punching test are listed in Table 3.3.

Table 3.3 - Values of the parameters of the constitutive model used in the numerical simulations of the punching test.

Poisson's ratio	$\nu = 0.15$
Initial Young's modulus	$E_c = 31000.0\ \mathrm{N/mm^2}$
Compressive strength	$f_c = 52.0\ \mathrm{N/mm^2}$
Trilinear tension softening diagram of SFRSCC (used in the numerical simulations of section 3.7.3. Parameters values obtained from inverse analysis)	$f_{ct} = 3.5\ \mathrm{N/mm^2}$; $G_f^I = 4.3\ \mathrm{N/mm}$; $\xi_1 = 0.009$; $\alpha_1 = 0.5$; $\xi_2 = 0.15$; $\alpha_2 = 0.59$
Trilinear tension softening diagram of plain concrete (used in a numerical simulation of section 3.7.3. Parameters obtained from the compressive strength of the SFRSCC according to CEB-FIP 1993 recommendations)	$f_{ct} = 3.5\ \mathrm{N/mm^2}$; $G_f^I = 0.08732\ \mathrm{N/mm}$; $\xi_1 = 0.072$; $\alpha_1 = 0.15$; $\xi_2 = 0.4432$; $\alpha_2 = 0.09$
Trilinear tension softening diagram of SFRSCC (used in the numerical simulations of section 3.7.4. Parameter values obtained by increasing/decreasing ±50% those obtained from inverse analysis)	$f_{ct} = 3.5\ \mathrm{N/mm^2}$; $G_f^I = -50\% \times 4.3\ \mathrm{N/mm}$; $\xi_1 = \pm 50\% \times 0.009$; $\alpha_1 = \pm 50\% \times 0.5$; $\xi_2 = \pm 50\% \times 0.15$; $\alpha_2 = \pm 50\% \times 0.59$ (±- depends on the numerical simulation)
Fracture energy (mode III) used in the out-of-plane shear stress-strain diagram	from $G_f^{III} = 1.0\ \mathrm{N/mm}$ to $G_f^{III} = 5.0\ \mathrm{N/mm}$ (depends on the numerical simulation)
Parameter defining the mode I fracture energy available to the new crack	$p_2 = 2$
Shear retention factor	Exponential ($p_1 = 2$)
Crack bandwidth	Square root of the area of the integration point
Threshold angle	$\alpha_{th} = 30^{\circ}$

$\alpha_1 = \sigma_{n,2}^{cr} / \sigma_{n,1}^{cr}$, $\alpha_2 = \sigma_{n,3}^{cr} / \sigma_{n,1}^{cr}$, $\xi_1 = \varepsilon_{n,2}^{cr} / \varepsilon_{n,u}^{cr}$, $\xi_2 = \varepsilon_{n,3}^{cr} / \varepsilon_{n,u}^{cr}$ (see Figure 3.6)

3.7.3 **Analysis based on the values obtained from inverse analysis**

3.7.3.1 Influence of the out-of-plane shear softening diagram

The results of the numerical simulations are compared with the experimental data obtained in the punching test of the panel module. The finite element idealization, load and support

conditions used in the numerical simulations of the punching test are shown in Figure 3.28a). Due to double symmetry, only one quarter of the panel is considered in the simulations. The mesh is composed of 6 × 6 eight-node serendipity plane shell elements. The elements are divided into 11 layers, each one being 10 mm thick. Since the panel has lightweight zones (shaded elements in Figure 3.28a), materialized by the suppression of 80 mm of concrete in the central zone, null stiffness is assigned to the 8 bottom layers of the corresponding finite elements (see Figure 3.28b). The material of the remaining three layers has an elastic-cracked behavior, as described in section 3.3.2.2. This model is also used in the elements located outside the central lightweight zone.

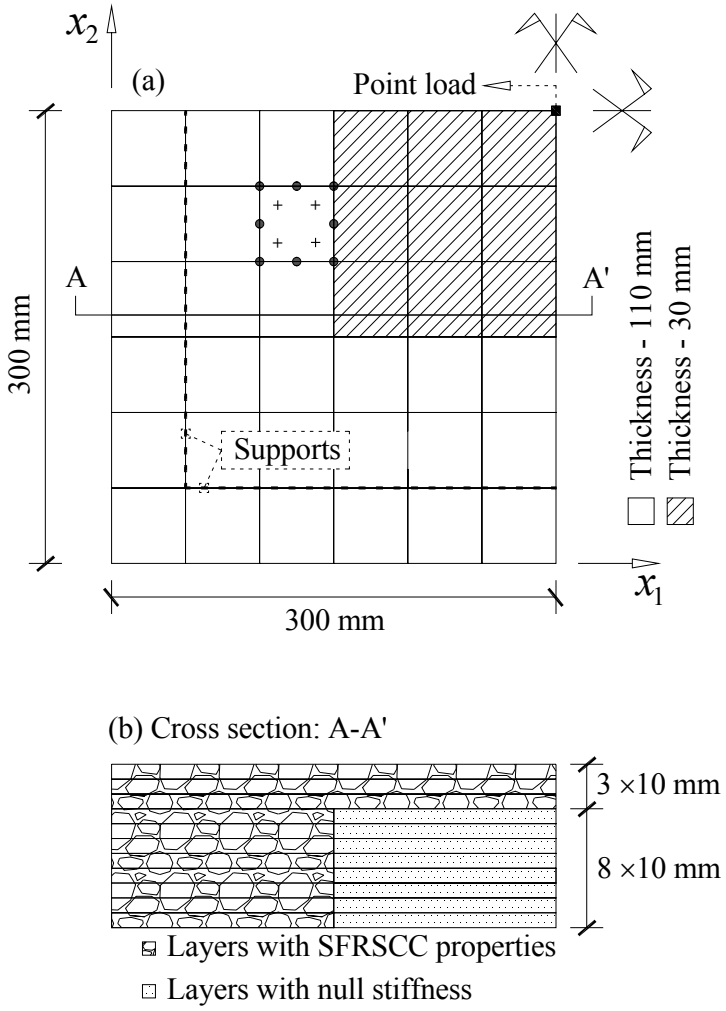

Figure 3.28 – (a) Geometry, mesh, load and support conditions used in the numerical simulation of the punching test – Coarse Mesh (CM); (b) Properties of the layered cross section.

A trial-and-error procedure is required to estimate reasonable values for the out-of-plane components of the elastic-cracked constitutive matrix, $\underline{D}_s^{crco}$ (see section 3.4), since their experimental evaluation is quite complex and beyond the scope of the present work. The out-of-plane shear fracture energy that leads to the best agreement with the experimental results of the punching tests, $G_f^{III} = 3.0\,N/mm$, is determined with this procedure.

The values of the mode I fracture parameters that take part in the in-plane elastic-cracked constitutive matrix for concrete, $\underline{D}_{mb}^{crco}$, are obtained by inverse analysis, as described in section 3.7.1.

In Figure 3.29 responses obtained with the numerical model are compared with the experimental results. A good agreement can be observed up to a deflection of 2.5 mm. For larger deflections, an overestimation of the load carrying capacity of the prototype panel occurs when a linear elastic behavior is assumed for the out-of-plane shear components. At a deflection of about 3 mm, the experimental curve suddenly falls, indicating the failure of the panel by punching, as visually confirmed in the experimental test. This load decay that is not reproduced when assuming a linear elastic behavior for the out-of-plane shear components is, however, well captured when the bilinear diagram represented in Figure 3.9 is used to model the softening behavior of the out-of-plane shear components, with $G_f^{III} = 3.0\,N/mm$, and assuming a crack bandwidth, l_b, equal to the square root of the area associated with the corresponding IP. The abrupt load decay from approximately 41 kN to 20 kN, which is observed in the experimental test, is accurately simulated by the numerical model, as well as the subsequent extended stage of residual load carrying capacity exhibiting a very small load decay.

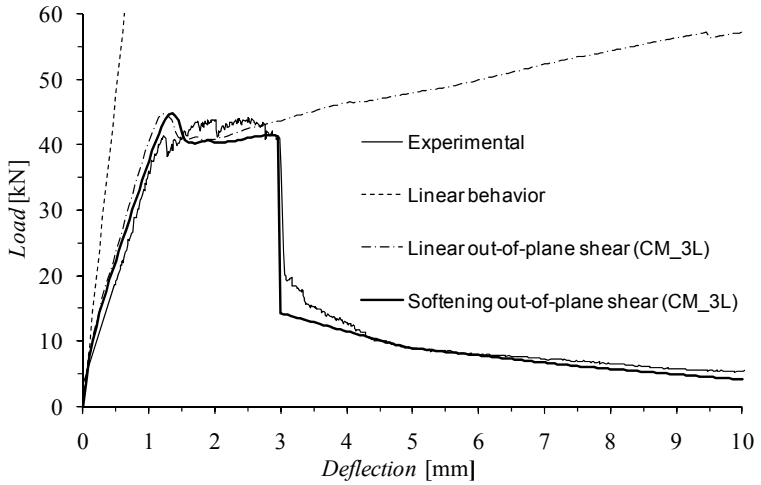

Figure 3.29 – Relationship between load and deflection at the center of the test panel.

Up to a 10 kN load, all the curves depicted in Figure 3.29 are practically coincident. Afterwards, the straight line that represents the response assuming a linear elastic behavior no longer follows the curves that correspond to the experimental test and to the numerical analysis with material nonlinear model. These results suggest that some cracks start to form at a very early stage of the experimental test. The nonlinear numerical model accurately captures the formation of bending cracks at the top surface (see Figure 3.30a), in agreement with the experimentally observed crack pattern. Figure 3.30b shows the crack pattern at the top surface observed at the end of the test sequence. The numerical model also indicates the formation of bending cracks at the bottom surface of the lightweight zone. These cracks initiate at the center of the panel, beneath the loaded area, and then progress to the corners of the lightweight zone, showing some similarities with the classical yield lines formed in square concrete slabs failing by flexure. These cracks can also be observed in the experimental test (Pereira 2006).

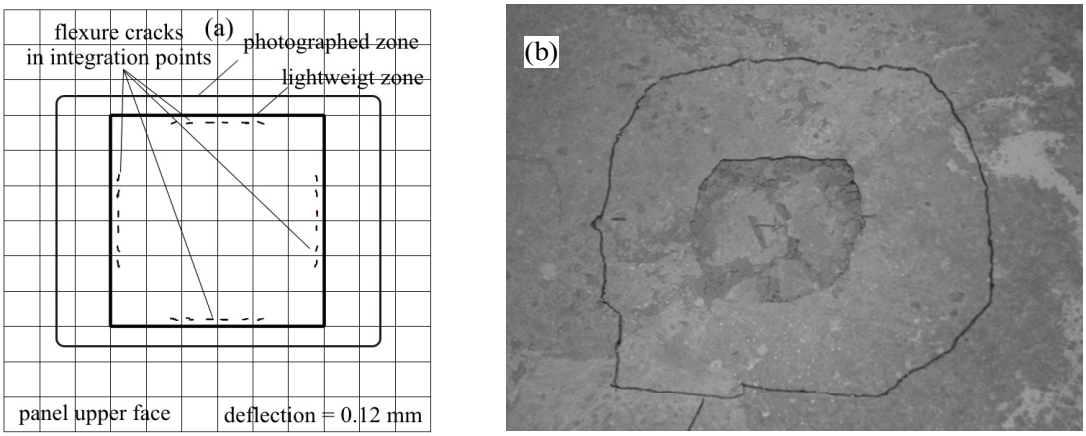

Figure 3.30 – Punching test simulation: (a) top surface cracks predicted by the numerical model (using a FEM mesh with 12 × 12 eight-node serendipity plane shell elements) , and (b) photograph showing the cracks at the top surface of the panel, at the end of the test sequence (Pereira 2006).

In conclusion, the results indicate that flexure mechanisms prevail in the deformational behavior up to a deflection of approximately 2.5 mm. For larger deflections, the punching failure mechanisms start to assume a greater relevance, and the overestimation of the panel out-of-plane rigidity components, when linear out-of-plane shear behavior is assumed, leads to a divergence between the numerical model and the experimental observations. With the adoption of a softening law for the out-of-plane shear components, the numerical model becomes much more accurate in the prediction of the complete behavior of the panel failing in punching, capturing the sudden load decay associated with punching failure mechanisms.

To estimate the contribution of fiber reinforcement to the punching resistance, a numerical simulation was performed adopting for the fracture mode I the parameters indicated in Table 3.3, which correspond to plain concrete with compressive strength matching the developed SFRSCC. Comparing the curves in Figure 3.31 it can be concluded that fibers not only increased significantly the punching resistance, but also, and especially, improved the ductility.

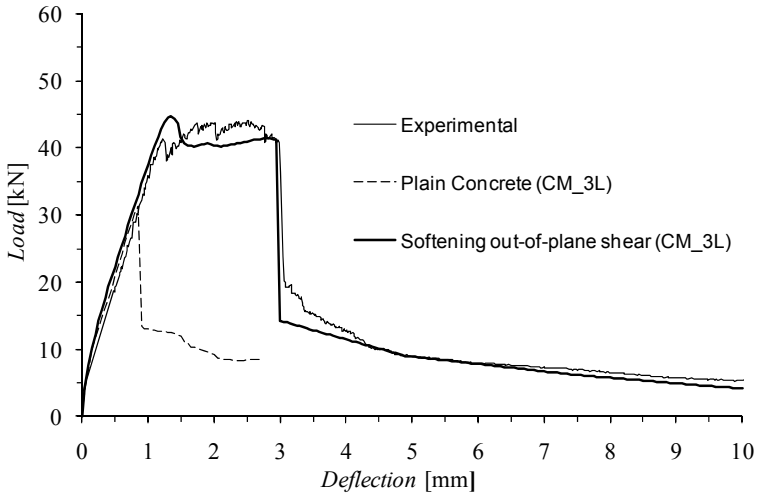

Figure 3.31 – Influence of fiber reinforcement in the punching resistance.

Figure 3.32 represents the vertical displacement field for a deflection of 10 mm at the center of the panel for the case of the numerical simulation considering out-of-plane shear softening. The obtained strong gradient of vertical displacements matches with high precision the experimentally observed location of the interception of the punching failure surface with the top panel face (see Figure 3.30b). This evidences the suitability of the developed approach for the simulation of this complex failure mode.

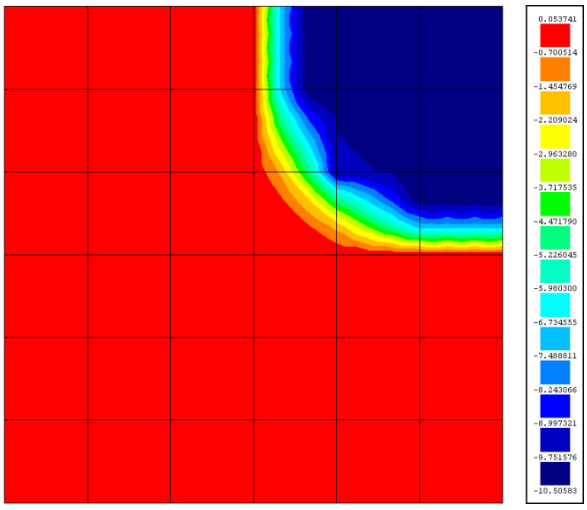

Figure 3.32 – Vertical displacement field (in mm) for the numerical simulation with out-of-plane shear softening (for a deflection of 10 mm at the center of the panel).

As already mentioned, the selection of a value for G_f^{III} has no experimental support. In order to analyze its influence on the results of the numerical simulation using a softening law for both out-of-plane components, a parametric analysis is carried out consisting in the variation of its value from 1.0 to 5.0 N/mm. The results depicted in Figure 3.33 show that a value of $G_f^{III} = 3.0\,\mathrm{N/mm}$ leads to a perfect prediction of the abrupt load decay experimentally observed at a deflection of about 3 mm. Increasing or decreasing the value of G_f^{III} implies the occurrence of the abrupt load decay at a larger or smaller deflection, respectively. The conclusion of this study is that, independently of the value of G_f^{III}, when using the model described in this work, it is essential to use a softening law for the out-of-plane shear components in order to simulate the sudden load decay observed in the punching test.

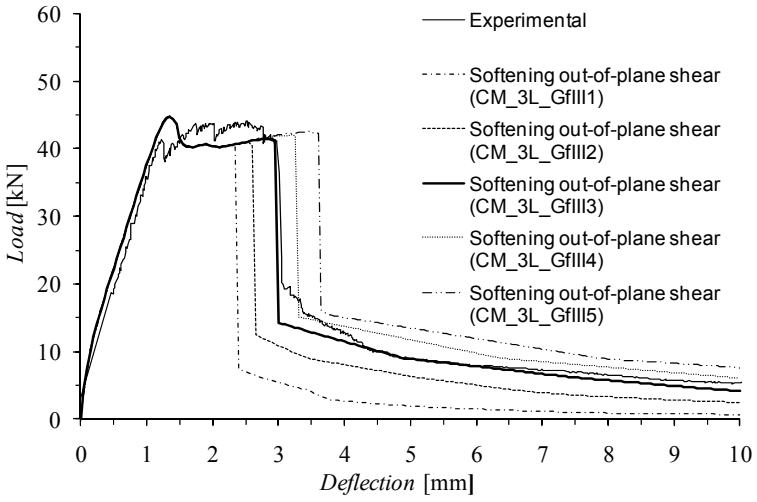

Figure 3.33 – Influence of G_f^{III}, using the in-plane coarse mesh and 3 layers in the lightweight zone, on the numerical relationship between load and deflection at the center of the test panel.

Similar results were obtained in numerical simulations in which the supports of the panel, represented in Figure 3.28a by the dashed line, were simulated with line springs with "infinite" stiffness in compression and null strength in tension using the linear-parabolic diagram described in section 3.6.2.1, in order to simulate the loss of contact between the panel and the support during the loading process (Ventura-Gouveia et al. 2007).

3.7.3.2 Influence of the through-thickness refinement of the panel

In this section, the influence of through-thickness refinement of the panel on the load-deflection relationship is analyzed. The parameters used to simulate the fracture mode I and the out-of-plane shear softening diagram are those that have best fitted the experimental results, according to the strategy described in the previous section.

For this purpose, the following two refinements are considered: 6 layers in the lightweight zone and 22 layers in the remaining parts; 10 layers in the lightweight zone and 26 layers in the other zones.

In Figure 3.34 the load-deflection relationships of these numerical simulations are compared with the experimental one, indicating CM_*j*L the curve obtained with a *j*-layer discretization in the lightweight zone.

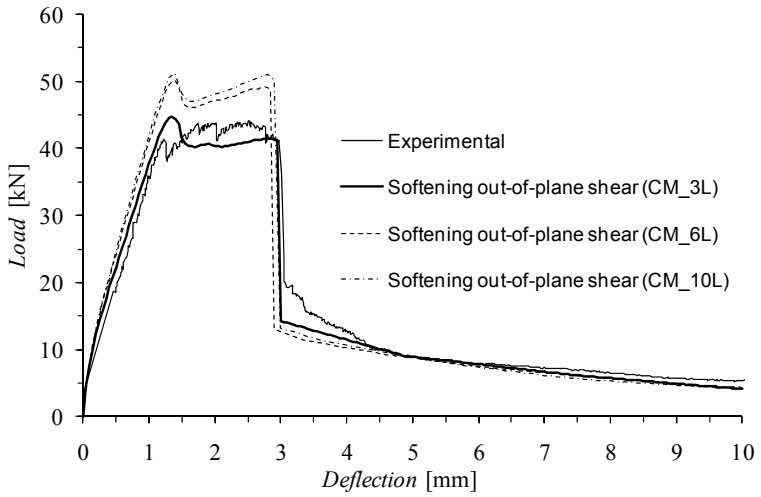

Figure 3.34 – Influence of the number of layers discretizing the thickness of the panel in the lightweight zone (results for 3, 6 and 10 layers are shown).

It can be observed that by increasing the number of layers in the lightweight zone from 3 to 6, the maximum load increases approximately 17%, and the stiffness corresponding to the branch between crack initiation and peak load also increases. This behavior can be justified by the fact that the flexural stiffness of each layer is not considered in the evaluation of the internal forces of the Mindlin shell finite elements when a material

nonlinear analysis is performed. Therefore, the larger the number of layers discretizing the element, the higher the flexural stiffness of the element is, resulting in a smaller deformability of the panel and a higher load carrying capacity. However, Figure 3.34 also shows that when the number of layers increases from 6 to 10, only a marginal increase of the maximum load is observed, which indicates that the increase ratio of the flexural stiffness and load carrying capacity of the layered Mindlin shell element decreases with the number of layers.

It is also interesting to observe that the deflection at the abrupt load decay, as well as the residual load carrying capacity of the panel, are very similar in all three numerical analyses.

3.7.3.3 Influence of the in-plane mesh refinement of the panel

In order to assess the influence of the in-plane mesh refinement on the load-deflection relationship, an alternative and more refined mesh (RM) is considered (see Figure 3.35), being the corresponding results presented below. Eight-node serendipity plane shell elements are used, with 10 layers in the lightweight zone and 26 layers in the other zones.

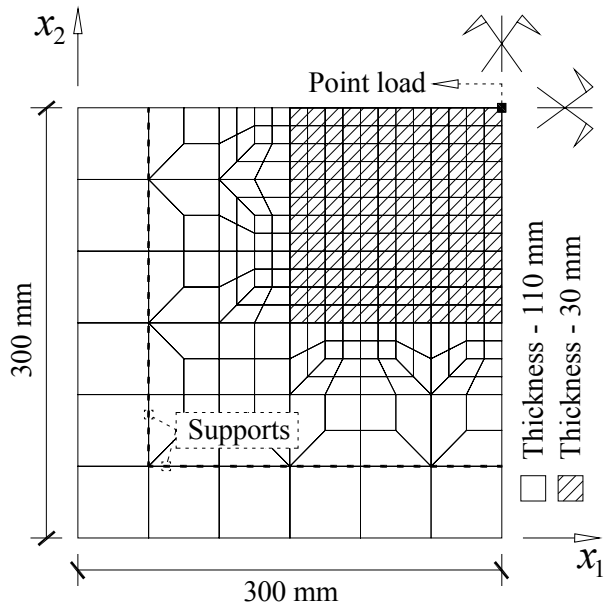

Figure 3.35 – Geometry, mesh, load and support conditions used in the numerical simulation of the punching test – Refined Mesh (RM).

The load-deflection relationship for the RM is represented in Figure 3.36, being compared with the one obtained with the previous coarse mesh (CM), and with the one experimentally registered. As expected, the deformability of the panel increases with the mesh refinement, causing the abrupt load decay to occur for a larger deflection (3.3 mm). Due to the higher flexibility of the panel discretized with the RM, a decrease of about 5% in terms of load carrying capacity is observed. Therefore, the shape of the load-deflection (F-u) curve for the RM is approximately the result of the rotation of the F-u curve for the CM about the point that corresponds to the crack initiation.

With the increase of the number of finite elements (and integration points), the concrete in cracked status and the corresponding consumed mode I fracture energy also increase. This can be a possible justification for the more deformable response in the numerical simulation of the in-plane RM .

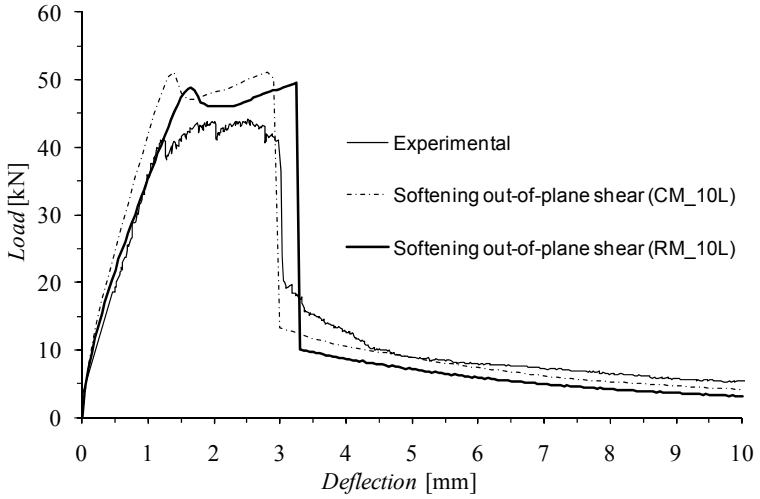

Figure 3.36 – Influence of the in-plane mesh refinement on the numerical load-deflection response at the center of the test panel.

3.7.3.4 Influence of the fracture energy (G_f^{III}) used in the out-of-plane shear softening diagram

To assess the influence of the fracture energy used to define the out-of-plane shear softening diagram, G_f^{III} , on the load-deflection relationship, its value is varied between

1.0 N/mm and 5.0 N/mm. In these analyses the in-plane CM and the RM are used, with 10 layers discretizing the thickness of the panel in the lightweight zone. The obtained numerical curves are represented in Figure 3.37 and Figure 3.38, respectively. It is observed that in the RM the G_f^{III} value mainly affects the residual load carrying capacity after the abrupt load decay. When using the CM, the value attributed to G_f^{III} not only affects the residual load carrying capacity but also influences the value of the deflection corresponding to the abrupt load decay. This influence, however, is less pronounced than when using an in-plane CM with 3 layers discretizing the thickness of the panel in the lightweight zone (see Figure 3.33). Therefore it can be concluded that when a RM is used, suitable predictions can be obtained with $G_f^{III} = G_f^I$, but further research needs to be carried out for a more reliable estimation of G_f^{III}.

Figure 3.39 and Figure 3.40 show the consumed out-of-plane fracture energy ($G_{f,c}^{III}$) up to a deflection of 3.5 mm for the in-plane CM and RM, respectively. At each integration point, this consumed fracture energy receives the contribution of the two out-of-plane shear components in all layers, and can be regarded as an indicator of damage due to the punching failure mode. It can be observed that the punching failure pattern is well predicted when using the RM. When using the in-plane CM refinement the shear failure bandwidth is larger, thus justifying the higher sensibility of the deflection corresponding to the abrupt load decay to the adopted G_f^{III} value (see Figure 3.37).

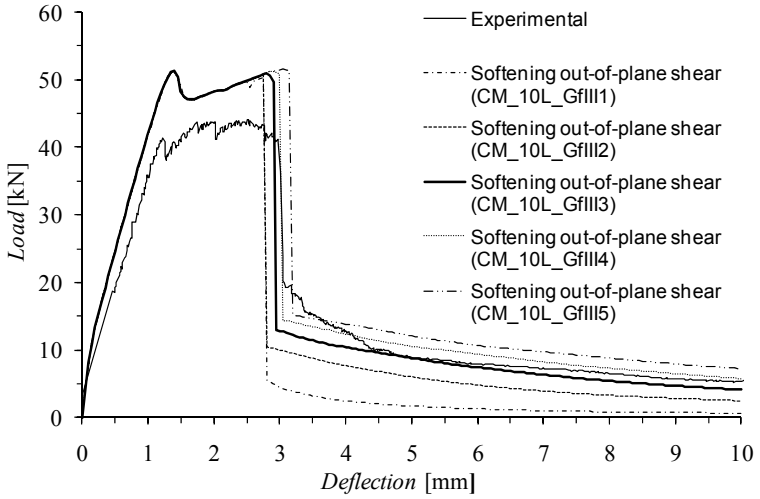

Figure 3.37 – Influence of G_f^{III} on the numerical relationship between load and deflection at the center of the panel, when using the in-plane coarse mesh and 10 layers in the lightweight zone.

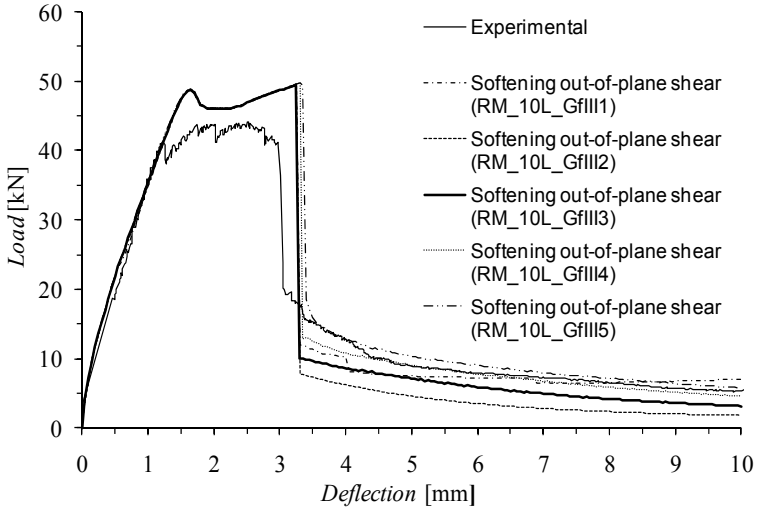

Figure 3.38 – Influence of G_f^{III} on the numerical relationship between load and deflection at the center of the panel, when using the in-plane refined mesh and 10 layers in the lightweight zone.

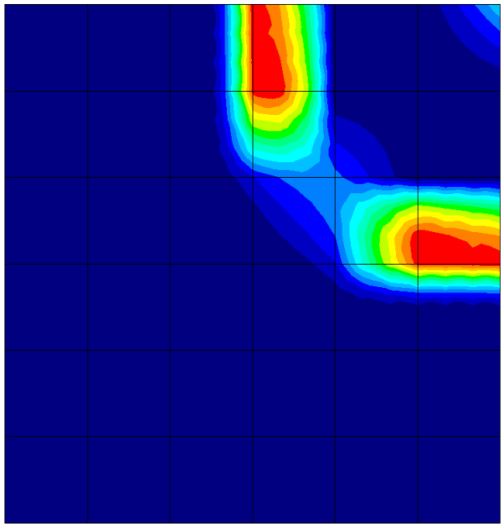

Figure 3.39 – Representation of the consumed out-of-plane fracture energy, $G_{f,c}^{III}$, when using the in-plane coarse mesh and 10 layers in the lightweight zone, for a deflection of 3.5 mm.

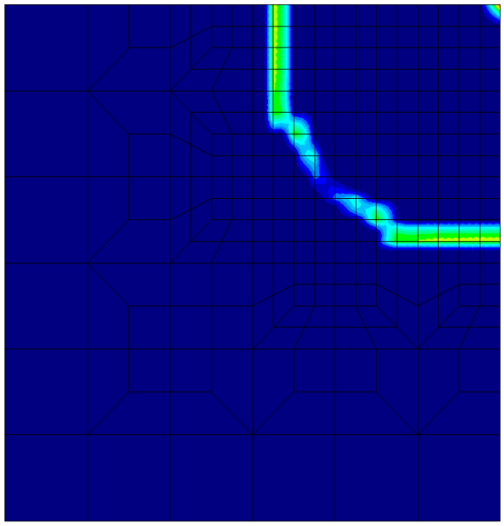

Figure 3.40 – Representation of the consumed out-of-plane fracture energy, $G_{f,c}^{III}$, when using the in-plane refined mesh and 10 layers in the lightweight zone, for a deflection of 3.5 mm.

3.7.4 **Influence of the parameters that define the fracture mode I**

In order to assess the influence of the parameters that define the fracture mode I constitutive law (Figure 3.6) on the load-deflection relationship predicted by the numerical model, the values of these parameters are decreased and increased by 50 % relatively to those obtained by inverse analysis. The crack stress vs. crack strain ($\sigma_n^{cr} - \varepsilon_n^{cr}$) for these analyses and the corresponding load-deflection relationships are depicted in Figure 3.41 to Figure 3.45.

All these numerical analyses utilize the refined mesh and use 10 layers for the discretization of the thickness of the lightweight part of the panel. From the analysis of these graphs it can be concluded that the inclination of the first branch of the $\sigma_n^{cr} - \varepsilon_n^{cr}$ diagram (D_{n1}^{cr} in Figure 3.6) governs the point corresponding to the first drop in the load-deflection relationship. In fact, the less abrupt this branch is, the higher the load at this point becomes. Consequently, it is observed that the load carrying capacity of the panel is quite sensible to the slope of this branch. Direct tensile tests with SFRSCC similar to the one used in the tested panels showed, in fact, an abrupt stress decay immediately after crack formation.

Figure 3.42b evidences that the numerically predicted load carrying capacity of the panel is quite dependent on the α_1 parameter, since a pronounced softening and a significant hardening deflection are estimated when a value of α_1 smaller or larger than the one obtained by inverse analysis is used (see Figure 3.42a). The higher strength $\sigma_n^{cr}\left(\varepsilon_n^{cr}\right)$ of the second branch of $\sigma_n^{cr} - \varepsilon_n^{cr}$, when adopting higher values for the α_1 parameter (see Figure 3.42a), also contributes to increase both the load carrying capacity of the panel and the deflection corresponding to the punching failure. However, Figure 3.44 reveals that the strength $\sigma_n^{cr}\left(\varepsilon_n^{cr}\right)$ corresponding to the first branch of $\sigma_n^{cr} - \varepsilon_n^{cr}$ diagram has a much higher influence on the load carrying capacity of the panel than the strength $\sigma_n^{cr}\left(\varepsilon_n^{cr}\right)$ of the second branch. Nevertheless, Figure 3.44 and Figure 3.45 also demonstrate that the slope of the load-deflection branch before the punching failure grows with the value of D_{n2}^{cr} (Figure 3.6). Finally, the decrease of the fracture energy is mainly reflected at the point corresponding to the first drop of the load-deflection relationship (Figure 3.45b). This decrease leads to a more abrupt decay of the first branch of the $\sigma_n^{cr} - \varepsilon_n^{cr}$ diagram (Figure 3.45a), resulting in a decrease of the load at this point.

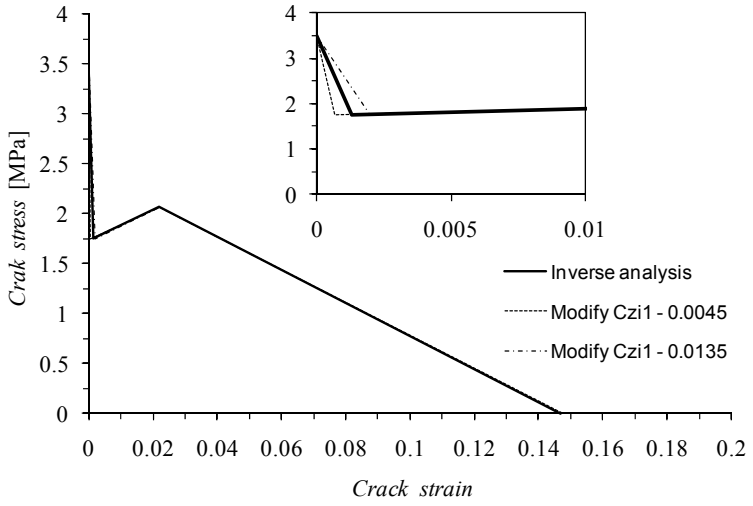

(a)

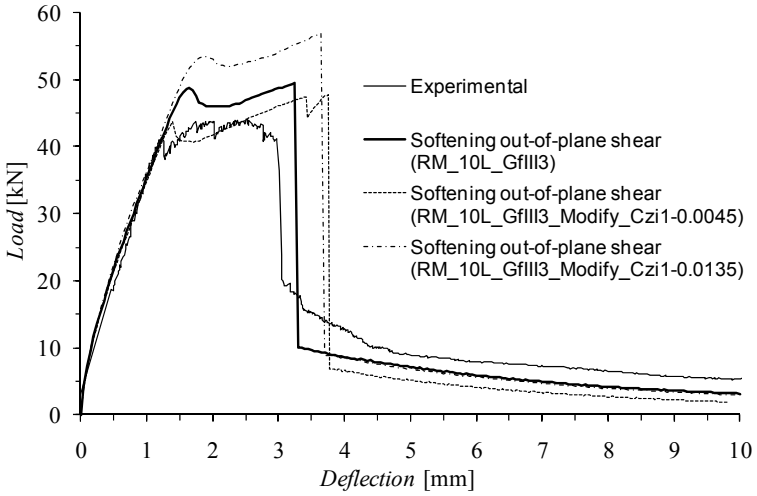

(b)

Figure 3.41 – Influence of the ξ_1 parameter: (a) trilinear softening diagrams and (b) relationship between load and deflection at the center of the test panel.

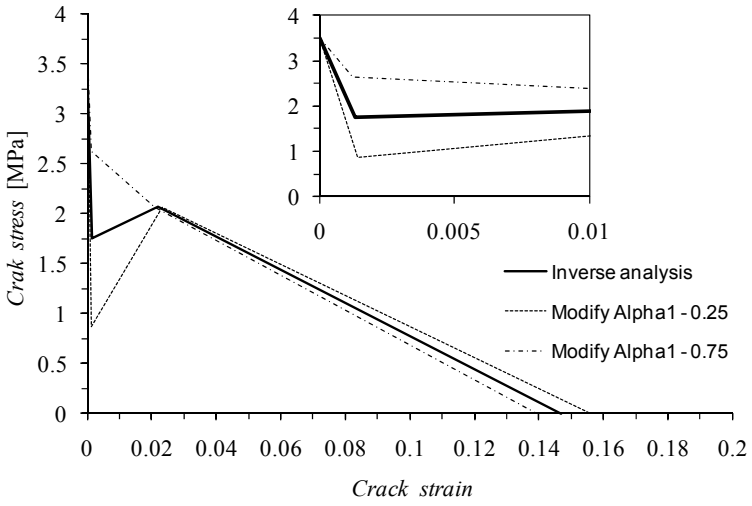

(a)

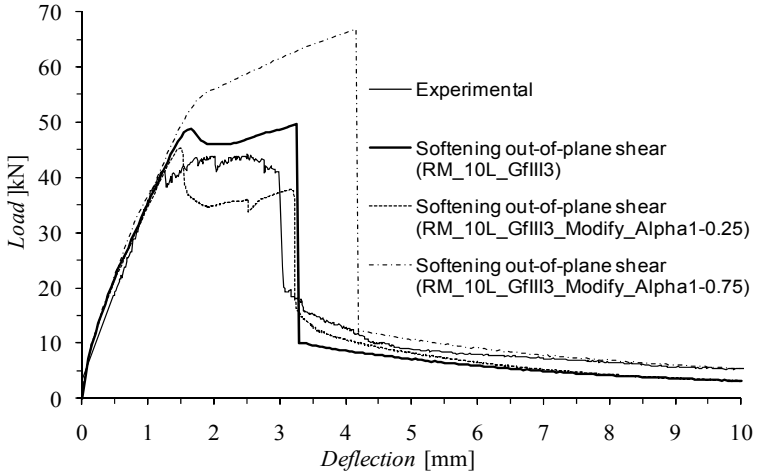

(b)

Figure 3.42 – Influence of the α_1 parameter: (a) trilinear softening diagrams and (b) relationship between load and deflection at the center of the test panel.

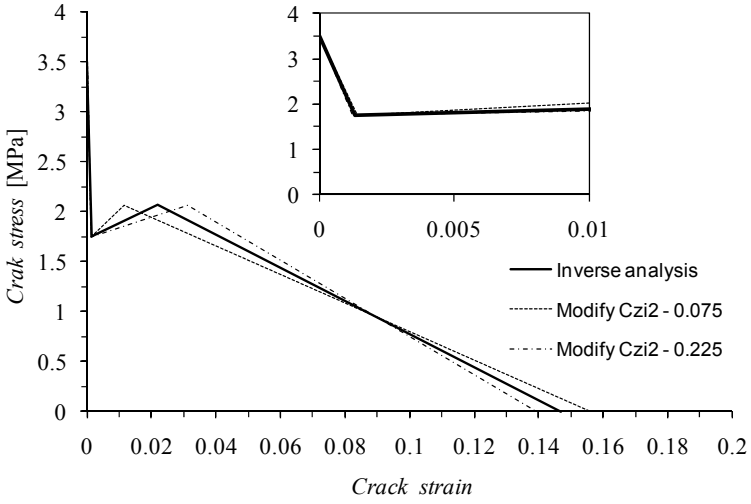

(a)

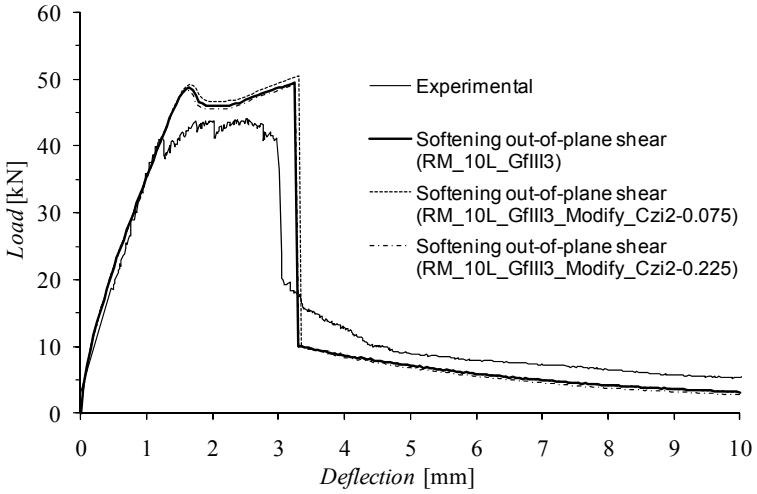

(b)

Figure 3.43 – Influence of the ξ_2 parameter: (a) trilinear softening diagrams and (b) relationship between load and deflection at the center of the test panel.

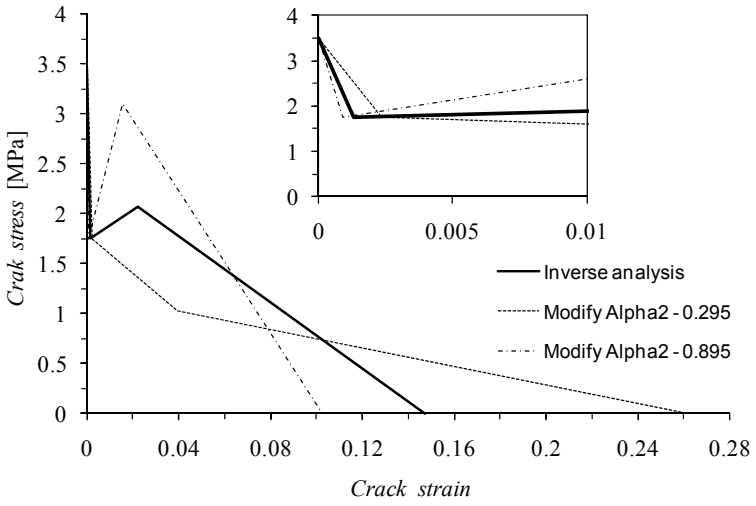

(a)

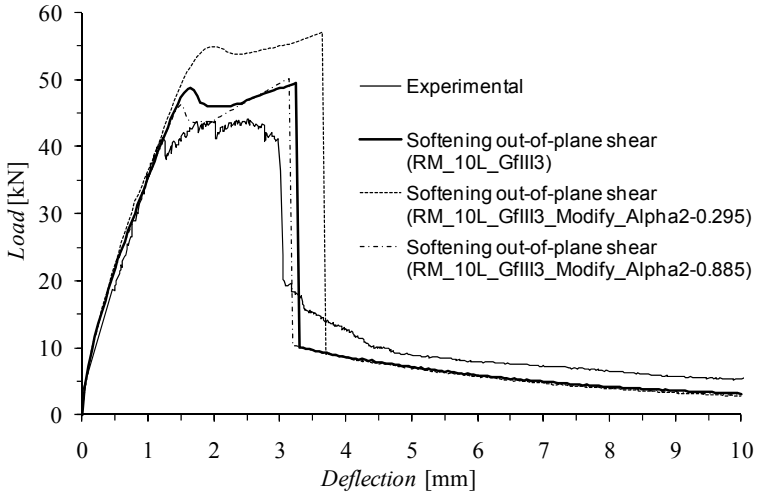

(b)

Figure 3.44 – Influence of the α_2 parameter: (a) trilinear softening diagrams and (b) relationship between load and deflection at the center of the test panel.

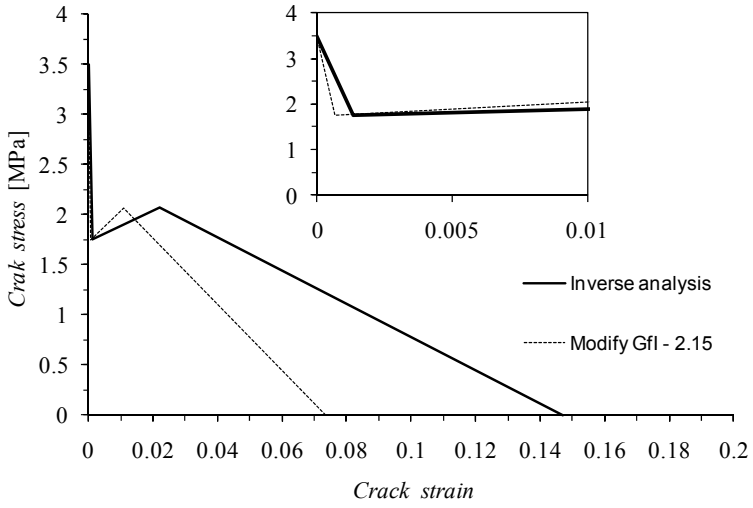

(a)

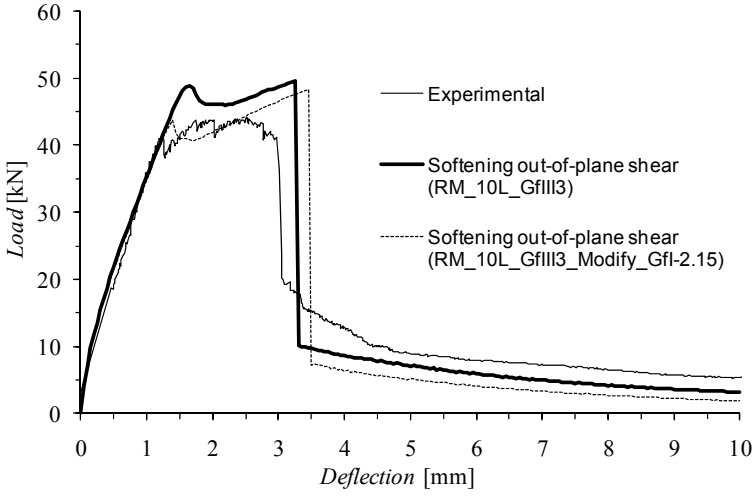

(b)

Figure 3.45 – Influence of G_f^I : (a) trilinear softening diagrams and (b) relationship between load and deflection at the center of the test panel.

3.8 NUMERICAL SIMULATION OF A PUNCHING TEST WITH A FLAT SLAB

An experimental program was carried out by Afonso (2010) with reinforced concrete slabs subjected to a test configuration that conducts to the punching failure of the tested slabs. In two slabs steel fibers were introduced in the concrete mix and one of them, FC0 (Afonso 2010), is in this section numerically simulated using the developed model.

The geometry, supports, load conditions and test setup are represented in Figure 3.46 and Figure 3.47. The square slab of 2500 mm edge has a thickness of 180 mm and the load is applied to a pile (250×250×320 mm^3) casted in the central zone of the slab to simulate a real field case. More details about the corresponding experimental program can be found elsewhere (Afonso 2011).

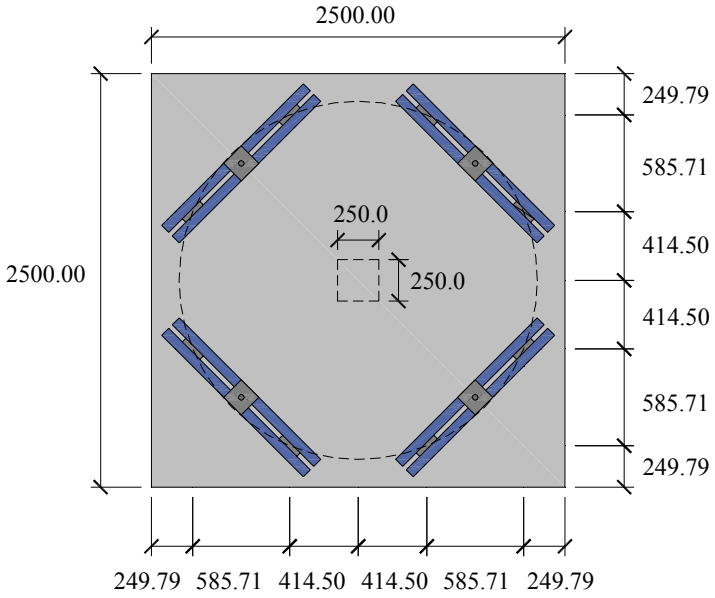

Figure 3.46 – Geometry and support conditions [all dimensions are in mm] (Moraes Neto et al. 2012).

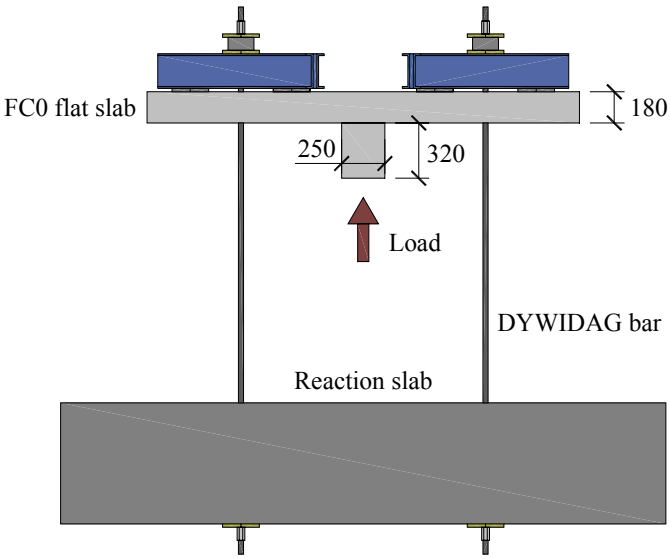

Figure 3.47 – Punching test setup [all dimensions are in mm] (Moraes Neto et al. 2012).

The finite element idealization, load and support conditions used in the numerical simulations of the flat slab punching test are shown in Figure 3.48. Due to double symmetry, only one quarter of the panel is considered in the simulations. The mesh is composed of eight-node serendipity plane shell elements. A Gauss-Legendre integration scheme with 3×3 IP is used. The elements are divided in 16 layers, being the first 12 layers 11.7192 mm thick, followed by a layer with 1.6848 mm thick (to simulate the tensile reinforcement – see Figure 3.49) and 3 layers with 11.9298 mm thick to simulate the concrete cover. The surface load is applied in the shaded elements shown in Figure 3.48, and the supports are simulated by point springs with a linear elastic behavior. The Newton-Raphson method with displacement control at a specific variable (central vertical displacement) is used in the nonlinear analysis (see section 2.4.3 of chapter 2).

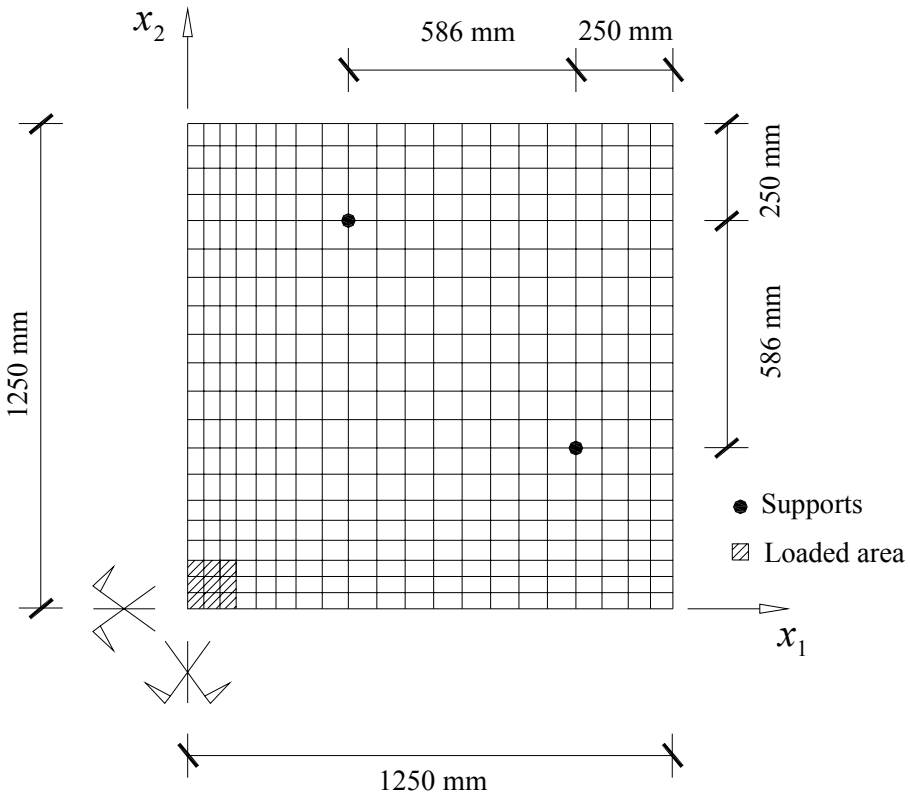

Figure 3.48 – Finite element mesh.

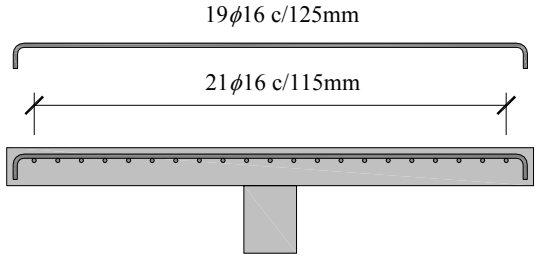

Figure 3.49 – Longitudinal steel bars – tensile reinforcement (Moraes Neto et al. 2012).

The values of the parameters of the constitutive model used in the numerical simulations are indicated in Table 3.4. The compressive strength, f_c, the concrete tensile strength, f_{ct}, and the modulus of elasticity, E_c, are determined experimentally (Afonso 2010), being the values for characterizing the trilinear tension softening diagram (see Figure 3.6) and out-of-plane shear stress-strain diagram (see Figure 3.9) obtained by back-fitting analysis in order to approximate as much as possible the experimental curve in the post-cracking phase, since no experimental data was available.

Tree numerical simulations are performed. One uses a linear elastic behavior for the concrete, and the others uses the proposed constitutive model varying only in the treatment of the ou-of-plane shear components. Figure 3.50 represents the experimental and numerical relationships between the load and the deflection at the central point for the tested FC0 flat slab. Using a linear elastic behavior for concrete the numerical response diverges from the experimental one just after crack initiation, indicating that some cracks start to form at a very early stage of the experimental test. When a linear elastic behavior is assumed for the out-of-plane shear components a good agreement can be observed up to a deflection of 11.8 mm. After this deflection the experimental curve indicates a decrease in the load carrying capacity and then suddenly falls, suggesting the failure of the flat slab by punching. This load decay is not well reproduced when assuming a linear elastic behavior for the out-of-plane shear components, and this numerical simulation has predicted a slight high load carrying capacity. However, if the bilinear diagram represented in Figure 3.9 is used to model the softening behavior of the out-of-plane shear components, the abrupt decay in the load carrying capacity is better captured.

Table 3.4 - Values of the parameters of the constitutive model used in the numerical simulation of the flat slab punching test.

Poisson's ratio	$\nu = 0.15$
Initial Young's modulus	$E_c = 25000.0\ \mathrm{N/mm^2}$
Compressive strength	$f_c = 39.3\ \mathrm{N/mm^2}$
Trilinear tension softening diagram (assigned to the concrete layers)	$f_{ct} = 3.5\ \mathrm{N/mm^2}$; $G_f^I = 0.015\,\mathrm{N/mm}$; $\xi_1 = 0.3$; $\alpha_1 = 0.5$; $\xi_2 = 0.5$; $\alpha_2 = 0.25$
Fictitious parameters assigned to the layer to simulate the tensile reinforcement	$f_{ct} = 450.0\ \mathrm{N/mm^2}$; $G_f^I = 120\,\mathrm{N/mm}$; $\xi_1 = 0.1$; $\alpha_1 = 1.0$; $\xi_2 = 0.25$; $\alpha_2 = 1.05$ $E_s = 205000.0\ \mathrm{N/mm^2}$
Fracture energy (mode III) used in the out-of-plane shear stress-strain diagram	$G_f^{III} = 0.015\ \mathrm{N/mm}$
Parameter defining the mode I fracture energy available to the new crack	$p_2 = 2$
Shear retention factor	Exponential ($p_1 = 2$)
Crack bandwidth	Square root of the area of the IP
Threshold angle	$\alpha_{th} = 30^{\circ}$
Maximum number of cracks per each IP	2

$\alpha_1 = \sigma_{n,2}^{cr} / \sigma_{n,1}^{cr}$, $\alpha_2 = \sigma_{n,3}^{cr} / \sigma_{n,1}^{cr}$, $\xi_1 = \varepsilon_{n,2}^{cr} / \varepsilon_{n,u}^{cr}$, $\xi_2 = \varepsilon_{n,3}^{cr} / \varepsilon_{n,u}^{cr}$ (see Figure 3.6)

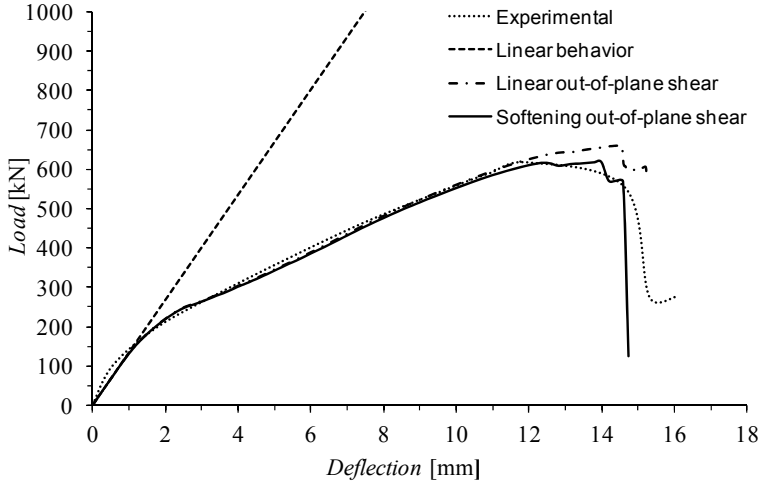

Figure 3.50 – Relationship between load and deflection at the center of the FC0 slab.

3.9 SUMMARY AND CONCLUSIONS

In the present work a model based on the finite element method is proposed to simulate concrete laminar structures failing in bending and shear. The Reissner-Mindlin theory in the context of layered shells is presented and special emphasis is placed on the treatment of the shear behavior.

The proposed model is based on a multi-directional and fixed smeared crack concept. By considering the nonlinear behavior of each shell layer, crack propagation through the thickness of these structures can be simulated.

Fracture mode I is modeled with a crack stress vs. crack strain trilinear diagram, whose defining parameters can be obtained by inverse analysis using the load-deflection relationship obtained with three-point notched beam tests, carried out according to the RILEM TC 162-TDF recommendations. With this strategy the values of the fracture parameters that define the normal stress-strain crack constitutive relationship are obtained. Since this type of test is much simpler and faster to execute, it becomes an advantageous alternative to the direct tensile tests recommended to evaluate the fracture mode I parameters of cement based materials. The adopted inverse analysis strategy is presented and discussed in section 3.7.1.

To simulate the out-of-plane strain gradient that occurs in punching tests, a softening diagram is proposed to model, after crack initiation, the out-of-plane shear components.

The formulation of linear and nonlinear support conditions, such as surface, line and point springs, is presented, and a special attention is dedicated to unilateral support conditions. With this approach, the loss of contact between the structure and the supporting system can be simulated, e.g., for the case of a slab supported on ground. A parametric study based on a steel fiber reinforced concrete slab supported on soil, using a nonlinear model for the simulation of the slab support conditions, is also presented.

The improvements made in the internal algorithms associated with the stress update and with the critical crack status changes are presented and their advantages are discussed.

The adequacy and accuracy of the proposed model is appraised using the results obtained in a punching test of a panel prototype built with steel fiber reinforced self-compacting concrete (SFRSCC) and in a punching test of a reinforced concrete flat slab that also included steel fibers in the concrete matrix. The proposed numerical strategy allows for an accurate simulation of the load-deformational process of the experimentally SFRSCC tested panel, which exhibited a brittle punching failure. Several numerical simulations are presented and discussed. Mesh refinement, data obtained with inverse analysis to define the trilinear diagram and a softening out-of-plane shear diagram are alternatives whose influence on the prediction of the experimental panel response is investigated. The load-deformational process of the experimentally tested reinforced concrete flat slab was also well predicted.

The use of softening laws to simulate the mode I crack opening and the out-of-plane shear components is crucial in order to obtain accurate numerical simulations The numerical simulations carried out with the proposed model and its comparison with the results of the experimental tests used in this work lead to the conclusion that the behavior of laminar structures failing in punching can be numerically predicted by a FEM-based Reissner-Mindlin shell approach as long as a crack constitutive model that includes a softening diagram for modeling both out-of-plane shear constitutive laws is used.

Chapter 4

Modeling of the crack shear component

4.1 INTRODUCTION

In the previous chapter a model for concrete laminar structures based on the formulation of the Reissner-Mindlin layered approach is described. Each layer is considered to be in a state of plane stress. To simulate the nonlinear behavior of the intervening materials, as occurs, for example, in the crack propagation through the thickness of a shell, a crack constitutive model is proposed and explained in section 3.3. To improve the predictive accuracy of the model for the simulation of the behavior of laminar structures failing in punching, special attention is dedicated to the treatment of the out-of-plane shear components by proposing a softening diagram after crack initiation (see section 3.4).

For the case of cracked concrete, stress and strain in-plane components are related by a cracked concrete constitutive matrix, $\underline{D}_{mb}^{crco}$, defined by equation (3.24). For the simulation of the mode I crack opening, two tensile-softening diagrams can be used, being the crack mode II (in-plane shear) modulus calculated using the concept of shear retention factor, β, defined as a constant value or as a function of the crack normal strain, as shown in equations (3.31) and (3.32). As observed, the adoption of a softening tensile-diagram to simulate the crack opening propagation is a suitable strategy to accurately assess the behavior of structures governed by flexural failure mode. However, an accurate simulation of structures failing in shear or in flexural/shear is still a challenge in the computational mechanics domain. To improve the predictive accuracy of the model for the simulation of

the behavior of structures governed by this type of failure, two strategies to simulate the crack shear component that appears in the formulation of the smeared crack constitutive model described in section 3.3.2.2 are presented and discussed in this chapter.

These strategies are exposed for the in-plane components of a specific k layer of the laminar structure, but they were also implemented in the already available smeared multi-fixed crack model developed for plane stress, as well as in the three-dimensional multi-fixed smeared crack model described in chapter 5. Therefore, for the exposition of these strategies the subscript mb used in the formulation presented in section 3.3 is not used.

The main purpose of the implementation of these two strategies is to improve the simulation of the degradation of the shear stress transfer with the crack opening evolution. One of the strategies is based on the adoption of a total approach for the crack shear stress-shear strain relationship. The other strategy is based on the introduction of a softening diagram for the relation between the crack shear stress-shear strain components. Numerical simulations are performed to evidence the main differences provided by both strategies when they are applied to shear-failure structures.

4.2 INCREMENTAL *VS.* TOTAL APPROACH FOR MODELING THE SHEAR CRACK COMPONENT

When the material corresponding to a specific integration point (IP) is assumed to be in a cracked state and is submitted to an incremental strain, $\Delta\underline{\varepsilon}$, the strain field in this IP is modified and the stress state must be updated.

In the following sections two formulations are presented for the stress update. The first one is an incremental approach for both, normal and shear crack components, and the second one is an incremental approach for the normal crack component and a total approach for the crack shear component. The formulations are restricted to one crack, but its generalization to the case of multiple cracks at each IP is a straightforward process.

The concept of the incremental and total approach for the crack shear stress-shear strain relationship is represented in Figure 4.1.

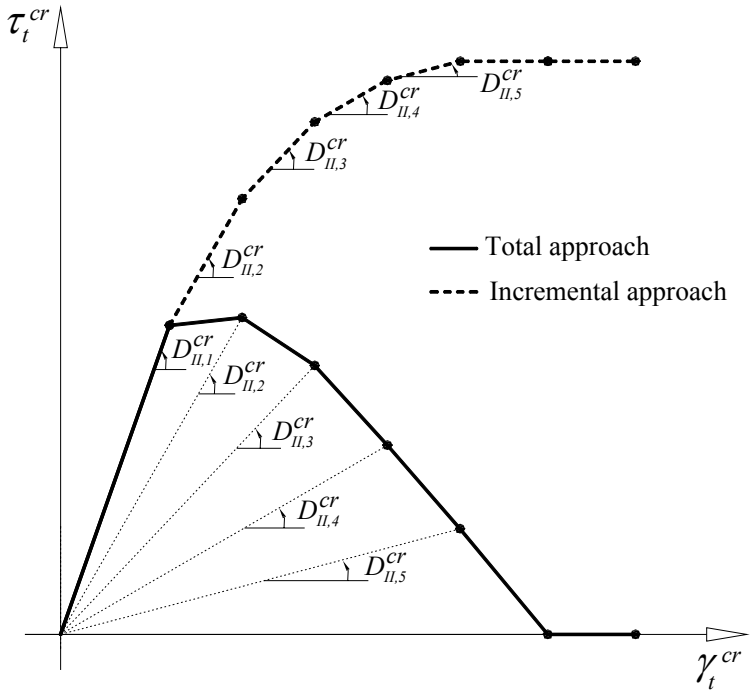

Figure 4.1 – Example of crack shear stress-strain relation for the incremental and total approaches.

In the incremental approach the crack shear stress τ_t^{cr} provided by the aggregate interlock effect at a certain crack shear strain stage is obtained with

$$\tau_t^{cr} = \tau_{t,prev}^{cr} + \Delta\tau_t^{cr} = \tau_{t,prev}^{cr} + D_{II}^{cr}\Delta\gamma_t^{cr} \tag{4.1}$$

where $\tau_{t,prev}^{cr}$ is the crack shear stress in a previous state at the same IP, $\Delta\tau_t^{cr}$ is the increment of the crack shear stress, D_{II}^{cr} is the mode II stiffness modulus, defined by equation (3.31), and $\Delta\gamma_t^{cr}$ is the incremental crack shear strain.

It can be observed in Figure 4.1 that the increment of the crack shear stress $\Delta\tau_t^{cr}$ is only null when $D_{II}^{cr} = 0$, i.e., for $\varepsilon_n^{cr} \geq \varepsilon_{n,u}^{cr}$ (see equations (3.31) and (3.32)). Therefore, even

when the crack width is increasing, the crack shear stress τ_t^{cr} can also increase up to an asymptotic value, regardless the crack is no longer capable of transferring normal tensile stresses. This can lead to the formation of a new crack, resulting in several cracks at an IP, which introduces severe difficulties in accomplishing the constitutive laws of the cracks formed at the IP, even when a rigorous strain-decomposition concept is adopted for this purpose (Sena-Cruz 2004). The occurrence of quite high crack shear stresses can also contribute to numerical predictions with higher stiffness and load carrying capacity than the values registered experimentally, mainly in elements failing in shear.

In the total approach the crack shear stress τ_t^{cr} at a certain crack shear strain stage is obtained with

$$\tau_t^{cr} = D_{II}^{cr}\ \gamma_t^{cr} = D_{II}^{cr}\left(\gamma_{t,prev}^{cr} + \Delta\gamma_t^{cr}\right) = D_{II}^{cr}\ \gamma_{t,prev}^{cr} + D_{II}^{cr}\ \Delta\gamma_t^{cr} \tag{4.2}$$

By observing Figure 4.1, it can be stated that for an increment of the crack shear strain $\Delta\gamma_t^{cr}$ a decrease in the crack shear stress τ_t^{cr} can occur due to a significant decrease of D_{II}^{cr}. Therefore, the aim of the total approach, proposed in the present work for modeling the fracture mode II, is to reproduce numerically a decrease of crack shear stress transfer τ_t^{cr} with the increase of the crack shear strain γ_t^{cr}, after a first phase where τ_t^{cr} increases with γ_t^{cr} (Abaqus 2002), as is expected when crack opening ε_n^{cr} is also increasing.

4.2.1 **Incremental approach**

The relationship between the in-plane stress components in the coordinate system of the finite element, $\underline{\sigma}$, and the crack stress components in the local crack coordinate system, $\underline{\sigma}_{\ell}^{cr}$, is obtained with equation (3.49), rewritten at this phase for convenience.

$$\underline{\sigma}_{\ell}^{cr} = \underline{T}^{cr}\,\underline{\sigma} \tag{4.3}$$

where

$$\underline{\sigma}_{\ell}^{cr} = \left[\sigma_n^{cr} \quad \tau_t^{cr}\right]^T \tag{4.4}$$

and

$$\underline{\sigma} = \left[\sigma_1 \quad \sigma_2 \quad \tau_{12}\right]^T \tag{4.5}$$

being σ_n^{cr} and τ_t^{cr} the crack normal and shear stresses in the crack, respectively, and $\underline{T}^{cr}$ is the matrix that transforms the stress components from the coordinate system of the finite element to the local crack coordinate system (see Figure 3.5) for a specific crack in the IP.

Taking into account equation (3.18), equation (4.3) can be rewritten as follows

$$\underline{\sigma}_{\ell,prev}^{cr} + \Delta\underline{\sigma}_{\ell}^{cr} = \underline{T}^{cr}\left(\underline{\sigma}_{prev} + \Delta\underline{\sigma}\right) \tag{4.6}$$

where the subscript *prev* indicates, in this case, the stress in a previous state in the IP, $\Delta\underline{\sigma}$ the incremental stress vector for the in-plane components in the coordinate system of the finite element defined by equation (3.14) and $\Delta\underline{\sigma}_{\ell}^{cr}$ the incremental local crack stress vector defined by

$$\Delta\underline{\sigma}_{\ell}^{cr} = \left[\Delta\sigma_n^{cr} \quad \Delta\tau_t^{cr}\right]^T \tag{4.7}$$

being $\Delta\sigma_n^{cr}$ and $\Delta\tau_t^{cr}$ the incremental crack normal and shear stress components, respectively.

Using the strain decomposition concept, $\Delta\underline{\varepsilon} = \Delta\underline{\varepsilon}^{co} + \Delta\underline{\varepsilon}^{cr}$ and knowing the relationship between the incremental crack strain components in the coordinate system of the finite element $\Delta\underline{\varepsilon}^{cr}$ and the crack strain components in the local crack coordinate system $\Delta\underline{\varepsilon}_{\ell}^{cr}$

$$\Delta\underline{\varepsilon}^{cr} = \left[\underline{T}^{cr}\right]^{T} \Delta\underline{\varepsilon}_{\ell}^{cr} \tag{4.8}$$

where

$$\Delta\underline{\varepsilon}_{\ell}^{cr} = \left[\Delta\varepsilon_{n}^{cr} \quad \Delta\gamma_{t}^{cr}\right]^{T} \tag{4.9}$$

and

$$\Delta\underline{\varepsilon} = \left[\Delta\varepsilon_{1} \quad \Delta\varepsilon_{2} \quad \Delta\gamma_{12}\right]^{T} \tag{4.10}$$

the incremental stress is obtained with

$$\Delta\underline{\sigma} = \underline{D}^{co}\Delta\underline{\varepsilon}^{co} = \underline{D}^{co}\left(\Delta\underline{\varepsilon} - \left[\underline{T}^{cr}\right]^{T} \Delta\underline{\varepsilon}_{\ell}^{cr}\right) \tag{4.11}$$

being $\underline{D}^{co}$ defined by equation (3.20).

Including equation (4.11) in equation (4.6) and making some arrangements, this equation can be written as

$$\underline{\sigma}_{\ell,prev}^{cr} + \Delta\underline{\sigma}_{\ell}^{cr} - \underline{T}^{cr}\,\underline{\sigma}_{prev} - \underline{T}^{cr}\,\underline{D}^{co}\Delta\underline{\varepsilon} + \underline{T}^{cr}\,\underline{D}^{co}\left[\underline{T}^{cr}\right]^{T} \Delta\underline{\varepsilon}_{\ell}^{cr} = \underline{0} \tag{4.12}$$

where $\Delta\underline{\sigma}_{\ell}^{cr}$ depends on $\Delta\underline{\varepsilon}_{\ell}^{cr}$, being obtained with this equation

$$\Delta \underline{\sigma}_{\ell}^{cr} = \begin{bmatrix} \Delta\sigma_n^{cr} \\ \Delta\tau_t^{cr} \end{bmatrix} = \begin{bmatrix} D_I^{cr} & 0 \\ 0 & D_{II}^{cr} \end{bmatrix} \begin{bmatrix} \Delta\varepsilon_n^{cr} \\ \Delta\gamma_t^{cr} \end{bmatrix} \tag{4.13}$$

In equation (4.13) D_I^{cr} and D_{II}^{cr} represents, respectively, the constitutive components of the crack opening mode I (normal) and crack sliding mode II (shear). The D_I^{cr} can be obtained with a diagram characterizing the crack fracture mode I propagation, while the D_{II}^{cr} can be determined from shear retention factor concept defined in the section 3.3.2.2 of chapter 3.

As referred in section 3.5.1, to solve the system of nonlinear equations represented in equation (4.12), where the unknowns are the components of the crack strain vector $\Delta \underline{\varepsilon}_{\ell}^{cr}$, two algorithms for the stress update are available, being one based on the Newton-Raphson method, and the other based on the fixed point iteration method. Both these methods are described elsewhere (Sena-Cruz 2004).

4.2.2 **Total approach**

The total approach is applied only to the shear components. In this case equation (4.6) can be written as

$$\begin{bmatrix} \sigma_{n,prev}^{cr} + \Delta\sigma_n^{cr} \\ \tau_t^{cr} \end{bmatrix}_{\ell} = \\ = \begin{bmatrix} \cos^2\theta & \sin^2\theta & 2\sin\theta\cos\theta \\ -\sin\theta\cos\theta & \sin\theta\cos\theta & \cos^2\theta - \sin^2\theta \end{bmatrix} \left(\begin{bmatrix} \sigma_1 \\ \sigma_2 \\ \tau_{12} \end{bmatrix}_{prev} + \begin{bmatrix} \Delta\sigma_1 \\ \Delta\sigma_2 \\ \Delta\tau_{12} \end{bmatrix} \right) \tag{4.14}$$

where

$$\Delta\sigma_n^{cr} = D_I^{cr} \Delta\varepsilon_n^{cr} \tag{4.15}$$

and τ_t^{cr} is defined by (4.2).

Substituting equations (4.15) and (4.2) in the left term of the equation (4.14)

$$\begin{bmatrix} \sigma_{n,prev}^{cr} \\ D_{II}^{cr}\ \gamma_{t,prev}^{cr} \end{bmatrix}_\ell + \begin{bmatrix} D_I^{cr}\Delta\varepsilon_n^{cr} \\ D_{II}^{cr}\Delta\gamma_t^{cr} \end{bmatrix}_\ell = \\ = \begin{bmatrix} \cos^2\theta & \sin^2\theta & 2\sin\theta\cos\theta \\ -\sin\theta\cos\theta & \sin\theta\cos\theta & \cos^2\theta-\sin^2\theta \end{bmatrix} \left(\begin{bmatrix} \sigma_1 \\ \sigma_2 \\ \tau_{12} \end{bmatrix}_{prev} + \begin{bmatrix} \Delta\sigma_1 \\ \Delta\sigma_2 \\ \Delta\tau_{12} \end{bmatrix} \right) \tag{4.16}$$

or in matrix form

$$\underline{\sigma}_{\ell,prev}^{cr^*} + \Delta\underline{\sigma}_\ell^{cr} = \underline{T}^{cr}\left(\underline{\sigma}_{prev} + \Delta\underline{\sigma}\right) \tag{4.17}$$

and introducing equation (4.11) in (4.17) results

$$\underline{\sigma}_{\ell,prev}^{cr^*} + \Delta\underline{\sigma}_\ell^{cr} - \underline{T}^{cr}\,\underline{\sigma}_{prev} - \underline{T}^{cr}\,\underline{D}^{co}\Delta\underline{\varepsilon} + \underline{T}^{cr}\,\underline{D}^{co}\left[\underline{T}^{cr}\right]^T\Delta\underline{\varepsilon}_\ell^{cr} = \underline{0} \tag{4.18}$$

being

$$\underline{\sigma}_{\ell,prev}^{cr^*} = \left[\sigma_{n,prev}^{cr} \quad D_{II}^{cr}\ \gamma_{t,prev}^{cr}\right]_\ell^T \tag{4.19}$$

the modified crack stress vector (only the shear component) from a previous state. The components of $\Delta\underline{\sigma}_\ell^{cr}$ are obtained with (4.13).

Similarly to the incremental approach, the crack strain vector $\Delta\underline{\varepsilon}_\ell^{cr}$ can be obtained with the Newton-Raphson or the fixed-point iteration methods.

Equation (4.18) can be reduced to

$$f\left(\Delta\underline{\varepsilon}_{\ell}^{cr}\right)=\underline{0} \tag{4.20}$$

At iteration q of the Newton-Raphson method the first derivative of f in order to the incremental crack strain vector $\Delta\underline{\varepsilon}_{\ell}^{cr}$ must be obtained, being defined by (see Appendix C)

$$\frac{\partial f\left(\Delta\underline{\varepsilon}_{\ell}^{cr}\right)}{\partial\Delta\underline{\varepsilon}_{\ell}^{cr}}=\underline{D}^{cr}+\overline{\underline{D}}^{cr}+\underline{T}^{cr}\,\underline{D}^{co}\left[\underline{T}^{cr}\right]^{T} \tag{4.21}$$

where

$$\overline{\underline{D}}^{cr}=\begin{bmatrix}0 & 0\\ \dfrac{\partial D_{II}^{cr}}{\partial\Delta\varepsilon_{n}^{cr}}\gamma_{t}^{cr} & 0\end{bmatrix} \tag{4.22}$$

being D_{II}^{cr} obtained with equation (3.31).

Equation (4.22) is similar to the one used in the incremental approach described in (Sena-Cruz 2004), being the main difference the replacement of the incremental shear crack strain, $\Delta\gamma_{t}^{cr}$, with the total shear crack strain, γ_{t}^{cr}.

4.2.3 **Numerical simulations**

As mentioned above, the total approach for the crack shear component is also included in the smeared crack model previously implemented for plane stress analysis with the incremental approach. In this section, to validate the exposed approaches, two numerical simulations are made. The first one is a more theoretical numerical simulation, whose main purpose is to show the differences between both approaches and the capabilities of the total approach to simulate the degradation of the stresses at an IP. The second example is

dedicated to the numerical simulation of reinforced concrete beams shear and flexurally strengthened with composite materials.

4.2.3.1 Single element

To compare the capabilities of the total and incremental approaches two numerical simulations are made in this section. One with an incremental approach for both crack normal and shear components, and the other with an incremental approach for the crack normal component and a total approach for the crack shear component.

A single element considered to be subjected to a plane stress state is used for both these numerical simulations. Figure 4.2 represents the geometry, load and support conditions of the element, and Table 4.1 includes the values of some parameters required by the model. A four-noded plane stress finite element with one IP (Gauss point) is used, and a tensile-softening trilinear diagram is adopted to simulate the mode I fracture propagation. The Newton-Raphson method with displacement control at a specific variable is utilized in this example.

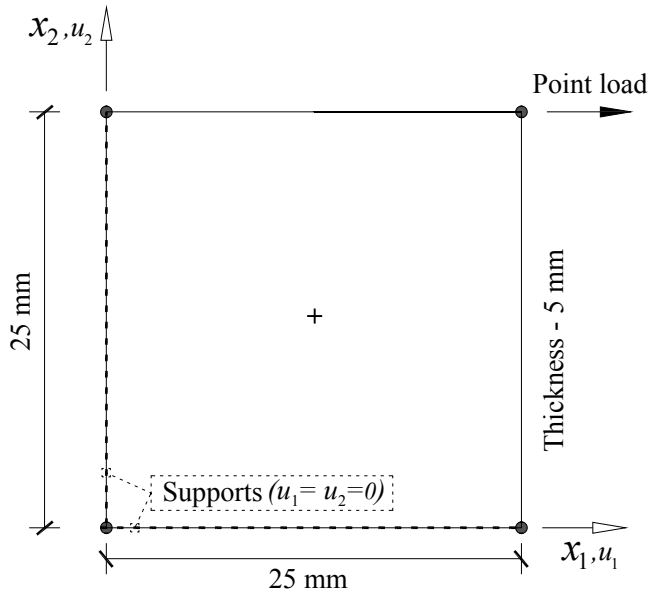

Figure 4.2 – Geometry, load and support conditions of the single element mesh.

Table 4.1 - Model properties used in the single element simulation.

Poisson's ratio	$\nu = 0.2$
Initial Young's modulus	$E_c = 31000.0\ \mathrm{N/mm^2}$
Compressive strength	$f_c = 38.0\ \mathrm{N/mm^2}$
Trilinear tension softening diagram	$f_{ct} = 2.9\ \mathrm{N/mm^2}$; $G_f^I = 0.075\ \mathrm{N/mm}$; $\xi_1 = 0.2$; $\alpha_1 = 0.7$; $\xi_2 = 0.75$; $\alpha_2 = 0.5$
Parameter defining the mode I fracture energy available to the new crack	$p_2 = 2$
Shear retention factor	Exponential ($p_1 = 2$)
Crack bandwidth	Square root of the area of the element
Threshold angle	$\alpha_{th} = 30^o$

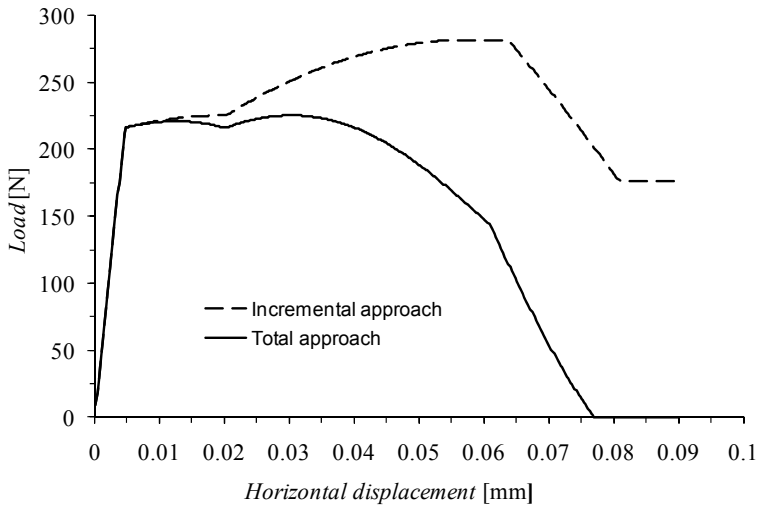

Figure 4.3 – Load-horizontal displacement relationship.

The load-horizontal displacement relationship is represented in Figure 4.3, using the total and the incremental approach for the crack shear component. Until a load of 216 N, a linear-elastic behavior is observed for both simulations. At this level cracking is initiated in the concrete and the curves follow different paths, mainly after 0.02 mm, which is where the incremental response presents a hardening behavior leading to a higher load carrying

capacity, maintaining a high residual load in comparison with the total curve that presents a softening behavior up to the complete loss of load carrying capacity.

This behavior can be justified by the analysis of the stress-strain relationship for fracture mode I and mode II obtained in the IP for each approach, and represented in Figure 4.4 and Figure 4.5.

Figure 4.4 represents the crack normal stress-strain relation in the crack coordinate system (CrCS), and Figure 4.5 the crack shear stress-strain relation in the same CrCS. As expected, both approaches provide similar crack normal stress strain diagram, because the total approach is only applied to the crack shear component. In fact, Figure 4.5 shows that quite different crack shear stress-strain diagrams can be obtained for both approaches. In the total approach the crack shear stress decreases with the crack opening process, while in the incremental approach the crack shear stress increases up to an asymptotic value.

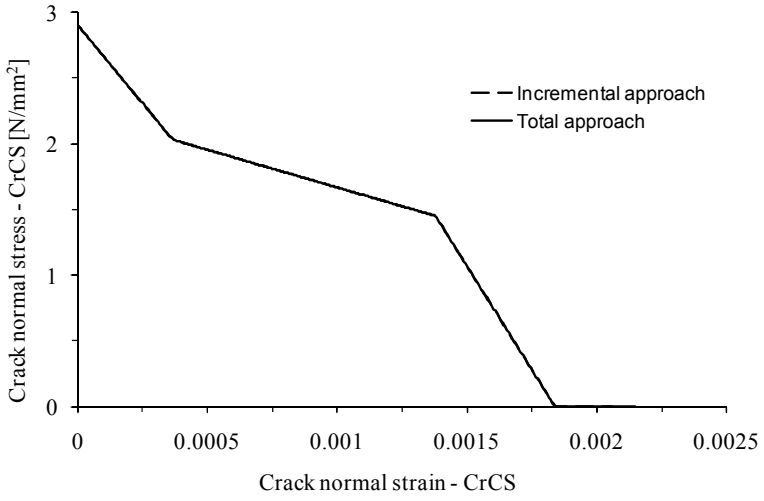

Figure 4.4 – Crack normal stress-strain relationship in CrCS.

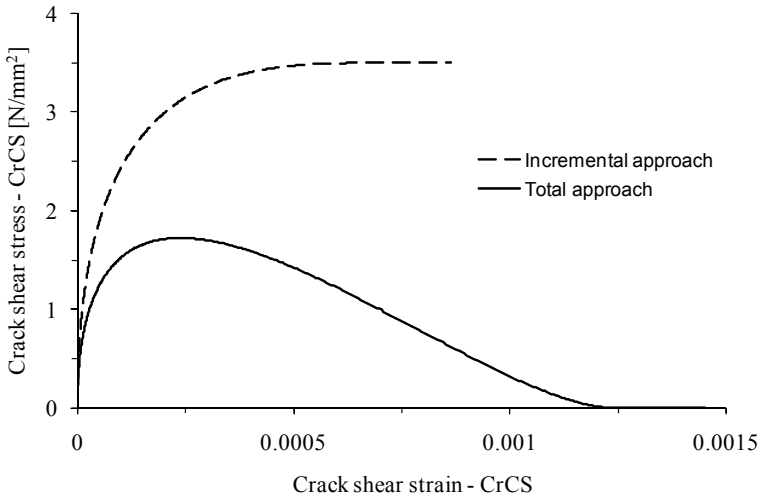

Figure 4.5 – Crack shear stress-strain relationship in CrCS.

The stresses and strains developed at the IP in the global coordinate system (GCS) are represented in Figure 4.6 to Figure 4.8. It can be observed in all of these charts that the behavior of each approach is similar up to crack initiation and, then, they gradually follow a different path, leading, for the cases of the x_2 normal stress and x_1x_2 shear stress, to a very different post-peak residual value (see Figure 4.7 and Figure 4.8). This difference can be justified by the fact that in the incremental approach the crack shear stress has an asymptotic residual value, as shown in Figure 4.5. Due to its contribution to the stresses in the global coordinate system, higher stress components are obtained using the incremental approach.

A numerical simulation of the single element with four integration points was also performed, and similar conclusions were obtained.

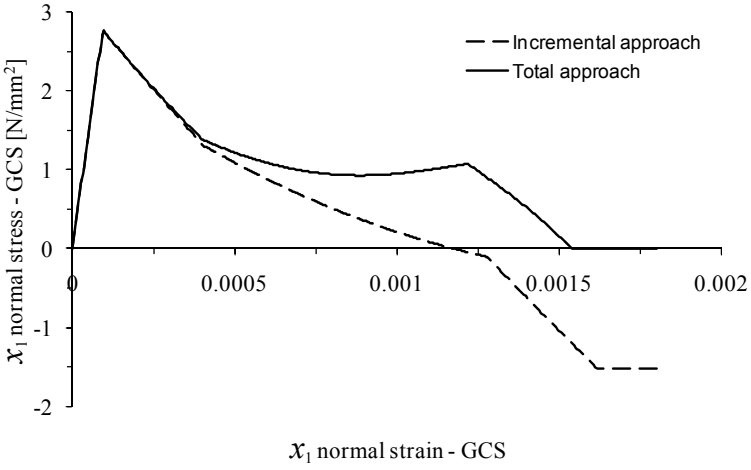

Figure 4.6 – x_1 normal stress-strain relationship in GCS.

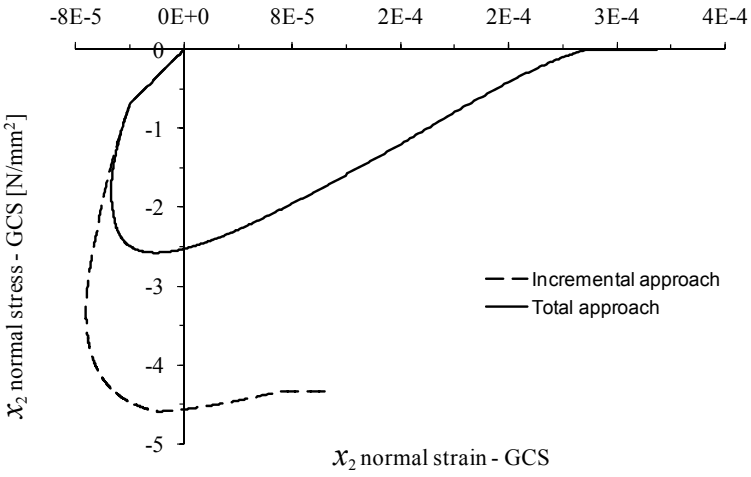

Figure 4.7 – x_2 normal stress-strain relationship in GCS.

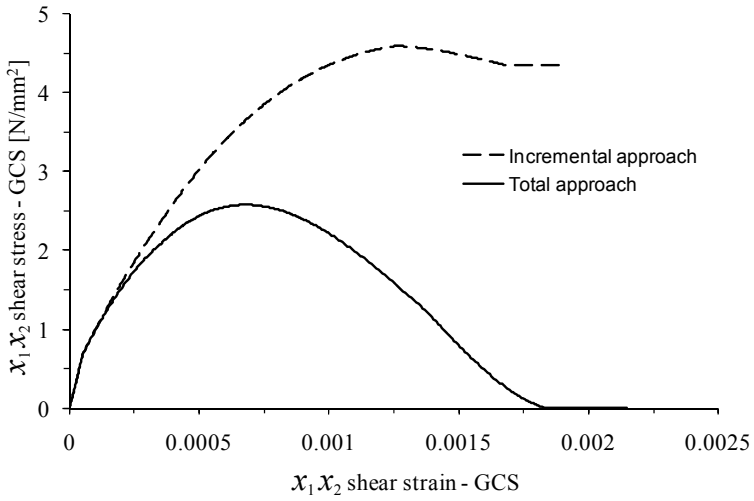

Figure 4.8 – x_1x_2 shear stress-strain relationship in GCS.

4.2.3.2 Strengthening of RC beams

The flexural strengthening of reinforced concrete (RC) beams with small concrete cover thickness by using the Near Surface Mounted (NSM) technique demands to cut the bottom arm of the still stirrups for the installation of the Carbon Fiber Reinforced Polymer (CFRP) laminates. To assess the influence of this intervention on the load carrying capacity of the beams, an experimental research program was carried out. The details of the experimental program composed of three series of beams of distinct cross section depth can be found elsewhere (Costa and Barros 2010).

The NSM technique for the flexural strengthening of RC beams or slabs consists of installing CFRP laminates into thin slits open onto the concrete cover of the RC elements to strengthen bonded with an epoxy adhesive to the surrounding concrete. The efficiency of this technique can be found elsewhere (Täljsten et al. 2003, El-Hacha and Rizkalla 2004, Sena-Cruz 2004, Barros and Fortes 2005, Bonaldo et al. 2008, Barros et al. 2008). In a tentative of avoiding the occurrence of shear failure in the NSM-flexurally strengthened beams, wet layup CFRP strips of sheet of U configuration were also applied according to the Externally Bonded Reinforcement (EBR) technique (ACI Committee 440, 2007). The U shape CFRP strips were placed between the existing steel stirrups (see Figure 4.9).

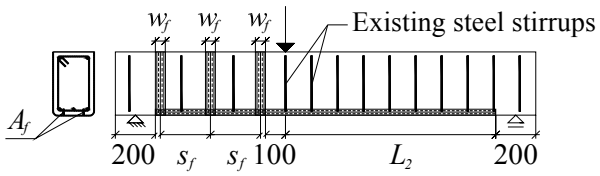

Figure 4.9 – Localization of the NSM CFRP laminates and of the EBR strip of wet layup CFRP sheet [dimensions in mm] (Barros et al. 2011).

In the numerical simulation of these beams, the total and incremental approaches for the crack shear component were used. In this section, only the numerical results of the beams of the first series are presented. The complete numerical research can be found in Barros et al. (2011).

The designations of the beams used in the experimental research are the following:

- VR1 - reinforced concrete reference beam;
- VE1 - VR1 beam with the bottom arm of the steel stirrups cut;
- VL1 - VE1 beam flexurally strengthened with NSM CFRP laminates;
- VLM1 - VL1 beam shear strengthened with EBR strips of wet layup CFRP sheets of U configuration.

The geometry, support and loading conditions of the beams are represented in Figure 4.10. For the case of the beams of series 1: $L_1 = 550mm$; $L_2 = 950mm$; $b = 200mm$; $h = 250mm$ longitudinal steel bars at bottom surface $A_s^+ = 2\phi 10 + 1\phi 6\left(185\text{mm}^2\right)$ and longitudinal steel bars at top surface $A_s^- = 2\phi 10\left(157\text{mm}^2\right)$.

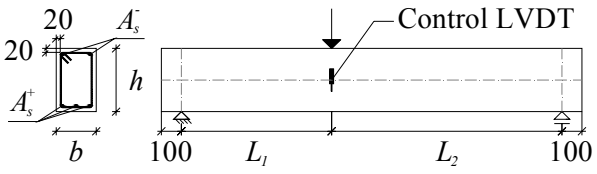

Figure 4.10 – Beam geometry, support and loading conditions [dimensions in mm] (Barros et al. 2011).

Under the framework of the finite element analysis, the tested beams are considered as a plane stress problem. Therefore, the beams are modeled with a mesh of 8-noded serendipity plane stress finite elements. A Gauss-Legendre integration scheme with 2×2 IP is used in all the concrete elements. The steel bars, the NSM laminates and the EBR CFRP strips are modeled with 2-noded perfectly bonded embedded cables (one degree-of-freedom per node).

For modeling the behavior of the steel bars, the stress-strain relationship available in the FEMIX computer code is used (Sena-Cruz 2004). The curve (under compressive or tensile loading) is defined by the points PT1 = $\left(\varepsilon_{sy},\sigma_{sy}\right)$, PT2 = $\left(\varepsilon_{sh},\sigma_{sh}\right)$ and PT3 = $\left(\varepsilon_{su},\sigma_{su}\right)$ and a parameter p that defines the shape of the last branch of the curve. Unloading and reloading linear branches with slope $E_s=\sigma_{sy}/\varepsilon_{sy}$ are assumed in the present approach. For modeling both the NSM laminates and EBR strips of sheet, a linear elastic stress-strain relationship is adopted.

The values of the parameters of the constitutive model used in the numerical simulations are indicated in Table 4.2, Table 4.3 and Table 4.4. Using the average compressive strength f_c, determined experimentally, and the equations proposed by CEB-FIP (1993), the concrete tensile strength f_{ct} and the fracture energy G_f^I are obtained.

As suggested by Stevens (1987), the tensile yield stress and the stress values corresponding to strains higher than the tensile yield strain of the steel bars are reduced by the term $\Delta\sigma_{ycr}=75f_{ct}/\phi_s$, being f_{ct} the concrete tensile strength in MPa, and ϕ_s the diameter of the steel bar in mm. This reduction is to take into account that the stress in the steel reinforcement at the concrete crack plane is higher than the average stress determined in the IP of the corresponding embedded cable element. This stress is obtained from the displacements of the "mother element" of the embedded cable.

Table 4.2 - Properties of CFRP laminates and strips of sheets.

	CFK Laminate	C Sheet 240
f_{fu} (MPa)	2783	3257
E_f (GPa)	157	237
ε_{fu} (‰)	17.8	13.77
t_f (mm)	1.42	0.117

Table 4.3 - Steel properties.

	ϕ_s=6 mm	ϕ_s=10 mm
f_{sym} (MPa)	571	548
f_{sum} (MPa)	662	648
ε_{sy} (‰)	3.1	3.0
σ_{sy} (MPa)	515	514
ε_{sh} (‰)	25	25
σ_{sh} (MPa)	579	576
ε_{su} (‰)	50	50
σ_{su} (MPa)	643	637
p	1	1

Table 4.4 - Model properties used for the beams simulation.

Poisson's ratio	$\nu = 0.2$
Initial Young's modulus	$E_c = 28900.0\ \mathrm{N/mm^2}$
Compressive strength	$f_c = 31.0\ \mathrm{N/mm^2}$
Trilinear tension softening diagram	$f_{ct} = 1.5\ \mathrm{N/mm^2}$; $G_f^I = 0.0665\ \mathrm{N/mm}$; $\xi_1 = 0.1$; $\alpha_1 = 0.5$; $\xi_2 = 0.3$; $\alpha_2 = 0.2$
Parameter defining the mode I fracture energy available to the new crack	$p_2 = 1$
Shear retention factor	Cubic ($p_1 = 3$)
Crack bandwidth	Square root of the area of the IP
Threshold angle	$\alpha_{th} = 30^o$
Maximum number of cracks per each IP	2

In Figure 4.11 the experimental relationship between the load and the deflection at the loaded section for the tested beams and the numerical ones obtained with the incremental

and the total approaches are compared. The dash-dot horizontal line corresponds to the maximum experimental load of each beam.

Figure 4.12 represents, for each beam and for the numerical simulations involving both approaches, the crack patterns at the end of the analysis, i.e., for the last converged load increment. The cracks are represented by quadrilateral 4-noded finite elements centered at the IP, being drawn with a width that is proportional to the crack normal strain, ε_n^{cr} . More details about the status of the cracks are supplied in the caption of the Figure 4.12.

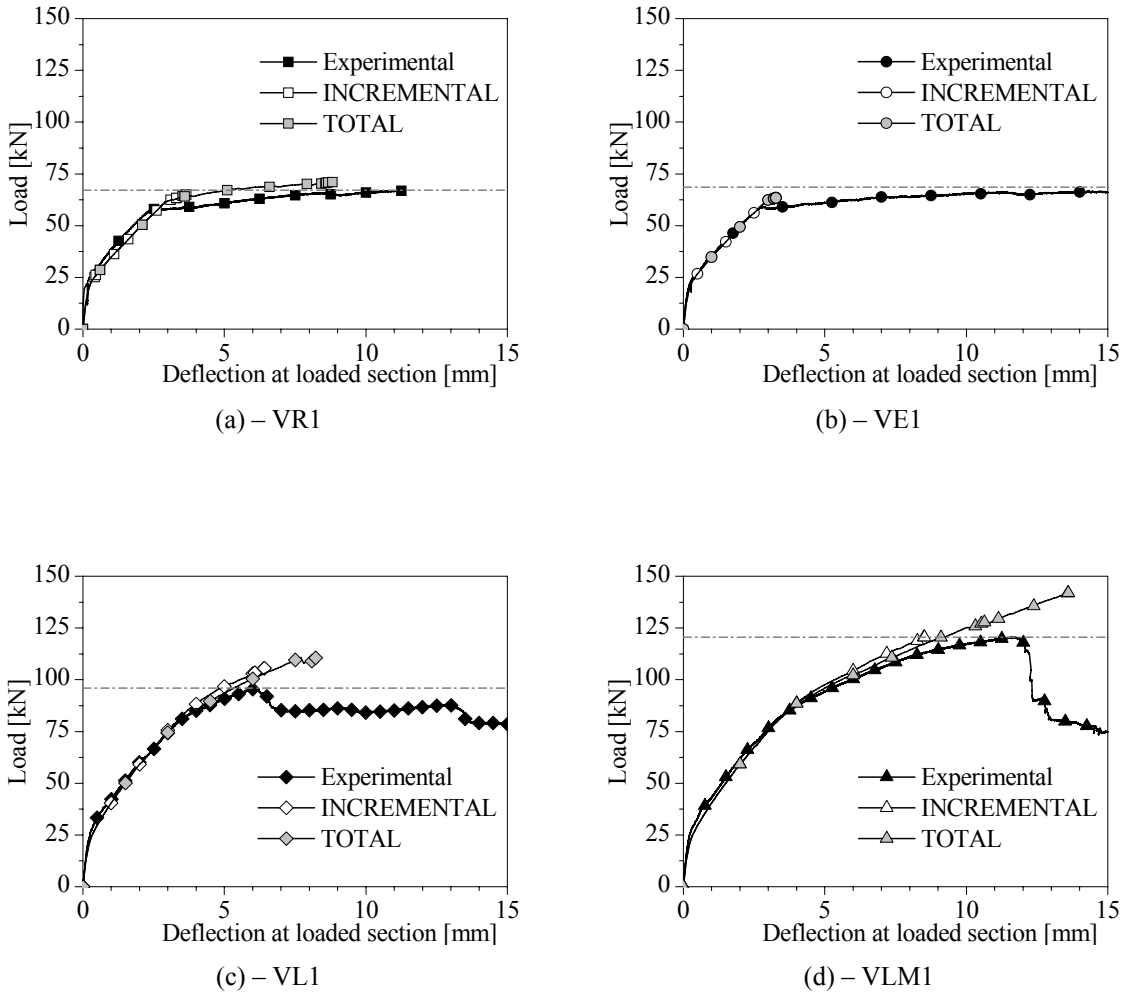

Figure 4.11 – Load-deflection at the loaded section for the beams of series 1 (Barros et al. 2011).

From the analysis of Figure 4.11 and Figure 4.12, it can be concluded that both numerical approaches simulated accurately the deformational response of the VR1 and VE1 beams,

and predicted with good accuracy the deformational response of the VL1 and VLM1 beams. However, comparing the crack pattern of VL1 beam represented in Figure 4.13 with the crack patterns obtained numerically and represented in Figure 4.12, it can be concluded that only the total approach captured with high precision the localization and profile of the shear failure crack.

The longitudinal steel bars of the VL1 and VLM1 beams have already yielded at the moment of the shear failure. This is well predicted by the numerical simulations using the total and incremental approaches, since vertical completely open cracks are observed near the loaded section (see Figure 4.12).

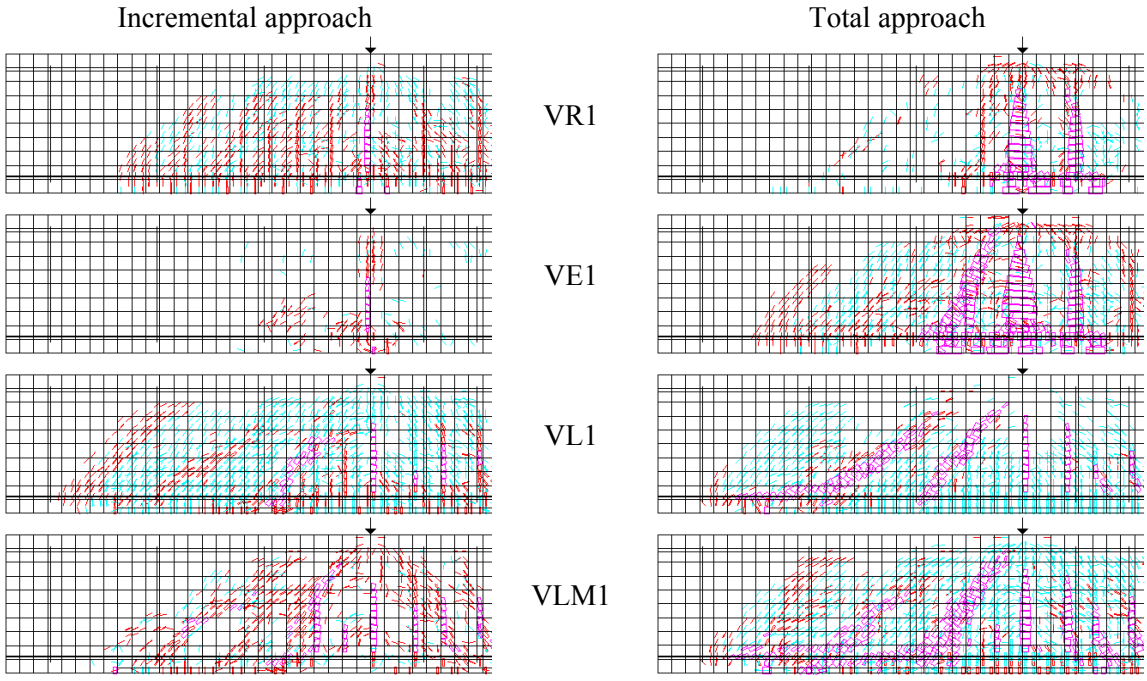

Figure 4.12 – Crack patterns of the beams of series 1 (in pink color: crack completely open ($\varepsilon_n^{cr} \geq \varepsilon_{n,u}^{cr}$); in red color: crack in the opening process; in cyan color: crack in the reopening process) (Barros et al. 2011).

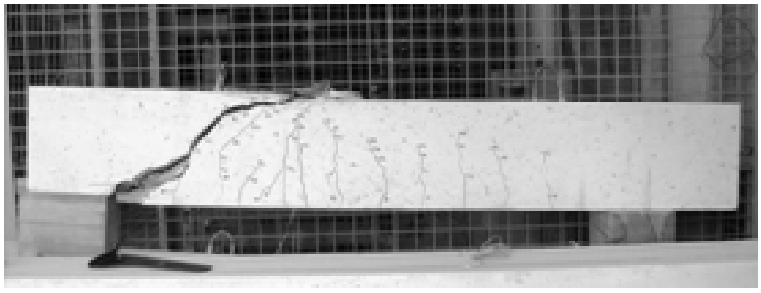

Figure 4.13 – Crack patterns at the end of the tested VL1 beam (Barros et al. 2011).

4.3 CRACK SHEAR SOFTENING DIAGRAM

The use of softening diagrams to reproduce the fracture mode I process is common in smeared and discrete crack models, but the use of softening diagrams to model the shear stress transfer across the crack is less usual. To simulate the fracture mode II process a shear retention factor is currently used (Rots and de Borst 1987). According to this last approach, the shear stress transfer between the crack planes decreases with the increase of the normal crack strain (see equation (3.32)). In most structures assumed to be in a state of plane stress, this strategy leads to simulations with reasonable accuracy. Exceptions occur in structures that fail by the formation of a critical shear crack. For these cases the simulation of the structural softening with high accuracy requires the adoption of a softening crack shear stress vs. crack shear strain relationship.

In this section a softening diagram to simulate the crack shear stress-strain behavior is described. This constitutive model is implemented in FEMIX, and can be used in the simulation of plane stress structures, Reissner-Mindlin shells and 3D structures discretized with solid elements. Its capabilities are assessed by performing a numerical simulation of an experimental test available in the literature (Arrea and Ingraffea 1982).

4.3.1 **Description of the diagram**

The proposed crack shear diagram is represented in Figure 4.14. The shear softening diagram starts at the origin because, according to the crack initiation criterion, when a crack initiates the crack shear stress is null. As a consequence of the rotation of the directions of principal stresses, shear stresses can develop across the surfaces of the crack

(Rots and de Borst 1987). The crack shear stress increases linearly until the crack shear strength is reached (first branch of the shear crack diagram), followed by a decrease in the shear residual strength (softening branch).

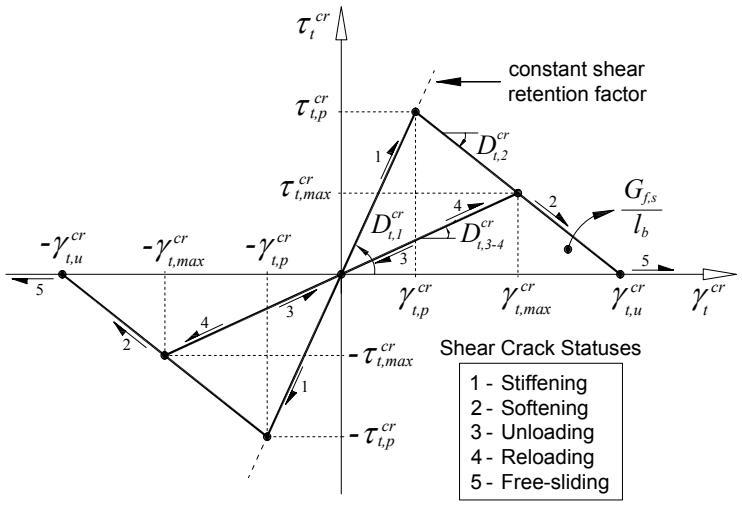

Figure 4.14 – Diagram to simulate the relationship between the crack shear stress and crack shear strain component and possible shear crack statuses.

The diagram represented in Figure 4.14 (based on Rots and de Borst 1987) is defined by the expressions shown in equation (4.23). The positive part of the diagram is explained here, being the treatment of the negative part straightforward.

$$\tau_t^{cr}\left(\gamma_t^{cr}\right)=\begin{cases} D_{t,1}\,\gamma_t^{cr} & 0<\gamma_t^{cr}\le\gamma_{t,p}^{cr} \\ \tau_{t,p}^{cr}-\dfrac{\tau_{t,p}^{cr}}{\left(\gamma_{t,u}^{cr}-\gamma_{t,p}^{cr}\right)}\left(\gamma_t^{cr}-\gamma_{t,p}^{cr}\right) & \gamma_{t,p}^{cr}<\gamma_t^{cr}\le\gamma_{t,u}^{cr} \\ 0 & \gamma_t^{cr}>\gamma_{t,u}^{cr} \end{cases} \tag{4.23}$$

The initial shear fracture modulus, $D_{t,1}^{cr}$, is defined by

$$D_{t,1}^{cr}=\frac{\beta}{1-\beta}G_c \tag{4.24}$$

where G_c is the concrete elastic shear modulus and β is the shear retention factor, defined as a constant value in the range]0,1[, in this case.

The peak crack shear strain, $\gamma_{t,p}^{cr}$, is obtained using the crack shear strength (from the input data), $\tau_{t,p}^{cr}$, and the crack shear modulus is obtained with equation (4.24)

$$\gamma_{t,p}^{cr} = \frac{\tau_{t,p}^{cr}}{D_{t,1}^{cr}} \tag{4.25}$$

The ultimate crack shear strain, $\gamma_{t,u}^{cr}$, depends on the crack shear strength, $\tau_{t,p}^{cr}$, on the shear fracture energy (mode II fracture energy for the case of in-plane shear), $G_{f,s}$, and on the crack bandwidth, l_b, as follows

$$\gamma_{t,u}^{cr} = \frac{2G_{f,s}}{\tau_{t,p}^{cr}\, l_b} \tag{4.26}$$

In the present approach it is assumed that the crack bandwidth, used to assure that the results are independent of the mesh refinement, is the same for both fracture mode I and mode II processes.

When the softening constitutive law represented in Figure 4.14 is used to evaluate the fracture mode II stiffness modulus D_{II}^{cr} of equation (3.26), its value depends on the branches defining the diagram. For this reason five shear crack statuses are proposed and their meaning is explained in the next section.

The crack mode II stiffness modulus of the first linear branch of the diagram is defined by equation (4.24), the second linear (softening) branch is defined by

$$D_{II}^{cr} = D_{t,2}^{cr} = -\frac{\tau_{t,p}^{cr}}{\gamma_{t,u}^{cr} - \gamma_{t,p}^{cr}} \tag{4.27}$$

and the crack shear modulus of the unloading and reloading branches is obtained from

$$D_{II}^{cr} = D_{t,3-4}^{cr} = \frac{\tau_{t,\max}^{cr}}{\gamma_{t,\max}^{cr}} \tag{4.28}$$

being $\gamma_{t,\max}^{cr}$ and $\tau_{t,\max}^{cr}$ the maximum crack shear strain already attained and the corresponding crack shear stress determined from the softening linear branch. Both components are stored to define the unloading/reloading branch (see Figure 4.14).

To increase the generality of the simulation of the post-peak crack shear stress, two alternative crack shear stress-strain diagrams are proposed, being their shapes represented in Figure 4.15 and Figure 4.16. For the case of Figure 4.15, the post-peak phase is simulated with a trilinear diagram, while in Figure 4.16 this branch is exponential.

The crack shear softening diagram of Figure 4.15 is defined by the expressions shown in equation (4.29). Similarly to equation (4.23), only the positive part of the diagram is treated in

$$\tau_t^{cr}\left(\gamma_t^{cr}\right) = \begin{cases} D_{t,1}\,\gamma_t^{cr} & 0 < \gamma_t^{cr} \le \gamma_{t,p}^{cr} \\ \tau_{t,p}^{cr} - \dfrac{\tau_{t,p}^{cr} - \tau_1^{cr}}{\gamma_1^{cr} - \gamma_{t,p}^{cr}}\left(\gamma_t^{cr} - \gamma_{t,p}^{cr}\right) & \gamma_{t,p}^{cr} < \gamma_t^{cr} \le \gamma_1^{cr} \\ \tau_1^{cr} - \dfrac{\tau_1^{cr} - \tau_2^{cr}}{\gamma_2^{cr} - \gamma_1^{cr}}\left(\gamma_t^{cr} - \gamma_1^{cr}\right) & \gamma_1^{cr} < \gamma_t^{cr} \le \gamma_2^{cr} \\ \tau_2^{cr} - \dfrac{\tau_2^{cr}}{\gamma_{t,u}^{cr} - \gamma_2^{cr}}\left(\gamma_t^{cr} - \gamma_2^{cr}\right) & \gamma_2^{cr} < \gamma_t^{cr} \le \gamma_{t,u}^{cr} \\ 0 & \gamma_t^{cr} > \gamma_{t,u}^{cr} \end{cases} \tag{4.29}$$

being

$$\tau_1^{cr} = c_1 \, \tau_{t,p}^{cr} \tag{4.30a}$$

$$\tau_2^{cr} = c_2 \, \tau_{tp}^{cr} \tag{4.30b}$$

$$\gamma_1^{cr} = d_1 \left(\gamma_{t,u}^{cr} - \gamma_{t,p}^{cr} \right) \tag{4.30c}$$

$$\gamma_2^{cr} = d_2 \left(\gamma_{t,u}^{cr} - \gamma_{t,p}^{cr} \right) \tag{4.30d}$$

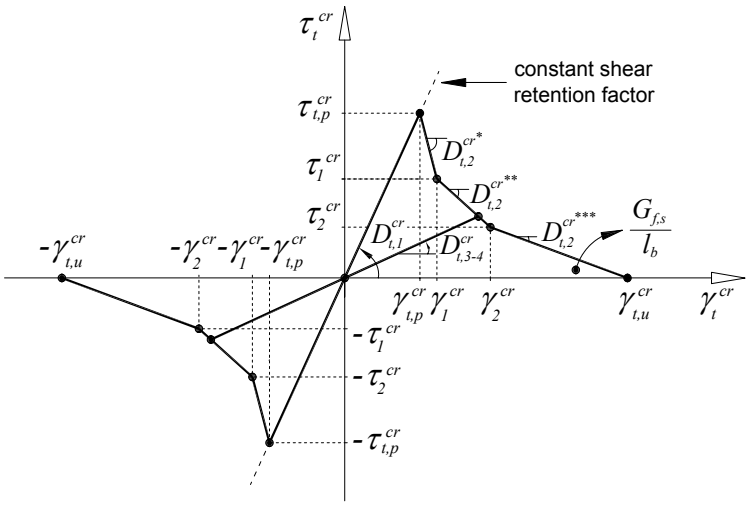

Figure 4.15 – Diagram to simulate the relationship between the crack shear stress and crack shear strain component with post-peak trilinear branches.

The ultimate crack shear strain, $\gamma_{t,u}^{cr}$, is defined as a function of the parameters c_i and d_i, the peak crack shear strain, $\gamma_{t,p}^{cr}$, the crack shear strength, $\tau_{t,p}^{cr}$, the mode II (for in-plane shear) fracture energy, $G_f^{II} = G_{f,s}$, and the crack bandwidth, l_b, as follows

$$\gamma_{t,u}^{cr} = \gamma_{t,p}^{cr} + \frac{2}{d_1 + c_1 d_2 - c_2 d_1 + c_2} \frac{G_{f,aux}^{II}}{\tau_{t,p}^{cr} \, l_b} \tag{4.31}$$

being

$$G_{f,aux}^{II} = \left(\frac{G_f^{II}}{l_b} - \frac{\tau_{t,p}^{cr} \, \gamma_{t,p}^{cr}}{2} \right) l_b \tag{4.32}$$

and

$$c_1 = \tau_1^{cr} \Big/ \tau_{t,p}^{cr} \tag{4.33a}$$

$$c_2 = \tau_2^{cr} \Big/ \tau_{t,p}^{cr} \tag{4.33b}$$

$$d_1 = \gamma_1^{cr} \Big/ \left(\gamma_{t,u}^{cr} - \gamma_{t,p}^{cr} \right) \tag{4.33c}$$

$$d_2 = \gamma_2^{cr} \Big/ \left(\gamma_{t,u}^{cr} - \gamma_{t,p}^{cr} \right) \tag{4.33d}$$

The crack mode II stiffness modulus of the first linear branch of the diagram is defined by equation (4.24), while for the post peak branches it is obtained from the following equations

$$D_{t,2}^{cr^*} = -\frac{\left(1-c_1\right)\left(d_1 + c_1 d_2 - c_2 d_1 + c_2\right)}{2d_1} \frac{l_b f_{ct}^2}{G_{f,aux}^{II}} \tag{4.34a}$$

$$D_{t,2}^{cr^{**}} = -\frac{\left(c_1 - c_2\right)\left(d_1 + c_1 d_2 - c_2 d_1 + c_2\right)}{2\left(d_2 - d_1\right)} \frac{l_b f_{ct}^2}{G_{f,aux}^{II}} \tag{4.34b}$$

$$D_{t,2}^{cr^{***}} = -\frac{c_2\left(\xi_1 + c_1 d_2 - c_2 d_1 + c_2\right)}{2\left(1-d_2\right)} \frac{l_b f_{ct}^2}{G_{f,aux}^{II}} \tag{4.34b}$$

For the unloading and reloading branches, the crack mode II stiffness modulus is determined by equation (4.28).

The exponential branch of the crack shear softening diagram represented in Figure 4.16 is based on the Cornelissen diagram used in the definition of the crack opening mode I. Equation (4.35) gives expressions of the positive part of the proposed softening diagram

$$\tau_t^{cr}\left(\gamma_t^{cr}\right)=$$

$$=\begin{cases} D_{t,1}^{cr}\,\gamma_t^{cr} & 0<\gamma_t^{cr}\le\gamma_{t,p}^{cr} \\ \tau_{t,p}^{cr}\left[\left(1+\left(c_1B\right)^3\right)\exp\left(-c_2B\right)-B\left(1+c_1^3\right)\exp\left(-c_2\right)\right] & \gamma_{t,p}^{cr}<\gamma_t^{cr}\le\gamma_{t,u}^{cr} \\ 0 & \gamma_t^{cr}>\gamma_{t,u}^{cr} \end{cases} \tag{4.35}$$

being

$$B=\frac{\gamma_t^{cr}-\gamma_{t,p}^{cr}}{\gamma_{t,u}^{cr}-\gamma_{t,p}^{cr}} \tag{4.36}$$

and $c_1 = 3.0$; c_2=6.93.

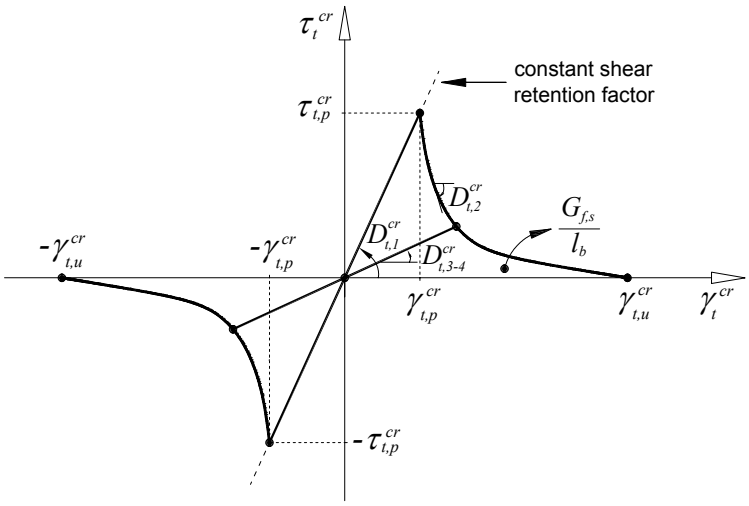

Figure 4.16 – Diagram to simulate the relationship between the crack shear stress and crack shear strain component with post-peak exponential branch.

The ultimate crack shear strain, $\gamma_{t,u}^{cr}$, of the crack shear softening diagram represented in Figure 4.16 is defined by

$$\gamma_{t,u}^{cr} = \gamma_{t,p}^{cr} + \frac{1}{k}\frac{G_{f,aux}^{II}}{\tau_{t,p}^{cr}\, l_b} \tag{4.37}$$

where the parameter k is defined by equation (3.30) and $G_{f,aux}^{II}$ by equation (4.32).

The crack mode II stiffness modulus of the first linear branch of the diagram is defined by equation (4.24), for the unloading and reloading branches by equation (4.28) and for the exponential (softening) branch by

$$\begin{aligned} D_{t,2}^{cr} = \tau_{t,p}^{cr}\Bigg[& 3\left(c_1\frac{\gamma_t^{cr}}{\gamma_{t,u}^{cr}}\right)^2\frac{c_1}{\gamma_{t,u}^{cr}}\exp\left(-c_2\frac{\gamma_t^{cr}}{\gamma_{t,u}^{cr}}\right)+ \\ & +\exp\left(-c_2\frac{\gamma_t^{cr}}{\gamma_{t,u}^{cr}}\right)\left(-\frac{c_2}{\gamma_{t,u}^{cr}}\right)\left(1+\left(c_1\frac{\gamma_t^{cr}}{\gamma_{t,u}^{cr}}\right)^3\right)-\frac{1+c_1^3}{\gamma_{t,u}^{cr}}\exp\left(-c_2\right)\Bigg] \end{aligned} \tag{4.38}$$

being $\gamma_{t,u}^{cr}$ obtained with equation (4.37).

4.3.2 **Crack shear status**

As a consequence of the formation of other cracks in the neighborhood of existing cracks, these existing cracks can close or reopen. The model must take into account this change of crack status. For the opening mode I the model takes this into account (Sena-Cruz 2004) and for the crack shear component a similar approach is used.

The shear crack status is shown in Figure 4.14 and its definition takes into account the following assumptions:

- Stiffening status, if the crack shear strain is less than the crack shear strain at peak crack shear stress, $\gamma_{t,p}^{cr}$, obtained with equation (4.25) and assuming a constant shear retention factor for the evaluation of the fracture mode II stiffness modulus;

- Softening status, after the crack shear strain has reached $\gamma_{t,p}^{cr}$. A decrease in the crack shear stress is observed with the increase of the crack shear strain;
- Unloading status, when a shear softening crack experiences a decrease of crack shear strain. In this case a secant approach is followed;
- Reloading status, when a crack with an unloading status experiences an increase of crack shear strain. The same branch of the unloading status is followed;
- Free-sliding status, when the crack shear strain is greater than the ultimate crack shear strain.

These crack shear statuses are stored to be used in the subsequent steps of the nonlinear analysis. With this procedure, at each instant the shear softening diagram is well defined. For example, Figure 4.17 to Figure 4.22 illustrate the possible paths that can be followed at each increment of crack shear strain, and, consequently, the complexity of the associated crack status changes.

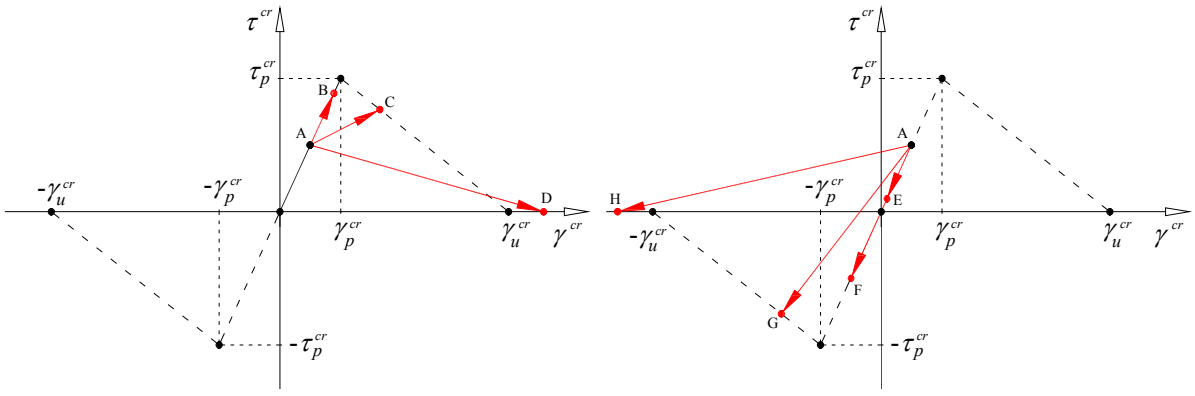

a) $\Delta\gamma^{cr} > 0$ b) $\Delta\gamma^{cr} < 0$

Figure 4.17 – Increment of the crack shear strain $\Delta\gamma^{cr}$: possible paths when the starting point is positive and in Stiffening shear crack status (point A).

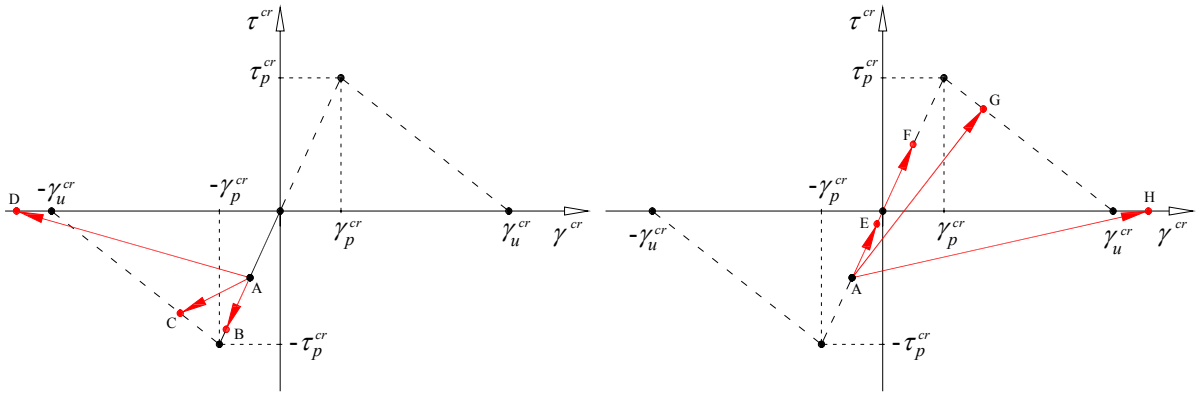

a) $\Delta\gamma^{cr} < 0$ b) $\Delta\gamma^{cr} > 0$

Figure 4.18 – Increment of the crack shear strain $\Delta\gamma^{cr}$: possible paths when the starting point is negative and in Stiffening shear crack status (point A).

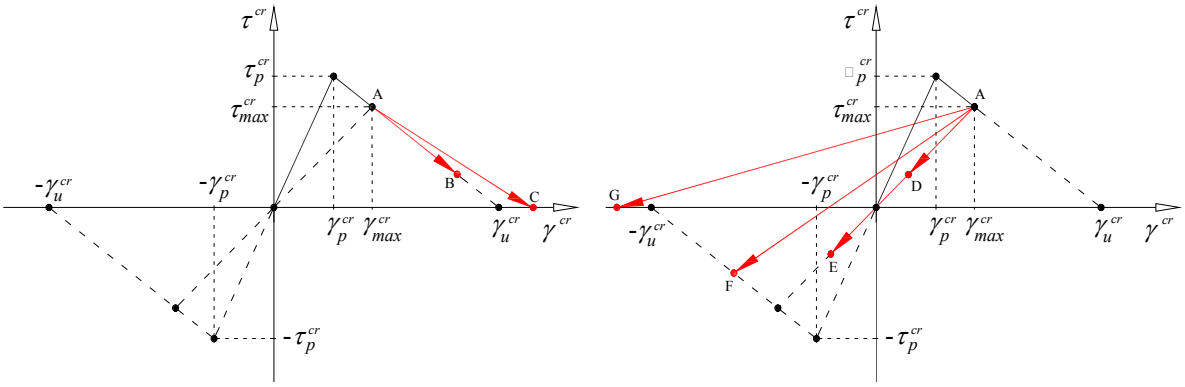

a) $\Delta\gamma^{cr} > 0$ b) $\Delta\gamma^{cr} < 0$

Figure 4.19 – Increment of the crack shear strain $\Delta\gamma^{cr}$: possible paths when the starting point is positive and in Softening shear crack status (point A).

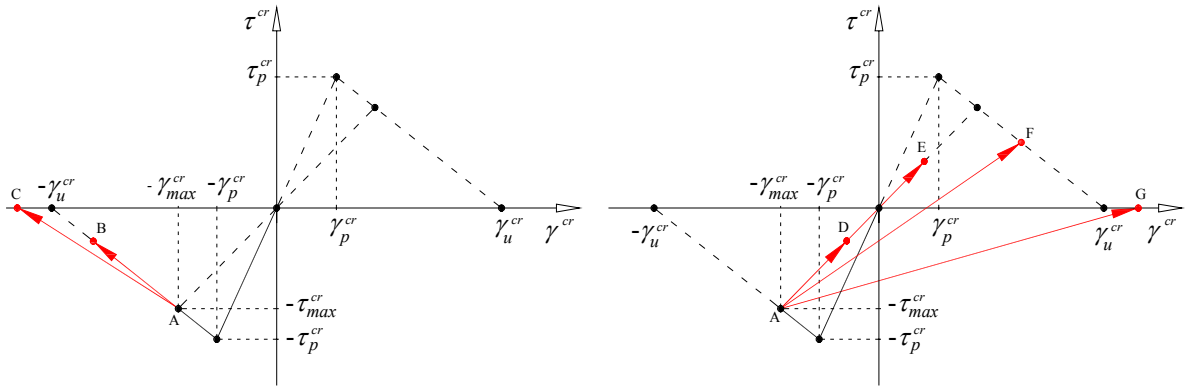

a) $\Delta\gamma^{cr} < 0$ b) $\Delta\gamma^{cr} > 0$

Figure 4.20 – Increment of the crack shear strain $\Delta\gamma^{cr}$: possible paths when the starting point is negative and in Softening shear crack status (point A).

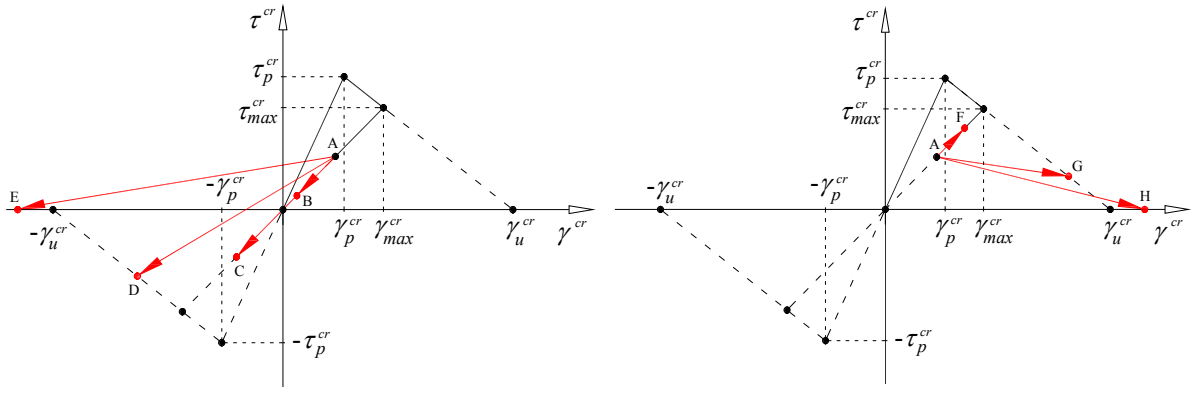

a) $\Delta\gamma^{cr} < 0$ b) $\Delta\gamma^{cr} > 0$

Figure 4.21 – Increment of the crack shear strain $\Delta\gamma^{cr}$: possible paths when the starting point is positive and in Unloading or Reloading shear crack status (point A).

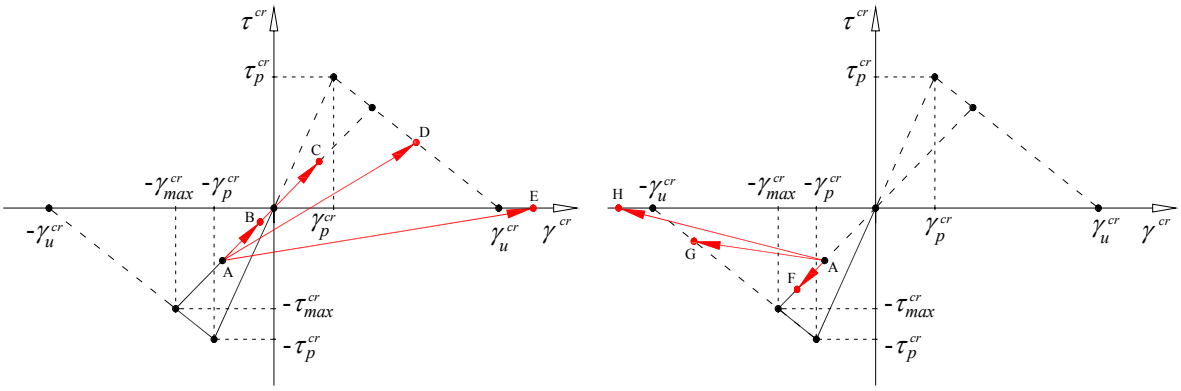

a) $\Delta\gamma^{cr} > 0$ b) $\Delta\gamma^{cr} < 0$

Figure 4.22 – Increment of the crack shear strain $\Delta\gamma^{cr}$: possible paths when the starting point is negative and in Unloading or Reloading shear crack status (point A).

In Free-sliding status the crack mode II stiffness modulus, $D_{II}^{cr} = D_{t,5}^{cr}$, is null. To avoid numerical instabilities in the calculation of the stiffness matrix and in the calculation of the internal forces, when the crack shear status is Free-sliding, a residual value is assigned to this term. This topic is described in chapter 5.

The control of the crack evolution is made by the opening mode I, whose behavior is defined by one of the tensile-softening diagrams discussed in section 3.3.2.2. When a softening diagram is also used for the crack shear component some assumption must be made since there is no coupling between the two softening diagrams used for the normal component and for the shear component. Therefore, the crack can be in a Softening status for the opening mode I and in an Unloading status for the mode II.

The following problem occurs in some analyses: the crack is Fully Open $\left(\varepsilon_n^{cr} > \varepsilon_{n,u}^{cr}\right)$ and the crack shear component, defined by one of the diagrams presented in the previous sections, is in Stiffening or in Softening status. It is obvious that if the crack is Fully Open the shear stress transfer between the crack planes is null. Therefore, the solution adopted is to assign a Free-sliding status to the shear crack status of this crack.

Another problem that sometimes occurs consists on the reopening of a closed crack. At the moment of closure, the crack adopts a linear elastic behavior in compression. If this closed

crack reopens at a subsequent step, i.e., the normal stress of the crack becomes tensile, the opening mode I behavior follows the unloading/reloading branch of the tensile-softening diagram (see for example Figure 3.6) and the data relative to strain and stress is updated. A more complex task is the update of the crack shear strain and stress when a softening diagram is used, because the crack shear stress at crack closure can be very different from the crack shear stress when the crack reopens. This is similar to the treatment of the rotation of the principal axes when the status of the crack is Closed. This problem was reported by Rots and de Borst (1987) and the proposed solution was to impose that the shear crack component enters immediately in a softening phase. For this purpose, the $\tau_{t,p}^{cr}$ and $\gamma_{t,p}^{cr}$ components (see Figure 4.14) that define the new shear softening diagram is the crack shear stress upon reopen and the stored crack shear strain at closure of the crack, respectively. The ultimate crack shear strain of the new diagram, $\gamma_{t,u}^{cr}$, is updated in order to maintain the same mode II fracture energy. This procedure was implemented in a first phase, but it could be observed that in some cases the value of the shear crack stress was very low upon reopen of the crack, implying that the new softening diagram could have an abnormal high ultimate crack shear strain because of the condition of preserving the mode II fracture energy. Therefore, a new approach is adopted and the corresponding assumptions are commented in Table 4.5 and illustrated in Figure 4.23. This approach takes into account the shear crack status before the closure of the crack, being the diagram updated in some cases, and maintained in others.

Figure 4.23 represents the different starting points in the crack shear softening diagram when the mode I crack status changes from Closed to Reopening. The value of τ_i^{cr} is the current crack shear stress at crack reopen, and γ_i^{cr} is the corresponding calculated crack shear strain. The symbol γ_{i-1}^{cr} represents the crack shear strain before the closure of the crack. If the crack shear stress, τ_i^{cr}, is negative the starting points are located on the negative branch of the crack shear softening diagram (see Figure 4.14). In accordance with Figure 4.23, Table 4.5 represents the conditions for the update of the shear crack status when a crack reopens.

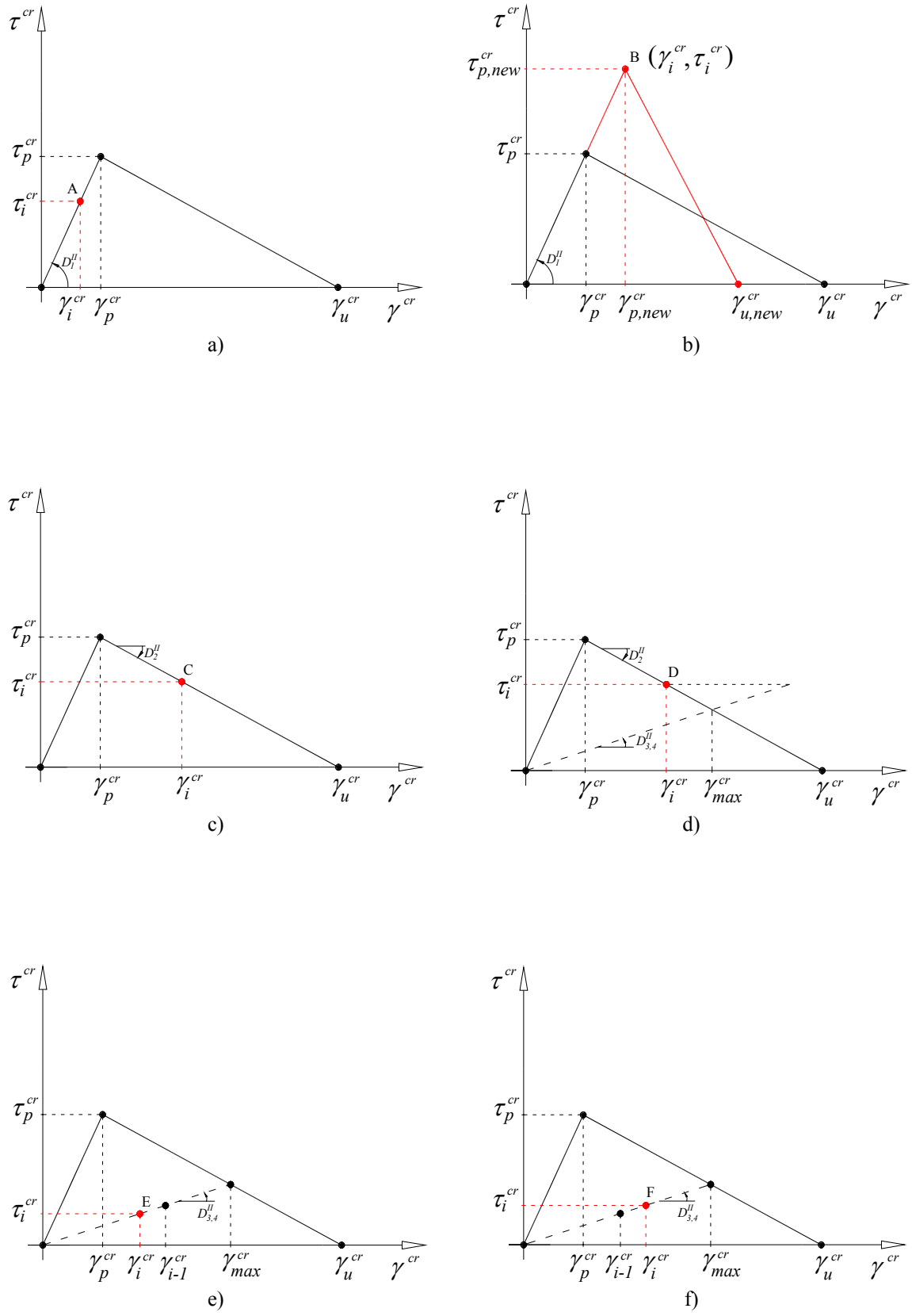

Figure 4.23 – Different starting points in the crack shear softening diagram when the mode I crack status changes from Closed to Reopening.

Table 4.5 – Update of shear crack status when a crack reopens

Shear crack status before crack closure	Conditions	Start Point	Shear crack status when crack reopens	Update shear crack strength	Update crack shear strain **
Stiffening	$\tau_i^{cr} < \tau_p^{cr}$	A	Stiffening *	-	$\gamma_i^{cr} = \frac{\tau_p^{cr}}{D_1^{II}}$
	$\tau_i^{cr} \geq \tau_p^{cr}$	B	Softening *	$\tau_{p,new}^{cr} = \tau_i^{cr}$	$\gamma_i^{cr} = \frac{\tau_{p,new}^{cr}}{D_1^{II}} = \gamma_{p,new}^{cr}$
Softening	$\tau_i^{cr} < \tau_p^{cr}$	C	Softening *	-	$\gamma_i^{cr} = \gamma_p^{cr} + \frac{\tau_i^{cr} - \tau_u^{cr}}{D_2^{II}}$
	$\tau_i^{cr} \geq \tau_p^{cr}$	B	Softening *	$\tau_{p,new}^{cr} = \tau_i^{cr}$	$\gamma_i^{cr} = \frac{\tau_{p,new}^{cr}}{D_1^{II}}$
Unloading or Reloading	$\tau_i^{cr} < \tau_p^{cr}$ $\frac{\tau_i^{cr}}{D_{3,4}^{II}} > \gamma_{\max}^{cr}$	D	Softening *	-	$\gamma_i^{cr} = \gamma_p^{cr} + \frac{\tau_i^{cr} - \tau_u^{cr}}{D_2^{II}}$
	$\tau_i^{cr} < \tau_p^{cr}$ $\frac{\tau_i^{cr}}{D_{3,4}^{II}} \leq \gamma_{\max}^{cr}$ $\frac{\tau_i^{cr}}{D_{3,4}^{II}} \leq \gamma_{i-1}^{cr}$	E	Unloading	-	$\gamma_i^{cr} = \frac{\tau_i^{cr}}{D_{3,4}^{II}}$
	$\tau_i^{cr} < \tau_p^{cr}$ $\frac{\tau_i^{cr}}{D_{3,4}^{II}} \leq \gamma_{\max}^{cr}$ $\frac{\tau_i^{cr}}{D_{3,4}^{II}} > \gamma_{i-1}^{cr}$	F	Reloading	-	$\gamma_i^{cr} = \frac{\tau_i^{cr}}{D_{3,4}^{II}}$
	$\tau_i^{cr} \geq \tau_p^{cr}$	B	Softening *	$\tau_{p,new}^{cr} = \tau_i^{cr}$	$\gamma_i^{cr} = \frac{\tau_{p,new}^{cr}}{D_1^{II}}$
Free-sliding	-	-	Free-sliding	-	$\gamma_i^{cr} = \gamma_{\max}^{cr}$ ***

* $\gamma_{\max}^{cr}$ - the maximum crack shear strain is updated;

** $D_1^{II} = \frac{\beta}{1-\beta} G_c$; $D_2^{II} = -\frac{\tau_p^{cr}}{\gamma_u^{cr} - \gamma_p^{cr}}$; $D_{3,4}^{II} = \frac{\tau_{\max}^{cr}}{\gamma_{\max}^{cr}}$;

*** the crack shear stress is assumed to be null: $\tau_i^{cr} = 0$.

4.3.3 **Numerical simulations**

To validate the implemented softening diagram of the shear crack component three numerical simulations are performed. The first one is dedicated to the simulation of a mixed-mode test (Arrea and Ingraffea 1982), while the second deals with the simulation of a reinforced concrete T cross section beam that has failed in shear (Dias and Barros 2010). The last example is dedicated to the numerical simulation of a reinforced concrete beam strengthened in shear with embedded through-section bars (Dalfré et al. 2011).

4.3.3.1 Mixed-mode test

In this section the experimental test from Arrea and Ingraffea (1982) is numerically simulated. This test is a benchmark for the validation of models taking into account the flexural and shear failure modes, being this phenomenon usually designated mixed-mode failure. Many researchers simulated this test numerically, being the results available elsewhere (Rots et al. 1985, de Borst 1986, Rots and de Borst 1987, Rots 1988, Ozbolt and Reinhardt 2000, Jirásek and Zimmermann 2001, Most and Bucher 2006).

Some material parameters used in the numerical simulations coincide with those used by Rots and de Borst 1987. The geometry, mesh, support and load conditions of the tested four point beam are illustrated in Figure 4.24. The beam is modeled with 8-noded plane stress finite elements. The elements outside the refined zone are assumed to exhibit a linear-elastic behavior. The multi-fixed smeared crack model is adopted for the elements of the refined zone thus taking into account the nonlinear behavior due to crack initiation and propagation. The Gauss-Legendre integration scheme with 3×3 IP is used in all the elements.

Three numerical simulations are performed, varying in the treatment of the crack shear component. The mode I fracture behavior is simulated with a bi-linear softening diagram, adapted from the trilinear diagram presented in chapter 3. The parameters defining this diagram are listed in Table 4.6. One of the numerical simulations considers a constant shear retention factor to obtain the mode II stiffness modulus, while the others use the softening diagram of Figure 4.14 to determine the crack shear modulus. The difference

between these last numerical simulations resides on the value used for the mode II fracture energy. The parameters defining these diagrams are presented in Table 4.6.

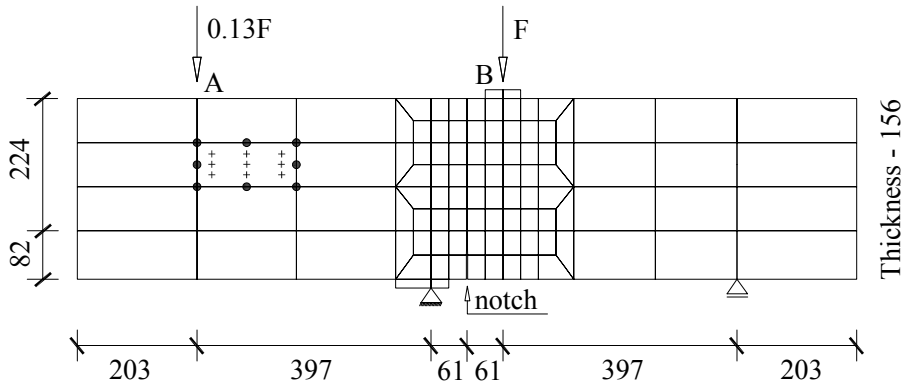

Figure 4.24 – Geometry, mesh, load and support conditions of the tested four point beam (all dimensions are in mm) [based on Rots and de Borst 1987].

Table 4.6 - Model properties used in the four point beam simulations.

Poisson's ratio	$\nu = 0.18$
Initial Young's modulus	$E_c = 24800.0\ \mathrm{N/mm^2}$
Compressive strength	$f_c = 48.0\ \mathrm{N/mm^2}$
Trilinear tension softening diagram	$f_{ct} = 2.8\ \mathrm{N/mm^2}$; $G_f^I = 0.075\ \mathrm{N/mm}$; $\xi_1 = 0.15$; $\alpha_1 = 0.3$; $\xi_2 = 0.4$; $\alpha_2 = 0.2$
Shear crack softening diagram	$\beta = 0.2$; $\tau_{t,p}^{cr} = 0.5\ \mathrm{N/mm^2}$; $G_f^{II} = 0.075\ \mathrm{N/mm}$ or $G_f^{II} = 0.01\ \mathrm{N/mm}$
Parameter defining the mode I fracture energy available to the new crack	$p_2 = 2$
Shear retention factor	0.2
Crack bandwidth	20.3 mm
Threshold angle	$\alpha_{th} = 60^{\circ}$
Maximum number of cracks in each IP	2

The numerical simulations are performed using the Newton-Raphson method, controlled by the relative displacement between two specific variables (see section 2.4.4). The controlling variables consist on a pair of vertical displacements, located at each tip of the notch. This type of control is named Crack Mouth Sliding Displacement or CMSD. With this procedure an eventual snap-back can be captured (de Borst 1986, Ventura-Gouveia et al. 2006).

Figure 4.25 shows the relation between the load at point B and the CMSD. The experimental pattern was obtained by Rots and de Borst 1987. It is observed that the three numerical simulations have similar behavior up to the peak load, and afterwards different paths are followed. With the constant shear factor the residual stress is close to the peak stress and practically no softening is predicted. With the introduction of the shear crack softening diagram a softening behavior is observed and a good agreement with the experimental results can be obtained, especially with the simulation that considers the mode II fracture energy equal to 0.075 N/mm. The abrupt load decay, from 47.7 kN to 9 kN, in the simulation with mode II fracture energy equal to 0.01 N/mm can be justified by the deformed mesh observed before and after this occurrence, as represented in Figure 4.26.

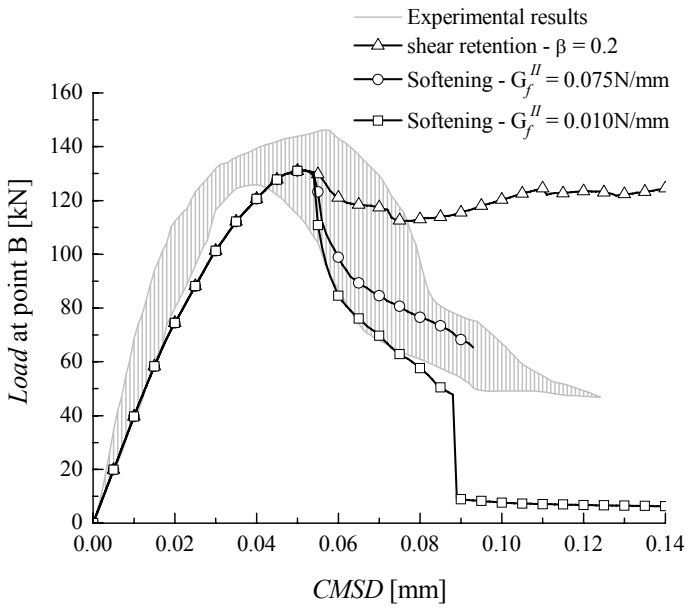

Figure 4.25 – Load at point B – crack mouth sliding displacement (CMSD) relationship.

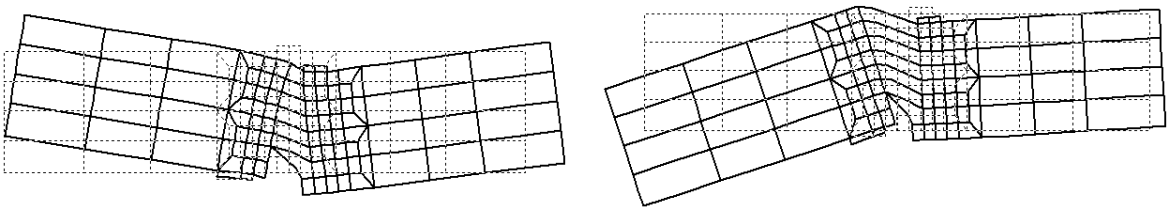

(a) (b)

Figure 4.26 – Numerical simulation with softening crack shear diagram considering $G_f^{II} = 0.01$ N/mm : deformed mesh (a) before and (b) after the abrupt load decay observed in Figure 4.25. The dashed line represents the undeformed mesh.

The crack pattern observed immediately before and immediately after the abrupt load decay is shown in Figure 4.27.

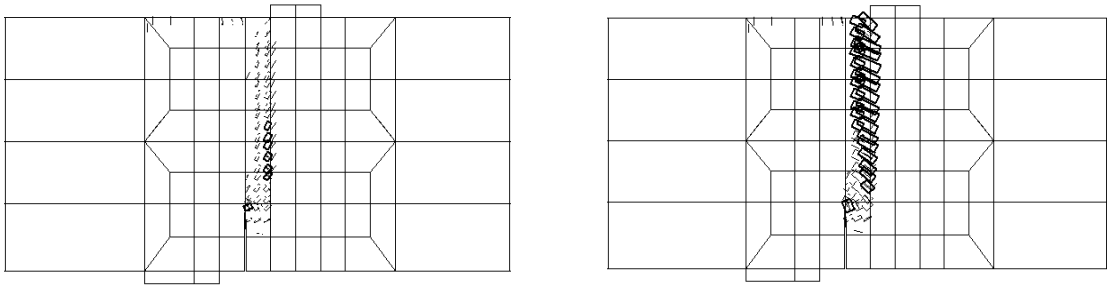

(a) (b)

Figure 4.27 – Numerical simulation with softening crack shear diagram considering $G_f^{II} = 0.01$ N/mm : crack pattern (a) before and (b) after the abrupt load decay observed in Figure 4.25. In dark quadrilateral, crack fully open, and the others in opening or closing process.

From the analysis of the two deformed meshes and respective crack pattern, it can be stated that the model is capable to reproduce numerically the decrease of the crack shear stress transfer during the crack opening process, and is able to evaluate the residual load carrying capacity. This residual load capacity is in most cases due to the aggregate interlock occurring at the crack.

In Figure 4.28 the load at point B is plotted against the crack mouth opening displacement (CMOD). Conclusions identical to the aforementioned ones can be extracted in terms of

using a softening diagram or the shear retention factor to simulate the degradation of the shear stress transfer during the crack opening process. An interesting phenomenon, captured numerically for the curve with $G_f^{II} = 0.01\,\mathrm{N/mm}$, is the snap-back of the CMOD at the sudden load decay. The explanation for this behavior can be found by examining the deformed meshes in Figure 4.26. Due to the rotation of the left side of the beam about the support point, the CMOD decreases at this instant and then progressively reopens. This reopening process in a residual phase is numerically reproduced and shown in Figure 4.28.

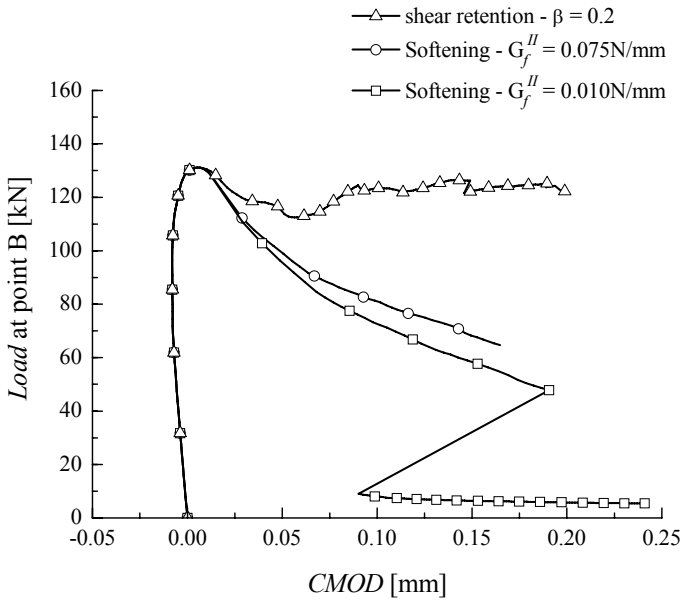

Figure 4.28 – Load at point B – crack mouth opening displacement (CMOD) relationship.

As observed by de Borst (1986) and Rots and de Borst (1987), a snap-back occurs after the peak load and is only achieved when the CMSD control is used in the nonlinear analysis. This snap-back is more pronounced when a crack softening diagram is used (see Figure 4.29). An interesting snap-back is observed after the abrupt load decay that occurs when the softening $G_f^{II} = 0.01\,\mathrm{N/mm}$ curve is used.

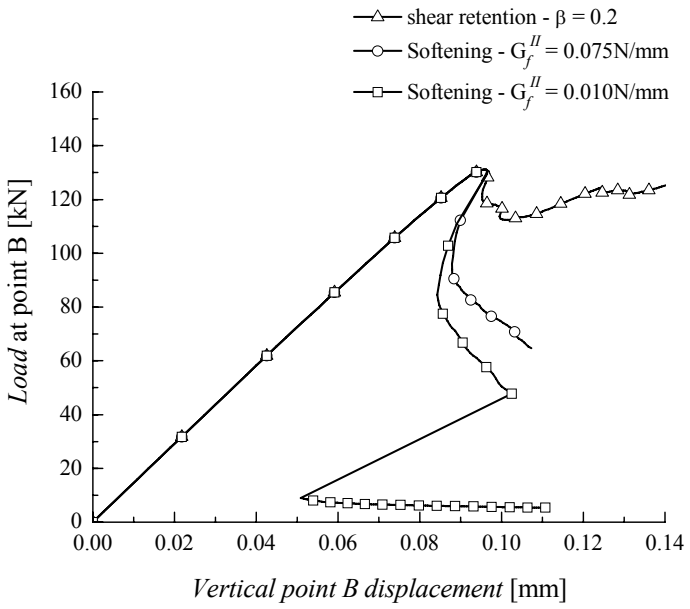

Figure 4.29 – Load - displacement at point B relationship.

4.3.3.2 T cross section reinforced concrete beam failing in shear

An experimental program was carried out by Dias and Barros (2010) with reinforced concrete (RC) T cross section beams in the scope of a research project for the assessment of the effectiveness of the near surface mounted (NSM) technique by using carbon fiber reinforced polymer (CFRP) laminates for the shear strengthening of RC T beams. Several RC T beams with different percentage of NSM CFRP laminates were tested. The geometry, support and loading conditions of the RC T reference beams are represented in Figure 4.30.

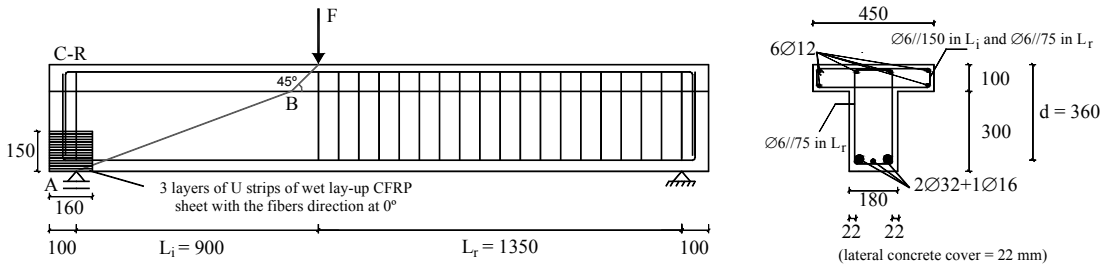

Figure 4.30 – Reinforced concrete T reference beam: geometry, support, steel reinforcement scheme and loading conditions [dimensions in mm] (Dias and Barros 2010).

The RC tested beam named 2S-R (see Figure 4.31) is numerically simulated, which corresponds to the control T beam of the series with two steel stirrups in the L_i span, i.e., without NSM CFRP laminates. To prevent concrete spalling near the most loaded support, a confinement system based on the use of wet layup CFRP strips of sheets of U configuration is applied as represented in Figure 4.30.

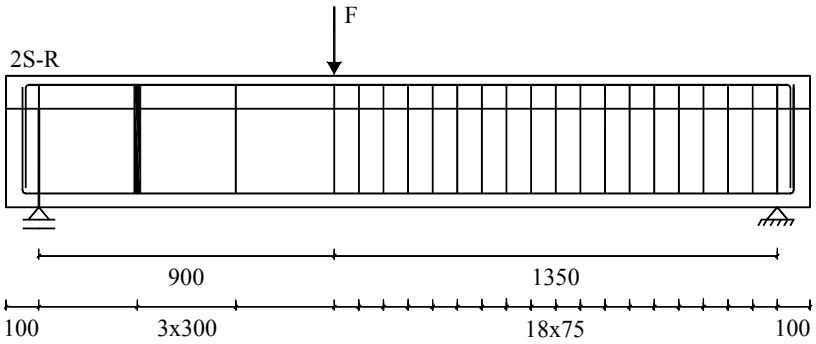

Figure 4.31 – 2S-R reinforced concrete T cross section beam [dimensions in mm] (Dias and Barros 2010).

For the finite element analysis, the beam is considered as a plane stress problem. Therefore, the beam is modeled with a mesh of 4-noded serendipity plane stress finite elements (see Figure 4.32). A Gauss-Legendre integration scheme with 2×2 IP is used in all concrete elements and CFRP strips of sheet elements. The steel bars are modeled with 2-noded perfectly bonded embedded cables (one degree-of-freedom per node). The Newton-Raphson method with displacement control at a specific variable is used in the nonlinear analysis (see section 2.4.3 of chapter 2).

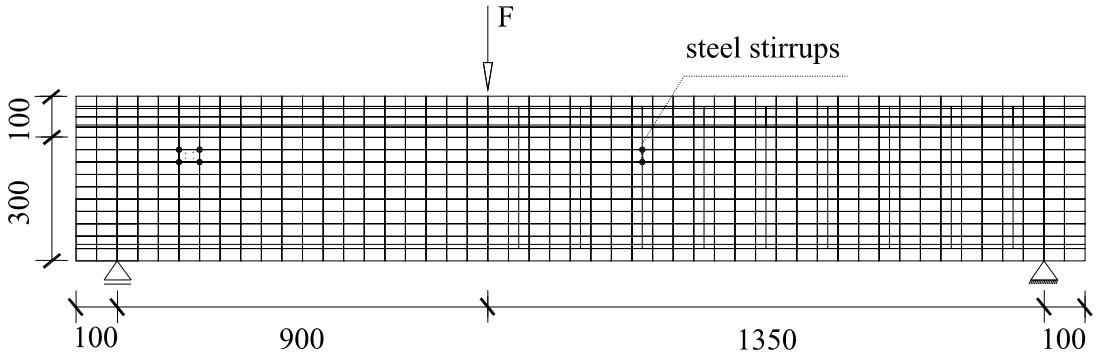

Figure 4.32 – Finite element mesh [dimensions in mm].

For modeling the behavior of the steel bars, the stress-strain relationship available in the FEMIX computer code is used (Sena-Cruz 2004). A linear elastic behavior is adopted for modeling CFRP strips of sheets.

The values of the parameters of the constitutive model used in the numerical simulations are indicated in Table 4.7, Table 4.8 and Table 4.9. Using the average compressive strength, f_c, determined experimentally, the concrete tensile strength, f_{ct}, and the mode I fracture energy, G_f^I, were initially obtained from equations proposed by CEB-FIP (1993), and then were slightly adjusted in order to fit with high accuracy the load at crack initiation. The values for characterizing the softening diagram of Figure 4.14 were obtained by back-fitting analysis in order to approximate as much as possible the experimental curve in the post-cracking phase. It can be observed that the mode II fracture energy value is similar to the value assigned to the mode I fracture energy.

Table 4.7 - Properties of CFRP strips of sheets.

	C Sheet 240
f_{fu} (MPa)	2863
E_f (GPa)	218
ε_{fu} (‰)	13.3
t_f (mm)	0.176

Table 4.8 - Steel properties.

	ϕ_s=6 mm	ϕ_s=12 mm	ϕ_s=16 mm ϕ_s=32 mm
ε_{sy} (‰)	3.0	2.8	3.0
σ_{sy} (MPa)	515	420	570
ε_{sh} (‰)	25	25	25
σ_{sh} (MPa)	542	453	740
ε_{su} (‰)	50	50	50
σ_{su} (MPa)	594	591	850
p	1	1	1

Table 4.9 - Model properties used for the T beam simulation.

Poisson's ratio	$\nu = 0.15$
Initial Young's modulus	$E_c = 33271.0\ \mathrm{N/mm^2}$
Compressive strength	$f_c = 39.7\ \mathrm{N/mm^2}$
Trilinear tension softening diagram	$f_{ct} = 2.2\ \mathrm{N/mm^2}$; $G_f^I = 0.086\ \mathrm{N/mm}$; $\xi_1 = 0.005$; $\alpha_1 = 0.4$; $\xi_2 = 0.2$; $\alpha_2 = 0.3$
Shear crack softening diagram	$\beta = 0.5$; $\tau_{t,p}^{cr} = 1.0\ \mathrm{N/mm^2}$; $G_f^{II} = 0.08\ \mathrm{N/mm}$
Parameter defining the mode I fracture energy available to the new crack	$p_2 = 3$
Shear retention factor	0.5
Crack bandwidth	Square root of the area of the IP
Threshold angle	$\alpha_{th} = 30^{\circ}$
Maximum number of cracks per each IP	2

Two numerical simulations are performed that differ in the treatment of the crack shear component. One uses the concept of shear retention factor with a constant value $(\beta = 0.5)$ and the other uses the shear crack softening diagram of Figure 4.14.

Figure 4.33 represents the experimental and numerical relationships between the load and the deflection at the loaded section for the tested 2S-R beam. It can be observed that the use of the concept of the shear retention factor conducts to an overestimation of the load carrying capacity. The curve derived from this numerical analysis starts diverging significantly from the experimental one for deflections larger than 1.5 mm. In the analysis where a shear crack softening diagram was used, a quite accurate simulation was obtained up to a load level that is 91.6 % of the ultimate load registered experimentally. In this case the numerical simulation was interrupted because convergence was never possible to attain due to the formation of a shear failure crack, as shown in Figure 4.34. This figure represents the crack patterns at a deflection of about 4.9 mm for both numerical simulations. The use of the shear crack softening diagram reproduces very well the shear failure observed at the end of the experimental test and represented Figure 4.35.

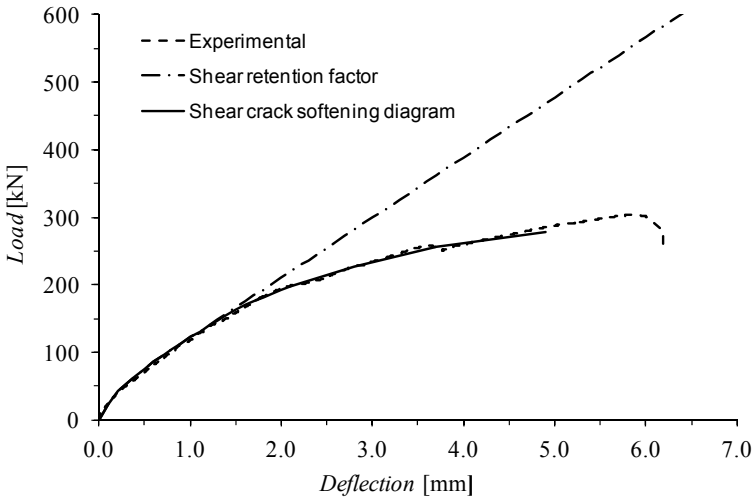

Figure 4.33 – Load-deflection at the loaded section for the T beam.

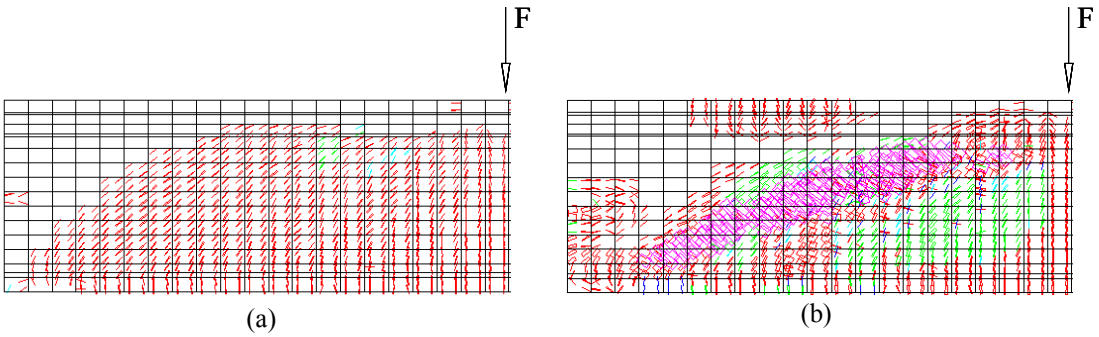

Figure 4.34 – Crack pattern of the 2S-R beam by using a: (a) shear retention factor; and (b) a shear crack softening diagram (in pink color: crack completely open ($\varepsilon_n^{cr} \geq \varepsilon_{n,u}^{cr}$); in red color: crack in the opening process; in cyan color: crack in the reopening process; in green color: crack in the closing process; in blue color: closed crack).

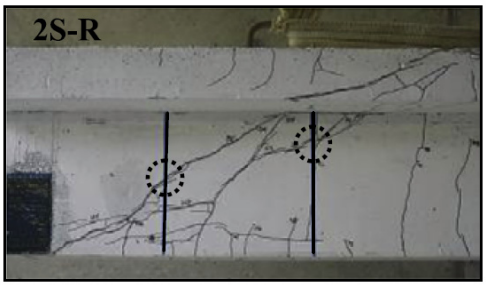

Figure 4.35 – Crack pattern at the end of the tested 2S-R beam (Dias and Barros 2010).

4.3.3.3 Reinforced concrete beam strengthened in shear with embedded through-section bars

In this section a beam strengthened in shear using the embedded through-section (ETS) technique is numerically simulated. The experimental program was carried out by Dalfré et al. (2011) and several beams were tested (see Figure 4.36) with the scope of assessing the performance of ETS technique in the shear strengthening as an alternative to the NSM shear strengthening based on the use of CFRP laminates. The ETS technique consists in the insertion of steel bars into previous drilled holes through the cross section of the RC beam to strengthen.

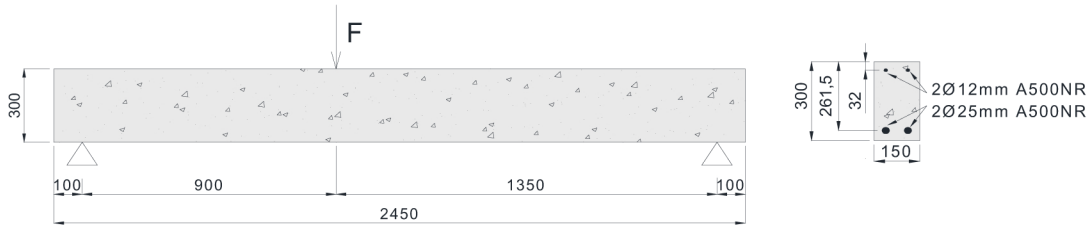

Figure 4.36 – Reinforced concrete beam: geometry, support, steel reinforcement scheme and loading conditions [dimensions in mm] (Dalfré et al. 2011).

Figure 4.37 represents the geometry, support and load conditions of the S225.90/E225.90 beam (Dalfré et al. 2011), containing in the shear span stirrups at 90° (3ϕ6 mm of 2 arms, 225 mm spacing) and ETS strengthening bars at 90° (4ϕ10 mm, 225 mm spacing).

Figure 4.37 – Reinforced concrete ETS strengthening beam: geometry, support, steel reinforcement scheme and loading conditions [dimensions in mm] (Dalfré et al. 2011).

The finite element mesh used for the simulations is represented in Figure 4.38. The beam is modeled with a mesh of 8-noded serendipity plane stress finite elements. A Gauss-Legendre integration scheme with 3×3 IP is used in all the concrete elements. The steel bars and the ETS strengthening bars are modeled with 3-noded perfectly bonded

embedded cables (one degree-of-freedom per node) and a Gauss-Legendre integration scheme with 3 IP is used.

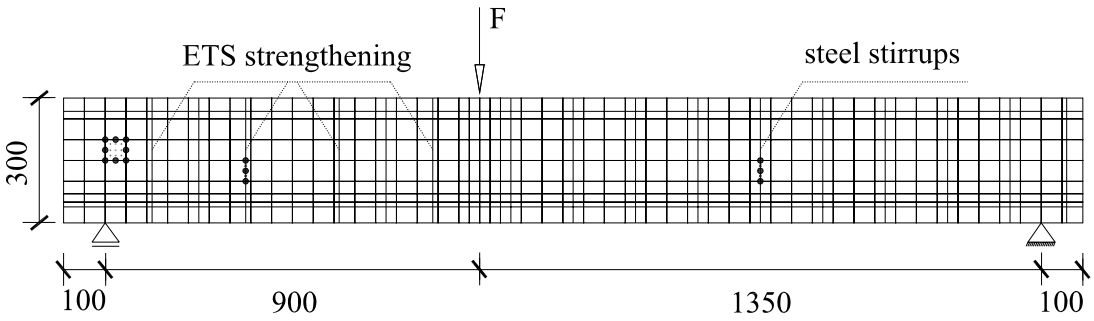

Figure 4.38 – Finite element mesh [dimensions in mm].

For modeling the behavior of the steel bars, the stress-strain relationship available in the FEMIX computer code is used (Sena-Cruz 2004). Two relationships are used in the numerical simulations and the values are presented in Table 4.10, since the strains were not measured in the experimental tests after the yield initiation of the steel bars. Therefore, for the strain and its corresponding stress that define the end of the second branch of the stress-strain diagram of the steel bars two pairs of values were considered, leading to the diagrams designated by A and B.

The values of the parameters of the constitutive model for the concrete elements used in the numerical simulations are indicated in Table 4.11. Using the average compressive strength, f_c, determined experimentally, the concrete tensile strength, f_{ct}, and the mode I fracture energy, G_f^I, were initially obtained from equations proposed by CEB-FIP (1993), and then were adjusted in order to fit with high accuracy the load at crack initiation. The values for characterizing the softening diagram of Figure 4.14 were obtained by back-fitting analysis in order to approximate as much as possible the experimental curve in the post-cracking phase.

Table 4.10 - Steel properties.

	ϕ_s=6 mm		ϕ_s=10 mm		ϕ_s=12 mm		ϕ_s=25 mm	
	A	B	A	B	A	B	A	B
ε_{sy} (‰)	2.75	2.75	2.66	2.66	2.35	2.35	2.27	2.27
σ_{sy} (MPa)	559.14	559.14	541.6	541.6	484.68	484.68	507.68	507.68
ε_{sh} (‰)	20.00	25.00	20.00	25.00	20.00	25.00	20.00	25.00
σ_{sh} (MPa)	708.14	559.14	643	541.6	655.00	484.68	743.00	507.68
ε_{su} (‰)	50.00	50.00	50.00	50.00	50.00	50.00	50.00	50.00
σ_{su} (MPa)	708.93	708.93	643.23	643.23	655.53	655.53	743.41	743.41
p	1	1	1	1	1	1	1	1

Table 4.11 - Model properties used for the ETS strengthening beam simulation.

Poisson's ratio	$\nu = 0.15$
Initial Young's modulus	$E_c = 31100.0\ \mathrm{N/mm^2}$
Compressive strength	$f_c = 30.78\ \mathrm{N/mm^2}$
Trilinear tension softening diagram (concrete elements near the bottom longitudinal steel bars)	$f_{ct} = 2.0\ \mathrm{N/mm^2}$; $G_f^I = 0.06\ \mathrm{N/mm}$; $\xi_1 = 0.01$; $\alpha_1 = 0.5$; $\xi_2 = 0.5$; $\alpha_2 = 0.2$
Trilinear tension softening diagram (other concrete elements)	$f_{ct} = 1.8\ \mathrm{N/mm^2}$; $G_f^I = 0.05\ \mathrm{N/mm}$; $\xi_1 = 0.01$; $\alpha_1 = 0.4$; $\xi_2 = 0.2$; $\alpha_2 = 0.2$
Shear crack softening diagram (concrete elements near the bottom longitudinal steel bars)	$\beta = 0.2$; $\tau_{t,p}^{cr} = 1.38\ \mathrm{N/mm^2}$; $G_f^{II} = 0.5\ \mathrm{N/mm}$
Shear crack softening diagram (other concrete elements)	$\beta = 0.2$; $\tau_{t,p}^{cr} = 1.38\ \mathrm{N/mm^2}$; $G_f^{II} = 0.3\ \mathrm{N/mm}$
Parameter defining the mode I fracture energy available to the new crack	$p_2 = 1$
Shear retention factor	0.2
Crack bandwidth	Square root of the area of the IP
Threshold angle	$\alpha_{th} = 30^{\circ}$
Maximum number of cracks per each IP	2

Tree numerical simulations are performed, varying in the treatment of the crack shear component and in the modeling of the behavior of the steel bars and the ETS strengthening bars. One uses the concept of shear retention factor with a constant value ($\beta = 0.2$) and the other two uses the shear crack softening diagram of Figure 4.14, differing only in the stress-strain relationship used for the simulation of the steel and the ETS strengthening bars (see Table 4.10).

Figure 4.39 represents the experimental and numerical relationships between the load and the deflection at the loaded section for the tested S225.90/E225.90 beam. In comparison to the experimental curve the use of the concept of the shear retention factor conducts to a more stiff response and the load carrying capacity is attained for a smaller deflection. The curve derived from this numerical analysis starts diverging from the experimental one for deflections larger than 3.5 mm. The analyses performed using the shear crack softening diagram improves significantly the numerical responses. A better accurate simulation is obtained using the properties B (see Table 4.10) for the steel bars and the ETS strengthening bars but the load carrying capacity is underestimated. Adopting the properties A (see Table 4.10) the ultimate load is better predicted with a response that is a little bit more stiff than the behavior recorded experimentally. In these numerical simulations the analyses were interrupted because convergence was never possible to attain due to the formation of shear failure cracks, as shown in Figure 4.40. This figure represents, for each numerical simulation, the crack patterns at maximum attained load. The use of the shear crack softening diagram improves significantly the shear failure observed at the end of the experimental test and schematically represented Figure 4.41.

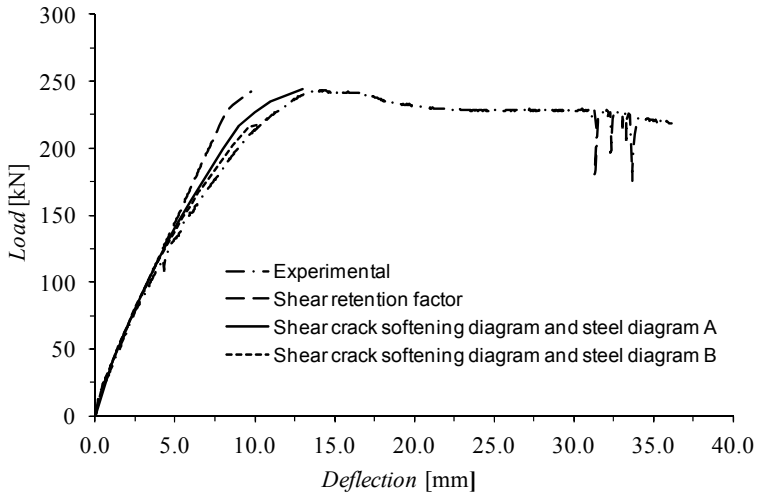

Figure 4.39 – Load-deflection at the loaded section for the ETS strengthening beam.

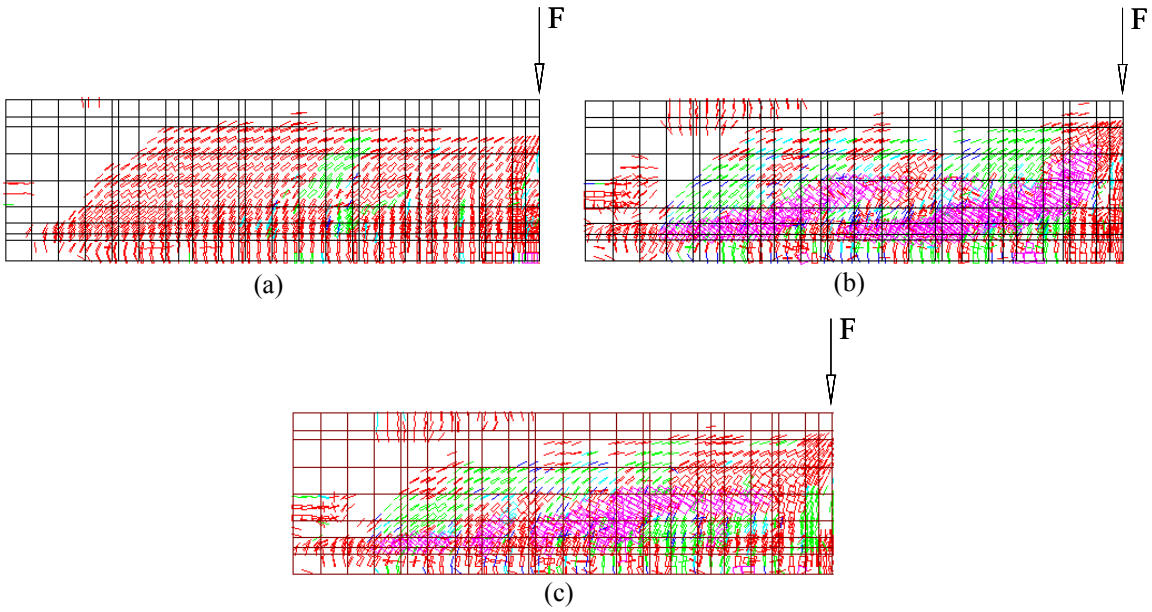

Figure 4.40 – Crack pattern of the S225.90/E225.90 beam by using: (a) shear retention factor; (b) shear crack softening diagram and steel diagram A; and (c) shear crack softening diagram and steel diagram B (in pink color: crack completely open ($\varepsilon_n^{cr} \geq \varepsilon_{n,u}^{cr}$); in red color: crack in the opening process; in cyan color: crack in the reopening process; in green color: crack in the closing process; in blue color: closed crack).

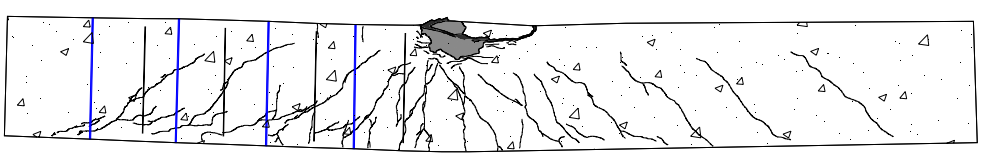

Figure 4.41 – Crack pattern at the end of the tested S225.90/E225.90 beam (Dalfré et al. 2011).

4.4 SUMMARY AND CONCLUSIONS

To accurately simulate the deformational behavior of the shear and flexural/shear failure modes, two alternative approaches are proposed for the treatment of the crack shear component. The former is the implementation of a total crack shear stress-shear strain approach to simulate the degradation of the shear stress transfer with the crack opening evolution, and the latter is based on the use of a constitutive softening relation between the crack shear stress and the crack shear strain component.

Each of these strategies is described and their capabilities are assessed by performing several numerical simulations. The results obtained are presented and discussed.

In conclusion, it can be said that the implementation of these new tools in the multi-fixed smeared crack model improves its capabilities to predict with higher accuracy the behavior of structures failing in shear or in flexural/shear.

Chapter 5

Multi-fixed smeared 3D crack model to simulate the behavior of concrete structures

5.1 INTRODUCTION

The type of model to be selected for the analysis of a certain structure depends on the specificities of this structure. Sometimes some simplifications can be adopted without compromise the relevance of the conclusions that can be extracted from the analysis, such is the case of assuming a structure like a bi-dimensional body. However, in some cases, due to complex loading and/or geometry conditions these simplifications are not appropriate, and to simulate the complex failure modes that can be formed in this type of structures three-dimensional (3D) approaches must be used.

In the present chapter a multi-fixed smeared 3D crack model, under the nonlinear FEM framework, is proposed to simulate the behavior of concrete structures. This model is suitable to be used with 3D solid elements available in the FEMIX computer code (Azevedo et al. 2003, Sena-Cruz et al. 2007).

The 3D model is described below and its performance is appraised by simulating a punching test with lightweight panels of steel fiber reinforced self-compacting concrete (SFRSCC).

5.2 NUMERICAL MODEL

5.2.1 Introduction

In the last decades the development of sophisticated 3D models to simulate the complex nonlinear behavior of concrete structures has been significant, and the applicability of these models to real structures is becoming possible due to the continuous progress in high-performance computing hardware (Barzegar and Maddipudi 1997a, 1997b).

In the present section the multi-fixed smeared 2D crack model, previously implemented in the FEMIX computer code by Sena-Cruz (2004), is generalized to a multi-fixed smeared 3D crack model, implemented with solid finite elements (Ventura-Gouveia et al. 2008). The fracture mode I is simulated with one of the tensile-softening stress-strain diagrams presented in section 3.3.2.2 of chapter 3. The characterization of the shear fracture modes is much more complex, since the shear stress transfer between the crack surfaces depends on several parameters, such as concrete lateral confinement, crack opening, roughness of the crack surfaces, concrete strength class, number of cracks and its relative orientation, etc. For its simulation, the classical shear crack retention factor concept can be used, associated with an incremental or total approach for the shear crack components, whose formulation is detailed in section 4.2 of chapter 4. Alternatively, the softening crack shear stress-strain diagram described in section 4.3 of the previous chapter can also be used in the simulation of the shear stress transfer between the crack surfaces.

5.2.2 Formulation

5.2.2.1 Crack strain and crack stress

As mentioned before, in a material nonlinear analysis the constitutive matrix depends on the stress or strain levels at a given stage of the loading process. To obtain a solution, the

external load is applied incrementally and an iterative technique is used to solve the resulting system of nonlinear equations (Zienkiewicz and Taylor 2000b, Ventura-Gouveia 2000, Ventura-Gouveia et al. 2006). The relationship between incremental strain and incremental stress is in this case given by

$$\Delta\underline{\sigma} = \underline{D}\ \Delta\underline{\varepsilon} \tag{5.1}$$

where $\Delta\underline{\sigma}$ represents the stress increment, $\Delta\underline{\varepsilon}$ is the strain increment and $\underline{D}$ is the tangent constitutive matrix.

The incremental strain associated with the cracked material is, in smeared crack models, decomposed into an incremental strain vector of the crack, $\Delta\underline{\varepsilon}^{cr}$, and an incremental strain vector of the uncracked concrete between the cracks, $\Delta\underline{\varepsilon}^{co}$ (de Borst and Nauta 1985, Rots et al. 1985, de Borst 1986, Rots 1988, Barros 1995). This incremental strain decomposition is useful for the inclusion of other phenomena, such as temperature, creep or shrinkage (de Borst and Nauta 1985, Hofstetter and Mang 1995, van Zijl et al. 2001). The inclusion of these time-dependent phenomena is treated in chapter 6.

$$\Delta\underline{\varepsilon} = \Delta\underline{\varepsilon}^{co} + \Delta\underline{\varepsilon}^{cr} \tag{5.2}$$

For the three-dimensional case the incremental local crack strain vector, $\Delta\underline{\varepsilon}_{\ell}^{cr}$, is defined by

$$\Delta\underline{\varepsilon}_{\ell}^{cr} = \left[\Delta\varepsilon_n^{cr} \quad \Delta\gamma_{t_1}^{cr} \quad \Delta\gamma_{t_2}^{cr}\right]^T \tag{5.3}$$

and, in the global coordinate system, by

$$\Delta\underline{\varepsilon}^{cr} = \left[\Delta\varepsilon_1^{cr} \quad \Delta\varepsilon_2^{cr} \quad \Delta\varepsilon_3^{cr} \quad \Delta\gamma_{23}^{cr} \quad \Delta\gamma_{31}^{cr} \quad \Delta\gamma_{12}^{cr}\right]^T \tag{5.4}$$

Equation (5.5) represents the relationship between $\Delta\underline{\varepsilon}_{\ell}^{cr}$ and $\Delta\underline{\varepsilon}^{cr}$

$$\Delta\underline{\varepsilon}^{cr} = \left[\underline{T}^{cr}\right]^{T} \Delta\underline{\varepsilon}_{\ell}^{cr} \tag{5.5}$$

where $\underline{T}^{cr}$ is the transformation matrix (see Figure 5.2) defined by

$$\underline{T}^{cr} = \begin{bmatrix} a_{11}^2 & a_{12}^2 & a_{13}^2 & 2a_{12}a_{13} & 2a_{11}a_{13} & 2a_{11}a_{12} \\ a_{11}a_{21} & a_{12}a_{22} & a_{13}a_{23} & a_{12}a_{23}+a_{13}a_{22} & a_{11}a_{23}+a_{13}a_{21} & a_{11}a_{22}+a_{12}a_{21} \\ a_{11}a_{31} & a_{12}a_{32} & a_{13}a_{33} & a_{13}a_{32}+a_{12}a_{33} & a_{13}a_{31}+a_{11}a_{33} & a_{12}a_{31}+a_{11}a_{32} \end{bmatrix} \tag{5.6}$$

The a_{11}, a_{12} and a_{13} components are the cosine directors of the unit vector of the axis normal to the crack plane, n; a_{21}, a_{22} and a_{23} are the cosine directors of the unit vector of the t_1 axis; finally, a_{31}, a_{32} and a_{33} are the cosine directors of the unit vectors of the t_2 axis. The n, t_1 t_2 axes form the local crack coordinate system.

In matrix form the components of $\underline{a}$ are defined by

$$\underline{a} = \begin{bmatrix} a_{11} & a_{12} & a_{13} \\ a_{21} & a_{22} & a_{23} \\ a_{31} & a_{32} & a_{33} \end{bmatrix} = \begin{bmatrix} \cos(n,x_1) & \cos(n,x_2) & \cos(n,x_3) \\ \cos(t_1,x_1) & \cos(t_1,x_2) & \cos(t_1,x_3) \\ \cos(t_2,x_1) & \cos(t_2,x_2) & \cos(t_2,x_3) \end{bmatrix} \tag{5.7}$$

The $\underline{T}^{cr}$ matrix transforms the stress components from the global coordinate system to the local crack coordinate system and its terms are extracted from the matrix that transforms the stress tensor between coordinate systems (Azevedo 1996, Silva 2006). It can be demonstrated that $\left[\underline{T}^{cr}\right]^{T}$ transforms the strain components from the local crack coordinate system to the global coordinate system (Azevedo 1985).

According to the fracture mechanics principles, three different types of fracture modes can be considered. The crack opening mode (fracture mode I), the shearing mode (fracture mode II - in-plane shear), and the tearing mode (fracture mode III - out-of-plane shear). A cracked body can be loaded in one of these modes or in a combination of the three modes (Wang 1996).

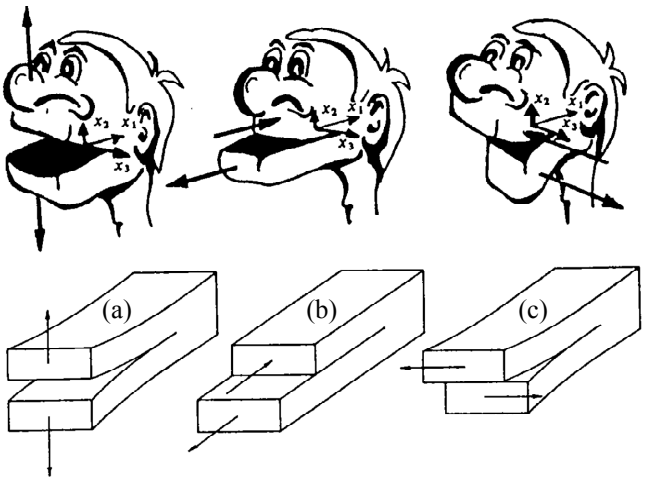

Figure 5.1 – Basic fracture modes: (a) opening mode (tensile), (b) shearing mode (in-plane shear) and (c) tearing mode (out-of-plane shear) [Wang 1996].

For the case of 3D solids, the distinction between mode II and mode III can be dropped (Hofstetter and Mang 1995). For this reason, in the present model mode II and mode III are designated as sliding modes in $\hat{t}_1$ and $\hat{t}_2$ directions, respectively.

The incremental local crack stress vector, $\Delta\underline{\sigma}_{\ell}^{cr}$, can be defined by

$$\Delta\underline{\sigma}_{\ell}^{cr} = \left[\Delta\sigma_n^{cr} \quad \Delta\tau_{t_1}^{cr} \quad \Delta\tau_{t_2}^{cr}\right]^T \tag{5.8}$$

where $\Delta\sigma_n^{cr}$ is the mode I incremental crack normal stress, $\Delta\tau_{t_1}^{cr}$ is the sliding mode incremental crack shear stress acting in $\hat{t}_1$ direction and $\Delta\tau_{t_2}^{cr}$ is the sliding mode incremental crack shear stress acting in $\hat{t}_2$ direction.

Figure 5.2 represents the crack stress components in the local coordinate system of the crack and the corresponding displacements: the opening displacement, w, the sliding displacement in $\hat{t}_1$ direction, s_1, and the sliding displacement in $\hat{t}_2$ direction, s_2.

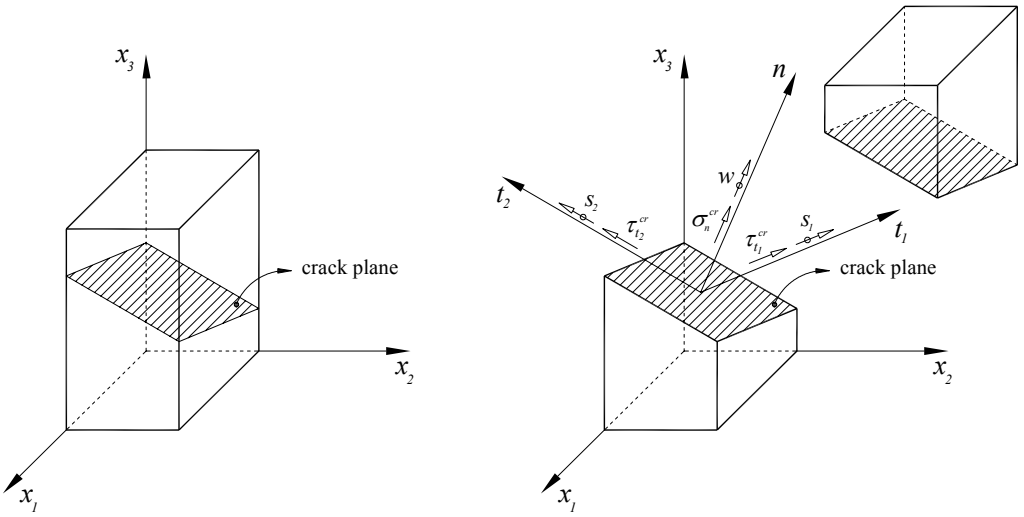

Figure 5.2 – Crack stress components, displacements and local coordinate system of the crack.

In the global coordinate system the incremental stress components are

$$\Delta\underline{\sigma} = \left[\Delta\sigma_1 \quad \Delta\sigma_2 \quad \Delta\sigma_3 \quad \Delta\tau_{23} \quad \Delta\tau_{31} \quad \Delta\tau_{12}\right]^T \tag{5.9}$$

The relationship between $\Delta\underline{\sigma}$ and $\Delta\underline{\sigma}_{\ell}^{cr}$ is

$$\Delta\underline{\sigma}_{\ell}^{cr} = \underline{T}^{cr}\Delta\underline{\sigma} \tag{5.10}$$

5.2.2.2 Constitutive law of the concrete

A linear elastic behavior is assumed for the concrete between cracks, being the relation between $\Delta\underline{\varepsilon}^{co}$ and $\Delta\underline{\sigma}$ given by

$$\Delta\underline{\sigma} = \underline{D}^{co}\Delta\underline{\varepsilon}^{co} \tag{5.11}$$

with

$$\underline{D}^{co} = \frac{E}{(1+\nu)(1-2\nu)}\begin{bmatrix} (1-\nu) & \nu & \nu & 0 & 0 & 0 \\ \nu & (1-\nu) & \nu & 0 & 0 & 0 \\ \nu & \nu & (1-\nu) & 0 & 0 & 0 \\ 0 & 0 & 0 & \frac{1-2\nu}{2} & 0 & 0 \\ 0 & 0 & 0 & 0 & \frac{1-2\nu}{2} & 0 \\ 0 & 0 & 0 & 0 & 0 & \frac{1-2\nu}{2} \end{bmatrix} \tag{5.12}$$

being E the Young's modulus and ν the Poisson's ratio of the undamaged concrete.

5.2.2.3 Constitutive law of the crack

At the crack zone (damaged concrete), the relationship between $\Delta\underline{\varepsilon}_{\ell}^{cr}$ and $\Delta\underline{\sigma}_{\ell}^{cr}$ is given by

$$\Delta\underline{\sigma}_{\ell}^{cr} = \underline{D}^{cr}\Delta\underline{\varepsilon}_{\ell}^{cr} \tag{5.13}$$

where

$$\underline{D}^{cr} = \begin{bmatrix} D_n^{cr} & 0 & 0 \\ 0 & D_{t_1}^{cr} & 0 \\ 0 & 0 & D_{t_2}^{cr} \end{bmatrix} \tag{5.14}$$

is the crack constitutive matrix.

In equation (5.14), D_n^{cr}, $D_{t_1}^{cr}$ and $D_{t_2}^{cr}$ represent, respectively, the fracture mode I stiffness modulus, the sliding stiffness modulus in the $\hat{t}_1$ direction and the sliding stiffness modulus in the $\hat{t}_2$ direction, and their values depend on the law assumed to simulate the crack behavior.

In the present approach the direct shear-normal coupling is ignored, thus justifying the diagonality of the crack constitutive matrix. Its effect may be indirectly obtained by allowing non-orthogonal cracks to form and defining the sliding fracture modes as a function of the crack normal strain (Rots 1988).

The fracture mode I modulus, D_n^{cr}, is defined by one of the tensile-softening diagrams described in section 3.3.2.2 of chapter 3.

The sliding fracture mode modulus, $D_{t_1}^{cr}$ or $D_{t_2}^{cr}$, can be obtained with,

$$D_{t_1}^{cr} = D_{t_2}^{cr} = \frac{\beta}{1-\beta} G_c \tag{5.15}$$

where G_c is the concrete elastic shear modulus and β is the shear retention factor, defined by a constant value or by equation (3.32) in section 3.3.2.2 of chapter 3. Alternatively, to model the crack shear stress transfer in $\hat{t}_1$ and $\hat{t}_2$ directions, and to improve the accuracy of the simulations of structures failing in shear, $D_{t_1}^{cr}$ or $D_{t_2}^{cr}$ can be obtained with one of the shear crack softening diagrams described in section 4.3 of chapter 4. In this case, each component follows an independent crack softening diagram.

5.2.2.4 Constitutive law of the cracked concrete

Taking into account equation (5.2) and equation (5.5), equation (5.11) can be written as follows

$$\Delta\underline{\sigma} = \underline{D}^{co}\left(\Delta\underline{\varepsilon} - \left[\underline{T}^{cr}\right]^{T}\Delta\underline{\varepsilon}_{\ell}^{cr}\right) \tag{5.16}$$

Multiplying this equation by the transformation matrix $\underline{T}^{cr}$ and taking into account equation (5.10), equation (5.16) becomes

$$\Delta\underline{\sigma}_{\ell}^{cr} + \underline{T}^{cr}\,\underline{D}^{co}\left[\underline{T}^{cr}\right]^{T}\Delta\underline{\varepsilon}_{\ell}^{cr} = \underline{T}^{cr}\,\underline{D}^{co}\Delta\underline{\varepsilon} \tag{5.17}$$

and substituting $\Delta\underline{\sigma}_{\ell}^{cr}$ using equation (5.13)

$$\underline{D}^{cr}\Delta\underline{\varepsilon}_{\ell}^{cr} + \underline{T}^{cr}\,\underline{D}^{co}\left[\underline{T}^{cr}\right]^{T}\Delta\underline{\varepsilon}_{\ell}^{cr} = \underline{T}^{cr}\,\underline{D}^{co}\Delta\underline{\varepsilon} \tag{5.18}$$

or

$$\Delta\underline{\varepsilon}_{\ell}^{cr} = \left(\underline{D}^{cr} + \underline{T}^{cr}\,\underline{D}^{co}\left[\underline{T}^{cr}\right]^{T}\right)^{-1}\underline{T}^{cr}\,\underline{D}^{co}\Delta\underline{\varepsilon} \tag{5.19}$$

Equation (5.19) establishes a relationship between the incremental local crack strain vector and the incremental strain vector in the global coordinate system. Including equation (5.16), the following constitutive law for the cracked concrete can be obtained

$$\Delta\underline{\sigma} = \left(\underline{D}^{co} - \underline{D}^{co}\left[\underline{T}^{cr}\right]^{T}\left(\underline{D}^{cr} + \underline{T}^{cr}\,\underline{D}^{co}\left[\underline{T}^{cr}\right]^{T}\right)^{-1}\underline{T}^{cr}\,\underline{D}^{co}\right)\Delta\underline{\varepsilon} \tag{5.20}$$

or

$$\Delta\underline{\sigma} = \underline{D}^{crco}\Delta\underline{\varepsilon} \tag{5.21}$$

being

$$\underline{D}^{crco} = \underline{D}^{co} - \underline{D}^{co}\left[\underline{T}^{cr}\right]^{T}\left(\underline{D}^{cr} + \underline{T}^{cr}\,\underline{D}^{co}\left[\underline{T}^{cr}\right]^{T}\right)^{-1}\underline{T}^{cr}\,\underline{D}^{co} \tag{5.22}$$

the constitutive matrix of the cracked concrete.

Although the preceding equations are obtained assuming only one crack per integration point (IP), the model can be applied to the case of n_{cr} cracks being formed at each IP. For this purpose, the crack constitutive matrix, $\underline{D}^{cr}$, and the transformation matrix, $\underline{T}^{cr}$, include the information that corresponds to these n_{cr} cracks

$$\underline{D}^{cr} = \begin{bmatrix} \underline{D}_1^{cr} & \underline{0} & \ldots & \underline{0} \\ \underline{0} & \underline{D}_2^{cr} & \ldots & \underline{0} \\ \ldots & \ldots & \ldots & \ldots \\ \underline{0} & \underline{0} & \ldots & \underline{D}_{n_{cr}}^{cr} \end{bmatrix} \tag{5.23}$$

and

$$\underline{T}^{cr} = \begin{bmatrix} \underline{T}_1^{cr} & \underline{T}_2^{cr} & \ldots & \underline{T}_{n_{cr}}^{cr} \end{bmatrix}^{T} \tag{5.24}$$

In equations (5.23) and (5.24), D_i^{cr} and $\underline{T}_i^{cr}$ correspond to the crack constitutive matrix and to the crack transformation matrix of the i^{th} crack.

5.2.2.5 Model implementation

A simple Rankine criterion is used to detect crack initiation. When the maximum principal tensile stress reaches the concrete tensile strength at an IP of a finite element, the material contained in its influence volume changes from uncracked to cracked state. The crack plane is considered to be normal to the direction of the maximum principal stress. The crack normal tensile stress follows the tensile-softening diagram characterized by the

fracture mode I modulus, D_n^{cr}. For the crack shear components two hypothesis are available: each crack shear stress follows a shear softening diagram characterized by the sliding fracture modes $D_{t_1}^{cr}$ and $D_{t_2}^{cr}$, which can be obtained from one of the diagrams represented in section 4.3 of chapter 4; or the shear stresses and the sliding fracture modes are determined by means of the shear retention factor concept, which is based on equation (5.15).

As a consequence of the rotation of the axes of the principal stresses during the subsequent load increments, a new smeared crack pattern can be initiated. Two conditions must be satisfied for the new crack initiation:

- the maximum principal tensile stress reaches the concrete tensile strength;
- the angle between the direction vector of the maximum principal tensile stress and the direction vector of the existing cracks is greater than a predefined angle, named threshold angle, α_{th}.

Values between 30º and 60º are recommended for the threshold angle (de Borst and Nauta 1985, de Borst 1986). To maintain the consistency of the crack initiation process, when the second condition is not satisfied, the tensile strength must be updated. This value can be significantly different from the initial concrete tensile strength, especially for large values of α_{th} (Rots 1988).

The formation of additional cracks in an previously cracked concrete can contribute to the modification of the crack status of these existing cracks. The previously developed multi-fixed 2D smeared crack model takes into account these crack status modifications. In the present 3D model a similar approach is used for the opening mode I (Sena-Cruz 2004), and for both sliding modes when the crack shear softening diagram is selected (see section 4.3 of chapter 4). An eventual coupling between the normal and shear modes is not considered in the 3D model. Therefore, a crack can, for example, unload in mode I, soften in $\hat{t}_1$ sliding mode, and reload in $\hat{t}_2$ sliding mode. For this reason, the model treats separately the normal crack status, the shear crack status in $\hat{t}_1$ direction, and the shear crack

status in $\hat{t}_2$ direction. For the case of the sliding modes the shear crack statuses are described in section 4.3.2 of chapter 4.

As a consequence of the material nonlinear behavior, the stress must be updated in order to satisfy the laws of the material response. This stress update is performed with the following equation

$$\underline{\sigma} = \underline{\sigma}_{prev} + \Delta\underline{\sigma} \tag{5.25}$$

where the subscript $prev$ means the stress at a previous state of the IP.

Multiplying equation (5.25) by the transformation matrix $\underline{T}^{cr}$ results

$$\underline{T}^{cr}\underline{\sigma} = \underline{T}^{cr}\left(\underline{\sigma}_{prev} + \Delta\underline{\sigma}\right) \tag{5.26}$$

and taking into account the incremental relation from equation (5.10), established in terms of total stresses, equation (5.26) results in

$$\underline{\sigma}_{\ell}^{cr} = \underline{\sigma}_{\ell,prev}^{cr} + \Delta\underline{\sigma}_{\ell}^{cr} = \underline{T}^{cr}\left(\underline{\sigma}_{prev} + \Delta\underline{\sigma}\right) \tag{5.27}$$

Combining equation (5.20) with this equation yields, after some arrangements,

$$\begin{aligned}&\underline{\sigma}_{\ell,prev}^{cr} + \Delta\underline{\sigma}_{\ell}^{cr} = \\ &\underline{T}^{cr}\underline{\sigma}_{prev} + \underline{T}^{cr}\underline{D}^{co}\Delta\underline{\varepsilon} - \underline{T}^{cr}\underline{D}^{co}\left[\underline{T}^{cr}\right]^{T}\left(\underline{D}^{cr} + \underline{T}^{cr}\underline{D}^{co}\left[\underline{T}^{cr}\right]^{T}\right)^{-1}\underline{T}^{cr}\underline{D}^{co}\Delta\underline{\varepsilon}\end{aligned} \tag{5.28}$$

and taking into account equation (5.19) the following equation is obtained

$$\underline{\sigma}_{\ell,prev}^{cr} + \Delta\underline{\sigma}_{\ell}^{cr} - \underline{T}^{cr}\,\underline{\sigma}_{prev} - \underline{T}^{cr}\,\underline{D}^{co}\Delta\underline{\varepsilon} + \underline{T}^{cr}\,\underline{D}^{co}\left[\underline{T}^{cr}\right]^{T}\Delta\underline{\varepsilon}_{\ell}^{cr} = \underline{0} \tag{5.29}$$

Since $\Delta\underline{\sigma}_{\ell}^{cr}$ is a function of $\Delta\underline{\varepsilon}_{\ell}^{cr}$ (see equation (5.13)), equation (5.29) can be written in the following form

$$f\left(\Delta\underline{\varepsilon}_{\ell}^{cr}\right) = \underline{\sigma}_{\ell,prev}^{cr} - \underline{T}^{cr}\,\underline{\sigma}_{prev} - \underline{T}^{cr}\,\underline{D}^{co}\Delta\underline{\varepsilon} + \left(\underline{D}^{cr} + \underline{T}^{cr}\,\underline{D}^{co}\left[\underline{T}^{cr}\right]^{T}\right)\Delta\underline{\varepsilon}_{\ell}^{cr} = \underline{0} \tag{5.30}$$

The Newton-Raphson method is used to solve equation (5.30), where the vector of unknowns is the local incremental crack strain vector, $\Delta\underline{\varepsilon}_{\ell}^{cr}$.

The first derivative of equation (5.30) in order to the incremental local crack strain vector is required in the q iteration of this method. Depending on the strategy assumed for the crack shear components, i.e., the use of the concept of shear retention factor or the use of a crack shear softening diagram, this derivative is defined by equation (5.31) or equation (5.37), respectively.

When the concept of shear retention factor is used to obtain the sliding fracture modulus, $D_{t_1}^{cr}$ or $D_{t_2}^{cr}$, the derivative of $f\left(\Delta\underline{\varepsilon}_{\ell}^{cr}\right)$ is

$$\frac{\partial f\left(\Delta\underline{\varepsilon}_{\ell}^{cr}\right)}{\partial\Delta\underline{\varepsilon}_{\ell}^{cr}} = \underline{D}^{cr} + \overline{\underline{D}}^{cr} + \underline{T}^{cr}\,\underline{D}^{co}\left[\underline{T}^{cr}\right]^{T} \tag{5.31}$$

where

$$\overline{\underline{D}}^{cr} = \begin{bmatrix} \overline{\underline{D}}_{1}^{cr} & \underline{0} & \cdots & \underline{0} \\ \underline{0} & \overline{\underline{D}}_{2}^{cr} & \cdots & \underline{0} \\ \cdots & \cdots & \cdots & \cdots \\ \underline{0} & \underline{0} & \cdots & \overline{\underline{D}}_{n_{cr}}^{cr} \end{bmatrix} \tag{5.32}$$

being

$$\underline{\bar{D}}_i^{cr} = \begin{bmatrix} 0 & 0 & 0 \\ \left.\dfrac{\partial D_{t_1}^{cr}}{\partial \Delta \varepsilon_n^{cr}} \Delta \gamma_{t_1}^{cr}\right|_i & 0 & 0 \\ \left.\dfrac{\partial D_{t_2}^{cr}}{\partial \Delta \varepsilon_n^{cr}} \Delta \gamma_{t_2}^{cr}\right|_i & 0 & 0 \end{bmatrix} \tag{5.33}$$

if an incremental approach is used for the crack shear components or

$$\underline{\bar{D}}_i^{cr} = \begin{bmatrix} 0 & 0 & 0 \\ \left.\dfrac{\partial D_{t_1}^{cr}}{\partial \Delta \varepsilon_n^{cr}} \gamma_{t_1}^{cr}\right|_i & 0 & 0 \\ \left.\dfrac{\partial D_{t_2}^{cr}}{\partial \Delta \varepsilon_n^{cr}} \gamma_{t_2}^{cr}\right|_i & 0 & 0 \end{bmatrix} \tag{5.34}$$

if a total approach is used for the crack shear components (see section 4.2 of chapter 4).

When equation (3.32) is adopted to define the shear retention factor used in equation (5.15), the derivative of the i^{th} sliding fracture modulus $D_{t_i}^{cr}$ in order to $\Delta \varepsilon_n^{cr}$ is

$$\frac{\partial D_{t_i}^{cr}}{\partial \Delta \varepsilon_n^{cr}} = -\frac{\left(1-A\right)^{p_1} G_c p_1}{\varepsilon_{n,u}^{cr}\left(1-A\right)\left(1-\left(1-A\right)^{p1}\right)} - \frac{\left(\left(1-A\right)^{p_1}\right)^2 G_c p_1}{\varepsilon_{n,u}^{cr}\left(1-A\right)\left(1-\left(1-A\right)^{p1}\right)^2} \tag{5.35}$$

being

$$A = \frac{\varepsilon_{n,prev}^{cr} + \Delta \varepsilon_n^{cr}}{\varepsilon_{n,u}^{cr}} \tag{5.36}$$

When a constant shear retention factor is used, the matrix $\underline{\bar{D}}^{cr}$ becomes a null matrix.

If a crack shear softening diagram is used to obtain the sliding fracture modulus, $D_{t_1}^{cr}$ or $D_{t_2}^{cr}$, the derivative of $f\left(\Delta\underline{\varepsilon}_{\ell}^{cr}\right)$ is

$$\frac{\partial f\left(\Delta\underline{\varepsilon}_{\ell}^{cr}\right)}{\partial\Delta\underline{\varepsilon}_{\ell}^{cr}} = \underline{D}^{cr} + \underline{T}^{cr}\,\underline{D}^{co}\left[\underline{T}^{cr}\right]^{T} \tag{5.37}$$

When the convergence of the Newton-Raphson method cannot be achieved, the fixed-point iteration method is used to attempt the solution of the system (5.30).

The solution of equation (5.30) is the incremental local strain vector of the cracks, $\Delta\underline{\varepsilon}_{\ell}^{cr}$. The crack strain vector in the global coordinate system is calculated using equation (5.5) and the crack strain is updated with

$$\underline{\varepsilon}^{cr} = \underline{\varepsilon}_{prev}^{cr} + \Delta\underline{\varepsilon}^{cr} \tag{5.38}$$

From equation (5.13) the incremental local crack stress vector is obtained and the local crack stress vector is updated with

$$\underline{\sigma}_{\ell}^{cr} = \underline{\sigma}_{\ell,prev}^{cr} + \Delta\underline{\sigma}_{\ell}^{cr} \tag{5.39}$$

From equation (5.16) the incremental stress is calculated and the stress is updated using equation (5.25).

To verify the consistency of the solution a verification is made, using equation (5.10), in terms of total stresses with

$$\underline{\sigma}_{\ell}^{cr} = \underline{T}^{cr}\,\underline{\sigma} \tag{5.40}$$

The improvements made in the stress update and in the critical crack status change, explained in section 3.5 of chapter 3 for the 2D multi-fixed smeared crack model, are also implemented in the 3D version of this model.

The evaluation of the internal forces requires the solution of (5.30), and the calculation of the stiffness matrix of an element depends on the constitutive matrix of the cracked concrete (5.22). For both these purposes the inversion of the matrix defined by (5.41) is required.

$$\underline{D}' = \underline{D}^{cr} + \underline{T}^{cr}\,\underline{D}^{co}\left[\underline{T}^{cr}\right]^{T} \tag{5.41}$$

When $\underline{D}^{cr}$ is a null matrix, i.e., when the cracks are in Fully Open status or for the case of using a crack shear softening diagram, the shear crack statuses are in Free-sliding, resulting in a null stiffness for the sliding fractures modes, eventual problems might arise in the inversion of $\underline{D}'$. To circumvent these difficulties the following residual values are assigned to the diagonal of $\underline{D}^{cr}$ (see equation (5.14))

$$D_{n}^{cr} = 10^{-6} f_{c} \;\; ; \;\; D_{t_i}^{cr} = 10^{-6} G_{c} \tag{5.42}$$

5.3 MODEL APPRAISAL

The performance of the proposed constitutive model is assessed by simulating the behavior observed in a punching test of a lightweight SFRSCC panel. The test layout and the test setup are represented in Figure 3.27 of chapter 3. The finite element model, the load and the support conditions used in the numerical simulation of the punching test are shown in Figure 5.3.

Only one quarter of the panel is used in the simulation due to double symmetry. Serendipity 20 node solid elements with 2×2×3 Gauss-Legendre integration scheme are used (three integration points in the through-thickness direction). Three solid elements are used through the thickness of 110 mm, while in the lightweight zone (shaded elements in Figure 5.3) only one solid element is used through the thickness. The dashed line represents the support of the panel.

The values of the parameters of the constitutive model used in the simulation of the punching test are listed in Table 5.1. The results of two numerical simulations are described below. In the first one, the shear stress transfer in both sliding modes is simulated according to equation (5.15) with the shear retention factor defined by equation (3.32) assuming $p_1 = 2$. In the second one, the crack shear stress vs. crack shear strain diagram represented in Figure 4.14 (see section 4.3.1 of chapter 4) is used to model both shear sliding modes. In both simulations the values of the properties associated with the fracture mode I are obtained with the inverse analysis described in section 3.7.1 of chapter 3. The force-deflection relationship registered experimentally and those obtained from both numerical simulations are presented in Figure 5.4.

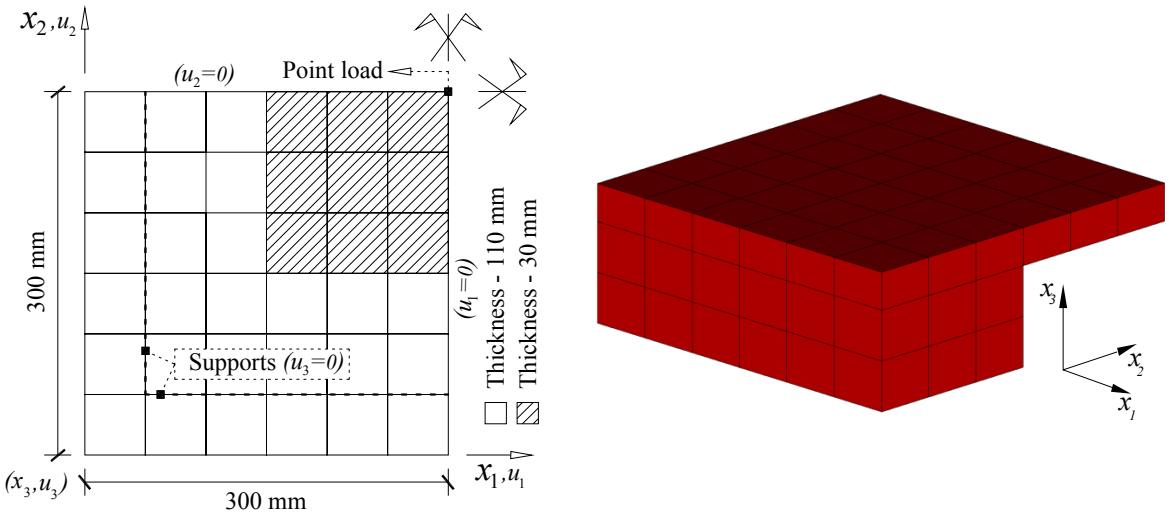

Figure 5.3 – Geometry, mesh, load and support conditions used in the numerical simulation of the punching test.

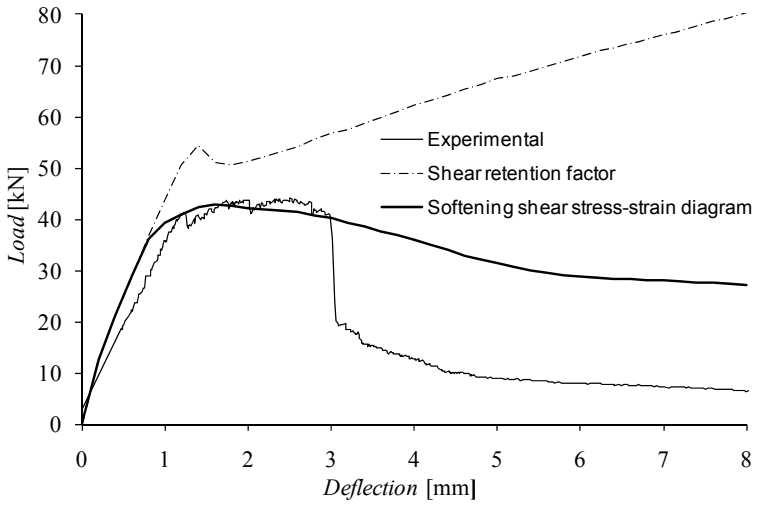

Figure 5.4 – Relationship between the force and the deflection at the center of the test panel.

Table 5.1 - Values of the parameters of the constitutive model used in the numerical simulation of the punching test.

Poisson's ratio	$\nu = 0.15$
Initial Young's modulus	$E_c = 31000.0 \text{ N/mm}^2$
Compressive strength	$f_c = 52.0 \text{ N/mm}^2$
Trilinear tension softening diagram of SFRSCC (see Figure 3.6 of section 3.3.2.2 of chapter 3)	$f_{ct} = 3.5 \text{ N/mm}^2$; $G_f^I = 4.3 \text{ N/mm}$; $\xi_1 = 0.009$; $\alpha_1 = 0.5$; $\xi_2 = 0.15$; $\alpha_2 = 0.59$
Parameter defining the mode I fracture energy available to the new crack	$p_2 = 2$
Softening crack shear stress-strain diagram (see Figure 4.14 of section 4.3.1 of chapter 4)	$\tau_{t,p}^{cr} = 2.0 \text{ N/mm}^2$; $G_{f,s} = 5.0 \text{ N/mm}$; $\beta = 0.5$
Shear retention factor	Exponential ($p_1 = 2$)
Crack bandwidth	Cube root of the volume of the integration point
Threshold angle	$\alpha_{th} = 30^o$

Figure 5.4 shows that, in the experimental test, for a deflection of about 1.2 mm at the central point, the panel load carrying capacity is almost retained up to a deflection of about 3 mm. Afterwards an abrupt load decay occurs due to the formation of a shear failure surface, typical of a punching rupture. However, using the concept of shear retention

factor, the model predicts an increase of the load carrying capacity with the increase of the panel deflection. According to this approach, the shear stresses in $\hat{t}_1$ and $\hat{t}_2$ sliding directions ($\tau_{t_1}^{cr}$, $\tau_{t_2}^{cr}$) increase with the increase of the corresponding shear strains ($\gamma_{t_1}^{cr}$, $\gamma_{t_2}^{cr}$). Only after the exhaustion of the mode I fracture energy ($\varepsilon_n^{cr} \geq \varepsilon_{n,u}^{cr}$, see Figure 3.6 of section 3.3.2.2), both crack shear stress components become constant (the incremental values are null, $\Delta\tau_{t_1}^{cr} = 0$, $\Delta\tau_{t_2}^{cr} = 0$). However, for this type of problem, where the crack shear constitutive components have a fundamental influence on the behavior the structure, mainly after a certain deflection, the formulation of these components should allow the shear stress components to decrease with the increase of the crack opening, which requires the use of a shear softening diagram, similar to that represented in Figure 4.14 of section 4.3.1. In fact, the second simulation, which is based on this approach, captured the plateau registered experimentally (see Figure 5.4), since the parameters of this diagram are evaluated by back-fitting analysis in order to reproduce this phase of the panel response. However, the abrupt load decay observed in the experimental test, at a deflection of about 3 mm, is not captured by this second approach, since the numerical simulation predicts a continuous, but smooth, degradation of the panel load carrying capacity. It could be verified that a decrease of $G_{f,s}$ (e.g $G_{f,s} = 4.0\ \mathrm{N/mm}$ or $G_{f,s} = 2.0\ \mathrm{N/mm}$) causes a decrease on the panel load carrying capacity, mainly in its structural softening phase, but the abrupt load decay is still not captured as shown in Figure 5.5.

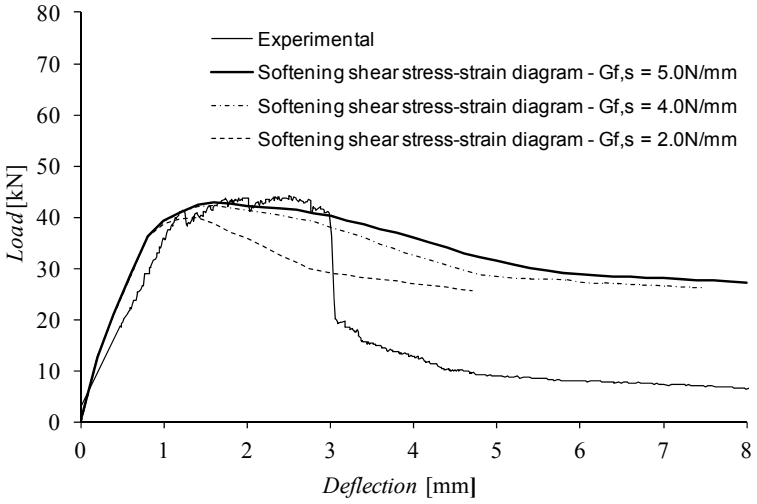

Figure 5.5 – Influence of $G_{f,s}$, on the numerical relationship between the force and the deflection at the center of the test panel.

5.4 SUMMARY AND CONCLUSIONS

In the present chapter a multi-fixed smeared 3D crack model is proposed. The developed model is based on the finite element method and is implemented in the FEMIX computer code. In an attempt to simulate the shear strain gradient that occurs in punching tests, a shear softening diagram is proposed in order to make both crack shear stress components dependent on the corresponding crack shear strains. The crack shear stress transfer can also be simulated using the concept of shear retention factor, which can be defined as a constant value or as a function of the crack normal strain. In this case the shear retention factor assumes a unitary value at crack initiation and a null value when the mode I fracture energy is exhausted.

The performance of the model is appraised by using the results obtained in a punching test with a lightweight panel prototype of steel fiber reinforced self-compacting concrete. Two numerical simulations are performed and discussed: one using the concept of shear retention factor and the other using a softening diagram to model both crack shear components. It is observed that the use of a softening diagram for the crack shear components improves the numerical simulation of the tested panel.

Chapter 6

Thermo-mechanical model

6.1 INTRODUCTION

In this chapter all relevant aspects related to the heat transfer and its implementation in the FEMIX computer code are described. The heat transfer problem is presented, and a numerical model is developed to simulate the heat transfer in structures built with materials whose mechanical behavior can be considered to be linear or nonlinear. The heat development due to the hydration process during the concrete hardening phase and its inclusion in the heat transfer model is also treated. The performance and the accuracy of the developed numerical model are assessed using results available in the literature.

The formulations of the time-dependent deformations due to shrinkage, creep and temperature variation are also presented, and the multi-fixed smeared 3D crack model proposed to simulate the behavior of concrete structures, described in chapter 5, is adapted to include these time-dependent effects.

6.2 THERMAL PROBLEM

6.2.1 Introduction

Heat transfer can be defined as the energy transferred between material bodies due to a temperature difference (Holman 1986, Lewis et al. 2004, Incropera et al. 2006). The heat flows from hot to cold mediums until an equilibrium state is reached (Silveira 1993), being

the process of heat transfer divided in three modes: conduction, convection and radiation. A briefly description of each mode, including its governing equations, is presented in this section. More details can be found elsewhere (Holman 1986, Silveira 1993, Lewis et al. 2004, Incropera et al. 2006, Lienhard IV and Lienhard V 2005, Azenha 2009).

Conduction heat transfer

From a simple point of view, this is the heat transfer that occurs inside a solid. The conduction heat transfer can occur in a steady-state regime, when the temperature field in a solid does not change with time or in a transient regime if the temperature field changes with respect to time.

The heat conduction rate equation is defined by the Fourier's law. For the case of one dimensional conduction this equation has the following form

$$q''_x = \frac{q_x}{A} = -k\frac{dT}{dx} \tag{6.1}$$

where q''_x is the heat flux in x direction, A is the area perpendicular to the direction of heat transfer, k is the material thermal conductivity and dT/dx is the temperature gradient. The minus sign signifies that the heat flows in the direction of the decreasing temperature.

Convection heat transfer

Convection is a process of heat transfer that occurs between a body surface and a fluid in movement when the temperatures differ between the two domains.

The heat convection rate equation is defined by the Newton's law of cooling,

$$q''_c = h_c\left(T - T_\infty\right) \tag{6.2}$$

where q''_c is the convective heat flux, h_c is the convection heat transfer coefficient, T is the temperature at the body surface and T_∞ is the fluid temperature.

Radiation heat transfer

Radiation is the mode of heat transfer that occurs when no contact exists between the body that emits heat and the body that receives it (this kind of heat transfer can occur in vacuum conditions).

The maximum flux emitted by radiation from a black body is defined by the Stefan-Boltzmann law equation,

$$q_e'' = \sigma T^4 \tag{6.3}$$

where q_e'' is the emitted heat flux, σ is the Stefan-Boltzmann constant, defined as $\sigma = 5.67 \times 10^{-8}\,\mathrm{Wm^{-2}K^{-4}}$, and T is the surface temperature.

Introducing in equation (6.3) the concept of emissivity, ε, to take into account that, in reality, the bodies emit less energy than black bodies, this equation is transformed into

$$q_e'' = \varepsilon \sigma T^4 \tag{6.4}$$

where $0 < \varepsilon < 1$.

The net rate radiant exchange, for the case of a heat transfer surface at temperature T_1 completely enclosed by a much larger surface maintained at temperature T_2, is obtained with (Holman 1986)

$$q_r'' = \varepsilon_1 \sigma \left(T_1^4 - T_2^4 \right) \tag{6.5}$$

This equation can be rewritten as

$$q_r'' = h_r \left(T_1 - T_2 \right) \tag{6.6}$$

where h_r is the radiation heat transfer coefficient that is defined by

$$h_r = \varepsilon_1 \sigma \left(T_1 + T_2\right)\left(T_1^2 + T_2^2\right) \tag{6.7}$$

Equation (6.6) is now analogous to the heat convection rate equation (6.2), which can be useful when convection and radiation occur in the same body surface.

6.2.2 **Heat conduction equation**

6.2.2.1 General remarks

In this section the heat conduction equation for the case of three-dimensional (3D) heat conduction analysis is directly derived by applying the conservation of energy principle to an infinitesimal control volume of a 3D body as represented in Figure 6.1.

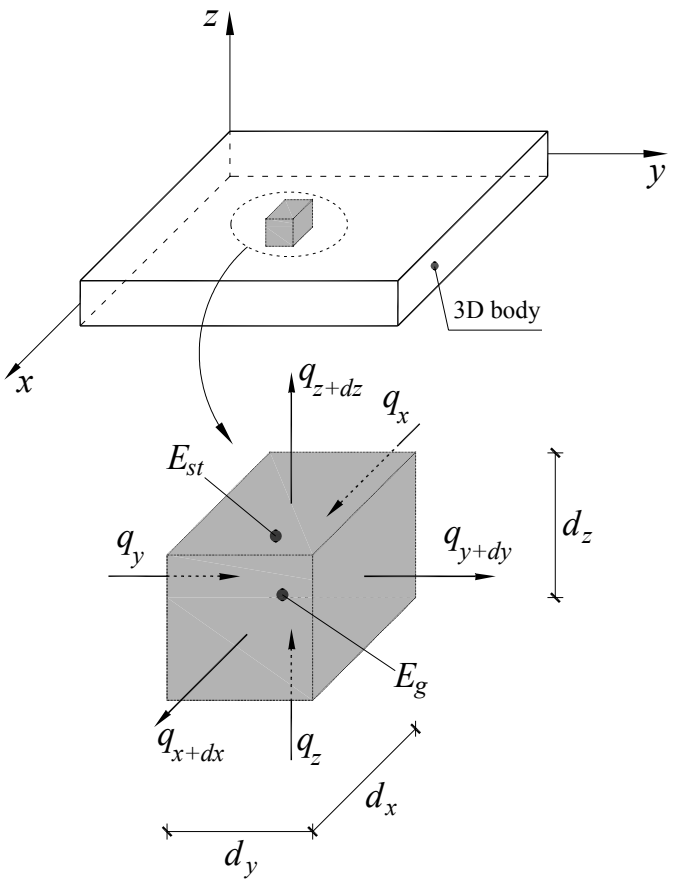

Figure 6.1 – Infinitesimal control volume of a 3D body.

The energy balance for the general case, represented in Figure 6.1, where the temperature may be changing with time and internal heat sources may be present, can be assured by (Incropera et al. 2006, Holman 1986)

$$\dot{E}_{in} + \dot{E}_g = \dot{E}_{st} + \dot{E}_{out} \tag{6.8}$$

being,

$\dot{E}_{in}$ the rate of energy conducted in the infinitesimal control volume, defined by

$$\dot{E}_{in} = q_x + q_y + q_z \tag{6.9}$$

$\dot{E}_g$ in equation (6.8) is the rate of thermal energy generation, given by

$$\dot{E}_g = \dot{Q}dxdydz \tag{6.10}$$

where $\dot{Q}$ is the internal heat generation rate per unit volume of the infinitesimal control volume,

$\dot{E}_{st}$ in equation (6.8) is the rate of the energy stored within the infinitesimal control volume, expressed as

$$\dot{E}_{st} = \rho c \frac{\partial T}{\partial t} dxdydz \tag{6.11}$$

where ρ is the mass per unit volume and c is the specific heat of the material. The ρc quantity represents the volumetric heat capacity and measures the capacity of a material to store thermal energy.

Finally, $\dot{E}_{out}$ in equation (6.8) is the rate of energy conducted out the infinitesimal control volume, defined by

$$\dot{E}_{out} = q_{x+dx} + q_{y+dy} + q_{z+dz} \tag{6.12}$$

By considering the first two terms of the Taylor series expansion, each term on the right-hand side of the previous equation becomes

$$q_{x+dx} = q_x + \frac{\partial q_x}{\partial x} dx \tag{6.13a}$$

$$q_{y+dy} = q_y + \frac{\partial q_y}{\partial y} dy \tag{6.13b}$$

$$q_{z+dz} = q_z + \frac{\partial q_z}{\partial z} dz \tag{6.13c}$$

Substituting equations (6.9) to (6.12) into equation (6.8), and considering equation (6.13), yields

$$\dot{Q} dx dy dz = \rho c \frac{\partial T}{\partial t} dx dy dz + \frac{\partial q_x}{\partial x} dx + \frac{\partial q_y}{\partial y} dy + \frac{\partial q_z}{\partial z} dz \tag{6.14}$$

From equation (6.1), it can be deducted that

$$q_x = -k_x dy dz \frac{\partial T}{\partial x}; \quad q_y = -k_y dx dz \frac{\partial T}{\partial y}; \quad q_z = -k_z dx dz \frac{\partial T}{\partial z} \tag{6.15}$$

Substituting (6.15) into (6.14) and making some arrangements, leads to the general three-dimensional heat conduction equation in Cartesian coordinates, as follows

$$\frac{\partial}{\partial x}\left(k_x \frac{\partial T}{\partial x}\right)+\frac{\partial}{\partial y}\left(k_y \frac{\partial T}{\partial y}\right)+\frac{\partial}{\partial z}\left(k_z \frac{\partial T}{\partial z}\right)+\dot{Q}=\rho c \frac{\partial T}{\partial t} \tag{6.16}$$

For the case of isotropic materials, the thermal conductivity is the same in all directions, i.e., $k_x = k_y = k_z = k$.

6.2.2.2 Initial and boundary conditions

To obtain the temperature distribution in a body, the heat conduction equation must be solved considering appropriated boundary conditions, and, for the case of time dependent temperature phenomena, the initial conditions must also be known.

The Dirichlet condition, or boundary condition of first order, is

$$T = \overline{T} \text{ on } S_T \tag{6.17}$$

where $\overline{T}$ is the prescribed temperature in the boundary, and S_T is the boundary surface where the temperature is imposed.

The Neumann conditions, or boundary conditions of second order, are the following

- Constant heat flux in the boundary:

$$q'' = -k\frac{\partial T}{\partial n} = \overline{q} \text{ on } S_q \tag{6.18}$$

where $\overline{q}$ is the heat flux imposed on the boundary, S_q is the boundary surface, and n is the direction vector normal to the boundary surface, defined by its direction cosines.

Therefore, equation (6.18) can be written as

$$q'' = -\left(k_x \frac{\partial T}{\partial x} n_x + k_y \frac{\partial T}{\partial y} n_y + k_z \frac{\partial T}{\partial z} n_z \right) = \overline{q} \text{ on } S_q \tag{6.19}$$

where n_x, n_y and n_y are the direction cosines of the normal to the S_q boundary surface.

- Insulated or adiabatic boundary:

$$q'' = -\left(k_x \frac{\partial T}{\partial x} n_x + k_y \frac{\partial T}{\partial y} n_y + k_z \frac{\partial T}{\partial z} n_z \right) = 0 \text{ on } S_q \tag{6.20}$$

The convection condition on the boundary surface is

$$q'' = -\left(k_x \frac{\partial T}{\partial x} n_x + k_y \frac{\partial T}{\partial y} n_y + k_z \frac{\partial T}{\partial z} n_z \right) = h_c \left(T - T_\infty \right) \text{ on } S_c \tag{6.21}$$

being h_c the convection heat transfer coefficient and $\left(T - T_\infty \right)$ the temperature difference between the surface and the fluid (e.g. the environment temperature).

The radiation heat transfer can be taken into account by substituting the convection heat transfer coefficient by an appropriate convection-radiation heat transfer coefficient, h_{cr}, (Silveira 1993, Azenha 2009).

For the case of a transient analysis the initial conditions must be known a priori. Thus, for a specific time t_0 the temperatures, T, of the entire 3D body must be supplied. This condition can be defined by

$$T = T_{init} \tag{6.22}$$

being T_{init} the initial temperature imposed to the 3D body at time t_0.

6.2.3 **Finite element method applied to heat transfer**

By applying the method of weighted residuals to the heat conduction equation (6.16)

$$\int_V wrdV = 0 \tag{6.23}$$

where the residual function is defined by

$$r = \frac{\partial}{\partial x}\left(k_x \frac{\partial T}{\partial x}\right) + \frac{\partial}{\partial y}\left(k_y \frac{\partial T}{\partial y}\right) + \frac{\partial}{\partial z}\left(k_z \frac{\partial T}{\partial z}\right) + \dot{Q} - \rho c \frac{\partial T}{\partial t} \tag{6.24}$$

and w is the weight function $w(x, y, x)$, yields

$$\begin{aligned} &\int_V w\left[\frac{\partial}{\partial x}\left(k_x \frac{\partial T}{\partial x}\right) + \frac{\partial}{\partial y}\left(k_y \frac{\partial T}{\partial y}\right) + \frac{\partial}{\partial z}\left(k_z \frac{\partial T}{\partial z}\right)\right] dV \\ &+ \int_V w\,\dot{Q} dV - \int_V w\rho c \frac{\partial T}{\partial t} dV = 0 \end{aligned} \tag{6.25}$$

By performing an integration by parts of the first term of equation (6.25) using the Green-Gauss theorem (Ottosen and Petersson 1992), results in

$$\begin{aligned} &\int_V w\left[\frac{\partial}{\partial x}\left(k_x \frac{\partial T}{\partial x}\right) + \frac{\partial}{\partial y}\left(k_y \frac{\partial T}{\partial y}\right) + \frac{\partial}{\partial z}\left(k_z \frac{\partial T}{\partial z}\right)\right] dV = \\ &-\int_V \left[\frac{\partial w}{\partial x} k_x \frac{\partial T}{\partial x} + \frac{\partial w}{\partial y} k_y \frac{\partial T}{\partial y} + \frac{\partial w}{\partial z} k_z \frac{\partial T}{\partial z}\right] dV \\ &+ \int_S w\left(k_x \frac{\partial T}{\partial x} n_x + k_y \frac{\partial T}{\partial y} n_y + k_z \frac{\partial T}{\partial z} n_z\right) dS \end{aligned} \tag{6.26}$$

Introducing the boundary conditions described in section 6.2.2.2 in the second integral of (6.26) yields

$$\begin{aligned}&\int_S w\left(k_x\frac{\partial T}{\partial x}n_x+k_y\frac{\partial T}{\partial y}n_y+k_z\frac{\partial T}{\partial z}n_z\right)dS\\&=\int_{S_T} w\left(-q_T\right)dS_T+\int_{S_q} w\left(-\bar{q}\right)dS_q+\int_{S_c} w\left[-h_c\left(T-T_\infty\right)\right]dS_c\end{aligned}\tag{6.27}$$

In this equation q_T is the unknown heat flux on the boundary where the temperature is prescribed, $\bar{q}$ is the imposed boundary heat flux (when $\bar{q}=0$ an insulated or adiabatic boundary is assumed), and $h_c\left(T-T_\infty\right)$ is the boundary convection heat flux (by substituting h_c with h_{cr}, convection-radiation heat transfer can be taken into account).

By considering (6.26) and (6.27), equation (6.25) becomes

$$\begin{aligned}&\int_V\left[\frac{\partial w}{\partial x}k_x\frac{\partial T}{\partial x}+\frac{\partial w}{\partial y}k_y\frac{\partial T}{\partial y}+\frac{\partial w}{\partial z}k_z\frac{\partial T}{\partial z}\right]dV+\int_{S_c} wh_cTdS_c+\int_V w\rho c\frac{\partial T}{\partial t}dV\\&=\int_V w\dot{Q}dV-\int_{S_T} w\left(q_T\right)dS_T-\int_{S_q} w\left(\bar{q}\right)dS_q+\int_{S_c} wh_cT_\infty dS_c\end{aligned}\tag{6.28}$$

The first integral of (6.28) can be written as

$$\int_V\left(\nabla w\right)^T\underline{D}\,\nabla T\,dV\tag{6.29}$$

where

$$\underline{D}=\begin{bmatrix}k_x&0&0\\0&k_y&0\\0&0&k_z\end{bmatrix}\tag{6.30}$$

The temperatures can be approximated using shape functions as follows

$$T=T\left(x,y,z,t\right)=\sum_{i=1}^{n}N_i\left(x,y,z\right)T_i\left(t\right)\tag{6.31}$$

where n is the number of nodes of the element, N_i is the shape function of element node i and T_i is the temperature of element node i. In a transient analysis this temperature field is a function of time.

In matrix form equation (6.31) can be written as

$$T = \underline{N}\underline{T}^e \tag{6.32}$$

being

$$\underline{N} = \begin{bmatrix} N_1 & N_2 & \dots & N_n \end{bmatrix} \tag{6.33}$$

and

$$\underline{T}^e = \begin{bmatrix} T_1 & T_2 & \dots & T_n \end{bmatrix}^T \tag{6.34}$$

By using the Galerkin method, the weight functions, w, are chosen to coincide with the functions that define the unknown variables (temperatures). In the present case these functions are the shape functions, N. Thus, equation (6.28) can be written for a specific finite element, considering (6.32) and (6.29), as

$$\begin{aligned} &\int_V \left(\nabla \underline{N}\right)^T \underline{D}\, \nabla \underline{N}\underline{T}^e dV + \int_{S_c} \underline{N}^T h_c \underline{N}\underline{T}^e dS_c + \int_V \underline{N}^T \rho c \frac{\partial\left(\underline{N}\underline{T}^e\right)}{\partial t} dV \\ &= \int_V \underline{N}^T \dot{Q} dV - \int_{S_T} \underline{N}^T \left(q_T\right) dS_T - \int_{S_q} \underline{N}^T \left(\overline{q}\right) dS_q + \int_{S_c} \underline{N}^T h_c T_\infty dS_c \end{aligned} \tag{6.35}$$

or

$$\left(\underline{K}_c^e + \underline{K}_{conv}^e\right)\underline{T}^e + \underline{K}_t^e \dot{\underline{T}}^e = \underline{F}^e \tag{6.36}$$

where $\underline{K}_c^e$ is the element conduction matrix defined by

$$\underline{K}_c^e = \int_V \left(\nabla \underline{N}\right)^T \underline{D}\, \nabla \underline{N} dV = \int_V \underline{B}^T \underline{D}\underline{B} dV \tag{6.37}$$

being

$$\underline{B} = \begin{bmatrix} \dfrac{\partial N_1}{\partial x} & \dfrac{\partial N_2}{\partial x} & \cdots & \dfrac{\partial N_n}{\partial x} \\ \dfrac{\partial N_1}{\partial y} & \dfrac{\partial N_2}{\partial y} & \cdots & \dfrac{\partial N_n}{\partial y} \\ \dfrac{\partial N_1}{\partial z} & \dfrac{\partial N_2}{\partial z} & \cdots & \dfrac{\partial N_n}{\partial z} \end{bmatrix} \tag{6.38}$$

$\underline{K}_{conv}^e$ is the element convection matrix

$$\underline{K}_{conv}^e = \int_{S_c} h_c \underline{N}^T \underline{N} dS_c \tag{6.39}$$

and $\underline{K}_t^e$ is the element transient matrix

$$\underline{K}_t^e = \int_V \rho c \underline{N}^T \underline{N} dV \tag{6.40}$$

The vector $\underline{F}^e$ can be divided into

$$\underline{F}^e = \underline{F}_L^e + \underline{F}_{q_T}^e \tag{6.41}$$

where $\underline{F}_L^e$ is defined by

$$\underline{F}_L^e = \underline{F}_{\dot{Q}}^e + \underline{F}_{\bar{q}}^e + \underline{F}_c^e \tag{6.42}$$

being $\underline{F}_{\dot{Q}}^e$ the vector corresponding to the element internal heat generation,

$$\underline{F}_{\dot{Q}}^{e} = \int_{V} \underline{N}^{T} \dot{Q} dV \tag{6.43}$$

$\underline{F}_{\bar{q}}^{e}$ is the vector corresponding to the boundary where the heat flux is imposed,

$$\underline{F}_{\bar{q}}^{e} = -\int_{S_q} \underline{N}^{T} \left(\bar{q}\right) dS_q \tag{6.44}$$

and $\underline{F}_{c}^{e}$ is the vector containing the values corresponding to the convection (or convection-radiation) boundary

$$\underline{F}_{c}^{e} = \int_{S_c} \underline{N}^{T} h_c T_\infty dS_c \tag{6.45}$$

In equation (6.41) $\underline{F}_{q_T}^{e}$ is the vector corresponding to the heat flux where the temperature is prescribed,

$$\underline{F}_{q_T}^{e} = -\int_{S_T} \underline{N}^{T} \left(q_T\right) dS_T \tag{6.46}$$

By considering a domain discretized into several finite elements, equation (6.36) is written in a global form as

$$\left(\underline{K}_c + \underline{K}_{conv}\right)\underline{T} + \underline{K}_t \dot{\underline{T}} = \underline{F} \tag{6.47}$$

In this equation the matrices and vectors take into account the contribution of each finite element of the domain.

6.2.4 **Steady-state linear analysis**

In this section the implementation of the heat conduction problem in the FEMIX computer code, for the case of a steady-state linear analysis, is presented. The performance and the accuracy of this implementation are appraised by performing a numerical simulation.

In a steady-state linear analysis equation (6.47) becomes

$$\left(\underline{K}_c + \underline{K}_{conv}\right)\underline{T} = \underline{F} \tag{6.48}$$

By taking into account (6.41), and considering $\underline{K} = \underline{K}_c + \underline{K}_{conv}$, results in

$$\underline{K}\,\underline{T} = \underline{F}_L + \underline{F}_{q_T} \tag{6.49}$$

For its solution equation (6.49) is written as

$$\begin{bmatrix} \underline{K}_{FF} & \underline{K}_{FP} \\ \underline{K}_{PF} & \underline{K}_{PP} \end{bmatrix} \begin{bmatrix} \underline{T}_F \\ \underline{T}_P \end{bmatrix} = \begin{bmatrix} \underline{F}_{L,F} \\ \underline{F}_{L,P} \end{bmatrix} + \begin{bmatrix} \underline{0} \\ \underline{F}_{q_T,P} \end{bmatrix} \tag{6.50}$$

where the subscript F (free) corresponds to the nodes of the domain where the temperature is not known, and the subscript P (prescribed) corresponds to the nodes of the domain where the temperature is prescribed.

In a first phase the temperatures are obtained by solving the following system of equations, using the Gauss elimination method

$$\underline{K}_{FF}\,\underline{T}_F = \underline{F}_{L,F} - \underline{K}_{FP}\,\underline{T}_P \tag{6.51}$$

and in a second phase, with the obtained temperatures, $\underline{T}_F$, the heat flux where the temperature is prescribed is calculated with

$$\underline{F}_{q_T,P} = \underline{K}_{PF}\underline{T}_F + \underline{K}_{PP}\underline{T}_P - \underline{F}_{L,P} \tag{6.52}$$

6.2.4.1 Numerical example

The performance of the model is appraised using an example from Lewis et al. (2004), as shown in Figure 6.2.

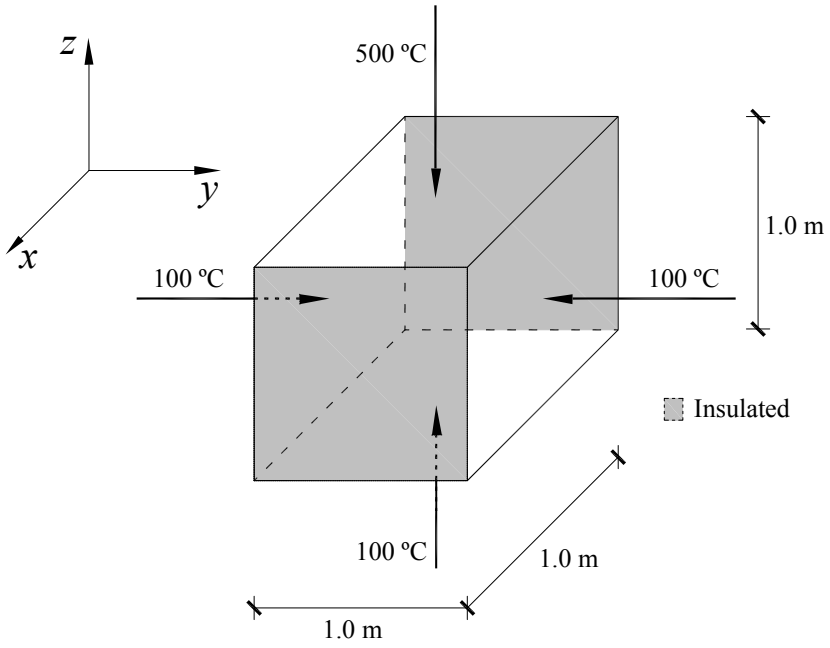

Figure 6.2 – Steady-state example (adapted from Lewis et al. 2004).

For the numerical analysis the domain is descritized with serendipity 8 node solid elements with a 3×3×3 Gauss-Legendre integration scheme. The thermal conductivity of the material, k, is constant and is equal to 10 $Wm^{-1}ºC^{-1}$.

Figure 6.3 represents the mesh and temperature field after the steady-state analysis. The temperature in the center of the cube (0.5, 0.5, 0.5) is 200.37ºC. Similar results were obtained by Lewis et al. (2004).

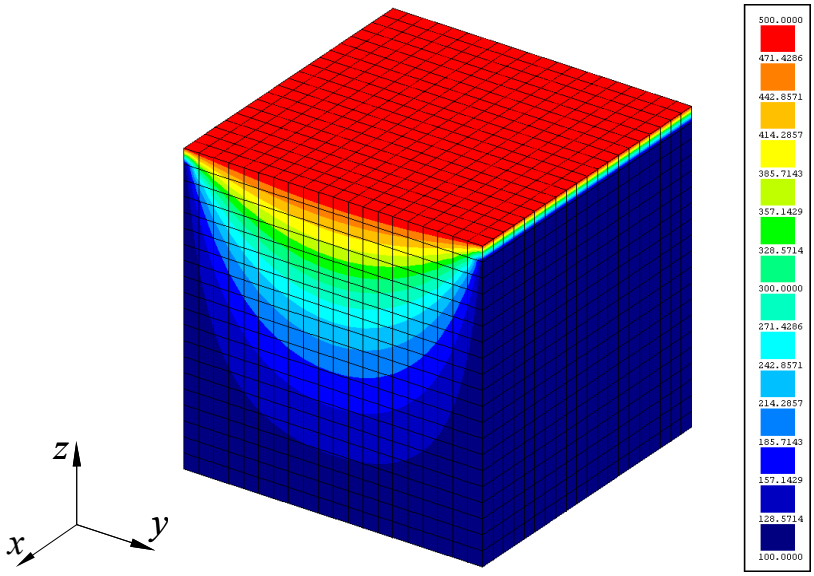

Figure 6.3 – Finite element mesh and temperature field.

6.2.5 **Transient linear analysis**

6.2.5.1 Time-discretization

Figure 6.4 represents the temperature variation with time for a one dimensional problem. In the incremental time step, Δt, a linear variation of the temperature is assumed. Thus, the derivative of temperature is approximated with

$$\dot{T}_n = \frac{\partial T_n}{\partial t} \approx \frac{T_{n+1} - T_n}{\Delta t} \tag{6.53}$$

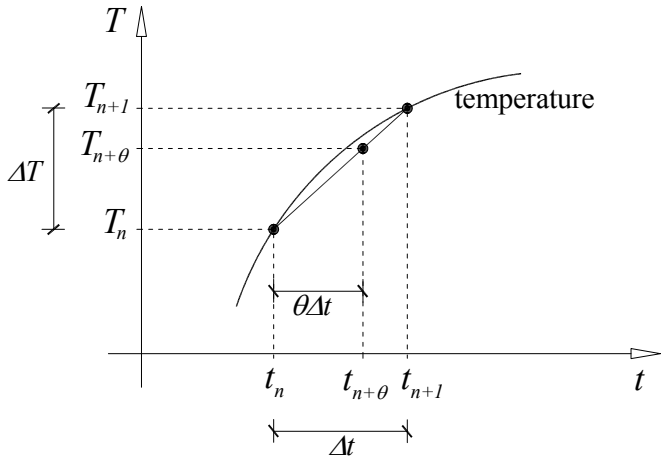

Figure 6.4 – Time-discretization for one dimensional problem.

Considering a multi-dimensional problem, the temperature at the time $t_{n+\theta}$ is calculated with

$$\underline{T}_{n+\theta} = \underline{T}_n + \theta\Delta t\left(\frac{\underline{T}_{n+1} - \underline{T}_n}{\Delta t}\right) = \theta\underline{T}_{n+1} + \left(1-\theta\right)\underline{T}_n \tag{6.54}$$

and its derivative with (see Figure 6.4)

$$\dot{\underline{T}}_{n+\theta} = \frac{\underline{T}_{n+\theta} - \underline{T}_n}{\theta\Delta t} = \frac{\underline{T}_{n+1} - \underline{T}_n}{\Delta t} \tag{6.55}$$

Writing equation (6.47) for the time $t_{n+\theta}$ results in

$$\left(\underline{K}_c + \underline{K}_{conv}\right)\underline{T}_{n+\theta} + \underline{K}_t\dot{\underline{T}}_{n+\theta} = \underline{F}_{n+\theta} \tag{6.56}$$

and by substituting (6.54) and (6.55) yields

$$\left(\underline{K}_c + \underline{K}_{conv}\right)\left[\theta\underline{T}_{n+1} + \left(1-\theta\right)\underline{T}_n\right] + \underline{K}_t\left(\frac{\underline{T}_{n+1} - \underline{T}_n}{\Delta t}\right) = \underline{F}_{n+\theta} \tag{6.57}$$

Considering for vector $\underline{F}_{n+\theta}$ the same type of approximation that is adopted for the temperature, equation (6.57) can be written as

$$\left(\underline{K}_c + \underline{K}_{conv}\right)\left[\theta\underline{T}_{n+1} + \left(1-\theta\right)\underline{T}_n\right] + \underline{K}_t\left(\frac{\underline{T}_{n+1} - \underline{T}_n}{\Delta t}\right) = \left[\theta\underline{F}_{n+1} + \left(1-\theta\right)\underline{F}_n\right] \tag{6.58}$$

or

$$\begin{aligned}&\left[\underline{K}_t+\theta\Delta t\left(\underline{K}_c+\underline{K}_{conv}\right)\right]\underline{T}_{n+1}\\&=\left[\underline{K}_t-\left(1-\theta\right)\Delta t\left(\underline{K}_c+\underline{K}_{conv}\right)\right]\underline{T}_n+\Delta t\left[\theta\underline{F}_{n+1}+\left(1-\theta\right)\underline{F}_n\right]\end{aligned} \tag{6.59}$$

By adopting different values for θ several time-stepping schemes can be obtained (Vila Real 1988, Lewis et al. 1996, Fonseca 1998, Lewis et al. 2004), and equation (6.59) can take the following formats:

Forward-Euler $\left(\theta=0\right)$

$$\underline{K}_t\underline{T}_{n+1}=\left[\underline{K}_t-\Delta t\left(\underline{K}_c+\underline{K}_{conv}\right)\right]\underline{T}_n+\Delta t\underline{F}_n \tag{6.60}$$

Backward-Euler $\left(\theta=1\right)$

$$\left[\underline{K}_t+\Delta t\left(\underline{K}_c+\underline{K}_{conv}\right)\right]\underline{T}_{n+1}=\underline{K}_t\underline{T}_n+\Delta t\underline{F}_{n+1} \tag{6.61}$$

Crank-Nicolson $\left(\theta=\frac{1}{2}\right)$

$$\left[\underline{K}_t+\frac{1}{2}\Delta t\left(\underline{K}_c+\underline{K}_{conv}\right)\right]\underline{T}_{n+1}=\left[\underline{K}_t-\frac{1}{2}\Delta t\left(\underline{K}_c+\underline{K}_{conv}\right)\right]\underline{T}_n+\frac{1}{2}\Delta t\left(\underline{F}_{n+1}+\underline{F}_n\right) \tag{6.62}$$

Galerkin $\left(\theta=\frac{2}{3}\right)$

$$\left[\underline{K}_t+\frac{2}{3}\Delta t\left(\underline{K}_c+\underline{K}_{conv}\right)\right]\underline{T}_{n+1}=\left[\underline{K}_t-\frac{1}{3}\Delta t\left(\underline{K}_c+\underline{K}_{conv}\right)\right]\underline{T}_n+\Delta t\left(\frac{2}{3}\underline{F}_{n+1}+\frac{1}{3}\underline{F}_n\right) \tag{6.63}$$

If $\theta\neq 0$ the time-stepping schemes are called implicit, and if $\theta=0$ the time-stepping scheme is called explicit. It is demonstrated in Lewis et al. (1996) that for $1/2\leq\theta\leq 1$ the

solution is unconditionally stable, and when $0 \le \theta < 1/2$ the solution is conditionally stable and the time step must be limited, such is the case of the *Forward-Euler* scheme. It is also concluded that the *Galerkin* time-stepping scheme leads to less oscillatory errors than the *Crank-Nicolson* time-stepping scheme, although this last one provides a higher accuracy (Zienkiewicz 2000a).

6.2.5.2 Computational strategies

The implementation of the heat conduction problem in the FEMIX computer code for the case of the transient linear analysis is presented in this section.

Considering the domain discretized into several finite elements and writing (6.59) in order to group the nodes where the temperature is unknown, subscript F (free), and in nodes where the temperature is prescribed, subscript P (prescribed), results in

$$\underline{E}_{n+1}\underline{T}_{n+1} = \underline{\overline{F}}_{n+1} \tag{6.64}$$

being

$$\underline{E}_{n+1} = \begin{bmatrix} \underline{K}_{t,FF} + \theta\Delta t\left(\underline{K}_{c,FF} + \underline{K}_{conv,FF}\right) & \underline{K}_{t,FP} + \theta\Delta t\left(\underline{K}_{c,FP} + \underline{K}_{conv,FP}\right) \\ \underline{K}_{t,PF} + \theta\Delta t\left(\underline{K}_{c,PF} + \underline{K}_{conv,PF}\right) & \underline{K}_{t,PP} + \theta\Delta t\left(\underline{K}_{c,PP} + \underline{K}_{conv,PP}\right) \end{bmatrix} \tag{6.65}$$

$$\underline{T}_{n+1} = \begin{bmatrix} \underline{T}_{n+1,F} \\ \underline{T}_{n+1,P} \end{bmatrix} \tag{6.66}$$

$$\begin{aligned} \underline{\overline{F}}_{n+1} = & \begin{bmatrix} \underline{K}_{t,FF} - (1-\theta)\Delta t\left(\underline{K}_{c,FF} + \underline{K}_{conv,FF}\right) & \underline{K}_{t,FP} - (1-\theta)\Delta t\left(\underline{K}_{c,FP} + \underline{K}_{conv,FP}\right) \\ \underline{K}_{t,PF} - (1-\theta)\Delta t\left(\underline{K}_{c,PF} + \underline{K}_{conv,PF}\right) & \underline{K}_{t,PP} - (1-\theta)\Delta t\left(\underline{K}_{c,PP} + \underline{K}_{conv,PP}\right) \end{bmatrix} \\ & \times \begin{bmatrix} \underline{T}_{n,F} \\ \underline{T}_{n,P} \end{bmatrix} + \begin{bmatrix} \Delta t\theta\underline{F}_{L,n+1,F} + \Delta t(1-\theta)\underline{F}_{L,n,F} \\ \Delta t\theta\underline{F}_{L,n+1,P} + \Delta t(1-\theta)\underline{F}_{L,n,P} \end{bmatrix} \\ & + \begin{bmatrix} \underline{0} \\ \Delta t\theta\underline{F}_{q_T,n+1,P} + \Delta t(1-\theta)\underline{F}_{q_T,n,P} \end{bmatrix} \end{aligned} \tag{6.67}$$

For the current time step, temperatures $\underline{T}_{n+1,F}$ are obtained by solving the following system of equations using the Gauss elimination method

$$\underline{E}_{n+1,FF}\underline{T}_{n+1,F} = \underline{\underline{\bar{F}}}_{n+1,F} \tag{6.68}$$

where $\underline{E}_{n+1,FF}$ is the free effective thermal transient matrix defined by

$$\underline{E}_{n+1,FF} = \underline{K}_{t,FF} + \theta\Delta t\left(\underline{K}_{c,FF} + \underline{K}_{conv,FF}\right) \tag{6.69}$$

and the $\underline{\underline{\bar{F}}}_{n+1,F}$ is the free load vector for the current time step defined by

$$\begin{aligned}\underline{\underline{\bar{F}}}_{n+1,F} = &\left[\underline{K}_{t,FF} - (1-\theta)\Delta t\left(\underline{K}_{c,FF} + \underline{K}_{conv,FF}\right)\right]\underline{T}_{n,F} \\ &+\underline{K}_{t,FP}\left(\underline{T}_{n,P} - \underline{T}_{n+1,P}\right) + \left(\underline{K}_{c,FP} + \underline{K}_{conv,FP}\right)\left[-(1-\theta)\Delta t\underline{T}_{n,P} - \theta\Delta t\underline{T}_{n+1,P}\right] \\ &+\left[\Delta t\theta\underline{F}_{L,n+1,F} + \Delta t(1-\theta)\underline{F}_{L,n,F}\right]\end{aligned} \tag{6.70}$$

For $\theta \neq 0$ the heat flux where the temperature is prescribed is calculated with

$$\begin{aligned}\underline{F}_{q_T,n+1,P} = &\underline{K}_{t,PF}\left(\frac{1}{\theta\Delta t}\underline{T}_{n+1,F} - \frac{1}{\theta\Delta t}\underline{T}_{n,F}\right) + \left(\underline{K}_{c,PF} + \underline{K}_{conv,PF}\right)\left[\underline{T}_{n+1,F} + \frac{(1-\theta)}{\theta}\underline{T}_{n,F}\right] \\ &+\underline{K}_{t,PP}\left(\frac{1}{\theta\Delta t}\underline{T}_{n+1,P} - \frac{1}{\theta\Delta t}\underline{T}_{n,P}\right) \\ &+\left(\underline{K}_{c,PP} + \underline{K}_{conv,PP}\right)\left[\underline{T}_{n+1,P} + \frac{(1-\theta)}{\theta}\underline{T}_{n,P}\right] \\ &+\left[-\underline{F}_{L,n+1,P} - \frac{(1-\theta)}{\theta}\underline{F}_{L,n,P}\right] + \left[-\frac{(1-\theta)}{\theta}\underline{F}_{q_T,n,P}\right]\end{aligned} \tag{6.71}$$

6.2.5.3 Numerical examples

To validate the implemented transient heat conduction model two numerical simulations have been performed, being the corresponding results presented below. The first simulation is a transient analysis based on the problem shown in Figure 6.2. The same element mesh and material properties are used. The initial temperature is set to 0ºC and a Crank-Nicolson scheme is used. The evolution of temperature with time at the center point (0.5, 0.5, 0.5) is plotted in Figure 6.5. It is verified that the temperature increases rapidly until a steady-state is reached. The temperature field at different times is represented in Figure 6.6, in the *yz* plane (see Figure 6.2).

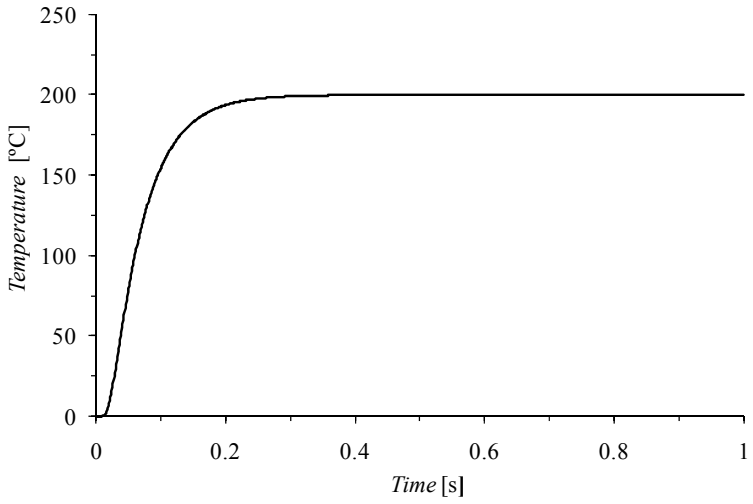

Figure 6.5 – Temperature vs. time at point (0.5, 0.5, 0.5).

The second example for model appraisal is a bi-dimensional transient analysis proposed by Zhou and Vecchio (2005). In the present case a three-dimensional representation of the domain is performed, being represented in Figure 6.7. The domain is discretized with 8-noded hexahedral elements, and a 2×2×2 Gauss-Legendre integration scheme is used. The conductivity of the material is constant and equal to 52 $Jm^{-1}s^{-1}K^{-1}$, the specific heat is 460.0 $Jkg^{-1}K^{-1}$, and the density is 7850 kg/m^3. The initial temperature is set to 0ºC and a Crank-Nicolson scheme is used. The temperature field at different instants is represented in Figure 6.8.

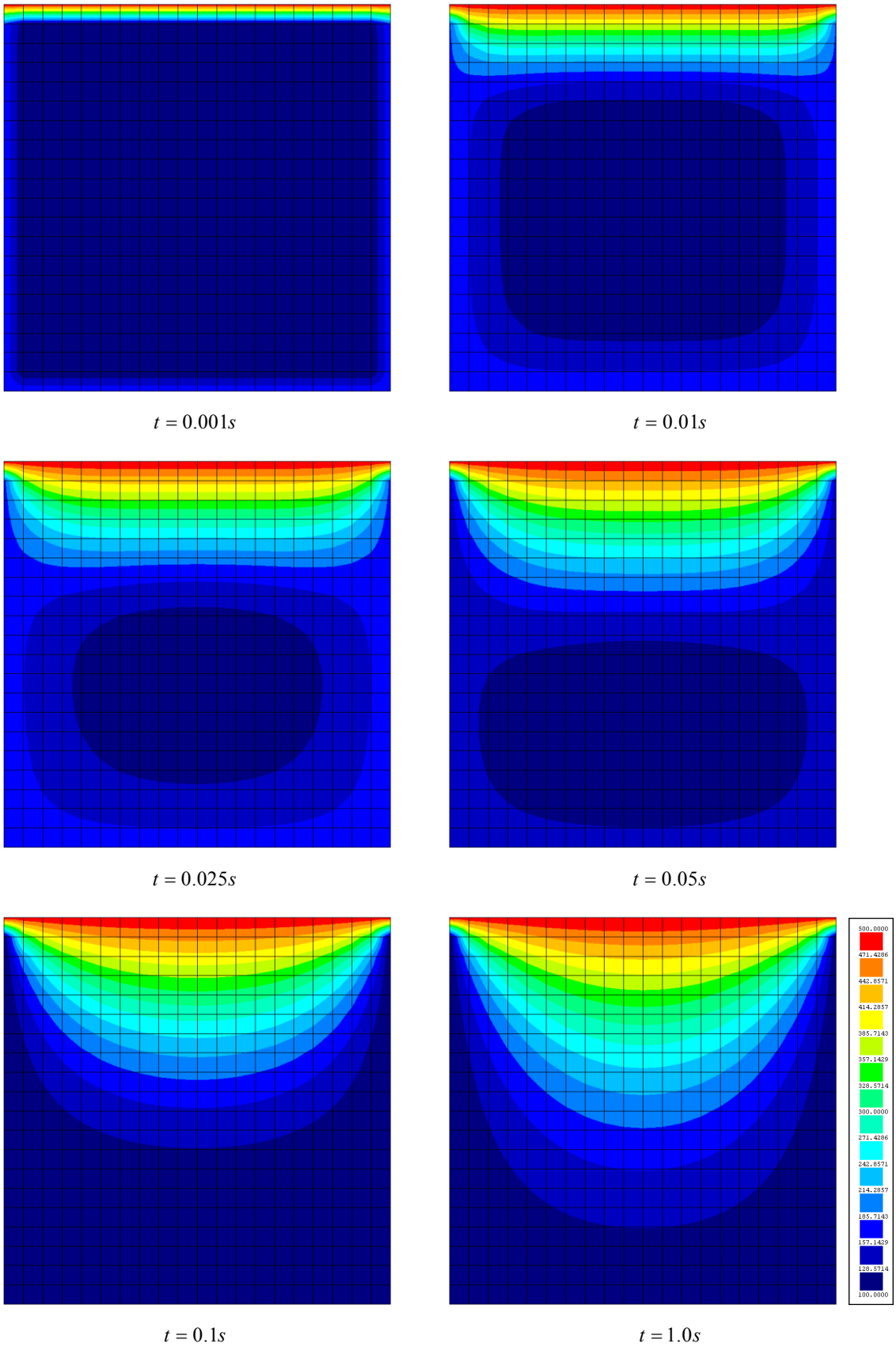

Figure 6.6 – Finite element mesh and temperature field for different instants of the transient analysis.

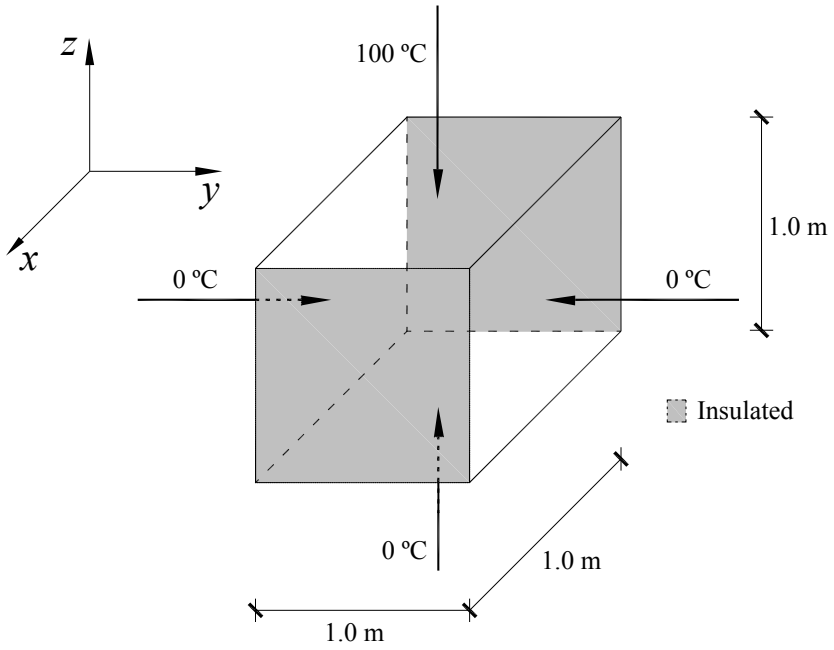

Figure 6.7 – Transient analysis – domain and temperature distribution.

Figure 6.9 represents the evolution of temperature through the depth of the cross section at the center line of the cube. It is verified that as time evolves the curves gradually tend to the steady-state response. Similar results were obtained by Zhou and Vecchio (2005) for the bi-dimensional analysis of the problem, and a comparison for different instants of the transient analysis is represented in Figure 6.10. The differences between the two types of analyses decrease with time, but even for the first instants the discrepancy is quite acceptable taking into account that the analyses have been performed assuming a 2D and a 3D discretization of the body.

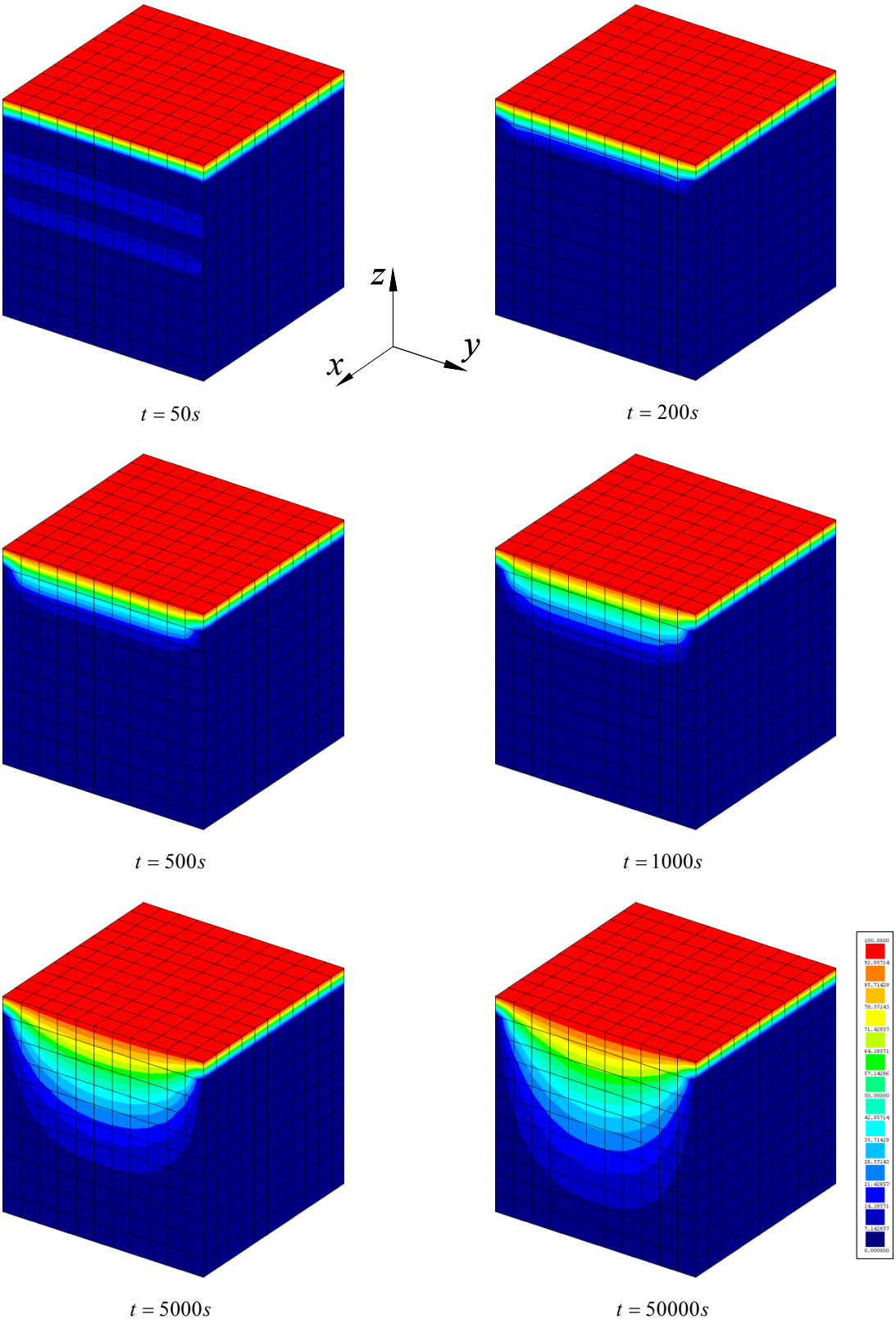

Figure 6.8 – Finite element mesh of the domain shown in Figure 6.7 and temperature field for different instants of the transient analysis.

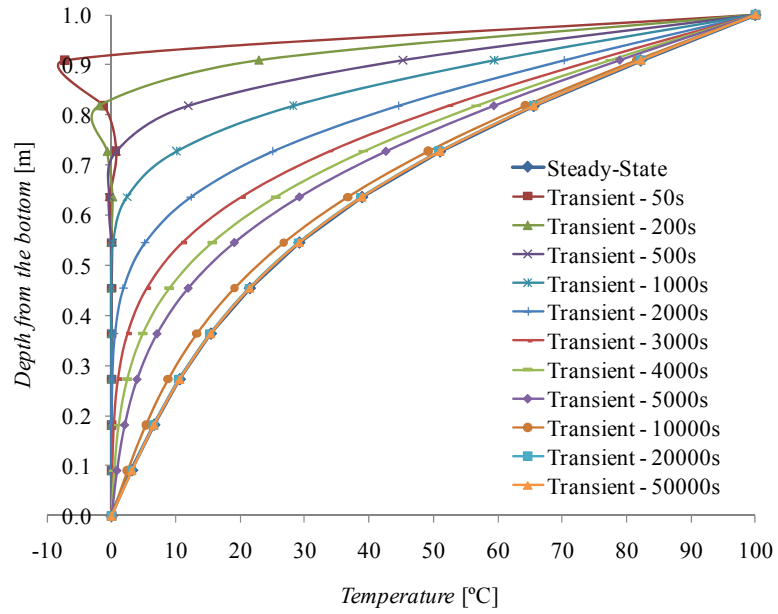

Figure 6.9 – Temperature variation through the depth of the cross section at the center line.

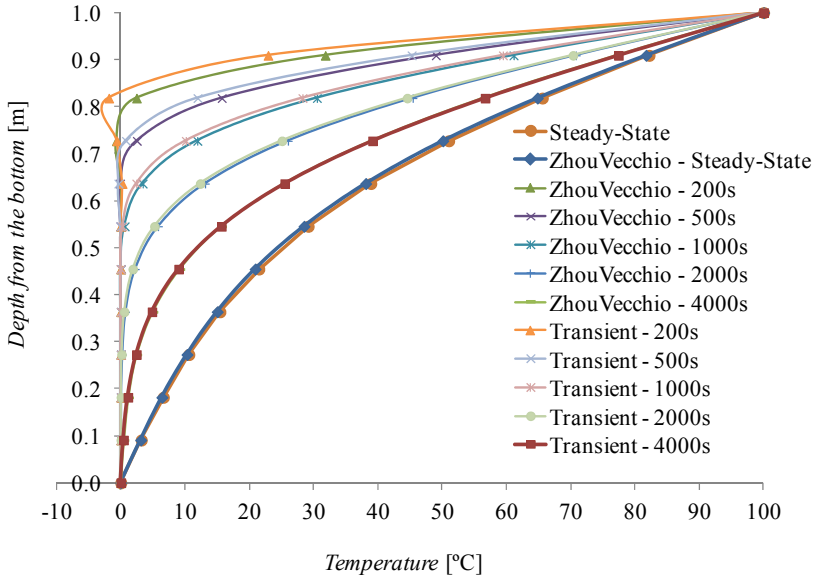

Figure 6.10 – Temperature variation through the depth of the cross section at the center line – comparison with the data from Zhou and Vecchio (2005).

6.2.6 **Transient nonlinear analysis**

In the presence of early age heat development, the heat generation rate of cement based materials can be obtained with the mathematical formulation proposed by Reinhardt et al. (1982) and based on the Arrhenius type relation, being defined by equation (6.72) (Azenha 2009).

$$\dot{Q} = f\left(\alpha_T\right) A_T e^{-\frac{E_a}{R(273.15+T)}} \tag{6.72}$$

In this equation $\dot{Q}$ is the heat generation rate to be introduced in equation (6.43), $f\left(\alpha_T\right)$ is the normalized heat generation rate directly obtained through experiments (de Borst and van den Boogaard 1984, Azenha 2009), A_T is a rate constant, E_a (Jmol^{-1}) is the apparent activation energy that depends on the type of cement, R is the universal gas constant (8.314 Jmol^{-1}K^{-1}), and T is the temperature in ºC. In this case the second member of equation (6.64) depends on the temperature and, for that reason, an iterative process is required at each time step to solve the nonlinear system of equations. The Newton-Raphson method is used for this iterative process.

For the current time step $n+1$, the equation of the unbalanced heat fluxes can be defined by

$$\underline{\Psi}\left(\underline{T}_{n+1}\right) = \underline{\bar{F}}_{n+1} - \underline{E}_{n+1}\underline{T}_{n+1} \tag{6.73}$$

being $\underline{\bar{F}}_{n+1}$ and $\underline{E}_{n+1}$ defined by equation (6.67) and equation (6.65), respectively. For the current time step $n+1$, it is intended that the vector $\underline{\Psi}\left(\underline{T}_{n+1}\right)$ is null, i.e.,

$$\underline{\Psi}\left(\underline{T}_{n+1}\right) = \underline{0} \tag{6.74}$$

Equation (6.74) can be solved by applying the Newton-Raphson method. Considering the first two terms of the Taylor series expansion, equation (6.74) can be approximated as

$$\underline{\Psi}\left(\underline{T}_{n+1}^{q}\right) \approx \underline{\Psi}\left(\underline{T}_{n+1}^{q-1}\right) + \left(\frac{\partial \underline{\Psi}}{\partial \underline{T}}\right)_{n+1}^{q-1} \delta \underline{T}_{n+1}^{q} = \underline{0} \tag{6.75}$$

where the subscript q is the iteration counter. In equation (6.75)

$$\left(\frac{\partial \underline{\Psi}}{\partial \underline{T}}\right)_{n+1}^{q-1} = -\left(\frac{\partial\left(\underline{\bar{F}} - \underline{ET}\right)}{\partial \underline{T}}\right)_{n+1}^{q-1} = -\left(\underline{E}_{T}\right)_{n+1}^{q-1} \tag{6.76}$$

is the Jacobian matrix. For simplification, the term $\partial \underline{\bar{F}}_{n+1}^{q-1} / \partial \underline{T}_{n+1}^{q-1}$ is dropped in the present formulation, being the Jacobian matrix equal to the effective tangential matrix, $\underline{E}_{T}$ of the $q-1$ iteration of the current time step, $n+1$. Substituting (6.76) into (6.75) yields

$$\left(\underline{E}_{T}\right)_{n+1}^{q-1} \delta \underline{T}_{n+1}^{q} = \underline{\Psi}\left(\underline{T}_{n+1}^{q-1}\right) \tag{6.77}$$

An iterative procedure is executed up to the solution of equation (6.74), and in each iteration the vector of the temperatures is updated as follows

$$\underline{T}_{n+1}^{q} = T_{n+1}^{q-1} + \delta \underline{T}_{n+1}^{q} = \underline{T}_{n} + \Delta \underline{T}_{n+1}^{q} \tag{6.78}$$

with

$$\Delta \underline{T}_{n+1}^{q} = \sum_{i=1}^{q} \delta \underline{T}_{n+1}^{i} = \Delta \underline{T}_{n+1}^{q-1} + \delta \underline{T}_{n+1}^{q} \tag{6.79}$$

being $\underline{T}_{n+1}^{0} = \underline{T}_{n}$ and $\Delta \underline{T}_{n+1}^{0} = \underline{0}$ at the beginning of the iterative process.

The normalized heat generation rate $f(\alpha_T)$ is obtained directly from experiments, and is a function of the degree of heat development α_T. This parameter describes the relative amount of heat generation due to the cement hydration (Ferreira et al. 2008, Azenha 2009)

$$\alpha_T = \frac{Q(t)}{Q_{total}} \tag{6.80}$$

where $Q(t)$ is the accumulated heat generated until a certain instant t, and Q_{total} is the final accumulated heat of the cement (or binder) hydration. An initial value for the degree of heat development $\alpha_{T,init}$ is necessary to numerically activate the nonlinear transient analysis due to early age heat development.

6.2.6.1 Numerical examples

An experimental program has been executed by Azenha (2009) with a concrete cube of 40 cm edge length. The cube was monitored with temperature sensors placed at several points within the cube. A thermography camera has also been used to obtain the temperature field (thermography pictures) during the hardening of concrete. Figure 6.11 represents schematically the geometry and the boundary conditions of the cube. Only one face is in contact with the environment, while in the others a wooden formwork separates the concrete from the environment.

The value of the heat transfer coefficient assigned to the face that is in contact with the environment is 10.0 $Wm^{-2}K^{-1}$, and for the other faces an equivalent heat transfer coefficient, h_{eq}, is used to account for the wooden formwork. The value is obtained with the electrical analogy (Holman 1986, Incropera et al. 2006, Azenha 2004)

$$h_{eq} = \left[\frac{1}{h_{cr}} + \sum_{i=1}^{n} \frac{L_i}{k_i} \right]^{-1} \tag{6.81}$$

being L_i and k_i the thickness and the thermal conductivity, respectively, of the i^{th} layer of the material located between the concrete and the environment. In the present case, the wooden formwork has a thickness of 1.85 cm and a conductivity of 0.2 $Wm^{-1}K^{-1}$, and a value of 5.2 $Wm^{-2}K^{-1}$ for h_{eq} is obtained. The wooden formwork of the lateral faces is removed 8.6 h after casting, and the corresponding faces of the concrete cube are made in contact with the environment, being a value of 10.0 $Wm^{-2}K^{-1}$ assigned to the heat transfer coefficient.

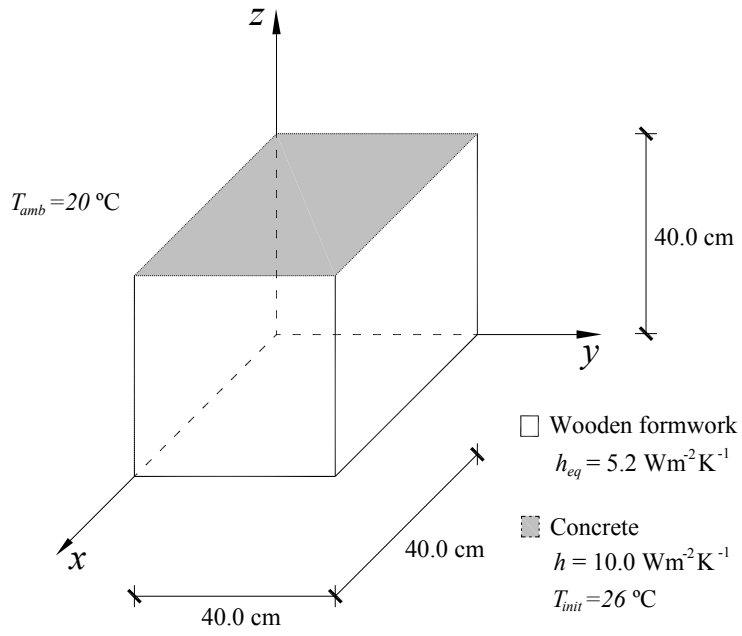

Figure 6.11 – Geometry and the boundary conditions.

In the numerical analysis the domain is discretized with 8-noded hexahedral elements with a 2×2×2 Gauss-Legendre integration scheme. The material conductivity, *k*, is constant and equal to 2.6 $Wm^{-1}K^{-1}$, the volumetric heat capacity, ρc, is 2400.0 $kJm^{-3}K^{-1}$ and the initial temperature is set to 26 ºC. The ambient temperature is 20 ºC and a Backward-Euler time integration scheme is used with an incremental time step of 864s.

The values that characterize the heat generation rate defined by equation (6.72) are dependent on the type of cement used in the experiment. A type I 52.5R cement content of

$430\,\mathrm{kg/m^3}$ has been used (Azenha 2009), with $A_T = 1.2053\text{E+}09 \times 430$, $E_a = 47.51\,\mathrm{kJ/mol}$ and $Q_{total} = 383.13 \times 430\,\mathrm{kJ/m^3}$. The normalized heat generation rate $f(\alpha_T)$ used in the analysis is represented in Figure 6.12, and a value of 0.05 is considered for $\alpha_{T,init}$.

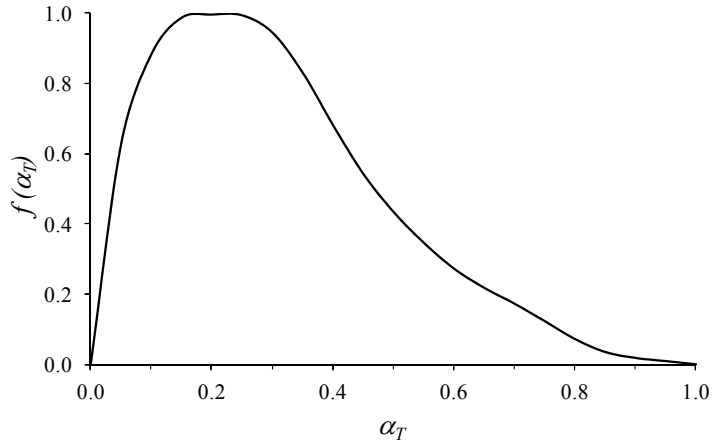

α_T	$f(\alpha_T)$
0.00	0.000
0.05	0.626
0.10	0.883
0.15	0.988
0.20	0.997
0.25	0.995
0.30	0.946
0.35	0.832
0.40	0.683
0.45	0.544
0.50	0.435
0.55	0.347
0.60	0.273
0.65	0.218
0.70	0.173
0.75	0.123
0.80	0.072
0.85	0.035
0.90	0.018
0.95	0.009
1.00	0.000

Figure 6.12 – Normalized heat generation rate.

As mentioned before, the cube is monitored by temperature sensors placed at several points. Azenha (2009) has compared the experimental results with numerical simulations and a good agreement was achieved. To assess the predictive performance of the developed thermal transient nonlinear model, the temperature due to heat generation during the first 24 h is compared with the numerical simulations of Azenha (2009) at two points (see Figure 6.13). One point (TP21) is located at the center of the top surface of the cube (0.2, 0.2, 0.4) and the other (TP9) is located at the center of the lateral surface (0.2, 0.4, 0.2). From Figure 6.13 it can be concluded that the present model matches perfectly the numerical simulations performed by Azenha (2009) at the predefined points. This figure also shows that, due to the presence of the lateral wooden formwork, a greater temperature gradient due to the heat generation has occurred at the point located on the face that contacts directly with the environment. When the lateral formwork is removed (8.6h after casting) an inflection point is observed in the TP9_ThermalModel curve, and its temperature curve tends to match the results of the TP21_ThermalModel. Both curves are almost coincident after a period of 12.0h.

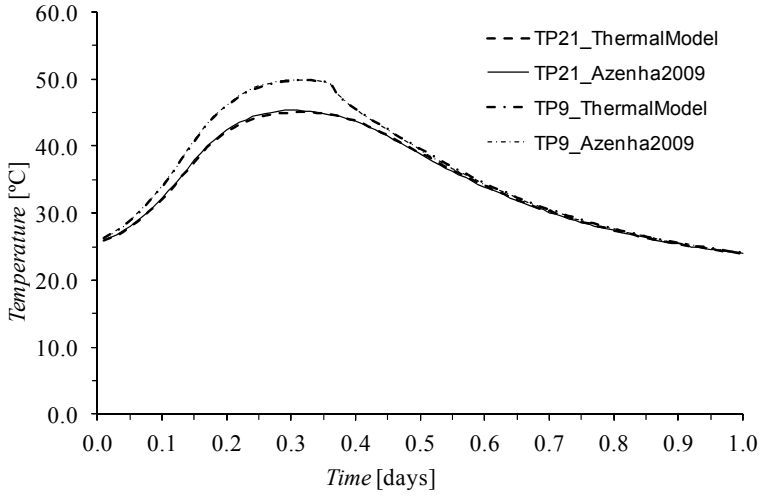

Figure 6.13 – Temperature evolution at two points of the cube during the first day.

Figure 6.14 represents the temperature field at two different times of the transient analysis. One is the temperature field at the first time step (t=0.24h) and the other is the temperature field at the last time step (t=24h). Some conclusions can be drawn by observing these temperature fields. At t=0.24h, only the top face of the cube is in direct contact with the environment, and it can be observed that the temperature gradient is smaller compared with the gradient of the faces that contact the wooden formwork. The observation of the temperature field at time t=24h leads to the conclusion that the lateral faces tend to exhibit a temperature distribution that is similar to the one observed on the top surface. However, the bottom face has a significantly different temperature field, with a greater temperature gradient. This is justified by the presence of the wooden formwork on this face during the whole test.

Another example for assessing the predictive performance of the implemented model is a concrete wall that is cast on a hardened concrete foundation. The analysis of this structure assuming plane strain conditions was analyzed by Lura and Breugel (2001). In the present work a three-dimensional representation of the domain is performed, assuming for the wall a length of 8 m, as shown in Figure 6.15. The domain is discretized with 20-noded hexahedral finite elements (see Figure 6.17), and a 3×3×3 Gauss-Legendre integration

scheme is used. The conductivity of the material is constant and equal to 2.6 $Wm^{-1}K^{-1}$, the volumetric heat capacity, ρc, is 2400.0 $kJm^{-3}K^{-1}$ and the initial temperature is set to 20 ºC. The ambient temperature is also 20 ºC and a Backward-Euler time integration scheme is used with an incremental time step of 1800s, being the total time of the analysis 120 h.

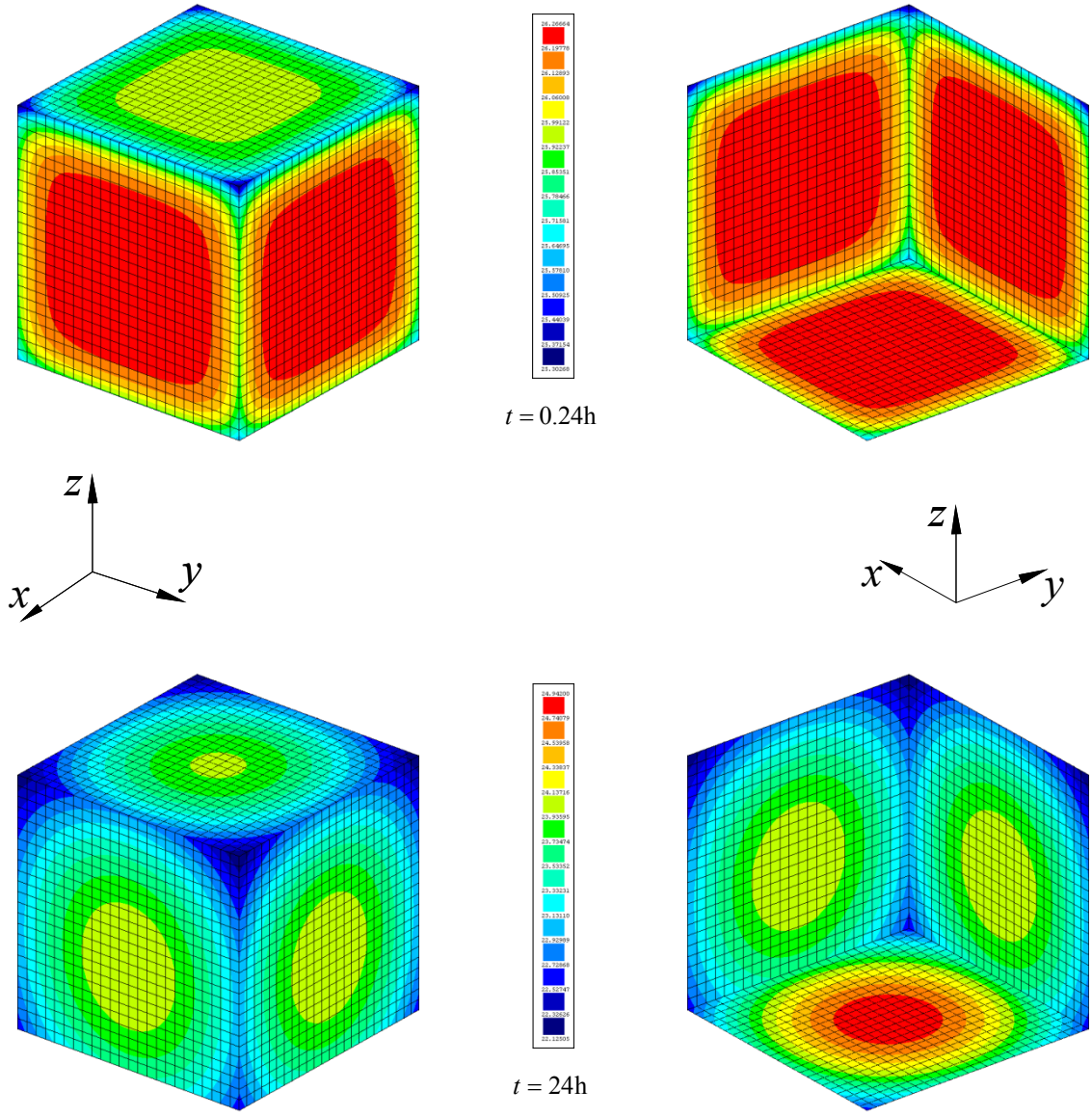

Figure 6.14 – Finite element mesh of the body represented in Figure 6.11, and temperature field for the first and last time step of the transient analysis.

Figure 6.15 represents schematically the geometry and the boundary conditions of the wall and the foundation. The top face of the wall is in contact with the environment, while a wooden formwork separates the others concrete surfaces from the environment until a curing period of 72h. After this time the wooden formwork is removed. An equivalent heat transfer coefficient, h_{eq}, is used to account for the wooden formwork, which is obtained with the electrical analogy by using equation (6.81).

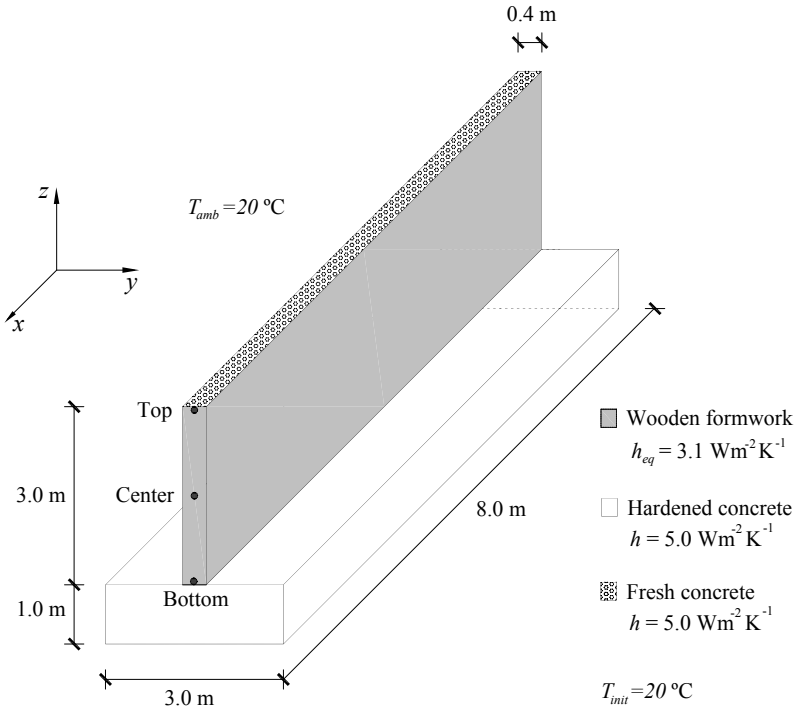

Figure 6.15 – Geometry and the boundary conditions.

As stated before, the values that characterize the heat generation rate defined by equation (6.72) are dependent on the type of cement used in the experiment. By the analysis of the type of cement used in Lura and Breugel (2001), cement content ($400\,\mathrm{kg/m^3}$) and activation energy ($45.7\ \mathrm{kJ/mol}$), the following data was derived, taking for this purpose information available in (Azenha 2009): a type I 52.5R cement with $A_T = 7.400\mathrm{E}{+}09 \times 400$, $E_a = 46.18\,\mathrm{kJ/mol}$ and $Q_{total} = 386.3 \times 400\,\mathrm{kJ/m^3}$. The normalized heat generation rate

$f(\alpha_T)$ used in the analysis is represented in Figure 6.16, and a value of 0.05 is considered for $\alpha_{T,init}$.

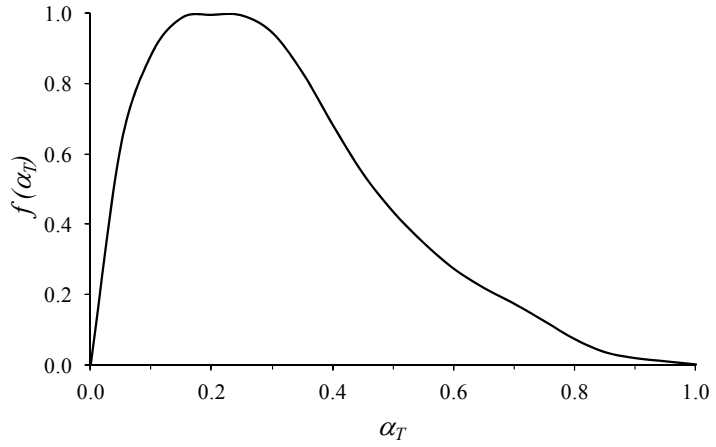

α_T	$f(\alpha_T)$
0.00	0.00
0.05	0.62
0.10	0.88
0.15	0.99
0.20	1.00
0.25	1.00
0.30	0.95
0.35	0.85
0.40	0.70
0.45	0.56
0.50	0.45
0.55	0.36
0.60	0.28
0.65	0.23
0.70	0.18
0.75	0.13
0.80	0.08
0.85	0.04
0.90	0.02
0.95	0.01
1.00	0.00

Figure 6.16 – Normalized heat generation rate.

Only one quarter of the wall-foundation system is used in the analysis, due to double symmetry of the problem. The temperature field for different time steps of the transient analysis is represented in Figure 6.17. It can be observed that the temperature is higher in the interior of the wall and tends, with time, of attaining the ambient temperature. Due to the high convection heat transfer in the external surfaces, the temperature field decreases from the core of the wall to these lateral surfaces, being the lowest temperature registered in the corners between the top and the front-lateral surface. This is more pronounced after a time of 72h, when the wooden formwork is removed.

Figure 6.18 represents the temperature evolution at three points of front edge of the wall (see Figure 6.15). It can be observed that the highest temperature development is in the center point and the lowest is at the bottom point in contact with the foundation. At a time of 72 h a smooth inflection point is observed in the curves due the removal of the wooden formwork. Similar results were obtained by Lura and Breugel (2001) and are presented in Figure 6.19. The main difference is the time corresponding to the peak temperature. By the observation of the adiabatic curve of hydration and heat release presented in Lura and Breugel (2001), the heat release up to 8h is abnormally very low.

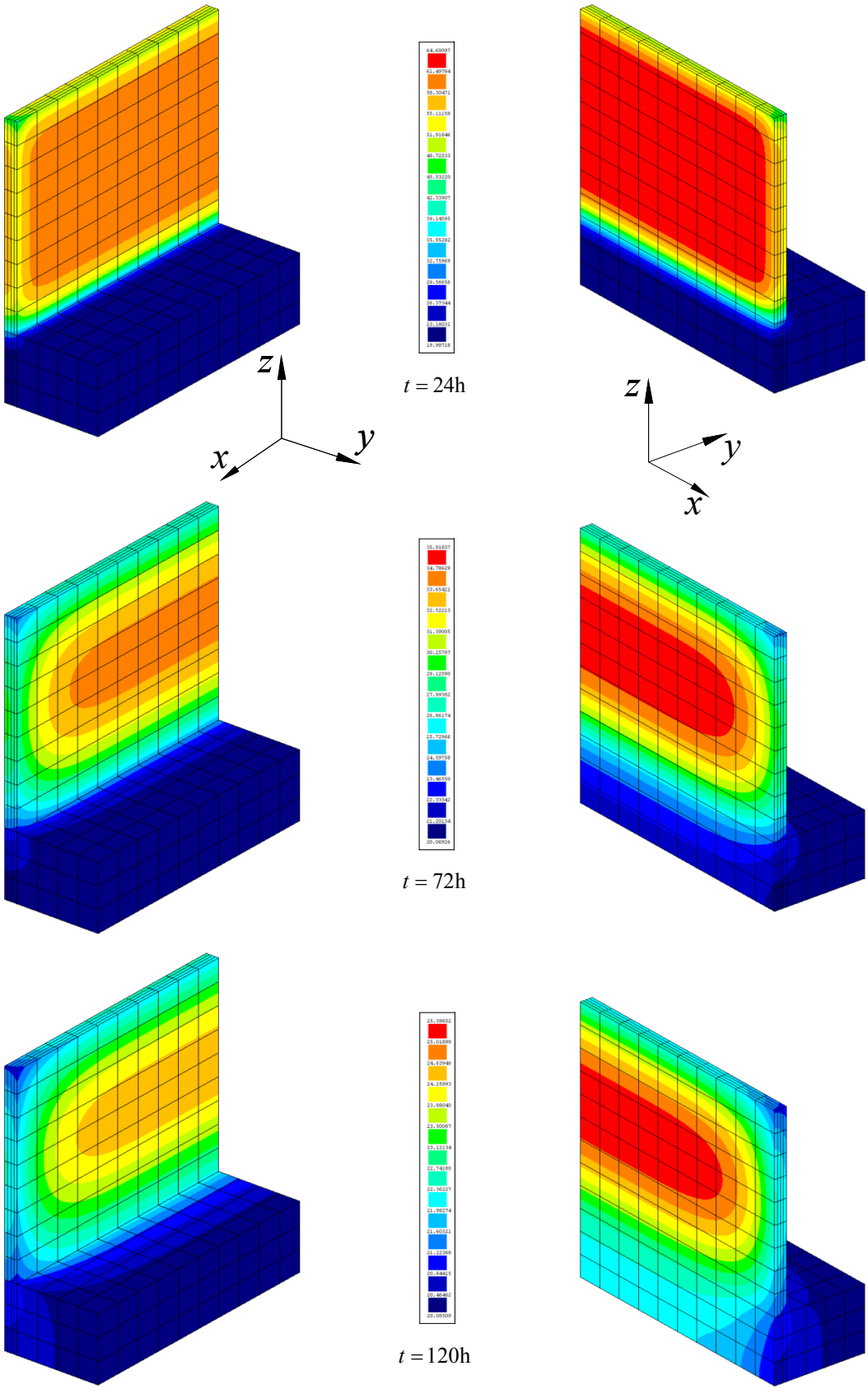

Figure 6.17 – Finite element mesh of the body represented in Figure 6.15, and temperature field for different time steps of the transient analysis.

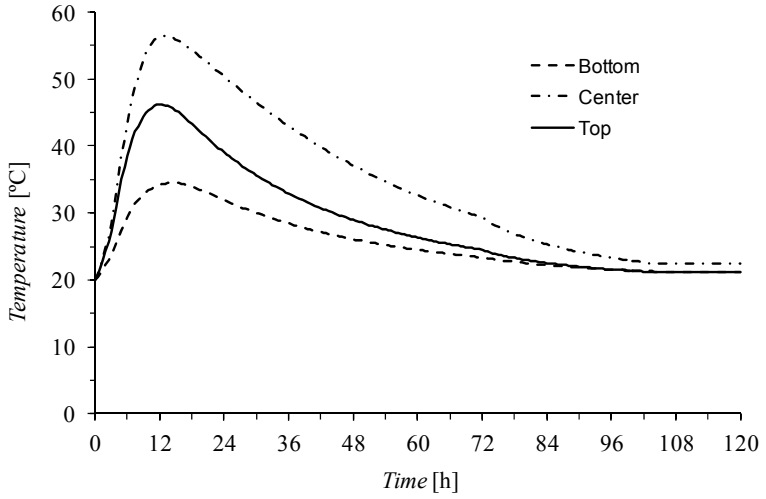

Figure 6.18 – Temperature evolution at three points of edge of the wall.

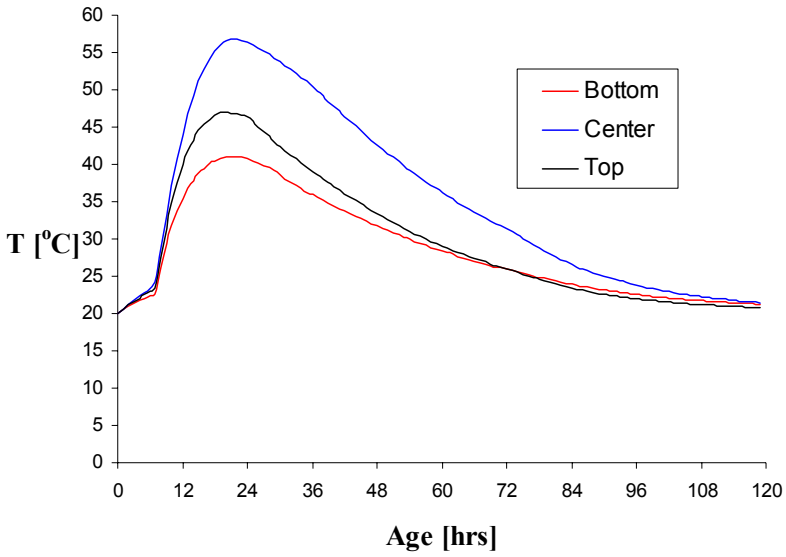

Figure 6.19 – Temperature evolution at three points of edge of the wall (Lura and van Breugel 2001).

6.3 TIME-DEPENDENT DEFORMATIONS

Using the concept of strain decomposition, the total strain at time t, $\varepsilon(t)$, of a concrete member uniaxially loaded at time t_0 with constant stress $\sigma(t_0)$ can be expressed by (Póvoas 1991, CEB-FIP 1993, Hofstetter and Mang 1995, Henriques 1998)

$$\varepsilon(t) = \varepsilon^{in}(t_0) + \varepsilon^{c}(t) + \varepsilon^{s}(t) + \varepsilon^{T}(t) \tag{6.82}$$

where $\varepsilon^{in}(t_0)$ is the initial strain at loading, $\varepsilon^{c}(t)$ is the creep strain at time $t > t_0$, $\varepsilon^{s}(t)$ is the shrinkage strain and $\varepsilon^{T}(t)$ is the thermal strain.

The strains $\varepsilon^{in}(t_0)$ and $\varepsilon^{c}(t)$ are caused by applied stresses, being thus called mechanical strains, while the other two components $\varepsilon^{s}(t)$ and $\varepsilon^{T}(t)$ are independent from the stress field (Bazant 1988).

The thermal strain $\varepsilon^{T}(t)$ can be obtained from the temperature field at a certain instant, e.g., using the results of the thermal model described in section 6.2 and performing the following calculation

$$\varepsilon^{T}(t) = \alpha \Delta T \tag{6.83}$$

being α the coefficient of thermal expansion and ΔT the temperature variation.

The procedures required to evaluate the shrinkage, $\varepsilon^{s}(t)$, and creep, $\varepsilon^{c}(t)$, strains are described in the following sections, which are based on the approaches proposed by the Eurocode 2 (EC2 2004), and by Bazant and Baweja 2000 (B3 model).

6.3.1 **Shrinkage**

6.3.1.1 Eurocode 2

The total shrinkage can be calculated with

$$\varepsilon^{s}\left(t\right)=\varepsilon_{ca}\left(t\right)+\varepsilon_{cd}\left(t,t_{s}\right) \tag{6.84}$$

where $\varepsilon_{ca}\left(t\right)$ is the autogenous shrinkage strain at time t defined by equation (6.92), and $\varepsilon_{cd}\left(t,t_{s}\right)$ is the drying shrinkage strain at time t, which can be determined with the following equation

$$\varepsilon_{cd}\left(t,t_{s}\right)=\beta_{ds}\left(t,t_{s}\right)k_{h}\varepsilon_{cd,0} \tag{6.85}$$

where

$$\beta_{ds}\left(t,t_{s}\right)=\frac{\left(t-t_{s}\right)}{\left(t-t_{s}\right)+0,04\sqrt{h_{0}^{3}}} \tag{6.86}$$

and k_h is a coefficient that depends on the notional size, h_0, and takes the values according to Table 6.1.

Table 6.1 – Values for k_h.

h_0 [mm]	k_h
100	1.0
200	0.85
300	0.75
≥ 500	0.70

In equation (6.85) $\varepsilon_{cd,0}$ is the notional drying shrinkage coefficient defined by

$$\varepsilon_{cd,0} = 0.85\left[\left(220+110\alpha_{ds1}\right)\exp\left(-\alpha_{ds2}\frac{f_{cm}}{10}\right)\right]10^{-6}\beta_{RH} \tag{6.87}$$

where α_{ds1} and α_{ds2} are coefficients that depend on the type of cement

$$\alpha_{ds1} = \begin{cases} 3 & \textit{for cement Class S} \\ 4 & \textit{for cement Class N} \\ 6 & \textit{for cement Class R} \end{cases} \tag{6.88}$$

$$\alpha_{ds2} = \begin{cases} 0.13 & \textit{for cement Class S} \\ 0.12 & \textit{for cement Class N} \\ 0.11 & \textit{for cement Class R} \end{cases} \tag{6.89}$$

and β_{RH} is the coefficient that introduces the effect of the relative humidity on drying

$$\beta_{RH} = -1.55\left[1-\left(\frac{RH}{100}\right)^3\right] \tag{6.90}$$

being RH the ambient relative humidity (%).

In the above equations, t is the age of concrete in days when the phenomenon is evaluated, t_s is the age of concrete in days at the beginning of the drying shrinkage, and in equation (6.86) h_0 is the notional size of the cross section, in mm, defined by

$$h_0 = \frac{2A_c}{u} \tag{6.91}$$

where A_c is the concrete cross sectional area, in mm^2, and u is the perimeter of the part of the cross section which is exposed to drying, in mm.

In equation (6.87) f_{cm} is the mean compressive strength of concrete at the age of 28 days in MPa.

The autogenous shrinkage strain, $\varepsilon_{ca}(t)$, is defined by

$$\varepsilon_{ca}(t) = \beta_{as}(t)\varepsilon_{ca}(\infty) \tag{6.92}$$

where $\beta_{as}(t)$ is a function defined by

$$\beta_{as}(t) = 1 - \exp\left(-0.2t^{0.5}\right) \tag{6.93}$$

and

$$\varepsilon_{ca}(\infty) = -2.5\left(f_{ck} - 10\right)\times 10^{-6} \tag{6.94}$$

where f_{ck} is the characteristic compressive strength of concrete at the age of 28 days in MPa. Its value can be estimated with

$$f_{ck} = f_{cm} - 8 \tag{6.95}$$

6.3.1.2 Model B3

According to this model the total shrinkage strain is calculated with

$$\varepsilon^{s}(t) = \varepsilon_{a}(t) + \varepsilon_{sh}(t, t_s) \tag{6.96}$$

where $\varepsilon_{a}(t)$ is the autogenous shrinkage strain obtained with equation (6.110), and $\varepsilon_{sh}(t, t_s)$ is the drying shrinkage strain defined by

$$\varepsilon_{sh}\left(t,t_s\right)=-\varepsilon_{sh\infty}k_h S\left(t\right) \tag{6.97}$$

where $S\left(t\right)$ represents the time-dependence

$$S\left(t\right)=\tanh\sqrt{\frac{t-t_s}{\tau_{sh}}} \tag{6.98}$$

k_h introduces the humidity dependence

$$k_h=\begin{cases}1-h^3 & for \quad h\le 0.98\\ -0.2 & for \quad h=1.0\ (swelling\ in\ water)\\ linear\ interpolation & for \quad 0.98<h<1.0\end{cases} \tag{6.99}$$

and $\varepsilon_{sh\infty}$ considers the time-dependence of ultimate shrinkage

$$\varepsilon_{sh\infty}=\varepsilon_{s\infty}\frac{E\left(607\right)}{E\left(t_s+\tau_{sh}\right)} \tag{6.100}$$

being

$$E\left(t\right)=E_{28}\sqrt{\left(\frac{t}{4+0.85t}\right)} \tag{6.101}$$

where E_{28} is the given by

$$E_{28}=4734\sqrt{f_{cm}} \tag{6.102}$$

In the above equations, t, t_s and f_{cm} have the meaning already presented in the previous section, and h is the ambient relative humidity, expressed as a decimal number in the range $0 \le h \le 1$. In equations (6.98) and (6.100) τ_{sh} is the shrinkage half-time in days given by

$$\tau_{sh} = k_t \left(k_s D\right)^2 \tag{6.103}$$

where k_t is a factor defined by

$$k_t = 8.5 t_0^{-0.08} f_{cm}^{-1/4} \tag{6.104}$$

The parameter k_s is the cross section shape factor, calculated according to

$$k_s = \begin{cases} 1.00 & \textit{for an infinite slab} \\ 1.15 & \textit{for an infinite cylinder} \\ 1.25 & \textit{for an infinite square prism} \\ 1.30 & \textit{for a sphere} \\ 1.55 & \textit{for a cube} \end{cases} \tag{6.105}$$

and D represents the effective cross section thickness, obtained with

$$D = \frac{2V}{S} \tag{6.106}$$

being V/S the volume to surface ratio in cm.

In equation (6.100) $\varepsilon_{s\infty}$ is calculated with

$$\varepsilon_{s\infty} = \alpha_1 \alpha_2 \left[1.9 \times 10^{-2} \omega^{2.1} f_{cm}^{-0.28} + 270 \right] \times 10^{-6} \tag{6.107}$$

where ω is the water content of the concrete mix, in kg/m^{-3}. The parameters α_1 and α_2 are defined by

$$\alpha_1 = \begin{cases} 1.00 & \textit{for type I cement} \\ 0.85 & \textit{for type II cement} \\ 1.10 & \textit{for type III cement} \end{cases} \tag{6.108}$$

and

$$\alpha_2 = \begin{cases} 0.75 & \textit{for steam-curing} \\ 1.20 & \textit{for sealed or normal curing in air with initial protection against drying} \\ 1.00 & \textit{for curing in water or at 100\% relative humidity} \end{cases} \tag{6.109}$$

The autogenous shrinkage strain, $\varepsilon_a(t)$, is defined by

$$\varepsilon_a(t) = \varepsilon_{a\infty} \left(0.99 - h_{a\infty} \right) S_a(t) \tag{6.110}$$

being $h_{a\infty}$ the final self-desiccation humidity, that can be assumed to be about 80% (Bazant and Baweja 2000), $\varepsilon_{a\infty}$ the final autogenous shrinkage strain and

$$S_a(t) = \tanh \sqrt{\frac{t - t_{set}}{\tau_a}} \tag{6.111}$$

In this equation t_{set} is the time of final set of cement in days, and τ_a is the half-time of autogenous shrinkage, depending on the rate of hardening of the type of concrete.

According to Bazant and Baweja (2000) the material parameters of equations (6.110) and (6.111) may be calibrated by performing shrinkage measurements in sealed specimens (autogenous shrinkage) and drying specimens (total shrinkage).

6.3.2 **Creep**

6.3.2.1 Eurocode 2

The creep strain at time t, $\varepsilon^c(t)$, for a constant stress, σ_c, applied at a concrete age t_0 is given by

$$\varepsilon^c(t) = \varphi(t,t_0)\frac{\sigma_c}{E_c} \tag{6.112}$$

where E_c is the tangent modulus of concrete, that can be considered equal to $1.05E_{cm}$, being E_{cm} the secant modulus of elasticity of concrete at an age of 28 days. In Equation (6.112) the creep coefficient $\varphi(t,t_0)$ is defined by

$$\varphi(t,t_0) = \varphi_0\beta_c(t,t_0) \tag{6.113}$$

where φ_0 is the notional creep coefficient determined from equation (6.114); $\beta_c(t,t_0)$ is the coefficient that describes the time dependent evolution of creep after loading, defined by equation (6.116), being t the age, in days, when the creep is evaluated, and t_0 the age of concrete at loading in days.

$$\varphi_0 = \varphi_{RH}\beta(f_{cm})\beta(t_0) \tag{6.114}$$

where

$$\varphi_{RH} = 1 + \frac{1 - RH/100}{0.1\sqrt[3]{h_0}} \qquad for \;\; f_{cm} \le 35\ MPa \tag{6.115a}$$

$$\varphi_{RH} = \left[1 + \frac{1 - RH/100}{0.1\sqrt[3]{h_0}} \alpha_1 \right] \alpha_2 \qquad for \;\; f_{cm} > 35\ MPa \tag{6.115b}$$

$$\beta\left(f_{cm}\right) = \frac{16.8}{\sqrt{f_{cm}}} \tag{6.115c}$$

$$\beta\left(t_0\right) = \frac{1}{0.1 + \left(t_0\right)^{0.2}} \tag{6.115d}$$

being RH the relative humidity of the ambient environment, in %, h_0 is defined by equation (6.91) and f_{cm} is the mean compressive strength of concrete at the age of 28 days in MPa. The term $\beta_c\left(t, t_0\right)$ in equation (6.113) is determined with

$$\beta_c\left(t, t_0\right) = \left[\frac{\left(t - t_0\right)}{\beta_H + t - t_0} \right]^{0.3} \tag{6.116}$$

being

$$\beta_H = 1.5\left[1 + \left(0.012RH\right)^{18} \right] h_0 + 250 \le 1500 \qquad for \;\; f_{cm} \le 35\ MPa \tag{6.117a}$$

$$\beta_H = 1.5\left[1 + \left(0.012RH\right)^{18} \right] h_0 + 250\alpha_3 \le 1500\alpha_3 \qquad for \;\; f_{cm} > 35\ MPa \tag{6.117b}$$

The coefficients α_1, α_2 and α_3 in equations (6.115) and (6.117) depend on the mean compressive strength of concrete, and are defined by

$$\alpha_1 = \left[\frac{35}{f_{cm}} \right]^{0.7} \qquad \alpha_2 = \left[\frac{35}{f_{cm}} \right]^{0.2} \qquad \alpha_3 = \left[\frac{35}{f_{cm}} \right]^{0.5} \tag{6.118}$$

The effects of temperature during the curing phase and type of cement on the creep coefficient of concrete may be taken into account by modifying the value of the parameter that considers the age at loading t_0

$$t_0 = t_{0,T}\left[\frac{9}{2+\left(t_{0,T}\right)^{1.2}}+1\right]^{\alpha} \geq 0.5\ days \tag{6.119}$$

where α is a parameter that depends on the type of cement

$$\alpha = \begin{cases} -1 & for\ cement\ Class\ S \\ 0 & for\ cement\ Class\ N \\ 1 & for\ cement\ Class\ R \end{cases} \tag{6.120}$$

and $t_{0,T}$ is the age of concrete at loading, in days, adjusted according to the following equation

$$t_{0,T} = \sum_{i=1}^{n} \mathrm{e}^{-\left(\frac{4000}{273+T(\Delta t_i)}-13.65\right)} \times \Delta t_i \tag{6.121}$$

being $T\left(\Delta t_i\right)$ the temperature in ºC during the time period Δt_i, in days.

When the compressive stress of concrete at age t_0 exceeds the value $0.45 f_{ck}(t_0)$ the nonlinearity of creep may be taken into account by considering

$$\varphi_{nl}\left(t,t_0\right) = \varphi\left(t,t_0\right)\exp\left[1.5\left(k_\sigma - 0.45\right)\right] \tag{6.122}$$

where $\varphi_{nl}(t,t_0)$ is the nonlinear notional creep coefficient and replaces $\varphi(t,t_0)$ and $k_\sigma = \sigma_c / f_{ck}(t_0)$, which is the stress-strength ratio, being $f_{ck}(t_0)$ the characteristic compressive strength of concrete at time of loading.

6.3.2.2 Model B3

The compliance function $J(t,t_0)$ or creep function, represents the strain (elastic plus creep) at time t, caused by a unit constant stress applied at age t_0, and is given by

$$J(t,t_0) = q_1 + C_0(t,t_0) + C_d(t,t_0,t_s) \tag{6.123}$$

where q_1 is the instantaneous strain due to unit stress

$$q_1 = \frac{0.6\times10^6}{E_{28}} \tag{6.124}$$

being E_{28} obtained from equation (6.102). The parameter $C_0(t,t_0)$ is the compliance function for basic creep, i.e., creep at constant moisture content and no moisture movement through the material (Bazant and Baweja 2000), obtained with

$$C_0(t,t_0) = q_2 Q(t,t_0) + q_3 \ln\left[1+(t-t_0)^n\right] + q_4 \ln\left(\frac{t}{t_0}\right) \tag{6.125}$$

where

$$q_2 = 185.4c^{0.5} f_{cm}^{-0.9} \;;\; q_3 = 0.29(w/c)^4 q_2 \;;\; q_4 = 20.3(a/c)^{-0.7} \tag{6.126}$$

and

$$Q(t,t_0) = Q_f(t_0)\left[1+\left(\frac{Q_f(t_0)}{Z(t,t_0)}\right)^{r(t_0)}\right]^{-\frac{1}{r(t_0)}} \tag{6.127}$$

in which

$$r(t_0) = 1.7(t_0)^{0.12} + 8 \tag{6.128a}$$

$$Z(t,t_0) = (t_0)^{-m}\ln\left[1+(t-t_0)^n\right] \tag{6.128b}$$

$$Q_f(t_0) = \left[0.086(t_0)^{2/9} + 1.21(t_0)^{4/9}\right] \tag{6.128c}$$

In equation (6.123) $C_d(t,t_0,t_s)$ is the additional compliance function due to drying given by

$$C_d(t,t_0,t_s) = q_5\left[\exp\left\{-8H(t)\right\} - \exp\left\{-8H(t_0')\right\}\right]^{1/2} \tag{6.129}$$

where t_0' is the time at which drying and loading first act simultaneously, $t_0' = \max(t_0,t_s)$, and

$$H(t) = 1-(1-h)S(t) \tag{6.130}$$

being $S(t)$ given by equation (6.98). The meaning of the parameter h is described in section 6.3.1.2, and t_s is the age of concrete in days when drying begins.

The value of q_5 in equation (6.129) is given by

$$q_5 = 7.57\times10^5 f_{cm}^{-1} \mid \varepsilon_{sh\infty} \mid^{-0.6} \tag{6.131}$$

where $\varepsilon_{sh\infty}$ is obtained with equation (6.100).

In the above equations $n=1.0$, $m=0.5$, c is the cement content, (w/c) the water to cement ratio, (a/c) is the aggregate to cement ratio and f_{cm} is the mean compressive strength of concrete at the age of 28 days in MPa.

According to (Bazant and Baweja 2000) the creep coefficient should be calculated from the compliance function as follows

$$\varphi(t,t_0)=E(t_0)J(t,t_0)-1 \tag{6.132}$$

where $E(t_0)$ is the modulus of elasticity at loading age t_0, being obtained with equation (6.101).

6.4 CONCRETE MATURITY

The concrete mechanical properties increases significantly with time and consequently these changes must be taken into account. The maturity of concrete is a consequence of the hydration process of the cement paste and its evolution is strongly affected by temperature, curing conditions and type of cement (Henriques 1998).

The recommendations of Eurocode 2 (EC2 2004) to simulate the evolution of the compressive strength, tensile strength and modulus of elasticity are the following

$$f_{cm}(t)=\beta_{cc}(t)f_{cm} \tag{6.133a}$$

$$f_{ctm}(t)=\left[\beta_{cc}(t)\right]^{\alpha} f_{ctm} \tag{6.133b}$$

$$E_{cm}(t)=\left[\beta_{cc}(t)\right]^{0.3} E_{cm} \tag{6.133c}$$

where f_{cm}, f_{ctm} and E_{cm} are the mean compressive strength, the mean value of the tensile strength, and the secant modulus of elasticity of concrete at an age of 28 days. In equation (6.133b) α is a parameter whose value depends on the considered age t

$$\alpha = \begin{cases} 1 & for\ t < 28\ days \\ \frac{2}{3} & for\ t \geq 28\ day \end{cases} \tag{6.134}$$

In equation (6.133) $\beta_{cc}(t)$ is determined from

$$\beta_{cc}(t) = \exp\left\{ s\left[1 - \left(\frac{28}{t} \right)^{1/2} \right] \right\} \tag{6.135}$$

being

$$s = \begin{cases} 0.38 & for\ cement\ Class\ S \\ 0.25 & for\ cement\ Class\ N \\ 0.20 & for\ cement\ Class\ R \end{cases} \tag{6.136}$$

To define the tensile diagrams described in section 3.3.2.2 of chapter 3, the mode I fracture energy must be supplied. An experimental program is necessary to obtain data to propose an equation that defines the evolution of the fracture energy with time. Since this experimental work is out of the scope of this thesis, a relation is proposed by using the coefficient of equation (6.135), which depends on the age of the concrete, t

$$G_f^I(t) = \left[\beta_{cc}(t) \right]^{\alpha_1} G_f^I \tag{6.137}$$

where G_f^I is the mode I fracture energy of concrete at an age of 28 days, and α_1 is a value that defines the evolution of $\beta_{cc}(t)$ While no more reliable information is available, the values indicated in equation (6.134) will be used in the present work.

If the mean temperature differs from the reference temperature, 20 ºC, the concept of equivalent age is commonly used. This concept can be defined as the age at which the hydration at the reference temperature has reached the same stage (Bosnjak 2000, Azenha 2009), and can be determined by

$$t_{eq} = \int_0^t \mathrm{e}^{-\frac{E_a}{R}\left(\frac{1}{273.15+T(t)}-\frac{1}{273.15+T_{ref}}\right)} dt \tag{6.138}$$

or in an incremental form

$$t_{eq} = \sum_{i=1}^{n} \mathrm{e}^{-\frac{E_a}{R}\left(\frac{1}{273.15+T(\Delta t_i)}-\frac{1}{273.15+T_{ref}}\right)} \times \Delta t_i \tag{6.139}$$

being E_a (Jmol^{-1}) the apparent activation energy that depends on the type of cement, R the ideal gas constant (8.314 Jmol^{-1}K^{-1}), T_{ref} the reference temperature (20 ºC) and $T(\Delta t_i)$ the temperature in ºC during the time period Δt_i in days.

Equation (6.139) is very similar to equation (6.121) proposed by EC 2 (2004) for the age adjustment. Making some calculations, the equation of EC 2 (2004) assumes an apparent activation energy of about 33256 Jmol^{-1} for a reference temperature of 20 ºC. These two approaches are available to the equivalent age calculation. The equivalent age is introduced in the above equations for the evaluation of the mechanical properties of concrete.

6.5 UPDATE OF THE MULTI-FIXED SMEARED 3D CRACK MODEL TO TAKE INTO ACCOUNT THE TIME DEPENDENT EFFECTS

In chapter 5 a multi-fixed smeared 3D crack model, under the nonlinear FEM framework, is proposed to simulate the behavior of concrete structures. In this section this model is adapted to include the time dependent effects.

In this smeared crack model the strain components of the cracked material is the addition of the strain components in the smeared cracks, $\underline{\varepsilon}^{cr}$, with the strain components in the uncracked concrete between cracks, $\underline{\varepsilon}^{co}$

$$\underline{\varepsilon} = \underline{\varepsilon}^{co} + \underline{\varepsilon}^{cr} \tag{6.140}$$

Taking into account the time dependent effects described in section 6.3, the strain vector of the uncracked concrete is decomposed in order to include these effects. So, equation (6.82) is adapted and results in

$$\underline{\varepsilon}(t) = \underline{\varepsilon}^{e}(t_0) + \underline{\varepsilon}^{c}(t) + \underline{\varepsilon}^{s}(t) + \underline{\varepsilon}^{T}(t) + \underline{\varepsilon}^{cr}(t) \tag{6.141}$$

where $\underline{\varepsilon}^{e}$, $\underline{\varepsilon}^{c}$, $\underline{\varepsilon}^{s}$ and , $\underline{\varepsilon}^{T}$ are the elastic, creep, shrinkage and thermal strain vectors, and $\underline{\varepsilon}^{cr}$ is the crack strain vector. A nonlinear transient analysis must be performed, since the total strain is time dependent, being its components evaluated during the time.

If the maximum compressive stress is less than 0.4 of the compressive strength of the concrete, the mechanical strain for a uniaxial loaded concrete specimen can be obtained with

$$\varepsilon^{m}(t) = \varepsilon^{e}(t_0) + \varepsilon^{c}(t) = J(t,t_0)\sigma(t_0) \tag{6.142}$$

where $J(t,t_0)$ is the compliance function or creep function, representing the strain, elastic plus creep, at time t caused by a unit constant uniaxial stress acting since time t_0. Since the elastic strain is defined by

$$\varepsilon^e(t_0)=\frac{\sigma(t_0)}{E(t_0)} \tag{6.143}$$

where $E_c(t_0)$ is the modulus of elasticity at the time t_0, the compliance function can be given by

$$J(t,t_0)=\frac{1}{E(t_0)}+C(t,t_0) \tag{6.144}$$

being $C(t,t_0)$ the specific creep. Therefore, the creep strain can be obtained with

$$\varepsilon^c(t)=C(t,t_0)\sigma(t_0)=\left(J(t,t_0)-\frac{1}{E(t_0)}\right)\sigma(t_0) \tag{6.145}$$

or introducing the creep coefficient $\varphi(t,t_0)=E(t_0)C(t,t_0)$, the creep strain can be determined from

$$\varepsilon^c(t)=\sigma(t_0)\frac{\varphi(t,t_0)}{E(t_0)} \tag{6.146}$$

Introducing equation (6.144) in equation (6.142) the mechanical strain is given by

$$\varepsilon^m(t)=\left(\frac{1}{E(t_0)}+C(t,t_0)\right)\sigma(t_0) \tag{6.147}$$

Assuming that the strain caused by a generic stress history $\sigma(t)$ can be determined by the decomposition of the stress history into small increments $d\sigma(t')$ applied at times t' (Bazant 1988), the mechanical strain is

$$\varepsilon^m(t) = \int_0^t J(t,t')\, d\sigma(t') \tag{6.148}$$

By performing

$$d\sigma(t') = \frac{d\sigma(t')}{dt'} dt' = \dot{\sigma}(t')\, dt' \tag{6.149}$$

equation (6.148) can be rewritten as

$$\varepsilon^m(t) = \int_0^t J(t,t')\, \dot{\sigma}(t')\, dt' \tag{6.150}$$

or, for a three-dimensional stress state,

$$\underline{\varepsilon}^m(t) = \int_0^t J(t,t')\, \underline{C}\, \underline{\dot{\sigma}}(t')\, dt' \tag{6.151}$$

where $\underline{C} = E\left(\underline{D}^{co}\right)^{-1}$, being $\underline{D}^{co}$ defined by equation (5.12) of chapter 5.

For an incremental time step Δt, the incremental mechanical strain vector is obtained with

$$\Delta\underline{\varepsilon}^m(t_n) = \underline{\varepsilon}^m(t_{n+1}) - \underline{\varepsilon}^m(t_n) \tag{6.152}$$

being $\underline{\varepsilon}^{m}\left(t_{n+1}\right)$ and $\underline{\varepsilon}^{m}\left(t_{n}\right)$ the mechanical strain vector at the time t_{n+1} and t_{n}, respectively.

Using equation (6.151) in (6.152) the mechanical strain increment vector is given by

$$\Delta\underline{\varepsilon}^{m}\left(t_{n}\right)=\int_{0}^{t_{n}}J\left(t_{n+1},t'\right)\underline{C}\dot{\underline{\sigma}}\left(t'\right)dt'+\int_{t_{n}}^{t_{n+1}}J\left(t_{n+1},t'\right)\underline{C}\dot{\underline{\sigma}}\left(t'\right)dt'-\int_{0}^{t_{n}}J\left(t,t'\right)\underline{C}\dot{\underline{\sigma}}\left(t'\right)dt' \tag{6.153}$$

or

$$\Delta\underline{\varepsilon}^{m}\left(t_{n}\right)=\int_{0}^{t_{n}}\left[J\left(t_{n+1},t'\right)-J\left(t,t'\right)\right]\underline{C}\dot{\underline{\sigma}}\left(t'\right)dt'+\int_{t_{n}}^{t_{n+1}}J\left(t_{n+1},t'\right)\underline{C}\dot{\underline{\sigma}}\left(t'\right)dt' \tag{6.154}$$

Multiplying this equation by the matrix $\underline{C}^{-1}$, and taking into account that $\underline{C}^{-1}=\underline{D}$, equation (6.154) becomes

$$\underline{D}_{co}\Delta\underline{\varepsilon}^{m}\left(t_{n}\right)=\int_{0}^{t_{n}}\left[J\left(t_{n+1},t'\right)-J\left(t,t'\right)\right]\dot{\underline{\sigma}}\left(t'\right)dt'+\int_{t_{n}}^{t_{n+1}}J\left(t_{n+1},t'\right)\dot{\underline{\sigma}}\left(t'\right)dt' \tag{6.155}$$

where $\underline{D}=E^{-1}\underline{D}^{co}$.

Considering that in the incremental time step, Δt, a linear variation of the stress is assumed, its derivative is approximated by

$$\dot{\underline{\sigma}}\left(t'\right)=\frac{\partial\underline{\sigma}\left(t'\right)}{\partial t'}\approx\frac{\underline{\sigma}\left(t_{n+1}\right)-\underline{\sigma}\left(t_{n}\right)}{t_{n+1}-t_{n}}\approx\frac{\Delta\underline{\sigma}\left(t_{n}\right)}{\Delta t} \tag{6.156}$$

Substituting this relation in the second integral of equation (6.155) and making some arrangements, results in

$$\Delta\underline{\sigma}\left(t_n\right)=\frac{\underline{D}\Delta\underline{\varepsilon}^{m}\left(t_n\right)-\int_{0}^{t_n}\left[J\left(t_{n+1},t'\right)-J\left(t,t'\right)\right]\underline{\dot{\sigma}}\left(t'\right)dt'}{\frac{1}{\Delta t}\int_{t_n}^{t_{n+1}}J\left(t_{n+1},t'\right)dt'} \tag{6.157}$$

This equation can be written as (de Borst and van den Boogaard 1984)

$$\Delta\underline{\sigma}\left(t_n\right)=\overline{E}(t^{*})\underline{D}_{co}\Delta\underline{\varepsilon}^{m}\left(t_n\right)+\overline{\sigma}(t_n) \tag{6.158}$$

where

$$\overline{E}(t^{*})=\frac{1}{\frac{1}{\Delta t}\int_{t_n}^{t_{n+1}}J\left(t_{n+1},t'\right)dt'} \tag{6.159}$$

and

$$\overline{\sigma}\left(t_n\right)=-E\left(t^{*}\right)\int_{0}^{t}\left[J\left(t_{n+1},t'\right)-J\left(t,t'\right)\right]\underline{\dot{\sigma}}dt' \tag{6.160}$$

with $t_{n+1}\le t^{*}\le t_n$ (using a generalized midpoint rule)

To overcome the inconvenient of storing the entire load history, the use of Dirichlet series is commonly used, so the approximation of the compliance function is made by a series of real exponentials (Bazant and Wu 1973, Bazant 1988)

$$J\left(t,t'\right)=\frac{1}{E\left(t'\right)}+\sum_{\mu=1}^{N}\frac{1}{\overline{\overline{E}}_{\mu}\left(t'\right)}\left(1-e^{\frac{-\left(t-t_0\right)}{\tau_{\mu}}}\right) \tag{6.161}$$

where τ_μ are constants designated by retardation times, $\overline{E}_\mu$ are coefficients only depending on t' that have the dimensions of an elastic moduli, and $E(t')$ is the instantaneous elastic modulus. The process for the determination of the retardations times, τ_μ, and the coefficients $\overline{E}_\mu$ can be found elsewhere (Bazant and Wu 1973, Bazant 1988, Póvoas 1991). Dirichlet series expansion of the compliance function, as presented in equation (6.161), can be interpreted as a Kelvin chain of *N* units (Bazant and Wu 1973).

The incremental mechanical strain vector, $\Delta\underline{\varepsilon}^m$, can be related to the other components of equation (6.141), rewritten in an incremental form for the a time step Δt

$$\Delta\underline{\varepsilon}^m(t_n) = \Delta\underline{\varepsilon}(t_n) - \Delta\underline{\varepsilon}^s(t_n) - \Delta\underline{\varepsilon}^T(t_n) - \Delta\underline{\varepsilon}^{cr}(t_n) \tag{6.162}$$

Introducing this equation in equation (6.158) results in

$$\Delta\underline{\sigma}(t_n) = \overline{E}(t^*)\underline{D}\left[\Delta\underline{\varepsilon}(t_n) - \Delta\underline{\varepsilon}^s(t_n) - \Delta\underline{\varepsilon}^T(t_n) - \Delta\underline{\varepsilon}^{cr}(t_n)\right] + \overline{\sigma}(t_n) \tag{6.163}$$

Considering equations (5.5), (5.10) and (5.13) of chapter 5, written for the time t_n, results in

$$\Delta\underline{\sigma}_\ell^{cr}(t_n) = \underline{T}^{cr}\Delta\underline{\sigma}(t_n) \tag{6.164a}$$

$$\Delta\underline{\varepsilon}^{cr}(t_n) = \left[\underline{T}^{cr}\right]^T \Delta\underline{\varepsilon}_\ell^{cr}(t_n) \tag{6.164b}$$

$$\Delta\underline{\sigma}_\ell^{cr}(t_n) = \underline{D}^{cr}\Delta\underline{\varepsilon}_\ell^{cr}(t_n) \tag{6.164c}$$

Introducing equation (6.163) in the second member of equation (6.164a), results in

$$\Delta\underline{\sigma}_{\ell}^{cr}(t_n) = \underline{T}^{cr}\left(\bar{E}(t^*)\underline{D}\left(\Delta\underline{\varepsilon}(t_n) - \Delta\underline{\varepsilon}^{s}(t_n) + \Delta\underline{\varepsilon}^{T}(t_n) + \Delta\underline{\varepsilon}^{cr}(t_n)\right) + \bar{\sigma}(t_n)\right) \tag{6.165}$$

Introducing equations (6.164b) and (6.164c) in equation (6.165), and making some arrangements, yields

$$\begin{aligned}\Delta\underline{\varepsilon}_{\ell}^{cr}(t_n) = &\left(\underline{D}^{cr} + \underline{T}^{cr}\bar{E}(t^*)\underline{D}\left[\underline{T}^{cr}\right]^{T}\right)^{-1} \times \\ &\left(\underline{T}^{cr}\bar{E}(t^*)\underline{D}\left[\Delta\underline{\varepsilon}(t_n) - \Delta\underline{\varepsilon}^{s}(t_n) - \Delta\underline{\varepsilon}^{T}(t_n)\right] + \underline{T}^{cr}\bar{\sigma}(t_n)\right)\end{aligned} \tag{6.166}$$

By including equation (6.166) in (6.164b), it can be obtained

$$\begin{aligned}\Delta\underline{\varepsilon}^{cr}(t_n) = &\left[\underline{T}^{cr}\right]^{T}\left[\left(\underline{D}^{cr} + \underline{T}^{cr}\bar{E}(t^*)\underline{D}\left[\underline{T}^{cr}\right]^{T}\right)^{-1} \times \right. \\ &\left.\left(\underline{T}^{cr}\bar{E}(t^*)\underline{D}\left[\Delta\underline{\varepsilon}(t_n) - \Delta\underline{\varepsilon}^{s}(t_n) - \Delta\underline{\varepsilon}^{T}(t_n)\right] + \underline{T}^{cr}\bar{\sigma}(t_n)\right)\right]\end{aligned} \tag{6.167}$$

and then introducing equation (6.167) in equation (6.163) and making some operations, the incremental stress vector is obtained with

$$\begin{aligned}\Delta\underline{\sigma}(t_n) = &\left(\underline{I} - \bar{E}(t^*)\underline{D}\left[\underline{T}^{cr}\right]^{T}\left(\underline{D}^{cr} + \underline{T}^{cr}\bar{E}(t^*)\underline{D}\left[\underline{T}^{cr}\right]^{T}\right)^{-1}\underline{T}^{cr}\right) \times \\ &\left(\bar{E}(t^*)\underline{D}\left(\Delta\underline{\varepsilon}(t_n) - \Delta\underline{\varepsilon}^{s}(t_n) - \Delta\underline{\varepsilon}^{T}(t_n)\right) + \bar{\sigma}(t_n)\right)\end{aligned} \tag{6.168}$$

Equation (6.168) replaces equation (5.20) in the multi-fixed 3D crack model presented in chapter 5.

The incremental shrinkage strain is obtained by one of the models described in section 6.3, and the incremental thermal strain is determined from the temperature field, e.g., using the results of the thermal model described in section 6.2. For the three-dimensional case, these vectors are defined by

$$\Delta\underline{\varepsilon}^{s}\left(t_n\right)=\left[\Delta\varepsilon^{s}\quad\Delta\varepsilon^{s}\quad\Delta\varepsilon^{s}\quad 0\quad 0\quad 0\right]^{T} \tag{6.169}$$

$$\Delta\underline{\varepsilon}^{T}\left(t_n\right)=\left[\Delta\varepsilon^{T}\quad\Delta\varepsilon^{T}\quad\Delta\varepsilon^{T}\quad 0\quad 0\quad 0\right]^{T} \tag{6.170}$$

and are obtained with

$$\Delta\underline{\varepsilon}^{s}\left(t_n\right)=\underline{\varepsilon}^{s}\left(t_{n+1}\right)-\underline{\varepsilon}^{s}\left(t_n\right)\ ;\ \Delta\underline{\varepsilon}^{T}\left(t_n\right)=\underline{\varepsilon}^{T}\left(t_{n+1}\right)-\underline{\varepsilon}^{T}\left(t_n\right) \tag{6.171}$$

6.5.1 **Numerical example**

The performance of the model is appraised by performing a thermo-mechanical analysis of a prefabricated reinforced concrete bridge beam with a U-shaped cross section (Ferreira et al. 2008), as represented schematically in Figure 6.20.

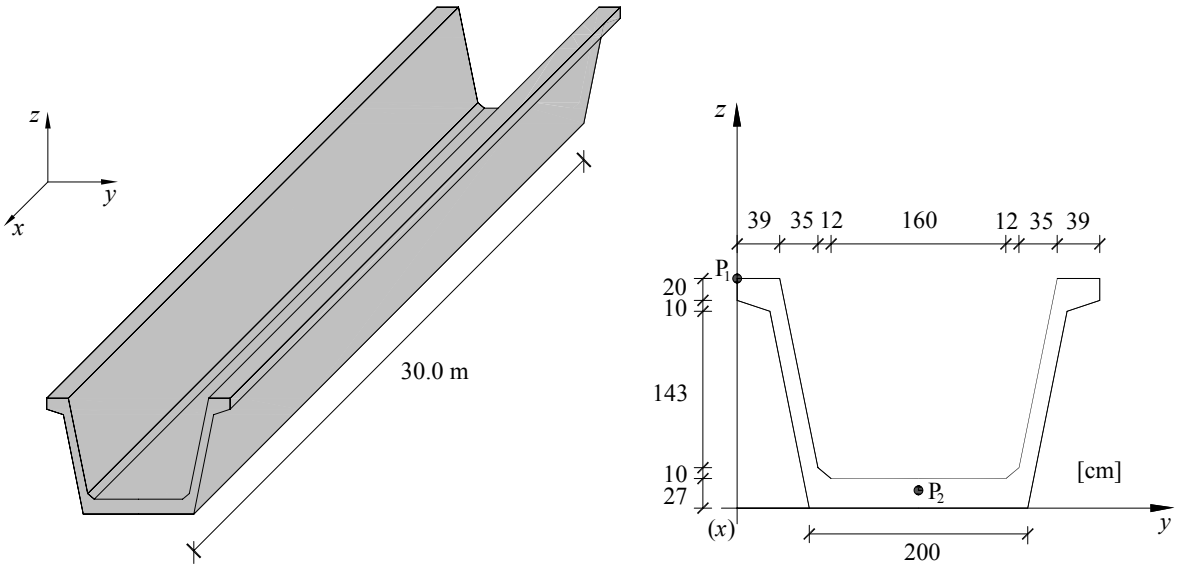

Figure 6.20 – Geometry of the prefabricated reinforced concrete bridge beam with a U-shaped cross section.

In the precast industry different heat curing regimes (Ferreira et al. 2008) are frequently used to provide an early age strength development capable of anticipating the process of demolding as much as possible. In the present numerical simulation, the beam is subjected to one of these heat curing regimes, and its consequence in the strength development and an eventual crack formation is assessed. In the analysis carried out, a beam segment of

10.0 m length is considered since Ferreira et al. (2008) has verified that lengths greater than 10.0 m have no influence on the results. Due to double symmetry of the problem, only one quarter of the beam is modeled in the thermal and mechanical analysis (see Figure 6.22). The ordinary rebars and the prestressing cables are not taking into account since Azenha (2009) has verified their marginal influence on the thermal analysis. For the mechanical analysis the reinforcement has also a reduced influence up to the hardened phase of concrete. However, if cracking occurs the influence of the reinforcement in the cracking process can be significant, but the computing time required for the inclusion of the rebars on the simulation has supported the decision to postpone this study for a future publication.

The values that characterize the heat generation rate defined by equation (6.72) are dependent on the type of cement used in the concrete of the beam. The following data was used to characterize the C50/60 self-compacting concrete (Ferreira et al. 2008): cement type I 52.5R $(332\,\mathrm{kg/m^3})$ with $A_T = 1.2053\mathrm{E}{+}09 \times 332$, $E_a = 47.51\,\mathrm{kJ/mol}$ and $Q_{total} = 383.13 \times 332\,\mathrm{kJ/m^3}$. The normalized heat generation rate $f(\alpha_T)$ used in the analysis is similar to that represented in Figure 6.12, and a value of 0.05 is considered for $\alpha_{T,init}$.

The domain is discretized with 20-noded hexahedral finite elements (see Figure 6.22), and a 3×3×3 Gauss-Legendre integration scheme is used. The conductivity of the material is constant and equal to 2.6 $\mathrm{Wm^{-1}K^{-1}}$, the volumetric heat capacity, ρc, is 2400.0 $\mathrm{kJm^{-3}K^{-1}}$ and the initial temperature is set to 25 ºC. The ambient temperature is defined by the heat curing regime imposed to the beam, and has the following development (see Figure 6.21): 30 ºC during 1h, followed by an increase of 10 ºC/h until a temperature of 80 ºC is reached, then this temperature is maintained during 3h, followed by a decrease of 10 ºC/h until the temperature of 20 ºC is attained. An equivalent heat transfer coefficient of 12.0 $\mathrm{Wm^{-2}K^{-1}}$ is assigned to all exposed faces of the beam. A Backward-Euler time integration scheme is used with an incremental time step of 3600s, being the total time of the analysis 72 h.

Figure 6.21 represents the temperature evolution at two points located in the cross section of the beam coinciding with the longitudinal symmetry plane, one at the top flange,

P_1 (0.0, 0.0, 210.0), and the other at the interior of the bottom flange, P_2 (0.0, 166.0, 18.0) (see Figure 6.20 and Figure 6.22). The temperature curing regime is also represented and it can be observed that the temperature at P_1 and P_2 points rapidly increases in the first 12 hours, and then decreases up to reach the ambient temperature. Temperature development in these points has similar shape format, but point P_1 located at the top flange presented a higher temperature decrease rate than point P_2 located at the interior of the bottom flange. Similar results were obtained by Ferreira et al. (2008), and the main difference between these two studies was registered in the peak temperature observed at about 12 hours after casting. A justification can reside on eventual small differences on the location of the points and on the boundary conditions adopted in both analyses, since this information is not clearly indicated in the reference Ferreira et al. (2008).

The temperature field for different time steps of the transient analysis is represented in Figure 6.22. It can be observed that due to the high convection heat transfer in the external surfaces, the temperature field decreases from the center of the U-shape beam walls to the external surfaces, and tends, with time, for the ambient temperature of 20 ºC.

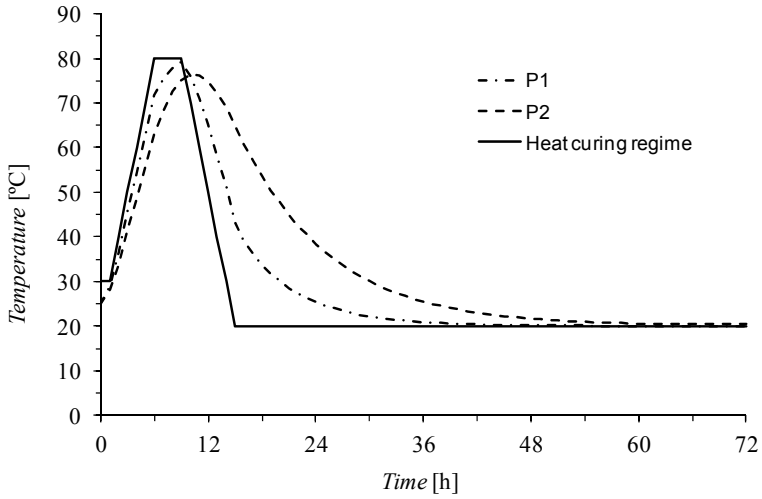

Figure 6.21 – Heat curing regime and temperature evolution at two points of the symmetry plane of the beam.

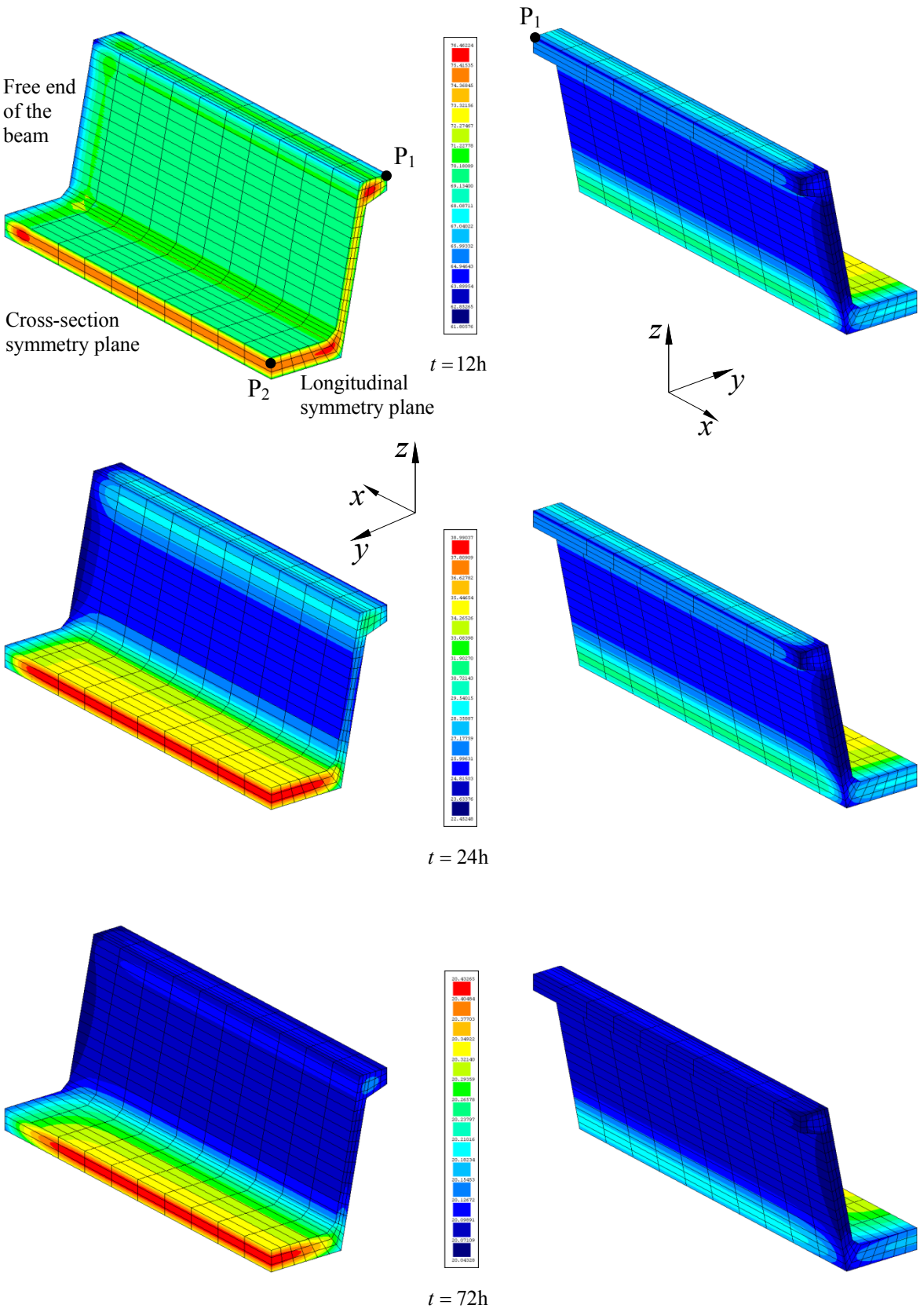

Figure 6.22 – Finite element mesh of the structure represented in Figure 6.20, and temperature field for different time steps of the transient analysis.

The temperature field from the thermal transient analysis was used in the mechanical transient model described in the previous section, in order to predict the corresponding stress field. The evolution of the material properties, such as compressive strength, tensile strength and modulus of elasticity, was simulated by using equation (6.133). The equivalent age concept (t_{eq}) obtained by equation (6.139) was used in equation (6.133), by substituting the time t by t_{eq}. The support conditions consist in prescribed displacements in *z* direction in all points of the bottom flange of the beam in order to simulate the vertical support provided by the formwork, and prescribed displacements to take into account the double symmetry of the beam. The material properties used in the numerical simulations are presented in Table 6.2. The values of the compressive strength, tensile strength and modulus of elasticity correspond to an age of 28 days for a C50/60 concrete strength class, and the value of the fracture energy for the same age is obtained according to CEB-FIP (1993). The value of the parameters that characterize the tensile softening diagram was also obtained according to CEB-FIP (1993) recommendations. The same finite element mesh and Gauss-Legendre integration scheme used in the thermal analysis is adopted in the mechanical transient analysis.

Table 6.2 - Values of the parameters of the constitutive model used in the mechanical numerical simulations.

Poisson's ratio	$\nu = 0.2$
Thermal coefficient	$\alpha = 1.0\times10^{-5}/^{\circ}\mathrm{C}$
Young's modulus	$E_{cm} = 37.0\ \mathrm{GPa}$
Compressive strength	$f_{cm} = 58.0\ \mathrm{MPa}$
Tension softening diagram	$f_{ctm} = 4.1\ \mathrm{MPa}$; $G_f^I = 198.53\times10^{-6}\ \mathrm{MN/m}$; $\xi_1 = 0.061$; $\alpha_1 = 0.15$; $\xi_2 = 0.4432$; $\alpha_2 = 0.09$
Parameter defining the mode I fracture energy available to the new crack	$p_2 = 0$
Shear retention factor	Exponential ($p_1 = 2$)
Crack bandwidth	Cubic root of the volume of the integration point
Threshold angle	$\alpha_{th} = 30^{\circ}$

$\alpha_1 = \sigma_{n,2}^{cr} / \sigma_{n,1}^{cr}$, $\alpha_2 = \sigma_{n,3}^{cr} / \sigma_{n,1}^{cr}$, $\xi_1 = \varepsilon_{n,2}^{cr} / \varepsilon_{n,u}^{cr}$, $\xi_2 = \varepsilon_{n,3}^{cr} / \varepsilon_{n,u}^{cr}$ (see Figure 3.6)

Three numerical analysis were performed, one considering the concrete with elastic behavior, a second one using the crack constitutive model, and the last one using the crack constitutive model and taking into account the autogenous shrinkage. For the evaluation of the autogenous shrinkage the Eurocode 2 model (EC2 2004) was considered. The concrete maturity was present in all numerical simulations.

Figure 6.23 and Figure 6.24 present the evolution of the normal stress in the *x* direction and the tensile strength development for points P_1 and P_2, respectively. From the analysis of the curves of Figure 6.23 it can be stated that until an age of about 13 h after casting, the stress development is similar in all the numerical simulations. An initial compression until an age of 9 h is observed, which is directly associated with the high imposed external heat curing that has conducted to an expansion of the concrete developing compression stresses in point P_1, located near the surface. A quite different behavior is observed after an age of 13 h for the analysis that assumes an elastic behavior for the concrete and for the analysis that simulates crack formation and propagation. The analysis assuming elastic behavior does not take into account that at this age the tensile stress is greater than the tensile strength and conducts to an unrealistic evolution of the stress field. Using the proposed updated 3D multi-fixed smeared crack model the real stress development at this point is captured. It is verified that at the moment of the interception of the stress development curve and the tensile strength curve, the concrete cracks and the stress starts decreasing immediately. It is also observed that the autogenous shrinkage has marginal effect on the stress evolution at this point.

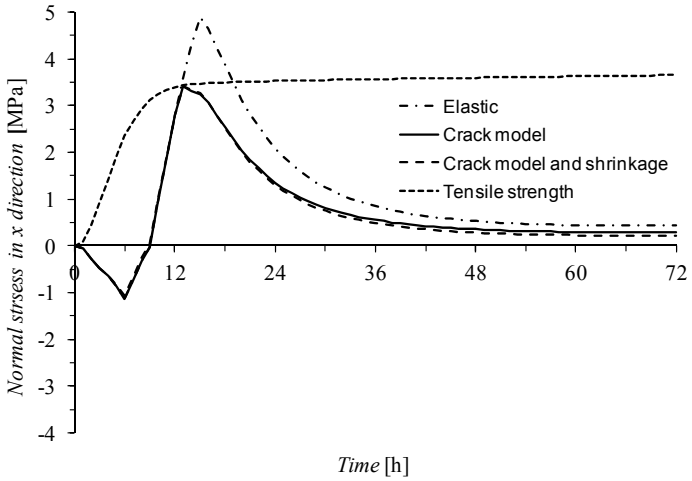

Figure 6.23 – Evolution of the normal stress in *x* direction and the tensile strength at point P_1.

From the analysis of the curves of Figure 6.24, which correspond to the stress evolution of the normal stress in *x* direction and the tensile strength development at point P_2, it can be concluded that all the simulations provide similar results. Only when the autogenous shrinkage is taken into account the numerical response has a small difference after an age of 18 h after casting. Up 9 h point P_2 is subjected to tensile stresses, and then to compressive stresses as observed in Figure 6.24. However, the tensile stress is always smaller than the tensile strength development, so concrete does not crack.

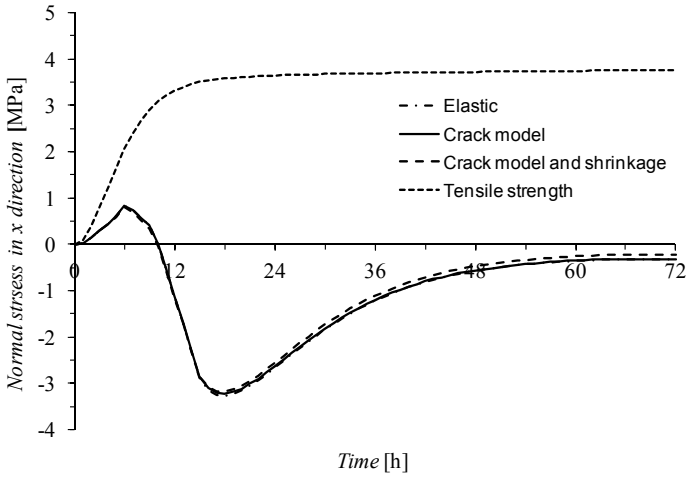

Figure 6.24 – Evolution of the normal stress in *x* direction and the tensile strength at point P_2.

The crack pattern for different times of the transient mechanical analysis using the crack constitutive model is represented in Figure 6.25. It is observed that for an age of 14 h, several cracks are formed, mainly in the exterior of the top flange and in the interception of the horizontal and lateral cross section walls near to the free end of the beam. In consequence of temperature decreasing, these cracks tend to close, as represented in the Figure 6.25 for an age of 24 h. However, for later stages the cracks reopen (see Figure 6.25 for t=72 h), which indicate that for the heat curing regime imposed to the beam, visible cracks can be formed, compromising the durability of the structure during its service life.

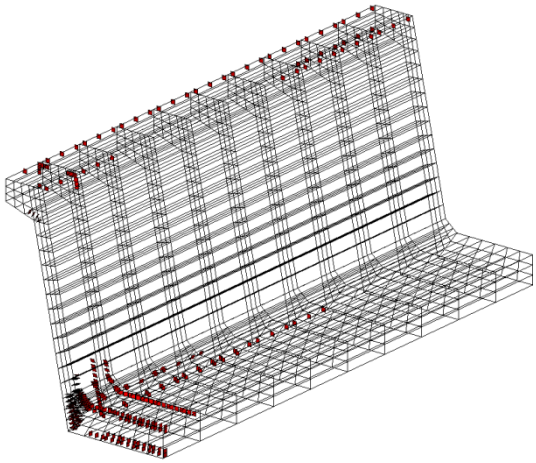

(a) $t = 14\text{h}$

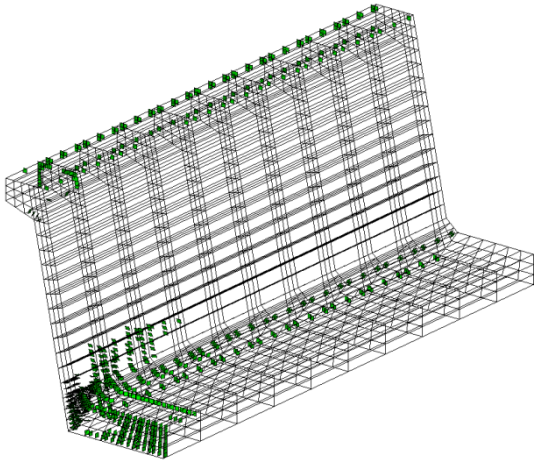

(b) $t = 24\text{h}$

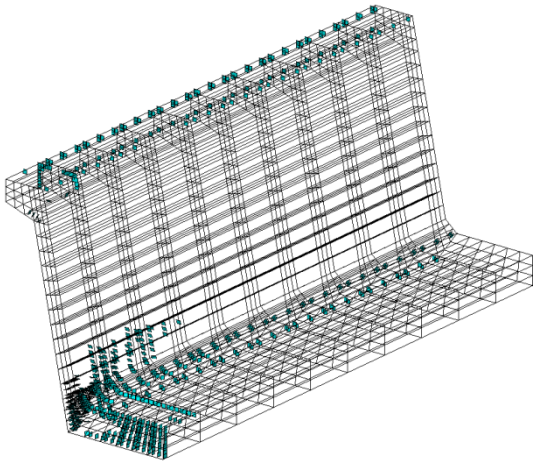

(c) $t = 72\text{h}$

Figure 6.25 – Crack pattern for different time steps of the transient analysis: (a) opening crack status; (b) closing crack status; (c) reopen crack status.

6.6 SUMMARY AND CONCLUSIONS

In the present chapter a thermal model with general purposes was described in detail, and all the relevant aspects for its implementation in the FEMIX computer code were discussed, in order to enable steady-state thermal analyses, transient linear thermal analyses or nonlinear thermal analyses. The heat development due to the hydration process during the concrete hardening phase was coupled to the thermal model, resulting in a model capable of simulating the behavior of a concrete structure since its early age. The

model was appraised using examples from the literature and a good agreement is observed. The formulations for the time-dependent deformations, such as shrinkage, creep and temperature were also described and they were coupled with the multi-fixed smeared 3D crack model. An example was studied to evidence the potentialities of this multiphysics approach.

Chapter 7

Conclusions

7.1 GENERAL CONCLUSIONS

The present work describes the development and the implementation of numerical tools for the simulation of the behavior of structures built with cement based materials. These tools have been implemented in the FEMIX computer code, which is based on the finite element method.

To simulate the behavior of concrete laminar structures failing in bending and shear, a model based on the Reissner-Mindlin theory in the context of layered shells has been developed with special emphasis on the treatment of the shear behavior. The model is based on a multi-directional fixed smeared crack concept. Crack propagation through the thickness of a slab or shell can be simulated by considering the nonlinear behavior of each of its layers. Fracture mode I is modeled with a crack stress vs. crack strain softening or stiffening diagram. To simulate the out-of-plane shear strain gradient that occurs in punching regions, a softening diagram is proposed to model, after crack initiation, the corresponding shear components. To simulate slabs on grade with an eventual loss of contact between the slab and the ground, linear and nonlinear support conditions, unilateral or not, have been implemented. In order to increase the robustness of the numerical simulations, the internal algorithms associated with the stress update and the critical crack status changes have been improved with respect to the previous version of the code.

To improve the performance of the numerical model in terms of predicting the behavior of concrete structures where shear and flexural/shear failure modes are critical, two alternative strategies are proposed for the treatment of the crack shear component. One is supported on a total crack shear stress-shear strain approach to simulate the degradation of the shear stress transfer with the crack opening evolution, and the other is based on a constitutive softening relation between the crack shear stress and crack shear strain components.

To predict the behavior of structures discretized with solid finite elements, a multi-fixed smeared 3D crack model is proposed. Softening diagrams are available in this model not only to model the fracture mode I, but also the two fracture sliding modes. With this strategy, the simulation of concrete structures governed by shear and punching failures modes can be improved.

A thermal model with general purposes has been implemented in the code, in order to be possible to perform steady-state thermal analysis, transient linear thermal analysis or nonlinear thermal analysis. The heat development due to the hydration process during the concrete hardening phase was coupled to the thermal model, resulting a model capable of simulating the behavior of concrete structures since its early ages.

A transient analysis algorithm was coupled to the developed multi-fixed smeared 3D crack model in order to allow the simulation of time-dependent effects in cement based materials, such as shrinkage, creep and temperature.

The predictive performance of these numerical tools was appraised by comparison with the results of numerical simulations available in the literature, and with the results obtained from experimental programs carried out with specimens made with steel fiber reinforced self-compacting concrete, SFRSCC, (Barros et al. 2005a) or in the context of assessing the effectiveness of Carbon Fibre Reinforced Polymer (CFRP) composite materials for the flexural and shear strengthening of reinforced concrete beams (Barros et al. 2011). It is verified that the proposed techniques are crucial to assure accurate numerical simulations, namely the use of the out-of-plane shear softening diagrams to simulate the behavior of

laminar structures failing in punching, as well as the adoption of shear-sliding softening diagrams in the multi-fixed smeared 3D crack model applied to structures discretized with solid finite elements. The solution procedures implemented in the scope of the present work for the nonlinear finite element analysis of structures are also essential to increase the robustness of the numerical simulations.

7.2 RECOMMENDATIONS FOR FUTURE RESEARCH

The pre-established objectives for the present work were successfully attained. In fact, a crack constitutive model for laminar structures was successfully implemented, the numerical instabilities associated with the internal algorithms of the stress updated have been overcome, and the accuracy of the numerical simulations was improved by the introduction in the computer code of new solution procedures for nonlinear finite element analysis. A multi-fixed smeared 3D crack model for the simulation of complex structures was implemented, and the time-dependent effects were also taken into account, enabling the transient analysis of cement based structures. However, some aspects deserve extra improvements in order to increase the accuracy, applicability and robustness of the developed models.

The coupling between the softening diagrams in order to simulate the interaction between crack opening and crack sliding should be investigated.

The behavior of concrete between cracks in the developed multi-fixed smeared 3D crack model was assumed to be linear-elastic. It is known, however, that the concrete behavior in compression is nonlinear and exhibits some irreversible deformations. Thus, a model based on the plasticity theory should be introduced in the developed 3D model resulting in an elasto-plastic multi-fixed smeared 3D crack model to simulate the behavior of concrete structures.

The transient nonlinear thermal model should be complemented, in order to allow the code to perform thermo-mechanical analyses of structures under fire.

The moisture transfer phenomenon should be coupled to the thermal and mechanical model, in order to add to the code the capability of performing thermo-hygro-mechanical analyses for concrete structures.

References

Abaqus (2002). ABAQUS Theory Manual – version 6.3 documentation, US. [available in CD-ROM].

ACI (1992), "Prediction of creep, shrinkage, and temperature effects in concrete structures (Reapproved 1997)", *Technical committee document 209R-92*, American Concrete Institute (ACI), Committee 209, 47 pp.

ACI (1993), "Guide for specifying, proportioning, mixing, placing, and finishing steel fiber reinforced concrete (Reapproved 1998)", *Technical committee document 544.3R-93*, American Concrete Institute (ACI), Committee 544, 10 pp.

ACI (1996), "State-of-the-art report on fiber reinforced concrete (Reapproved 2002)", *Technical committee document 544.1R-96*, American Concrete Institute (ACI), Committee 544, 66 pp.

ACI (2001), "Control of cracking in concrete structures", *Technical committee document 224R-01*, American Concrete Institute (ACI), Committee 224, 46 pp.

ACI (2005), "Building code requirements for structural concrete (ACI 318-05) and commentary (ACI 318R-05)", *Technical committee document*, American Concrete Institute (ACI), Committee 318, 430 pp.

ACI Committee 440 (2007), "Guide for the design and construction of externally bonded FRP systems for strengthening concrete structures", *American Concrete Institute*, 118 pp.

Afonso, C.L.M. (2010), "Lajes Fungiformes. Contribuições para a compreensão do seu comportamento (Flat slabs. Contributions to the understanding of their behavior)", *PhD Thesis*, Civil Eng. Dept., Faculty of Engineering, University of Porto, Portugal [in Portuguese].

Altoubat S.A. and Lange, D.A. (2001), "Creep, shrinkage, and cracking of restrained concrete at early age", *ACI Materials Journal*, 98(4), 323-331.

Arrea, M. and Ingraffea, A.R. (1982), "Mixed-mode crack propagation in mortar and concrete", *Report nº 81-13*, Department of Structural Engineering, Cornell University, Ithaca, N.Y.

Azenha, M.A.D. (2004), "Comportamento do betão nas primeiras idades. Fenomenologia e análise termo-mecânica (Behavior of concrete at early ages. Phenomenology and thermo-mechanical analysis)", *MSc Thesis*, Faculty of Engineering of the University of Porto [in Portuguese].

Azenha, M.A.D. (2009), "Numerical simulation of the structural behaviour of concrete since its early ages", *PhD Thesis*, Faculty of Engineering of the University of Porto.

Azevedo, A.F.M. (1985), "Análise não linear de estruturas planas de betão armado pelo método dos elementos finitos (Nonlinear analysis of reinforced concrete plane structures by the finite element method)", *MSc Thesis*, Civil Eng. Dept., Faculty of Engineering, University of Porto, Portugal [in Portuguese].

Azevedo, A.F.M. (1996), "Mecânica dos sólidos (Solid mechanics)", Civil Eng. Dept., Faculty of Engineering, University of Porto, Portugal [in Portuguese].

Azevedo, A.F.M, Barros, J.A.O., Sena-Cruz, J.M. and Ventura-Gouveia, A. (2003), "Software no ensino e no projecto de estruturas (Software in education and in project of structures)", *III Engineering Luso-Mozambican Congress, Eds. J.S. Gomes, C.F. Afonso, C.C. António e A.S. Matos*, volume I, 81-92, Maputo, Mozambique, 19-21 of August [in Portuguese].

Barros, J.A.O. (1989), "Modelos de análise de estruturas laminares e de compósitos laminados (Models for the analysis of laminar structures and laminate composites)", *MSc Thesis*, Civil Eng. Dept., Faculty of Engineering, University of Porto, Portugal [in Portuguese].

Barros, J.A.O. (1995), "Comportamento do betão reforçado com fibras - análise experimental e simulação numérica (Behavior of FRC – experimental analysis and numerical simulation)", *PhD Thesis*, Civil Eng. Dept., Faculty of Engineering, University of Porto, Portugal [in Portuguese].

Barros, J.A.O. and Figueiras, J.A. (1998), "Experimental behaviour of fiber concrete slabs on soil", *Journal Mechanics of Cohesive-frictional Materials*, Vol. 3, 277-290.

Barros, J.A.O. and Figueiras, J.A. (2001), "Nonlinear analysis of steel fibre reinforced concrete slabs on grade", *Computers & Structures Journal*, 79(1), 97-106.

Barros, J.A.O., Gettu, R. and Barragan, B.E. (2004), "Material nonlinear analysis of Steel fibre reinforced concrete beams failing in shear", *6th International RILEM Symposium on fibre reinforced concrete - BEFIB 2004*, Edts. M. di Prisco, R. Felicetti, G.A. Plizarri, Vol. 1, 711-720, 20-22 September.

Barros J.A.O. and Fortes A.S. (2005), "Flexural strengthening of concrete beams with CFRP laminates bonded into slits", *Journal Cement and Concrete Composites*, 27(4), 471-480.

Barros, J.A.O., Pereira, E.N.B., Cunha, V.M.C.F., Ribeiro, A.F., Santos, S.P.F. and Queirós, P.A.A.A.V. (2005a), "PABERFIA - Lightweight sandwich panels in steel fiber reinforced self compacting concrete", *Technical Report 05-DEC/E-29*, Dep. Civil Eng., School Eng. University of Minho, 63 pp, November.

Barros J.A.O., Cunha, V.M.C.F., Ribeiro, A.F. and Antunes, J.A.B. (2005b), "Post-cracking behaviour of steel fibre reinforced concrete", *RILEM Materials and Structures Journal*, 38(275), 47-56.

Barros, J.A.O., Ventura-Gouveia, A., Sena-Cruz, J.M., Antunes, J.A.B. and Azevedo, A.F.M. (2005c), "Design methods for steel fiber reinforced concrete industrial floors", *ConMat'05 and Mindess Symposium, N. Banthia, T. Uomoto, A. Bentur and S.P. Shah (eds.)*, Vancouver, 10 pp.

Barros, J.A.O., Pereira, E.B. and Santos, S.P.F. (2007a), "Lightweight panels of steel fiber reinforced self-compacting concrete", *Journal of Materials in Civil Engineering*, 19(4), 295-304.

Barros, J.A.O., Pereira, E.N.B., Ventura-Gouveia, A. and Azevedo, A.F.M. (2007b), "Numerical simulation of thin steel fiber self-compacting concrete structures", *ACI 435/544 Fall 2007 Puerto Rico Session 1: Deflection and stiffness issues in FRC and thin structural elements (Structural Implications and Material Properties)*, in CD, 25 pp.

Barros J.A.O., Dalfré G.M. and Dias J.P.S.E. (2008), "Numerical simulation of continuous RC slabs strengthened using NSM technique", *2nd International Conference on Concrete Repair, Rehabilitation and Retrofitting (ICCRRR 2008)*, 24-26 November.

Barros, J.A.O., Costa, I.G. and Ventura-Gouveia, A. (2011), "CFRP flexural and shear strengthening technique for RC beams: experimental and numerical research", *Advances in Structural Engineering Journal*, doi:10.1260/1369-4332.14.3.551.

Barzegar, F. and Maddipudi, S. (1997a), "Three-dimensional modeling of concrete structures. I: plain concrete", *Journal of Structural Engineering*, ASCE, 123(10), 1339-1346.

Barzegar, F. and Maddipudi, S. (1997b), "Three-dimensional modeling of concrete structures. II: Reinforced Concrete", *Journal of Structural Engineering*, ASCE, 123(10), 1347-1356.

Bashir-Ahmed, M. and Xiao-zu, S. (2004), "Arc-length technique for nonlinear finite element analysis", *Journal of Zhejiang University SCIENCE*, 5(5), 618-628.

Bastos, P.K.X. and Cincotto, M.A. (2000), "Retracção de compósitos à base de cimento (Shrinkage of cement-based composites)", São Paulo University, Brasil [In Portuguese].

Batoz, J.L. and Dhatt, G. (1979), "Incremental displacement algorithms for nonlinear problems", *Int. J. Num. Methods Engrg.*, 14 , 1262-1267.

Bazant, Z.P. and Wu S.T. (1973), "Dirichlet series creep function for aging concrete", *Journal of Engineering Mechanics Division*, ASCE, 99(EM2), 367-387.

Bazant, Z.P. and Oh, B.H. (1983), "Crack band theory for fracture of concrete", *Materials and Structures*, RILEM, 16(93), 155-177.

Bazant, Z.P. (1984), "Microplane model for strain controlled inelastic behavior", *In: Desai, C.S., Gallagher, R.H. (Eds.)*, Mechanics of Engineering Materials. J. Wiley, London, 5–59 (Chapter 3).

Bazant, Z.P. (1988), "Material models for structural creep analysis", *Mathematical Modelling of Creep and Shrinkage of Concrete*, Z.P. Bazant (ed.), John Wiley & Sons Ltd., 99-215.

Bazant, Z.P., and Baweja, S. (2000), "Creep and shrinkage prediction model for analysis and design of concrete structures – Model B3", *Adam Neville Symposium: Creep and Shrinkage-Structural Design Effects*, ACI SP-194, A. Al-Manaseer (ed.), Am. Concrete Institute, Farmington Hills, Michigan, 1-83.

Bissonnette, B., Pigeon, M. and Vaysburd, A.M. (2007), "Tensile creep of concrete: study of its sensitivity to basic parameters", *ACI Materials Journal – Technical Paper*, July-August, 360-368.

Bonaldo E., Barros J.A.O. and Lourenço P.J.B. (2008), "Efficient strengthening technique to increase the flexural resistance of existing RC slabs", *Journal of Composites for Construction*, 12(2), 149-159.

Bosnjak, D. (2000), "Self-induced cracking problems in hardening concrete structures", *PhD Thesis*, Structural Eng. Dept., Norwegian University of Science and Technology, Trondheim, Norway.

CEB-FIP (1993), "Model Code 1990 - Design code", *Comité Euro-International du Béton*, Thomas Telford, Lausanne, Switzerland.

Cook, R.D, (1995), "Finite element modeling for stress analysis", *John Wiley & Sons*, Inc., US.

Cornelissen, H.A.W., Hordijk, D.A. and Reinhardt, H.W. (1986), "Experimental determination of crack softening characteristics of normalweight and lightweight concrete", *HERON*, 31(2), 45-56.

Costa, I.G., and Barros, J.A.O. (2010), "Flexural and shear strengthening of RC beams with composites materials – the influence of cutting steel stirrups to install CFRP strips", *Cement and Concrete Composites Journal*, 32, 544-553.

Crisfield, M.A. (1983), "An arc-length method including line searches and accelerations", *International Journal for Numerical Methods in Engineering*, 19, 1269-1289.

Crisfield, M.A. (1986), "Snap-through and snap-back response in concrete structures and the dangers of under-integration", *International Journal for Numerical Methods in Engineering*, 229, 751-767.

Crisfield, M.A. (1991), "Non-linear finite element analysis of solids and structures. Volume 1: essentials", *John Wiley & Sons*, Chichester, England.

D'Ambrosia, M. D., Altoubat, S. A., Park, C. and Lange, D. A. (2001), "Early age tensile creep and shrinkage of concrete with shrinkage reducing admixtures", in *Creep, Shrinkage and Durability Mechanics of Concrete and other Quasi-Brittle Materials*, ed. F. Ulm, Z. Bazant, F.H. Wittman, Proc. of CONCREEP '01, 685-690, Boston, Aug. 13-15.

Dahlblom O. and Ottosen N.S. (1990), "Smeared crack analysis using generalized fictitious crack model", *Journal of Engineering Mechanics*, ASCE, 116(1), 55-76.

Dalfré, G.M., Barros, J.A.O., Machado, D. (2011), "Comportamento da ligação varões de aço-betão no contexto de reforço ao corte segundo a técnica ETS para vigas de betão armado (Behavior of the connection of steel bars-concrete in the context of ETS shear strengthening technique for reinforced concrete beams)", *53º Brazilian Conference on Concrete (IBRACON 2011)* [In Portuguese].

de Borst, R and Nauta, P. (1985), "Non-orthogonal cracks in a smeared finite element model", *Engineering Computations*, 2 (1), 35-46.

de Borst, R. (1986), "Non-linear analysis of frictional materials", *PhD thesis*, Delft University Technology.

de Borst, R. (1987), "Smeared cracking, plasticity, creep and thermal loading - a unified approach", *Computational Methods in Applied Mechanics Engineering*, 62, 89-110.

de Borst, R and van den Boogaard, A.H. (1984), "Finite-element modeling of deformation and cracking in early-age concrete", *Jounal of Engineering Mechanics*, ASCE, 120(12), 2519-2534.

de Borst, R. and Gutiérrez, M.A. (1999), "A unified framework for concrete damage and fracture models including size effects", *International Journal of Fracture*, 95, 261-277.

de Borst, R. (2002), "Fracture in quasi-brittle materials: a review of continuum damage-based approaches", *Engineering Fracture Mechanics*, 69, 95-112.

de Borst, R., Remmers, J.J.C., Needleman, A. and Marie-Angele, A. (2004), "Discrete vs. smeared crack models for concrete fracture: bridging the gap", *Int. J. Numer. Anal. Meth. Geomech.*, 28, 583–607.

Dhonde, H.B., Mo, Y.L., Hsu, T.T.C. and Vogel, J. (2007), "Fresh and hardened properties of self-consolidating fiber-reinforced Concrete", *ACI Materials Journal*, 104(5), September-October, 491-500.

Dias, S.J.E. and Barros, J.A.O. (2010) "Performance of reinforced concrete T beams strengthened in shear with NSM CFRP laminates", *Engineering Structures*, 32(2), 373-384.

EC2 (2004), "Eurocode 2 - Design of Concrete Structures—Part 1-1: General rules and rules for buildings", *CEN, EN 1992-1-1*, Brussels, Belgium, 225 pp.

El-Hacha R. and Rizkalla S.H. 2004, "Near-surface-mounted fiber-reinforced polymer reinforcements for flexural strengthening of concrete structures", *ACI Structural Journal*, 101(5), 717-726.

Ferreira, D., Azenha, M. and Faria R. (2008), "Parametric study of the influence of heat curing methods in residual stresses of a precast concrete bridge beam", *CCC2008 – Challenges for Civil Construction – International Conference, Torres Marques et al. (eds.)*, Paper published in CD-FEUP, 11 pp., Porto, 16-18 April.

Fib (2001), "Punching of structural concrete slabs", *fib Bulletin nº 12 Technical report*, Lausanne, Switzerland, 307 pp.

Fonseca, E.M.M (1998), "Modelação Numérica do comportamento termo-mecânico de perfis metálicos sujeitos à acção do fogo (Numerical modelling of thermomechanical behaviour of hot-rolled steel profiles submitted to fire)", *MSc Thesis*, University of Porto, Portugal [in Portuguese].

Henriques, A.A.R. (1998), "Aplicação de novos conceitos de segurança no dimensionamento do betão estrutural (Application of new safety concepts in the design of structural concrete)", *PhD Thesis*, University of Porto, Portugal [in Portuguese].

Hofstetter, G. and Mang, H.A. (1995), "Computational mechanics of reinforced concrete structures", *Friedr. Vieweg & Sohn Verlagsgesellschaft mbH*, Germany.

Holman, J.P. (1986), "Heat transfer", International Student Edition, *McGraw-Hill Book Company*, sixth edition.

Huang, Hou-Cheng (1989), "Static and dynamic analyses of plates and shells – Theory, software and applications", *Springer-Verlag Berlin Heidelberg*.

Incropera, F.P., DeWitt , D.P., Bergman,T.L., Lavine, A.S. (2006), "Fundamentals of heat and mass transfer", *Wiley*, sixth edition.

Jirásek, M. and Zimmermann, T. (2001), "Embedded crack model. Part II: Combination with smeared cracks", *Int. J. Numer. Meth. Engng*, 50:1291-1305.

Koenigsfeld, D. and Myers, J.J. (2003), "Secondary reinforcement for fiber reinforced polymers reinforced concrete panels", *Report CIES 03-45*, Center for Infrastructure Engineering Studies, University of Missouri-Rolla.

Lewis, R.W., Morgan, K., Thomas, H.R. and Seetharamu, K.N. (1996), "The finite element method in heat transfer analysis", *John Wiley & Sons, Ltd*.

Lewis, R.W., Nithiarasu, P. and Seetharamu, K.N. (2004), "Fundamentals of the finite element method for heat and fluid flow", *John Wiley & Sons, Ltd*.

Li, V.C. and Fischer G. (2002), "Reinforced ECC – An evolution from materials to structures", *Proceedings of the 1st fib Congress – Session 5: Composite Structures*, Osaka, Japan, October, 105-122.

Lienhard IV, J.H. and Lienhard V, J.H. (2005), "A heat transfer textbook", *Phlogiston Press*, third Edition, Cambridge, Massachusetts, U.S.A.

Lourenço, P.B, de Borst, R. and Rots, J.G. (1997), "A plane stress softening plasticity model for orthotropic materials", *Int. J. Numer. Meth. Engng.*, 40, 4033-4057.

Lura, P. and van Breugel, K. (2001), "Thermal properties of concrete: sensitivity studies", *Report BE96-3843/2001:15-X*, Published by Department of Civil & Mining Engineering Division of Structural Engineering, Delft University of Technology.

Mindlin, R.D. (1951), "Influence of rotary inertia and shear on flexural motions of isotropic elastic plates", *Journal of Appl. Mech.*, 18(1), Trans. ASME, Vol. 73, 31-38.

Moraes Neto, B.N., Barros, J.A.O. and Melo, G. (2012), "Punçoamento de lajes de betão reforçado com fibras (Punching of fiber reinforced concrete slabs)", *Technical Report nº 12-DEC/E-10*, Department of Civil Engineering of the University of Minho [in Portuguese]. [in press].

Most T. and Bucher C. (2006), "Energy-based simulation of concrete cracking using an improved mixed-mode cohesive crack model within a meshless discretization"*, Int. J. Numer. Anal. Meth. Geomech.*, doi: 10.1002/nag.536.

Naaman, A.E. and Reinhardt, H.W., (2003), "High performance fiber reinforced cement composites HPFRCC-4: International RILEM Workshop", *Materials and Structures*, Vol. 36, December, 710-712.

Naaman, A.E. (2007), "High performance fiber reinforced cement composites: classification and applications", *CBM-CI International Workshop*, Karachi, Pakistan, 10-11 December, 389-401.

Ngo, Tuan. D. (2001), "Punching shear resistance of high-strength concrete slabs", *Electronic Journal of Structural Engineering*, 1(1), 2-14.

Okamura, H. (1997), "Ferguson Lecture for 1996: Self-compacting high-performance concrete", *Concrete International*, ACI 19(7), 50-4.

Okamura, H. and Ouchi, M. (2003), "Self-compacting concrete", *Journal of Advanced Concrete Technology*, Japan Concrete Institute, 1 (1), 5-15.

Oliver, J. (1989), "A consistent characteristic length for smeared cracking models", *Int. J. Num. Meth. Engng.*, 28(2), 461-474.

Oñate, E. (1995), "Cálculo de estructuras por el metodo de elementos finitos. Análisis estático lineal", *Centro Internacional de Métodos Numéricos en Ingeniería, 2ª edicion*, Setembro.

Ottosen, N. and Petersson, H. (1992), "Introduction to the finite element method", *Prentice Hall*.

Ozbolt J. and Reinhardt H.W. (2000), "Numerical study of mixed-mode fracture in concrete structures", *Otto-123 Graf-Journal*, Vol. 11.

Pereira, E.N.B. (2006), "Steel fibre reinforced self-compacting concrete: from material to mechanical behavior", *Dissertation for Pedagogical and Scientific Aptitude Proofs*, Department of Civil Engineering, University of Minho, 188 pp.

Pereira, E.B., Barros, J.A.O. and Camões, A.F.F.L. (2008), "Steel fiber reinforced self-compacting concrete – experimental research and numerical simulation", *Journal of Structural Engineering*, 134(8), 1310-1321.

Polak, M.A. (2005), "Shell finite element analysis of RC plates supported on columns for punching shear and flexure", *Engineering Computations: International Journal for Computer-Aided Engineering and Software*, 22(4), 409-428.

Póvoas, R.H.C.F. (1991), "Modelos não-lineares de análise e dimensionamento de estruturas laminares de betão incluindo efeitos diferidos (Nonlinear models of analysis and design of concrete laminar structures including time-dependent effects)", *PhD Thesis*, Faculty of Engineering, University of Porto, Portugal [in Portuguese].

Precast/Prestressed Concrete Institute (2003), "Interim guidelines for the use of self-consolidating concrete in precast/prestressed concrete institute member plants", *TR-6-03*, Chicago, Illinois, USA.

Reihardt, H. W., Blaauwendraad, J., and Jongedijk, J. (1982), "Temperature development in concrete structures taking account of state dependenty properties", *Proc. Int. Conf. Concrete at Early Ages*, Paris, France.

Reissner, E. (1945), "The effect of transverse shear deformation on the bending elastic plates", *Journal Appl. Mech.*, 12, 69-76.

Riks, E. (1970), "On the numerical solution of snapping problems in the theory of elastic stability", *Dissertation*, Stanford University, Stanford, California, USA.

Rots, J.G., Nauta, P., Kusters; G.M.A., and Blaauwendraad, J. (1985), "Smeared crack approach and fracture localization in concrete", *HERON*, 30(1), 1-48.

Rots, J.G. and de Borst, R. (1987), "Analysis of mixed-mode fracture in concrete", *Journal of Engineering Mechanics*, ASCE, 113(11), 1739-1758.

Rots, J.G. (1988), "Computational modeling of concrete fracture", *PhD Thesis*, Delft University of Technology.

Sena-Cruz, J.M. (2004), "Strengthening of concrete structures with near-surface mounted CFRP laminate strips", *PhD Thesis*, Department of Civil Engineering, University of Minho, http://www.civil.uminho.pt/composites.

Sena-Cruz, J.M., Barros, J.A.O., Ribeiro, A.F., Azevedo, A.F.M. and Camões, A.F.F.L. (2004), "Stress-crack opening relationship of enhanced performance concrete", *9th Portuguese Conference on Fracture*, ESTSetubal, Portugal, 395-403.

Sena-Cruz, J.M., Barros, J.A.O., Azevedo, A.F.M. and Ventura-Gouveia, A. (2007), "Numerical simulation of the nonlinear behavior of RC beams strengthened with NSM CFRP strips", *Proceedings of CMNE/CILAMCE Congress*, FEUP, Porto, Portugal, 13-15 June.

Silva, V.D. (2006), "Mechanics and strength of materials", *Springer-Verlag Berlin Heidelberg*.

Silveira, A.P.C. (1993), "A influência das acções térmicas no comportamento de pontes de betão armado pré-esforçado (The influence of the thermal actions in the behavior of prestressed concrete bridges)", *PhD Thesis*, IST-LNEC, Lisbon [in Portuguese].

Stevens N.J. (1987), "Analytical modelling of reinforced concrete subjected to monotonic and reversed loadings", *Publication No. 87-1, ISBN 0-7727-7088-3*, University of Toronto, January.

Täljsten B., Carolin A. and Nordin H. (2003), "Concrete structures strengthened with near surface mounted reinforcement of CFRP". *Advances in Structural Engineering*; 6(3), 201-213.

Timoshenko, S.P. and Woinkowsky-Krieger, S. (1959), "Theory of Plates and Shells", *McGraw-Hill Book Company*, NY, second edition.

Ugural, A.C. (1981), "Stresses in plates and shells", *McGraw-Hill, Inc.*

van Zijl, G.P.A.G, de Borst, R. and Rots, J.G. (2001), "A numerical model for the time-dependent cracking of cementitious materials" , *Int. J. Numer. Meth. Engng.*, doi: 10.1002/nme.211.

Vandewalle, L. *et al.* (Technical Committee) (2002), "Test and design methods for steel fibre reinforced concrete - Final Recommendation", *Materials and Structures*, 35(253), 579-582.

Ventura-Gouveia, A. (1996), "Análise de estruturas reticuladas segundo o método dos deslocamentos (Analysis of Structures According to the Displacement Method)", *Report to obtain the graduation in Civil Engineering by the School of Engineering of the University of Minho*, September [in Portuguese].

Ventura Gouveia, A. (2000), "Análise Experimental e Simulação Numérica de Elementos de Barra de Pórtico Tridimensional de Betão Armado (Experimental Analysis and Numerical Simulation of Reinforced Concrete 3D Frame Elements)", *MSc Thesis*, Department of Civil Engineering, University of Minho, July [in Portuguese].

Ventura-Gouveia, A., Barros, J.A.O., Azevedo, A.F.M. and Sena-Cruz, J.M. (2006), "Implementação da técnica do arc-length e métodos relacionados no programa de elementos finitos FEMIX (Arc-length and related methods in FEMIX finite element program)", *Technical Report nº 06-DEC/E-20*, Department of Civil Engineering of the University of Minho, 50 pp., November [in Portuguese].

Ventura-Gouveia, A., Barros, J.A.O., Azevedo, A.F.M. and Sena-Cruz, J.M. (2007), "Crack Constitutive Model to Simulate the Behavior of Fiber Reinforced Concrete Structures Failing in Punching", *CMNE 2007 - Congress on Numerical Methods in Engineering and XXVIII CILAMCE - Iberian Latin American Congress on Computational Methods in Engineering*, Abstract pp. 287, Paper nº 232 published in CD – FEUP, 13 pp., Porto, 13-15 June.

Ventura-Gouveia, A., Barros, J.A.O., Azevedo, A.F.M. and Sena-Cruz, J.M. (2008), "Multi-fixed smeared 3D crack model to simulate the behavior of fiber reinforced concrete structures", *CCC2008 – Challenges for Civil Construction – International Conference, Torres Marques et al. (eds.)*, Abstract pp. 82-83, Paper published in CD – FEUP, 11 pp., Porto, 16-18 April.

Ventura-Gouveia, A., Barros, J.A.O. and Azevedo, A.F.M. (2011), "Crack constitutive model for the prediction of punching failure modes of fiber reinforced concrete laminar structures", *Computers & Concrete*, 8(6), 735-755.

Vila Real, P.J.M.M.F. (1988), "Modelação por elementos finitos do comportamento térmico e termo-elástico de sólidos sujeitos a elevados gradientes térmicos (Finite element modeling of thermal and thermo-elastic behavior of solids subjected to high thermal gradients)", *MSc Thesis*, Faculty of Engineering, University of Porto, Portugal [in Portuguese].

Wang, C.H. (1996), "Introduction to fracture mechanics", *DSTO-GD-0103*, Airframes and Engines Division Aeronautical and Maritime Research Laboratory.

Weiss, W. J., Yang, W. and Shah, S.P. (1998), "Shrinkage cracking of restrained concrete slabs", *Journal of Engineering Mechanics*, July, 765-774.

Weiss, W. J. (1999), "Prediction of early-age shrinkage cracking in concrete", *PhD Thesis*, Northwestern University, Evanston, Illinois.

Wempner, G.A. (1971), "Discrete approximations related to nonlinear theories of solids", *Int. J. Solids & Structures*, 7, 1581-1599.

Yu, R.C., Gonzalo, R. and Chaves, E.W.V. (2007), "A comparative study between discrete and continuum models to simulate concrete fracture", *Engineering Fracture Mechanics*, doi:10.1016/j.engfracmech.2007.03.031.

Zhou, C.E. and Vecchio, F.J. (2005), "Nonlinear finite element analysis of reinforced concrete structures subjected to transient thermal loads", *Computers and Concrete*, 2(6), 455-479.

Zienkiewicz, O.C. and Taylor, R.L. (2000a), "The finite element method (Fifth edition) Volume 1: The Basis", *Butterworth-Heinemann*.

Zienkiewicz, O.C. and Taylor, R.L. (2000b), "The finite element method (Fifth edition) Volume 2: Solid Mechanics", *Butterworth-Heinemann*.

Appendix A

Procedure for the determination of $\delta\lambda^q$

The deduction of equation (2.20), which permits the determination of $\delta\lambda^q$, is exposed below.

The incremental displacement vector at the iteration q of combination n is given by

$$\Delta\underline{a}_n^q = \sum_{i=1}^{q} \delta\underline{a}_n^i = \Delta\underline{a}_n^{q-1} + \delta\underline{a}_n^q \tag{A.1}$$

being $\Delta\underline{a}_n^{q-1}$ the incremental displacement vector of the previous iteration, $q-1$, and $\delta\underline{a}_n^q$ the iterative displacement vector defined by equation (2.15), here rewritten for convenience

$$\delta\underline{a}_n^q = \delta\overline{\underline{a}}_n^{q-1} + \delta\lambda^q \delta\overline{\underline{a}}_n^{q-1} \tag{A.2}$$

Substituting (A.2) into (A.1) yields

$$\Delta\underline{a}_n^q = \sum_{i=1}^{q} \delta\underline{a}_n^i = \Delta\underline{a}_n^{q-1} + \delta\underline{a}_n^q = \Delta\underline{a}_n^{q-1} + \delta\overline{\underline{a}}_n^{q-1} + \delta\lambda^q \delta\overline{\underline{a}}_n^{q-1} \tag{A.3}$$

The product of $\left[\Delta a_n^q\right]^T \Delta a_n^q$ is developed taking into account equation (A.3), resulting

$$
\begin{aligned}
\left[\Delta\underline{a}_n^q\right]^T\Delta\underline{a}_n^q &= \Delta\underline{a}_n^q\left|\Delta\underline{a}_n^q\right.\\
&= \left(\Delta\underline{a}_n^{q-1}+\delta\underline{a}_n^{q-1}+\delta\lambda^q\delta\underline{\underline{a}}_n^{q-1}\right)\left|\left(\Delta\underline{a}_n^{q-1}+\delta\underline{a}_n^{q-1}+\delta\lambda^q\delta\underline{\underline{a}}_n^{q-1}\right)\right.\\
&= \left(\Delta\underline{a}_n^{q-1}+\delta\underline{a}_n^{q-1}+\delta\lambda^q\delta\underline{\underline{a}}_n^{q-1}\right)\left|\Delta\underline{a}_n^{q-1}+\right.\\
&\quad+\left(\Delta\underline{a}_n^{q-1}+\delta\underline{a}_n^{q-1}+\delta\lambda^q\delta\underline{\underline{a}}_n^{q-1}\right)\left|\delta\underline{a}_n^{q-1}+\right.\\
&\quad+\left(\Delta\underline{a}_n^{q-1}+\delta\underline{a}_n^{q-1}+\delta\lambda^q\delta\underline{\underline{a}}_n^{q-1}\right)\left|\delta\lambda^q\delta\underline{\underline{a}}_n^{q-1}\right.\\
&= \Delta\underline{a}_n^{q-1}\left|\Delta\underline{a}_n^{q-1}+\delta\underline{a}_n^{q-1}\right|\Delta\underline{a}_n^{q-1}+\delta\lambda^q\delta\underline{\underline{a}}_n^{q-1}\left|\Delta\underline{a}_n^{q-1}+\right.\\
&\quad+\Delta\underline{a}_n^{q-1}\left|\delta\underline{a}_n^{q-1}+\delta\underline{a}_n^{q-1}\right|\delta\underline{a}_n^{q-1}+\delta\lambda^q\delta\underline{\underline{a}}_n^{q-1}\left|\delta\underline{a}_n^{q-1}+\right.\\
&\quad+\Delta\underline{a}_n^{q-1}\left|\delta\lambda^q\delta\underline{\underline{a}}_n^{q-1}+\delta\underline{a}_n^{q-1}\right|\delta\lambda^q\delta\underline{\underline{a}}_n^{q-1}+\delta\lambda^q\delta\underline{\underline{a}}_n^{q-1}\left|\delta\lambda^q\delta\underline{\underline{a}}_n^{q-1}\right.\\
&= \left[\Delta\underline{a}_n^{q-1}\right]^T\Delta\underline{a}_n^{q-1}+\left[\delta\underline{a}_n^{q-1}\right]^T\Delta\underline{a}_n^{q-1}+\left[\delta\lambda^q\delta\underline{\underline{a}}_n^{q-1}\right]^T\Delta\underline{a}_n^{q-1}+\\
&\quad+\left[\Delta\underline{a}_n^{q-1}\right]^T\delta\underline{a}_n^{q-1}+\left[\delta\underline{a}_n^{q-1}\right]^T\delta\underline{a}_n^{q-1}+\left[\delta\lambda^q\delta\underline{\underline{a}}_n^{q-1}\right]^T\delta\underline{a}_n^{q-1}+\\
&\quad+\left[\Delta\underline{a}_n^{q-1}\right]^T\delta\lambda^q\delta\underline{\underline{a}}_n^{q-1}+\left[\delta\underline{a}_n^{q-1}\right]^T\delta\lambda^q\delta\underline{\underline{a}}_n^{q-1}+\\
&\quad+\left[\delta\lambda^q\delta\underline{\underline{a}}_n^{q-1}\right]^T\delta\lambda^q\delta\underline{\underline{a}}_n^{q-1}\\
&= \left[\delta\underline{\underline{a}}_n^{q-1}\right]^T\delta\underline{\underline{a}}_n^{q-1}\left(\delta\lambda^q\right)^2+\\
&\quad+\left(\left[\delta\underline{\underline{a}}_n^{q-1}\right]^T\Delta\underline{a}_n^{q-1}+\left[\delta\underline{\underline{a}}_n^{q-1}\right]^T\delta\underline{a}_n^{q-1}+\left[\Delta\underline{a}_n^{q-1}\right]^T\delta\underline{\underline{a}}_n^{q-1}\right.\\
&\quad\left.+\left[\delta\underline{a}_n^{q-1}\right]^T\delta\underline{\underline{a}}_n^{q-1}\right)\delta\lambda^q+\\
&\quad+\left[\Delta\underline{a}_n^{q-1}\right]^T\Delta\underline{a}_n^{q-1}+\left[\delta\underline{a}_n^{q-1}\right]^T\Delta\underline{a}_n^{q-1}+\left[\Delta\underline{a}_n^{q-1}\right]^T\delta\underline{a}_n^{q-1}+\\
&\quad+\left[\delta\underline{a}_n^{q-1}\right]^T\delta\underline{a}_n^{q-1}\\
&= \left[\delta\underline{\underline{a}}_n^{q-1}\right]^T\delta\underline{\underline{a}}_n^{q-1}\left(\delta\lambda^q\right)^2+\\
&\quad+\left[2\left[\delta\underline{\underline{a}}_n^{q-1}\right]^T\left(\Delta\underline{a}_n^{q-1}+\delta\underline{a}_n^{q-1}\right)\right]\delta\lambda^q+\\
&\quad+\left[\Delta\underline{a}_n^{q-1}+\delta\underline{a}_n^{q-1}\right]^T\left(\Delta\underline{a}_n^{q-1}+\delta\underline{a}_n^{q-1}\right)
\end{aligned}
\tag{A.4}
$$

Equation (2.19) can be rewritten as

$$
\left(\lambda^q\right)^2=\left(\lambda^{q-1}+\delta\lambda^q\right)^2=\left(\lambda^{q-1}\right)^2+2\lambda^{q-1}\delta\lambda^q+\left(\delta\lambda^q\right)^2 \tag{A.5}
$$

Considering now equation (2.12b), the inclusion of equation (A.4) and equation (A.5) leads to

$$\begin{aligned}&\left[\delta\underline{\overline{\overline{a}}}_n^{q-1}\right]^T\delta\underline{\overline{\overline{a}}}_n^{q-1}\left(\delta\lambda^q\right)^2+\left[2\left[\delta\underline{\overline{\overline{a}}}_n^{q-1}\right]^T\left(\Delta\underline{a}_n^{q-1}+\delta\underline{\overline{a}}_n^{q-1}\right)\right]\delta\lambda^q+\\&+\left[\Delta\underline{a}_n^{q-1}+\delta\underline{\overline{a}}_n^{q-1}\right]^T\left(\Delta\underline{a}_n^{q-1}+\delta\underline{\overline{a}}_n^{q-1}\right)+\\&+b^2\left[\left(\lambda^{q-1}\right)^2+2\lambda^{q-1}\delta\lambda^q+\left(\delta\lambda^q\right)^2\right]\left[\Delta\underline{F}\right]^T\Delta\underline{F}-\Delta L^2=0\end{aligned}\tag{A.6}$$

or

$$\begin{aligned}&\left(\left[\delta\underline{\overline{\overline{a}}}_n^{q-1}\right]^T\delta\underline{\overline{\overline{a}}}_n^{q-1}+b^2\left[\Delta\underline{F}\right]^T\Delta\underline{F}\right)\left(\delta\lambda^q\right)^2+\\&\left[2\left[\delta\underline{\overline{\overline{a}}}_n^{q-1}\right]^T\left(\Delta\underline{a}_n^{q-1}+\delta\underline{\overline{a}}_n^{q-1}\right)+2b^2\lambda^{q-1}\left[\Delta\underline{F}\right]^T\Delta\underline{F}\right]\delta\lambda^q+\\&+\left[\Delta\underline{a}_n^{q-1}+\delta\underline{\overline{a}}_n^{q-1}\right]^T\left(\Delta\underline{a}_n^{q-1}+\delta\underline{\overline{a}}_n^{q-1}\right)+b^2\left(\lambda^{q-1}\right)^2\left[\Delta\underline{F}\right]^T\Delta\underline{F}-\Delta L^2=0\end{aligned}\tag{A.7}$$

Equation (A.7) can be written in the following form

$$a_1\left(\delta\lambda^q\right)^2+a_2\delta\lambda^q+a_3=0\tag{A.8}$$

being

$$\begin{aligned}a_1&=\left[\delta\underline{\overline{\overline{a}}}_n^{q-1}\right]^T\delta\underline{\overline{\overline{a}}}_n^{q-1}+b^2\left[\Delta\underline{F}\right]^T\Delta\underline{F}\\a_2&=2\left[\delta\underline{\overline{\overline{a}}}_n^{q-1}\right]^T\left(\Delta\underline{a}_n^{q-1}+\delta\underline{\overline{a}}_n^{q-1}\right)+2b^2\lambda^{q-1}\left[\Delta\underline{F}\right]^T\Delta\underline{F}\\a_3&=\left[\Delta\underline{a}_n^{q-1}+\delta\underline{\overline{a}}_n^{q-1}\right]^T\left(\Delta\underline{a}_n^{q-1}+\delta\underline{\overline{a}}_n^{q-1}\right)+b^2\left(\lambda^{q-1}\right)^2\left[\Delta\underline{F}\right]^T\Delta\underline{F}-\Delta L^2\end{aligned}\tag{A.9}$$

Appendix B

Tensile-softening diagrams

The expressions defining the diagrams to simulate the fracture mode I crack propagation described in section 3.3.2.2 are exposed in this appendix. For a better explanation of these expressions, Figure 3.6 and Figure 3.7 are represented again.

B.1 Tensile-Softening trilinear stress-strain diagram

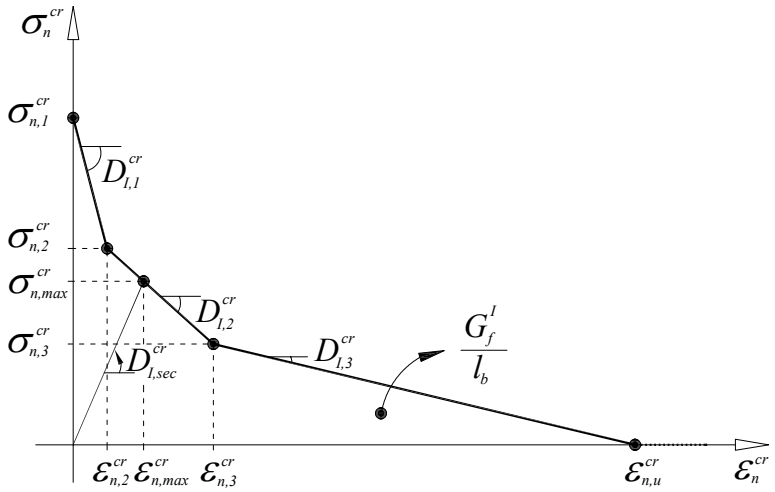

Figure B.1 – Trilinear stress-strain diagram to simulate the fracture mode I crack propagation.

The definition of the tensile-softening trilinear crack stress-strain diagram is made by the expressions (B.1)

$$\sigma_n^{cr}\left(\varepsilon_n^{cr}\right)=\begin{cases}\sigma_{n,1}^{cr}-\dfrac{\sigma_{n,1}^{cr}-\sigma_{n,2}^{cr}}{\varepsilon_{n,2}^{cr}}\varepsilon_n^{cr} & 0<\varepsilon_n^{cr}\le\varepsilon_{n,2}^{cr}\\ \sigma_{n,2}^{cr}-\dfrac{\sigma_{n,2}^{cr}-\sigma_{n,3}^{cr}}{\varepsilon_{n,3}^{cr}-\varepsilon_{n,2}^{cr}}\left(\varepsilon_n^{cr}-\varepsilon_{n,2}^{cr}\right) & \varepsilon_{n,2}^{cr}<\varepsilon_n^{cr}\le\varepsilon_{n,3}^{cr}\\ \sigma_{n,3}^{cr}-\dfrac{\sigma_{n,3}^{cr}}{\varepsilon_{n,u}^{cr}-\varepsilon_{n,3}^{cr}}\left(\varepsilon_n^{cr}-\varepsilon_{n,3}^{cr}\right) & \varepsilon_{n,3}^{cr}<\varepsilon_n^{cr}\le\varepsilon_{n,u}^{cr}\\ 0 & \varepsilon_n^{cr}>\varepsilon_{n,u}^{cr}\end{cases} \tag{B.1}$$

were

$$\sigma_{n,1}^{cr} = f_{ct} \tag{B.2a}$$

$$\sigma_{n,2}^{cr} = \alpha_1 \, \sigma_{n,1}^{cr} \tag{B.2b}$$

$$\sigma_{n,3}^{cr} = \alpha_2 \, \sigma_{n,1}^{cr} \tag{B.2c}$$

$$\varepsilon_{n,2}^{cr} = \xi_1 \, \varepsilon_{n,u}^{cr} \tag{B.2d}$$

$$\varepsilon_{n,3}^{cr} = \xi_2 \, \varepsilon_{n,u}^{cr} \tag{B.2e}$$

and $\varepsilon_{n,u}^{cr}$ obtained by equation (3.27).

Performing $\dfrac{d\sigma_n^{cr}\left(\varepsilon_n^{cr}\right)}{d\varepsilon_n^{cr}}$ and take into account the relations (B.2) and (3.27), the crack mode I stiffness modulus of each branch of the trilinear diagram is defined by the following equations

$$D_{I,1}^{cr} = -\frac{\left(1-\alpha_1\right)\left(\xi_1 + \alpha_1\xi_2 - \alpha_2\xi_1 + \alpha_2\right)}{2\xi_1}\frac{l_b f_{ct}^2}{G_f^I} \tag{B.3a}$$

$$D_{I,2}^{cr} = -\frac{\left(\alpha_1-\alpha_2\right)\left(\xi_1 + \alpha_1\xi_2 - \alpha_2\xi_1 + \alpha_2\right)}{2\left(\xi_2-\xi_1\right)}\frac{l_b f_{ct}^2}{G_f^I} \tag{B.3b}$$

$$D_{I,3}^{cr} = -\frac{\alpha_2\left(\xi_1 + \alpha_1\xi_2 - \alpha_2\xi_1 + \alpha_2\right)}{2\left(1-\xi_2\right)}\frac{l_b f_{ct}^2}{G_f^I} \tag{B.3 c}$$

B.2 Tensile-softening exponential stress-strain diagram

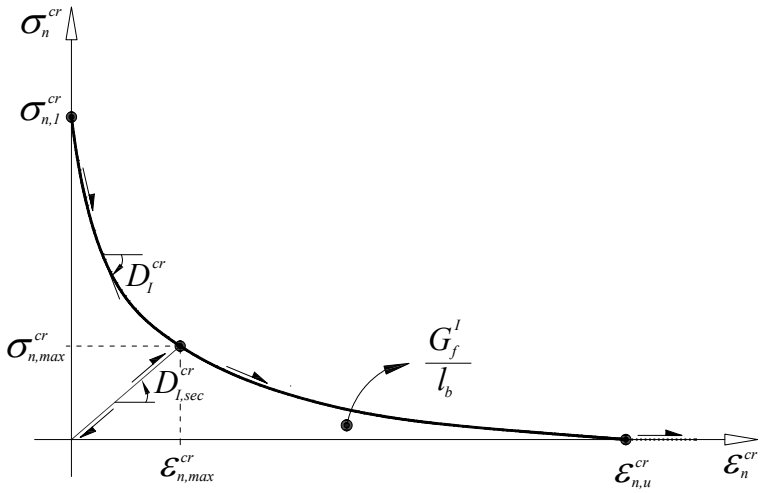

Figure B.2 – Exponential stress-strain diagram to simulate the fracture mode I crack propagation.

The definition of the tensile-softening exponential (Cornelissen et al. 1986) crack stress-strain diagram is made by the expressions (B.4)

$$\sigma_n^{cr}\left(\varepsilon_n^{cr}\right) =$$

$$= \begin{cases} \sigma_{n,1}^{cr}\left[\left(1+\left(c_1\dfrac{\varepsilon_n^{cr}}{\varepsilon_{n,u}^{cr}}\right)^3\right)\exp\left(-c_2\dfrac{\varepsilon_n^{cr}}{\varepsilon_{n,u}^{cr}}\right)-\dfrac{\varepsilon_n^{cr}}{\varepsilon_{n,u}^{cr}}\left(1+c_1^3\right)\exp\left(-c_2\right)\right] & 0<\varepsilon_n^{cr}\le\varepsilon_{n,u}^{cr} \\ 0 & \varepsilon_n^{cr}>\varepsilon_{n,u}^{cr} \end{cases} \quad \text{(B.4)}$$

being $c_1 = 3.0$ and c_2=6.93 for normalweight concrete.

Performing $\dfrac{d\sigma_n^{cr}\left(\varepsilon_n^{cr}\right)}{d\varepsilon_n^{cr}}$ and take into account that $\sigma_{n,1}^{cr} = f_{ct}$, the crack mode I stiffness modulus is defined by

$$D_I^{cr} = f_{ct}\left[3\left(c_1\frac{\varepsilon_n^{cr}}{\varepsilon_{n,u}^{cr}}\right)^2\frac{c_1}{\varepsilon_{n,u}^{cr}}\exp\left(-c_2\frac{\varepsilon_n^{cr}}{\varepsilon_{n,u}^{cr}}\right)+\right.$$
$$\left.+\exp\left(-c_2\frac{\varepsilon_n^{cr}}{\varepsilon_{n,u}^{cr}}\right)\left(-\frac{c_2}{\varepsilon_{n,u}^{cr}}\right)\left(1+\left(c_1\frac{\varepsilon_n^{cr}}{\varepsilon_{n,u}^{cr}}\right)^3\right)-\frac{1+c_1^3}{\varepsilon_{n,u}^{cr}}\exp\left(-c_2\right)\right] \tag{B.5}$$

were $\varepsilon_{n,u}^{cr}$ is obtained by equation (3.29).

In both tensile-softening diagrams a secant approach is used when unloading or reloading occur during the crack propagation. In this case the crack mode I stiffness modulus is calculated using this relation

$$D_{I,\sec}^{cr} = \frac{\sigma_{n,\max}^{cr}}{\varepsilon_{n,\max}^{cr}} \tag{B.6}$$

were $\sigma_{n,\max}^{cr}$ and $\varepsilon_{n,\max}^{cr}$ are the maximum crack normal stress and the maximum crack normal strain stored in the softening branch before the unloading occur (see Figure B.1 and Figure B.2).

Appendix C

First derivative of the function *f*

In this appendix the first derivative of the function f defined by equation (4.20) in order to the incremental crack strain vector $\Delta\underline{\varepsilon}_{\ell}^{cr}$ is presented.

Equation (4.18) can be rewritten as follows

$$f\left(\Delta\underline{\varepsilon}_{\ell}^{cr}\right)=\underline{\sigma}_{\ell,prev}^{cr^*}+\Delta\underline{\sigma}_{\ell}^{cr}-\underline{T}^{cr}\,\underline{\sigma}_{prev}-\underline{T}^{cr}\,\underline{D}^{co}\Delta\underline{\varepsilon}+\underline{T}^{cr}\,\underline{D}^{co}\left[\underline{T}^{cr}\right]^{T}\Delta\underline{\varepsilon}_{\ell}^{cr} \tag{C.1}$$

Considering

$$\underline{\sigma}_{\ell,prev}^{cr^*}=\begin{bmatrix}\sigma_{n,prev}^{cr}\\ D_{II}^{cr}\,\gamma_{t,prev}^{cr}\end{bmatrix}_{\ell}\;;\;\Delta\underline{\sigma}_{\ell}^{cr}=\begin{bmatrix}D_{I}^{cr}\Delta\varepsilon_{n}^{cr}\\ D_{II}^{cr}\Delta\gamma_{t}^{cr}\end{bmatrix}_{\ell}\;;\;\underline{T}^{cr}\,\underline{\sigma}_{prev}=\begin{bmatrix}A_1\\ A_2\end{bmatrix} \tag{C.2a}$$

and

$$\underline{T}^{cr}\,\underline{D}^{co}\Delta\underline{\varepsilon}=\begin{bmatrix}B_1\\ B_2\end{bmatrix}\;;\;\underline{T}^{cr}\,\underline{D}^{co}\left[\underline{T}^{cr}\right]^{T}=\begin{bmatrix}C_{11} & C_{12}\\ C_{21} & C_{22}\end{bmatrix} \tag{C.2b}$$

equation (C.1) can be written as

$$\begin{bmatrix}F_1\\ F_2\end{bmatrix}=\begin{bmatrix}\sigma_{n,prev}^{cr}\\ D_{II}^{cr}\,\gamma_{t,prev}^{cr}\end{bmatrix}_{\ell}+\begin{bmatrix}D_{I}^{cr}\Delta\varepsilon_{n}^{cr}\\ D_{II}^{cr}\Delta\gamma_{t}^{cr}\end{bmatrix}_{\ell}-\begin{bmatrix}A_1\\ A_2\end{bmatrix}-\begin{bmatrix}B_1\\ B_2\end{bmatrix}+\begin{bmatrix}C_{11} & C_{12}\\ C_{21} & C_{22}\end{bmatrix}\begin{bmatrix}\Delta\varepsilon_{n}^{cr}\\ \Delta\gamma_{t}^{cr}\end{bmatrix} \tag{C.3}$$

The first derivative of (C.1) is necessary for the iteration q of the Newton-Raphson method. Taking into account equation (C.3), the evaluation of the first derivative of (C.1) becomes

$$\frac{\partial f\left(\Delta \underline{\varepsilon}_{\ell}^{cr}\right)}{\partial \Delta \underline{\varepsilon}_{\ell}^{cr}} = \begin{bmatrix} \dfrac{\partial F_1}{\partial \Delta \varepsilon_n^{cr}} & \dfrac{\partial F_1}{\partial \Delta \gamma_t^{cr}} \\ \dfrac{\partial F_2}{\partial \Delta \varepsilon_n^{cr}} & \dfrac{\partial F_2}{\partial \Delta \gamma_t^{cr}} \end{bmatrix} \tag{C.4}$$

being

$$\frac{\partial F_1}{\partial \Delta \varepsilon_n^{cr}} = D_I^{cr} + C_{11} \quad ; \quad \frac{\partial F_1}{\partial \Delta \gamma_t^{cr}} = C_{12} \tag{C.5a}$$

and

$$\begin{aligned} \frac{\partial F_2}{\partial \Delta \varepsilon_n^{cr}} &= \frac{\partial D_{II}^{cr}}{\partial \Delta \varepsilon_n^{cr}} \gamma_{t,prev}^{cr} + \frac{\partial D_{II}^{cr}}{\partial \Delta \varepsilon_n^{cr}} \Delta \gamma_t^{cr} + C_{21} = \frac{\partial D_{II}^{cr}}{\partial \Delta \varepsilon_n^{cr}} \left(\gamma_{t,prev}^{cr} + \Delta \gamma_t^{cr}\right) + C_{21} \\ &= \frac{\partial D_{II}^{cr}}{\partial \Delta \varepsilon_n^{cr}} \gamma_t^{cr} + C_{21} \end{aligned} \tag{C.5b}$$

$$\frac{\partial F_2}{\partial \Delta \gamma_t^{cr}} = D_{II}^{cr} + C_{22} \tag{C.5c}$$

Substituting equation (C.5) in equation (C.4), results

$$\frac{\partial f\left(\Delta \underline{\varepsilon}_{\ell}^{cr}\right)}{\partial \Delta \underline{\varepsilon}_{\ell}^{cr}} = \begin{bmatrix} D_I^{cr} + C_{11} & C_{12} \\ \dfrac{\partial D_{II}^{cr}}{\partial \Delta \varepsilon_n^{cr}} \gamma_t^{cr} + C_{21} & D_{II}^{cr} + C_{22} \end{bmatrix} \tag{C.6}$$

or

$$\frac{\partial f\left(\Delta \underline{\varepsilon}_{\ell}^{cr}\right)}{\partial \Delta \underline{\varepsilon}_{\ell}^{cr}} = \begin{bmatrix} D_I^{cr} & 0 \\ 0 & D_{II}^{cr} \end{bmatrix} + \begin{bmatrix} 0 & 0 \\ \dfrac{\partial D_{II}^{cr}}{\partial \Delta \varepsilon_n^{cr}} \gamma_t^{cr} & 0 \end{bmatrix} + \begin{bmatrix} C_{11} & C_{12} \\ C_{21} & C_{22} \end{bmatrix} \tag{C.7}$$

Knowing that

$$\underline{D}^{cr} = \begin{bmatrix} D_I^{cr} & 0 \\ 0 & D_{II}^{cr} \end{bmatrix} \tag{C.8}$$

and taking into account the second equation of (C.2b), equation (C.7) can be written in a matrix form as follows

$$\frac{\partial f\left(\Delta \underline{\varepsilon}_{\ell}^{cr}\right)}{\partial \Delta \underline{\varepsilon}_{\ell}^{cr}} = \underline{D}^{cr} + \overline{\underline{D}}^{cr} + \underline{T}^{cr}\ \underline{D}^{co}\left[\underline{T}^{cr}\right]^{T} \tag{C.9}$$

where

$$\overline{\underline{D}}^{cr} = \begin{bmatrix} 0 & 0 \\ \dfrac{\partial D_{II}^{cr}}{\partial \Delta \varepsilon_n^{cr}} \gamma_t^{cr} & 0 \end{bmatrix} \tag{C.10}$$